3D Morpho-kinematic modeling of Supernova Remnants

PhD Thesis

Sophia Derlopa

National Observatory of Athens

University of Athens - Department of Physics

July 2021

Supervisor Dr. Panos Boumis - National Observatory of Athens

ΕΛΛΗΝΙΚΗ ΔΗΜΟΚΡΑΤΙΑ
Εθνικόν και Καποδιστριακόν
Πανεπιστήμιον Αθηνών
ΙΔΡΥΘΕΝ ΤΟ 1837

IAASARS

3D Morpho-kinematic modeling
of Supernova Remnants

PhD Thesis

Sophia Derlopa

National Observatory of Athens

University of Athens - Department of Physics

July 2021

Consultant Committee

Dr. Panos Boumis

Research Director - National Observatory of Athens

Prof. Despina Hatzidimitriou

Professor - National Kapodistrian University of Athens,

Department of Physics

Dr. Wolfgang Steffen

Researcher A - University of Mexico

Στους γονείς μου,

Μαρίνα και Κωνσταντίνο

To my parents,

Marina and Konstantinos

Αν κοιτάζεις τη φύση και δεν βλέπεις τον Θεό σε αυτήν,

ποια λόγια να βρω εγώ για να σε πείσω;

Άγιος Ιωάννης ο Χρυσόστομος

If you look at the nature around you and you cannot see God,

what words can I find to convince you?

Saint John Chrysostom

Abstract

The subject of research of the current Thesis, was the reconstruction -for the first time- of the three dimensional (3D) Morpho-kinematic (MK) modeling of a Supernova Remnant (SNR). The innovation of this project lies in the fact that, for the first time, high resolution observational data in imaging and spectroscopy were used for the creation of a model that would reproduce both the morphology and the kinematic field of a Supernova Remnant.

SNRs are these very beautiful and also complicated nebulae that remain after the massive explosion (Supernova) of certain types of stars. Their gaseous debris carry information about the properties of the progenitor star, and also manifest the attributes of the ambient circum-stellar (CSM)/ interstellar (ISM) medium. Therefore, SNRs are an ideal "laboratory" for probing the aftermaths of certain types of stars and their environment, and subsequently, to deeper understand the stellar evolution mechanisms and to decode an interstellar region.

With respect to their morphology, although there are cases of spherically symmetric SNRs, however -traditionally- they illustrate a wide range of complex structures. Any deviation from symmetry implies inhomogeneity in the initial explosion conditions and/or in the CSM/ISM medium in the vicinity of the SNR. This is depicted in the velocity field of the remnant as well, as different parts of it may expand at different velocities, depending on the environment they encounter during their expansion.

In order to study the morphology of a SNR, we obtain telescope images. However, the fact that these images are two-dimensional (2D), is a physical restriction that prevents us from having an overall perspective of the object under study. Therefore, in order to surmount this obstacle and to obtain the now missing information in the 3rd dimension, we create 3D models of the objects. The information in the 3rd dimension that a 3D modeling provide us with, renders the 3D visualization of an object a very powerful tool in the field of investigation.

In particular, a 3D Morpho-kinematic model presents i) the structure of the object and ii) its velocity field, both in three dimensions. It is a time- and distance-independent model, that presents the object at the time of its observation. Through this model, the object "reveals" itself and from the derived information we can trace back to the explosion conditions and obtain indirect evidences for the vicinity of the SNR.

For the modeling we employed the astronomical software SHAPE, in which imaging and spectroscopic data are used for the reconstruction of the 3D modeling. SHAPE is already established in the field of Planetary Nebulae (PNe), where many important projects have been performed by its use. However, it had never been applied in a SNR before, due to the high degree of complexity that SNRs present (both in morphology and kinematics), and due to the

large amount of observational data needed for the full covering of extended objects like SNRs. This is why, for the needs of code-learning, I first applied SHAPE code in the case of the Planetary Nebula Hb4, which was already under study.

Hb4 shows an unusual kinematic behaviour as, its expelled bipolar outflows decelerate as they recede from the central star. The model helped us to clarify the nature and the morphology of these outflows and to investigate their kinematics. Furthermore, the model revealed the periodicity in the ejection of the outflows, while it also gave us clues about the characteristics of the progenitor star, and the conditions of the local ISM. The results were published in Derlopa et al. 2019, and are described in Chapter 4.

After the modeling of Hb4 and having obtained experience in SHAPE, I proceeded to the much more complicated case of the modeling of a SNR, which is the first 3D Morpho-kinematic model of a SNR ever created.

The selected object was the SNR VRO 42.05.01. It is a remnant of great scientific interest, whose peculiar morphology indicates a very active evolutionary history. The physical results that the model gave, contributed a lot to a more thorough interpretation of the observational data. For example, the model revealed a third component in the structure of VRO that was not obvious in the 2D data, along with the regions of two shock break-outs. The results were published in Derlopa et al. 2020, and are described in Chapter 5.

Finally, it is worth mentioning that the results of a 3D MK model can be used as input information for the creation of Hydrodynamical (HD) models too. This has already been tested in the case of VRO, where the MK and the HD models acted complimentary for the interpretation of VRO properties and evolutionary history.

Completing the 3D MK modeling of VRO and having in mind the very important physical results deduced from the model, we can argue that a new, valuable tool to the methods of probing SNRs has been added. Since morphology and kinematics are indissolubly linked to each other, it was showed that such a 3D visualisation can contribute to the decoding of the complexity of SNRs both in their shape and their velocity field. This opens the way for a more thorough investigation of these very interesting and complicated objects, the probing of which contributes to the understanding of stellar evolution.

Περίληψη

Το αντικείμενο έρευνας της παρούσας Διδακτορικής διατριβής, είναι η δημιουργία τού πρώτου τρισ-διάστατου (3Δ) Μορφοκινηματικού (ΜΚ) μοντέλου ενός Υπολείμματος Υπερκαινοφανούς Αστέρος (ΥΥΑ). Η πρωτοτυπία αυτής της εργασίας έγκειται στο ότι για πρώτη φορά, υψηλής ανάλυσης εικόνες και φάσματα χρησιμοποιούνται για την αναπαραγωγή τής μορφολογίας και της κινηματικής ενός ΥΥΑ. Η εργασία αυτή ήταν ιδιαίτερα απαιτητική λόγω της πολυπλοκότητας της μορφολογίας τού υπό μελέτη αντικειμένου, καθώς και των διαφορετικών ταχυτήτων των υποπεριοχών του, όπως αναλυτικά θα παρουσιαστεί παρακάτω.

-Τί είναι τα ΥΥΑ και γιατί τα μελετούμε:

Τα ΥΥΑ είναι εκείνα τα πολύ όμορφα αλλά ταυτόχρονα περίπλοκα νεφελώματα που απομένουν μετά την καταστροφική έκρηξη αστέρων συγκεκριμένων τύπων, οι οποίοι ονομάζονται προγεννήτορες αστέρες. Η έκρηξη αυτή σηματοδοτεί τον "θάνατο" (Supernova explosion) του αστεριού και είναι της τάξεως των 10^{51} erg. Ο προγεννήτορας αστέρας (με βάση τα επικρατέστερα μοντέλα) μπορεί να είναι ή αστέρι μεγάλης μάζας ($M > 8$ ηλιακές μάζες) που υπό ορισμένες συνθήκες καταρρέει υπό το βάρος τής ίδιας του της βαρύτητας, ή λευκός νάνος που ανήκει σε διπλό σύστημα αστέρων και τελικώς υφίσταται μία θερμοπυρηνική έκρηξη.

Αυτά τα αέρια θραύσματα "κουβαλούν" πληροφορίες σχετικά με τις φυσικές ιδιότητες του προγεν-νήτορος αστέρος που τα δημιούργησε. Τα νεφελώματα αυτά δεν είναι στατικά, αλλά εξελίσσονται και διαδίδονται στον μεσοαστρικό χώρο λόγω τής ορμής που προσλαμβάνουν από το κύμα σοκ τής αρ-χικής έκρηξης. Κατά τη διάδοσή τους αυτή αλληλεπιδρούν με το ενδοαστρικό ή/και το μεσοαστρικό υλικό, αποκαλύπτοντας έτσι τα ιδιαίτερα χαρακτηριστικά των τελευταίων (π.χ. παρουσία μοριακών νεφελωμάτων, βαθμίδες στην πυκνότητα, διακυμάνσεις σε συγκέντρωση χημικών στοιχείων). Επι-πλέον, τα ΥΥΑ είναι υπεύθυνα για την "τροφοδοσία" τού μεσοαστρικού περιβάλλοντος με χημικά στοιχεία, τα οποία παρήχθησαν στο εσωτερικό τού προγεννήτορος αστέρος και εκτινάχθηκαν στον διαστρικό χώρο μέσω τής έκρηξης. Δεδομένου ότι με τον θάνατο αυτό των αστέρων απελευθερώνο-νται τεράστια ποσά ενέργειας, αυτή η ενέργεια επηρεάζει τη δυναμική ισορροπία τού γαλαξία (ή τής περιοχής του) που φιλοξενεί αυτού τού τύπου τα αστέρια.

Από τα παραπάνω αντιλαμβανόμαστε ότι, ακριβώς επειδή τα ΥΥΑ χρονικά ανήκουν στο "μεταθανά-τιο στάδιο" των αστέρων, αποτελούν τον συνδετικό κρίκο μεταξύ τού τελευταίου σταδίου τής ζωής ενός αστέρος και της αλληλεπίδρασής του με το μεσοαστρικό περιβάλλον. Συνεπώς, οι πληροφορίες που μπορούμε να εξάγουμε από αυτά είναι πολύτιμες, διότι τελικώς συνεισφέρουν στα μοντέλα τής αστρικης εξέλιξης.

-Τρισδιάστατη (3Δ) μοντελοποίηση στην Αστροφυσική:

Οι εικόνες που λαμβάνουμε με τα τηλεσκόπια είναι δισδιάστατες (2Δ). Αυτομάτως αυτό σημαίνει ότι δεν έχουμε καμία πληροφορία για την τρίτη διάσταση του αντικείμενου που μελετούμε, δηλαδή για τη μεριά του που σε εμάς δεν είναι ορατή. Αυτό είναι είναι ένας φυσικός περιορισμός, η άρση τού οποίου μπορεί να επιτευχθεί μέσα από τη δημιουργία ενός 3Δ μοντέλου τού αντικειμένου αυτού.

Πιο συγκεκριμένα, ένα 3Δ μοντέλο μπορεί να αποκαλύψει κατ΄ αρχάς τυχόν αποκλίσεις από τη συμμετρία τού αντικειμένου. Αυτό είναι ιδιαιτέρως σημαντικό, διότι οι ασυμμετρίες οποιασδήποτε φύσεως (μορφολογικής, κινηματικής, χημικής διαστρωμάτωσης κτλ) έμμεσα μαρτυρούν ασυμμετρία α) στον αρχικό μηχανισμό έκρηξης ή/και β) στο περιβάλλον μέσα στο οποίο το ΥΥΑ εξελίσσεται και διαδίδεται. Επιπλέον, με τη δημιουργία τού 3Δ μοντέλου, μπορούν να αποκαλυφθούν εσωτερικές δομές οι οποίες είναι ¨αόρατες᾿ σε μία 2Δ εικόνα. Ένα άλλο κλασικό πρόβλημα των 2Δ εικόνων που παίρνουμε με τα τηλεσκόπια, είναι ότι δεν γνωρίζουμε την κλίση τού αντικειμένου σε σχέση με το επίπεδο τού ουρανού (βλέπουμε μόνο την προβολή του πάνω στο επίπεδο τού ουρανού). Με τη δημιουργία ενός 3Δ μοντέλου λοιπόν, μπορούμε να περιορίσουμε -κατά το δυνατόν- τη γεωμετρία τού αντικειμένου τόσο στη μορφολογία του όσο και στον προσανατολισμό του. Όλες οι παραπάνω πληρο-φορίες που μπορούν να αντληθούν από ένα 3Δ μοντέλο, συνεισφέρουν κατά πολύ στην πληρέστερη εικόνα τού αντικειμένου και εν τέλει στην καλύτερη ερμηνεία των παρατηρησιακών του δεδομένων.

-3Δ Μορφοκινηματική (ΜΚ) μοντελοποίηση:

Στην παρούσα εργασία, το είδος τού 3Δ μοντέλου που παρουσιάζεται ονομάζεται Μορφοκι-νηματικό. Ουσιαστικά, το μοντέλο αυτό αποτυπώνει ένα στιγμιότυπο τού αντικειμένου (δηλ. δεν παρουσιάζει την εξέλιξη του στο χρόνο) και αναπαράγει τη μορφολογία του και το πεδίο ταχυτήτων του στις τρεις διαστάσεις.

Για την πραγματοποίηση αυτού του μοντέλου χρησιμοποιήσαμε τον αστρονομικό κώδικα SHAPE (Steffen et al. 2011). Πρόκειται για ένα λογισμικό, ήδη πολύ επιτυχημένο και καθιερωμένο στον τομέα των Πλανητικών Νεφελωμάτων (ΠΝ), με τη χρήση τού οποίου έχει παραχθεί πλήθος δημοσιεύσεων σχετικών με την 3Δ μοντελοποίηση της συγκεκριμένης κατηγορίας αστρονομικών αντικειμένων.

Ο τρόπος λειτουργίας του μπορεί να περιγραφεί συνοπτικά σε τρία βήματα:

1) Στο SHAPE χρησιμοποιούμε δύο ειδών παρατηρησιακά δεδομένα: α) μία εικόνα σε συγκεκριμένο μήκος κύματος που να αποτυπώνει όλη τη μορφολογία τού αντικειμένου, και β) φάσματα υψηλής ανάλυσης τύπου echelle στο ίδιο μήκος κύματος, από τα οποία εξάγουμε τα λεγόμενα διαγράμ-ματα Θέσης-Ταχύτητας (ΘΤ). Από τα διαγράμματα αυτά λαμβάνουμε την κινηματική πληροφορία που χρειαζόμαστε για το μοντέλο, καθότι μας δίνουν την ταχύτητα κατά μήκος τής ευθείας οράσεως της περιοχής τού αντικειμένου όπου έχουμε πάρει φάσμα.

2) Στη συνέχεια, χρησιμοποιώντας τα εργαλεία τού SHAPE ξεκινάμε με τη δημιουργία μιας 3Δ δομής σε μορφή πλέγματος, η οποία να είναι κατά το δυνατόν όμοια με τη δομή που βλέπουμε στην 2Δ

παρατηρησιακή εικόνα. Με βάση αυτό το 3Δ πλέγμα, το SHAPE δημιουργεί το αντίστοιχο συνθετικό διάγραμμα ΘΤ που αντιστοιχεί σε μια συγκεκριμένη περιοχή τού αντικειμένου που έχουμε επιλέξει.

3) Αφού έχουμε αναπαράγει σε πρώτη φάση τα συνθετικά δεδομένα σε μορφολογία και κινηματική, ο στόχος τώρα είναι να επιτύχουμε την καλύτερη δυνατή συμφωνία μεταξύ των συνθετικών και των παρατηρησιακών δεδομένων. Αυτό το επιτυγχάνουμε χρησιμοποιώντας μία σειρά από εργαλεία που μας παρέχει το SHAPE και ονομάζονται Τροποποιητές (Modifiers). Με τους Τροποποιητές μπορούμε να επιλέξουμε και να μεταβάλλουμε φυσικές παραμέτρους τού μοντέλου (π.χ. ταχύτητα, πυκνότητα, σκόνη κτλ) αλλά και γεωμετρικές (π.χ. σχήμα δομής, κλίση, προσανατολισμό κτλ). Συνεχίζουμε να τροποποιούμε κατάλληλα τις παραμέτρους αυτές, συγκρίνοντας πάντα το αποτέλεσμα του μοντέλου με τα παρατηρησιακά δεδομένα σε εικόνα και διαγράμματα ΘΤ. Τέλος, καταλήγουμε σε εκείνο το μοντέλο που αναπαράγει πιο πιστά τις παρατηρήσεις, και ταυτόχρονα έχει φυσικό νόημα.

Παρόλο που το λογισμικό SHAPE είναι ευρέως διαδεδομένο στον τομέα των Πλανητικών Νεφε-λωμάτων, ωστόσο ποτέ δεν είχε εφαρμοσθεί στην περίπτωση ενός ΥΥΑ μέχρι στιγμής. Ο πρώτος λόγος είναι ότι, συνήθως τα ΥΥΑ είναι πολύ εκτενέστερα αντικείμενα σε σχέση με τα ΠΝ. Αυτό σημαίνει ότι απαιτείται μεγάλος όγκος παρατηρησιακών δεδομένων προκειμένου να καλυφθεί όλη η περιοχή τους, ειδικά στο κομμάτι των φασματοσκοπικών παρατηρήσεων. Επιπλέον, οι ανομοιογένειες που τα ΥΥΑ συνήθως παρουσιάζουν τόσο στη μορφολογία τους όσο και στην κινηματική τους, είναι ένας επιπλέον παράγοντας δυσκολίας για την 3Δ μοντελοποίησή τους.

Για τους λόγους αυτούς, πριν προχωρήσω απευθείας στην μοντελοποίηση ενός ΥΥΑ, πρώτα εφήρ-μοσα τον κώδικα στην περίπτωση του Πλανητικού Νεφελώματος Hb4, το οποίο ήδη ήταν υπό μελέτη. Μετά την ολοκλήρωση αυτής της εργασίας, τα αποτελέσματα της οποίας δημοσιεύθηκαν στο έγκριτο επιστημονικό περιοδικό MNRAS (Derlopa et al. 2019), και έχοντας αποκτήσει την απαιτούμενη εμ-πειρία στην εφαρμογή τού SHAPE, προχώρησα στην -κατά πολύ πολυπλοκότερη- περίπτωση του 3Δ μοντέλου τού ιδιαιτέρως περίπλοκου ΥΥΑ VRO 42.05.01 (Derlopa et al. 2020) Στη συνέχεια παρουσιάζονται διαδοχικά τα μοντέλα και για τα δύο αυτά αντικείμενα.

Πλανητικό Νεφέλωμα Hb4:

Στην Εικ. 3.1, σελ. 107 φαίνεται η εικόνα του ΠΝ από το Hubble Space Telescope - HST. Όπως μπορούμε να δούμε, αποτελείται από ένα νεφέλωμα το οποίο περιβάλλει τον κεντρικό αστέρα, ενώ εκατέρωθεν αυτού του νεφελώματος διακρίνουμε ένα ζεύγος εκροών (bipolar outflows). Σύμφωνα με τη θεωρία τής εξέλιξης των ΠΝ, το νεφέλωμα αυτό είναι ουσιαστικά τα εξωτερικά στρώματα της ατμόσφαιρας του αστέρα, τα οποία ο αστέρας απέβαλε κατά το τέλος της AGB φάσης του. Στη συνέχεια, το νεφέλωμα αυτό ιονίζεται λόγω των υπεριωδών φωτονίων που εκπέμπονται από τον κεντρικό αστέρα.

Σχετικά με τις εκροές που αναφέραμε, το χαρακτηριστικό τους είναι ότι, ενώ αρχικά είχαν χαρακτηριστεί σαν jets, που σημαίνει ότι θα περιμέναμε να έχουν ενιαία ταχύτητα σε όλη τους την έκταση, ωστόσο το φάσμα τους έδειξε ότι στο εσωτερικό τους υπήρχε βαθμίδα ταχύτητας. Για την ακρίβεια, τα μέρη των jets που είναι πιο κοντά στον αστέρα κινούνται πιο γρήγορα σε σχέση με τα πιο απομακρυσμένα από τον αστέρα. Αυτή η ιδιαιτερότητα ήταν το κίνητρό μας για να προχωρήσουμε στην 3Δ μοντελοποίηση αυτού του αντικειμένου, με σκοπό την αποσαφήνιση της φύσης και της μορφολογίας αυτών των εκροών, καθώς και περαιτέρω μελέτη της κινηματικής τους συμπεριφοράς.

Τα παρατηρησιακά δεδομένα που χρησιμοποιήσαμε στο SHAPE είναι α) εικόνα από το HST στην [N II] γραμμή εκπομπής (βλ. Εικ. 3.1, σελ. 107), και β) υψηλής ανάλυσης echelle φάσμα, επίσης στην [N II] γραμμή (βλ. Εικ. 3.3 σελ. 109). Προκειμένου να οριοθετήσουμε -κατά το δυνατόν- την κατεύθυνση της εκπομπής των εκροών, πρώτα ξεκινήσαμε με την μοντελοποίηση του τόρου τού ΠΝ, ώστε να τον έχουμε σαν σημείο αναφοράς.

Το τελικό μοντέλο παρουσιάζεται στην Εικ. 4.2, σελ. 128. Σε αυτό, η μπλε έλλειψη είναι ο τόρος τού Πλανητικού, η πορτοκαλί γραμμή είναι μια ευθεία κάθετη στο επίπεδο του τόρου, ενώ το ζεύγος των εκροών είναι μοντελοποιημένο εκατέρωθεν του τόρου. Τα αποτελέσματα τού μοντέλου είναι τα εξής:

- Σχετικά με τη φύση των εκροών, καταλήξαμε στο ότι δεν πρόκειται για ενιαίες δομές jets, αλλά για ομάδες αερίων συσσωματωμάτων που ονομάζονται knots. Στο SHAPE τα knots μοντελοποιήθηκαν σαν μικρές σφαίρες, όπως φαίνεται και στην Εικ. 4.2. Για καθεμία από αυτές τις σφαίρες βρήκαμε την ταχύτητα εκτόξευσής της, την απόστασή της από τον κεντρικό αστέρα, καθώς και την κινηματική της ηλικία (χρονικό διάστημα από τη στιγμή τής εκτόξευσής τής μέχρι να φτάσει στο σημείο που την παρατηρούμε τώρα). Οι ίδιες παράμετροι υπολογίστηκαν και για τον τόρο.

- Με βάση το μοντέλο, τα knots δεν εκπέμφθηκαν κατά τυχαίο τρόπο, αλλά κατά ζευγάρια εκατέρωθεν του κεντρικού αστέρα. Για την ακρίβεια, και με βάση την ανάλυση (resolution) της εικόνας και του φάσματος, βρήκαμε τέσσερα ζευγάρια knots. Στο μοντέλο, τα knots που ανήκουν στο ίδιο ζευγάρι παρουσιάζονται με το ίδιο χρώμα.

- Ιδιαίτερου ενδιαφέροντος είναι η περιοδικότητα που παρουσιάζουν τα ζευγάρια αυτά: εκπέμπονται περίπου κάθε 200-250 χρόνια. Επίσης, αναφορικά με τη γωνία εκτόξευσής τους, αυτή δεν είναι κάθετη στο επίπεδο τού τόρου, αλλά παρουσιάζει μια απόκλιση ∼5 μοίρες. Αυτό μπορεί να έχει προκληθεί από περιστροφή τού κεντρικού αστέρα τού Πλανητικού.

- Η επιβράδυνση που παρουσιάζουν τα knots κατά την απομάκρυνσή τους από τον κεντρικό αστέρα είναι όντως υπαρκτή, και παρουσιάζεται στο διάγραμμα στην Εικ. 4.6, σελ. 131. Πράγματι, τα πιο απομακρυσμένα ζευγάρια knots κινούνται πιο αργά σε σχέση με τα κοντινότερα στον κεντρικό αστέρα. Αυτό μπορεί να αποδοθεί σε μία παρουσία βαθμίδας πυκνότητας στην περιοχή τού Πλανητικού, η οποία προκάλεσε αυτή την επιβράδυνση.

- Σχετικά με τον τόρο, η ταχύτητα διαστολής του σύμφωνα με το μοντέλο (∼14 km/sec) είναι σύμφωνη με τις ταχύτητες τοροειδών δομών σε Πλανητικά Νεφελώματα από τη βιβλιογραφία, στα οποία όμως ο κεντρικός αστέρας είναι "τύπου Wolf-Rayet" ([WR]). Αυτό δεν σημαίνει ότι έχει τη μάζα που έχουν οι κλασικοί Wolf-Rayet αστέρες, αλλά ότι μόνο το φάσμα του συμφωνεί με αυτό ενός Wolf-Rayet αστέρα.

- Επιλέον, η διπολική εκροή μάζας που παρουσιάζει το Πλανητικό, είναι ισχυρή ένδειξη διπολικού συστήματος αστέρων στο εσωτερικό του. Με βάση τα παραπάνω, μπορούμε να πούμε ότι ο ένας εκ των δύο αστέρων τού συστήματος αυτού, πιθανόν να είναι [WR].

- Προτεινόμενο μοντέλο για το Πλανητικό Νεφέλωμα Hb4:

Το 3Δ Μορφοκινηματικό μοντέλο τού ΠΝ Hb4 αποκάλυψε τη μορφολογία και την κινηματική των διπολικών του εκροών, που ήταν και από τους αρχικούς στόχους αυτής της εργασίας, αλλά επιπλέον έδωσε πολύ σημαντικά αποτελέσματα που συνεισφέρουν στην περιγραφή βασικών του χαρακτηριστικών. Με βάση τα αποτελέσματα του 3Δ μοντέλου λοιπόν, το σενάριο που προτείνουμε για την ερμηνεία των φυσικών χαρακτηριστικών τού αντικειμένου αυτού, είναι ότι πρόκειται για έναν περιστρεφόμενο αστέρα τύπου Wolf-Rayet, ο οποίος εκπέμπει knots εκατέρωθεν του κεντρικού του αστέρα με περίοδο 200-250 χρόνια. Παρόμοιος μηχανισμός έχει προταθεί για τα Πλανητικά Νεφελώματα NGC 6778 και Fleming 1, στα οποία έχουν παρατηρηθεί ¨καμπυλωμένες εκροές από συνεχόμενη εκπομπή knots".

Υπόλειμμα Υπερκαινοφανούς Αστέρα: VRO 42.05.01

Το γαλαξιακό ΥΥΑ VRO 42.05.01, ή απλά VRO σε συντομογραφία, είναι ένα αντικείμενο που, λόγω της ιδιαίτερης μορφολογίας του, έχει τραβήξει το ενδιαφέρον τής επιστημονικής κοινότητας εδώ και πολλές δεκαετίες. Όπως φαίνεται στην Εικ. 5.2, σελ. 145, αποτελείται από δύο βασικές δομές: α) μία σχεδόν σφαιρική που ονομάζεται "shell", και β) μία πιο επιμηκυμένη/τοξοειδή που ονομάζεται "wing". Τα μοντέλα που έχουν προταθεί για την ερμηνεία τής μορφολογίας του (Landecker et al. 1982, Pineault et al. 1987, Arias et al. 2018,2019) στηρίζονται στο ίδιο σενάριο (εξαίρεση αποτελεί το σενάριο για το VRO που έχει προταθεί από τον Αλέξανδρο Χιωτέλλη, και που παρουσιάζεται ξεχωριστά παρακάτω). Σύμφωνα με αυτό, η έκρηξη του προγεννήτορος αστέρος συνέβει κοντά στο όριο δύο περιοχών διαφορετικών πυκνοτήτων. Το μέρος τού εκτιναχθέντος -λόγω της έκρηξης-υλικού διαδόθηκε στην περιοχή υψηλής πυκνότητας δημιουργώντας το "shell", ενώ το υπόλοιπο εκτιναχθέν υλικό διαδόθηκε στην περιόχή χαμηλής πυκνότητας δημιουργώντας έτσι το "wing". Παρόλο που αυτό το προτεινόμενο σενάριο ήταν αποδεκτό για πάνω από 30 χρόνια, ωστόσο έχει το βασικό μειονέκτημα ότι απαιτεί πολύ συγκεκριμένες συνθήκες πυκνότητας στην περιοχή τού ΥΥΑ. Επιπλέον σύμφωνα με τη δημοσίευση τής Arias et al. 2019, δεν υπάρχει τέτοια ένδειξη διαφοράς πυκνότητας στον περιβάλλοντα χώρο τού VRO. Συνεπώς, υπήρχε η ανάγκη για ένα καινούριο μοντέλο που να

εξηγεί επαρκώς τα χαρακτηριστικά αυτού του αντικειμένου. Αυτό ακριβώς ήταν το κίνητρό μας ώστε να επιλέξουμε το συγκεκριμένο αντικείμενο για τη δημιουργία τού πρώτου 3Δ Μορφοκινηματικού μοντέλου ενός ΥΥΑ.

Τα παρατηρησιακά δεδομένα που αποκτήθηκαν για την παρούσα εργασία, ήταν α) εικόνες ευρέως πεδίου στα φίλτρα Hα, [O III] και [N II] (βλ. Εικ. 5.2, σελ. 145) οι οποίες πάρθηκαν στο Αστε-ροσκοπείο τού Σκίνακα (Κρήτη). Επιπλέον, πήραμε εικόνες υψηλής ανάλυσης από το Αστεροσκοπείο τού Χελμού με το τηλεσκόπιο ¨Αρίσταρχος¨, με σκοπό να δούμε σε μεγαλύτερη λεπτομέρεια τις νηματοειδείς δομές που είναι χαρακτηριστικές τού αντικειμένου (βλ. Εικ. 5.3, σελ. 146). β) echelle φάσματα υψηλής ανάλυσης. Τα φάσματα πάρθηκαν στο Αστεροσκοπείο San Pedro Martir στο Μεξικό, χρησιμοποιώτας τον φασματογράφο MES-SPM. Όπως εξηγήσαμε παραπάνω, από τα φάσματα εξάγουμε τα διαγράμματα Θέσης-Ταχύτητας, τα οποία στη συνέχεια χρησιμοποιούμε στο SHAPE. Στην Εικ. 5.5, σελ. 148, παρουσιάζεται το VRO μαζί με τις θέσεις όπου έχουμε πάρει φάσμα (μπλε και κόκκινες γραμμές), καθώς και το διάγραμμα Θέσης-Ταχύτητας που αντιστοιχεί σε κάθε θέση. Βλέπουμε ότι έχει καλυφθεί σχεδόν όλη η περιοχή τού VRO με φάσματα, που σημαίνει ότι έχουμε κινηματική πληροφορία για καθεμία περιοχή που βλέπουμε στην εικόνα.

Τα νέα παρατηρησιακά αυτά δεδομένα χρησιμοποιήθηκαν στο λογισμικό SHAPE ακολουθώντας την ίδια διαδικασία που εξηγήθηκε παραπάνω για τη λειτουργία τού SHAPE. Οι επιλέον δυσκολίες για την μοντελοποίηση αυτού του αντικειμένου, ήταν α) η ασυμμετρία που παρουσιάζει στο σχήμα του, και β) το γεγονός ότι έπρεπε να υπάρξει ταυτόχρονη συμφωνία και των 26 συνθετικών διαγραμμάτων ΘΤ τού SHAPE με τα παρατηρησιακά διαγράμματα ΘΤ. Πράγματι, η συμφωνία αυτή επιτεύχθηκε αρκετά ικανοποιητικά, και παρουσιάζεται στην Εικ. 5.8, σελ. 152. Το γεγονός αυτό, σε συνδυασμό με την μορφολογική απεικόνιση του VRO, πιστοποιεί την εγκυρότητα του 3Δ αυτού μοντέλου.

Το τελικό μοντέλο παρουσιάζεται στην Εικ. 5.6, σελ. 149, και τα αποτελέσματα είναι τα εξής:

- Όλο το ΥΥΑ έχει μία κλίση ∼3-5 μοίρες σε σχέση με το επίπεδο του ουρανού.

- Η δεξιά μεριά τού "wing" είναι γερμένη σε σχέση με την αριστερή. Αυτό μπορεί να αποδοθεί σε αλληλεπίδραση αυτού τού μέρους τού "wing" με κάποιο πυκνότερο μεσοαστρικό υλικό.

- Η ταχύτητα όλου τού συστήματος είναι -17 km/sec, και είναι μικρότερη σε σχέση με την τιμή -34 που δίνεται στη δημοσίευση του Landecker et al. 1989.

- Εκτός από το "shell" και το "wing", το μοντέλο έδειξε την παρουσία και μίας τρίτης δομής που την ονομάσαμε "hat". Η δομή αυτή φαίνεται να προεξέχει από το κάτω μέρος τού "wing", και επίσης έχει διαφορετική ταχύτητα από το υπόλοιπο "wing", όπως θα δούμε αμέσως τώρα.

- Αναφορικά, λοιπόν, με τις ταχύτητες διάδοσης τού κάθε τμήματος, βρήκαμε ότι τα "shell" και "wing" έχουν την ίδια ταχύτητα ∼115 km/sec, ενώ το "hat" διαδίδεται με ταχύτητα ∼90 km/sec. Ωστόσο, το πάνω μέρος τού "shell" παρουσιάζει μεγαλύτερη ταχύτητα σε σχέση με το υπόλοιπο "shell", ∼155 km/sec, που είναι και η μεγαλύτερη όλου του VRO. Αυτό το κομμάτι είναι η πράσινη

περιοχή που φαίνεται στην Εικ. 5.6, σελ. 149. Στην ίδια εικόνα, τα μαύρα βελάκια αναπαριστούν τα διανύσματα ταχύτητας στις δύο αυτές σχεδόν διαμετρικές περιοχές τού VRO, δηλαδή στην πράσινη περιοχή και στο "hat". Ως προς την φυσική σημασία αυτού του αποτελέσματος, προτείνουμε ότι στις δύο αυτές περιοχές, αυτό που βλέπουμε πιθανόν να είναι δύο κύματα σοκ (shock break-outs). Η άποψη αυτή ενισχύεται από το καινούριο σενάριο που προτάθηκε από τον Αλέξανδρο Χιωτέλλη σχετικά με την εξελικτική πορεία τού VRO (Chiotellis et al. 2019), και που επιβεβαιώθηκε από τα αποτελέσματα του 2Δ Υδροδυναμικού μοντέλου (ΥΔ) που έτρεξε. Ο λόγος που υποστηρίζουμε αυτό το σενάριο είναι διότι μπορεί και αναπαράγει την μορφολογία αυτού τού αντικειμένου, χωρίς την παραδοχή ιδιαίτερων βαθμίδων πυκνότητας όπως στα σενάρια που μέχρι τότε υπήρχαν.

-2Δ Υδροδυναμικό μοντέλο για το VRO:

Σύμφωνα με το σενάριο αυτό (βλ. Εικ. 5.13, σελ. 158), ο προγεννήτορας αστέρας τού VRO ήταν ένα υπερηχητικά κινούμενο περιστρεφόμενο αστέρι, με έντονους αστρικούς ανέμους ενισχυμένους στο επίπεδο του ισημερινού του. Ο συνδυασμός τής κίνησής του αυτής και της αποβολής μάζας μέσω αστρικών ανέμων, δημιούργησε στην γύρω του περιοχή μία κοιλότητα (wind-cavity) η οποία έχει το ίδιο σχήμα με την περίμετρο του VRO. Στη συνέχεια, το αστέρι εξεράγει μέσα σε αυτήν την κοιλότητα, και το εκτιναχθέν υλικό διαχύθηκε μέσα σε αυτήν, δημιουργώντας το ΥΥΑ που παρατηρούμε σήμερα.

-Σύνδεση 3Δ Μορφοκινηματικού και 2Δ Υδροδυναμικού μοντέλου:

Λαμβάνοντας υπ΄όψιν το νέο αυτό σενάριο καθώς και τα αποτελέσματα του 2Δ ΥΔ μοντέλου, θεωρούμε ότι στις δύο αυτές διαμετρικές περιοχές τού VRO που αναφέραμε, έχουμε δύο shock break-outs μέσα από την κοιλότητα μέσα στην οποία δημιουργήθηκε το VRO.

Αξίζει να σημειωθεί πως στην περίπτωση του VRO, δύο μοντέλα διαφορετικού τύπου λειτούργησαν συμπληρωματικά για την ερμηνεία των φυσικών χαρακτηριστικών αυτού του πολύπλοκου αντικειμένου.

- Εκπομπή [Ο ΙΙΙ] από το VRO:

Ιδιαίτερου ενδιαφέροντος είναι η εκομπή που παρουσιάζει το VRO στην απαγορευμένη γραμμή τού οξυγόνου (5007Å), όπως φαίνεται στην Εικ. 5.9, σελ. 154. Η εκπομπή αυτή είναι πολύ έντονη στο πάνω μέρος τού "shell" καθώς και στην περιοχή τού "hat", ενώ είναι σχεδόν ανύπαρκτη στο "wing". Όπως προκύπτει από θεωρητικά μοντέλα, αλλά έχει παρατηρηθεί και σε πολλά ΥΥΑ, στις περιοχές όπου έχουμε μέτωπο σοκ (shock front) έχουμε και ισχυρή εκπομπή [Ο ΙΙΙ], κάτι που συμφωνεί με την πρότασή μας για shock break-outs στις δύο αυτές περιοχές.

Δημιουργήσαμε το 3Δ ΜΚ μοντέλο τού VRO στην γραμμή εκπομπής [Ο ΙΙΙ], και είδαμε ότι μορφολογικά είναι το ίδιο με το μοντέλο στην γραμμή Ηα. Υπάρχει, ωστόσο, μια μικρή διαφορά στην κινηματική. Όπως βλέπουμε και στον πίνακα 5.1 σελ. 155, τα κάτω όρια των ταχυτήτων του "wing" και του "hat" στο [Ο ΙΙΙ], συμπίπτουν με τα άνω όρια των ταχυτήτων τους στην Ηα γραμμή, όπως αυτές προέκυψαν από το μοντέλο. Μέσα σε αυτά τα όρια τού σφάλματος λοιπόν, μπορούμε να θεωρήσουμε ότι οι ταχύτητες και στις δύο γραμμές είναι πρακτικά οι ίδιες.

** Ολοκληρώνοντας την περιγραφή τής εργασίας πάνω στα 3Δ Μορφοκινηματικά μοντέλα των δύο αντικειμένων που παρουσιάσαμε, καταλήγουμε στο ότι το λογισμικό SHAPE μπορεί να εφαρμοστεί τόσο σε Πλανητικά Νεφελώματα όσο και σε Υπολείμματα Υπερκαινοφανών Αστέρων.

Ειδικότερα αναφορικά με το μοντέλο τού VRO και λαμβάνοντας υπ'όψιν τα φυσικά αποτελέσματα τού μοντέλου, είναι προφανές ότι ένα μοντέλο αυτού τού τύπου δεν είναι μια απλή 3Δ απεικόνιση ενός αντικειμένου. Τα φυσικά αποτελέσματα που προέκυψαν συνέβαλαν κατά πολύ στην απάντηση ερωτημάτων σχετικά με το συγκεκριμένο ΥΥΑ, στην πληρέστερη ερμηνεία των παρατηρησιακών δεδομένων, αλλά έφεραν στο φως και χαρακτηριστικά του που δεν ήταν εμφανή στα 2Δ παρατηρησιακά δεδομένα.

Συνεπώς, με την δημιουργία τού πρώτου 3Δ ΜΚ μοντέλου ενός ΥΥΑ, ένα καινούριο και πολύ χρήσιμο εργαλείο έχει προστεθεί στις μεθόδους μελέτης των ΥΥΑ. Επίσης αξιοσημείωτο είναι ότι τα αποτελέσματα του 3Δ ΜΚ μοντέλου, μπορούν να χρησιμοποιηθούν ως δεδομένα εισαγωγής σε Υδροδυναμικό μοντέλο. Το γεγονός αυτό ανοίγει το δρόμο για μια πιο ενδελεχή έρευνα αυτών των πολύπλοκων αντικειμένων, τα αποτελέσματα της οποίας συμβάλλουν τελικά στην κατανόηση τής αστρικής εξέλιξης.

Acknowledgements

Ευχαριστίες

Θα ήθελα να εκφράσω την ευγνωμοσύνη μου στο πρόσωπο του επιβλέποντος καθηγητή μου, Δρ. Πάνου Μπούμη, για την ευκαιρία που μου έδωσε για την εκπόνηση της συγκεκριμένης διδακτορικής διατριβής. Η εργασία που μου εμπιστεύτηκε αποδείχθηκε το καλύτερο σχολείο για μένα καθώς, ειδικά μέσα από τις πολλές της δυσκολίες, μπόρεσα και είδα την ομορφιά που υπάρχει στην έρευνα στο πεδίο τής Αστροφυσικής, και να αποφασίσω για τον εαυτό μου ότι αυτή είναι η εργασία που μου δίνει τη μεγαλύτερη χαρά. Η συνολική του καθοδήγηση κατά τη διάρκεια όλων αυτών των χρόνων, αποτελεί ένα ζωντανό παράδειγμα για μένα για το πώς πρέπει να είναι ένας καθηγητής ώστε να προετοιμάσει έναν διδακτορικό φοιτητή για να γίνει ένας μελλοντικός ερευνητής.

Πολλά ευχαριστώ στον Δρ. Σταύρο Άκρα ο οποίος, χάρη στη μεγάλη του εμπειρία, μου παρείχε τα κατάλληλα ''εργαλεία'' ώστε να ξεκινήσω την έρευνα στην 3Δ μοντελοποίηση, και να μπορέσω να ανταποκριθώ στην πολύ απαιτητική περίπτωση της εργασίας μου. Στον Δρ. Αλέξανδρο Χιωτέλλη ο οποίος, με τη βαθιά του θεωρητική γνώση και εμπειρία στη μοντελοποίηση, έδωσε τεράστια ώθηση στην εργασία αυτή την κατάλληλη στιγμή. Επίσης, στον Δρ. Wolfgang Steffen για τα πολύτιμα σχόλιά του πάνω στο μοντέλο. Στην Καθηγήτρια κ. Δέσποινα Χατζηδημητρίου για όλη τη βοήθειά της και τις συμβουλές της.

Ένα μεγάλο ευχαριστώ στους Μαρία Κοψαχείλη, Μιχάλη Κουρνιώτη, Ζωή Σπετσιέρη, Αλέξη Λιάκο, Γιάννη Αλικάκο και Αλέξη Γουρζέλα για τη βοήθειά τους στην ανάλυση δεδομένων και την εκπαίδευση πάνω στο τηλεσκόπια.

Ιδιαιτέρως ευχαριστώ τον Karol MacGearailt για τη βοήθειά του σε -ανυπέρβλητα για μένα!- προβλήματα υπολογιστών.

Βασιλεία, Ming, Άγγελε, Αναστάση, Δημήτρη, Angel, Γιώργο, Γρηγόρη, Μαρία, Έκτορα, Βαγγέλη, Σταυρούλα, Έμμυ, Stefan και Frank ... σχεδόν κάθε μέρα όλοι μαζί στο αστεροκοπείο και όχι μόνο!

Σας ευχαριστώ που ήσαστε εκεί.

Contents

Chapter 1

1 Introduction

In this chapter we present the basic theory of the stellar evolution of low and high-mass stars. We emphasize on the evolutionary path followed by the high-mass stars, as these are the progenitors of the Supernova Remnants, which are the objects studied in the current Thesis.

1.1 Protostar formation

Although stars seem like "constant lights" in the night sky, in reality they are celestial objects that are born in galaxies, evolved and eventually they die. A protostar is formed by the gravitational collapse of molecular gas (mostly composed of Hydrogen (H)) and dust[1]. The collisions between the H atoms in this spinning cloud heat up the gas. When the temperature reaches up to $T = 10^7 \ K$ in its core, H fuses into Helium (He)[2] and the protostar begins to glow. When the mass is stabilized, then the star is located in the Main Sequence (MS) of the Hertzsprung-Russel (HR) diagram (Fig. 1.1). The beginning of the MS phase, which is signalled by the onset of H fusion into He, is called the Zero Age Main Sequence (ZAMS) and corresponds to the thin diagonal line that crosses the HR diagram from the top left corner to the bottom right in Fig. 1.1.

While in MS, two conditions must be preserved for the stability of the star (Fig. 1.2): a) the star must be in Hydrostatic Equilibrium: outwards thermal pressure (pressure due to the

---

[1]This cloud may consists of other elements too, which were present in this area due to a previous nearby Supernova explosion (Section 1.6) that had taken place in this region.

[2]This chemical reaction is the onset of what is called *stellar nucleosynthesis* which is the formation of heavier elements from the fusion of lighter elements in stars. In Astronomy, as heavier elements are considered these that are heavier than He. Elements heavier than He and up to Iron (Fe) are made in the cores of the stars, while elements heavier than Iron are made in Core-Collapse Supernova explosions (see Section 1.6.3).
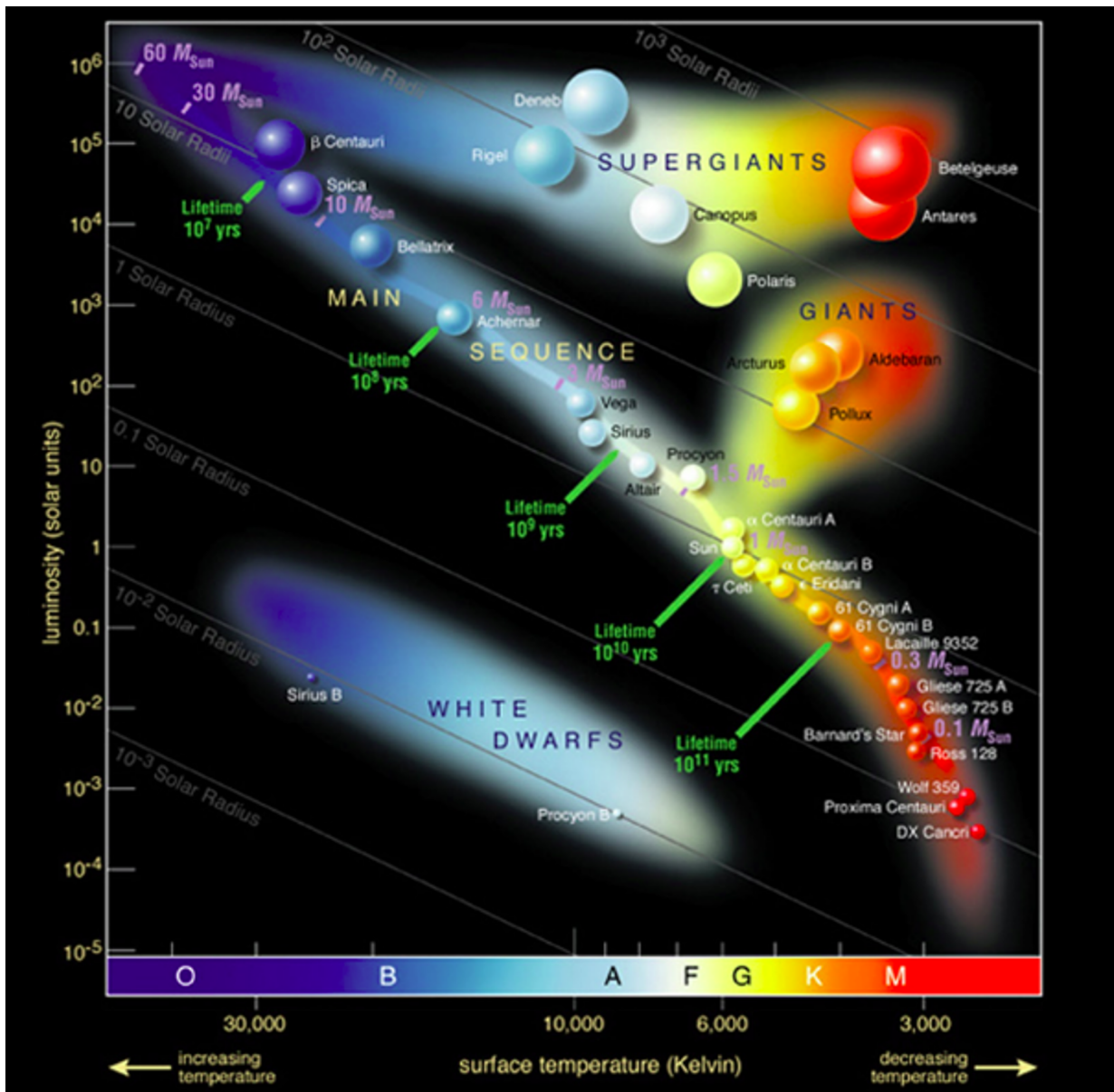
Figure 1.1: The Hertzsprung-Russel (HR) diagram. It illustrates the relationship between the temperature T (K) of a star, along with its Luminosity (L), its mass (M) and its radius (R) in solar units.

random movement of the particles) balances inwards gravity - no motion of the star b) the star must be in Thermal Equilibrium: energy generation through nuclear fusion at the core, is not trapped inside the star, but is transferred to the surface and is emitted away. In "normal" stars this energy transport can occur through radiation (energy is carried by photons) or convection (energy carried by bulk motion of gas - case of bubbles movement in boiled water). In a White Dwarf (see Section 1.2.7), which is the ultra dense C–O core of a star, the energy released from the core is transferred to the surface through conduction (energy carried by particle motions - example of a spoon heated by a candle).

The mass of the initially collapsing H clouds determine the mass of the newly born star. This amount of mass is responsible for the gravitational force that exerts onto the star's particles,
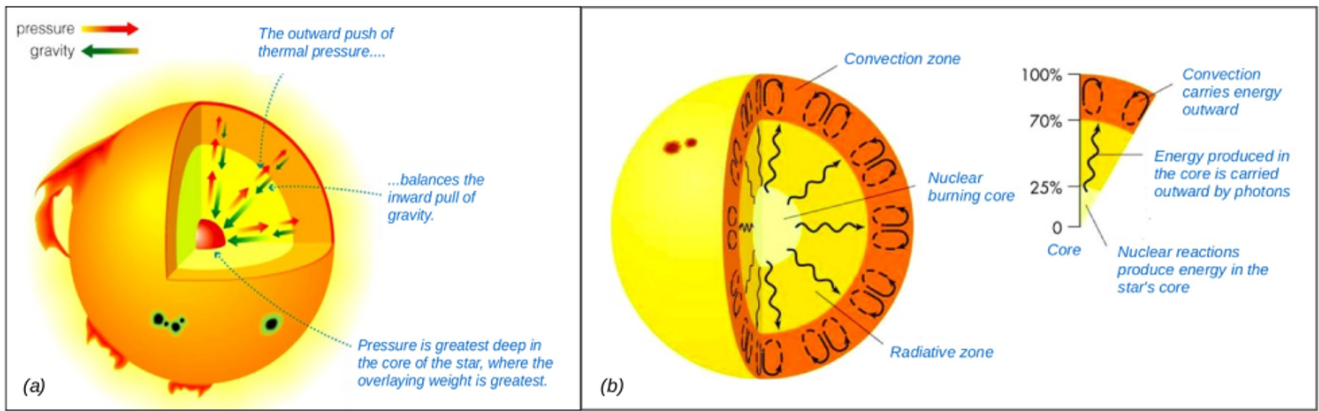
Figure 1.2: (a) Hydrostatic Equilibrium (b) Thermal Equilibrium. For description, see in the text.

defining its core pressure and temperature, and subsequently the fusion rate of the fuel present in its core. This fusion rate is called luminosity (L; produced energy per unit of time) and the equation that connects the mass (M) of the star with the produced luminosity is:

$$L \propto M^{3.5} \tag{1.1}$$

The time (t_{MS}) that a star will spend in the MS burning its H into He in its core, is related to its mass (M) and its luminosity (L) through the equations:

$$t_{MS} = \frac{M}{L} \tag{1.2}$$

$$t_{MS} = \ t_{\odot} \times \left(\frac{M}{M_{\odot}} \right)^{-2.5} \tag{1.3}$$

where $t_{\odot}$ = 1.2 × 10^{10} years, is the time span for the Sun to fuse H into He in its core, M is the mass of the star, and $M_{\odot}$ = 1.98 × 10^{30} kg is the mass of the Sun. In general, stars spend almost 90% of their total lifetime in the MS phase, before they continue their rest evolutionary course.

A direct conclusion we can draw from Eqs. 1.1-1.3 is that more massive stars are more luminous, and tend to consume their H fuel in their cores at a quick rate. On the contrary, lower-mass stars are characterized by lower luminosity and they spend their H fuels with savings. The reason for this, is the kind of nuclear reactions through which H is fused into He in the core of a star: low-mass stars follow the proton-proton chain reaction (see Section 1.2), while high-mass stars burn H into He in their core via the much faster CNO cycle (see Section 1.3).

When the H of the core is fully converted into He then the MS stage stops, and the star continues its rest evolutionary path. The latter depends strongly on the star's initial mass in the MS, on the mass loss that it undergoes during its lifetime (for single stars the only means

of mass loss are the stellar winds -*see* Section 1.9.1, while in a binary system mass deposition on the other companion is an additional reason), and on its metallicity. Detailed description is beyond the scope of this thesis, but can be found in a number of papers (e.g. Heger et al. 2003).

Stars are roughly separated into two basic groups: those with initial mass below 8 $M_\odot$ (low/intermediate-mass stars) and those with initial mass above this value (high-mass stars). The distinction depends on whether the core of the star may undergo any further nuclear burning after a point of its evolution, or not. However, when the mass $M \leq 0.08$ $M_\odot$, this object is not termed as a "star" for inward gravity is not strong enough for nuclear burning to start. This is why Jupiter with 0.0009543 $M_\odot$ is not a star, but a planet. On the other hand, when $M \geq 150$ $M_\odot$, gravity is extremely high, the star is too unstable to live and finally collapses. However, this upper threshold seems to have been crossed, with R136a1 in the Large Magellanic Cloud to currently hold the record as the more massive star known in the universe ($M \sim 265$ $M_\odot$).

In the following Sections 1.2 - 1.5, I outline the evolution of the stars with M lower or greater than 8 $M_\odot$ after their departure from the MS phase, according to the currently widely accepted models. For high-mass stars, their end-point as a Supernova and their subsequent evolution as Supernova remnants is presented separately in Sections 1.6 - 1.8.5.

1.2 Evolution of low/intermediate-mass stars, with 0.4 $M_\odot \leq M \leq 8\ M_\odot$

As low/intermediate-mass stars are considered these with mass-range 0.4 $M_\odot \leq M \leq 8\ M_\odot$. The relatively small gravitational forces that such a star exerts on its material imply that the pressure and the temperature in its inner regions are of low magnitudes too. Low temperatures (not lower than $T = 10^7\ K$ though) imply low rate of H fusion into He in the core, which means low rate of energy production, i.e. lower luminosity L. So, as Eq. 1.2 indicates, low mass stars tend to spend long time in MS phase until they burn almost all of their H in their core into He. In low-mass stars, this happens through the proton-proton chain nuclear reaction (Fig. 1.3) according to which four H nuclei (protons) in total, are combined in order to eventually form one He nucleus (alpha particle). The released energy from this reaction is proportional to $\sim T^4$. At the end of the MS phase, the star consists of an He core surrounded by a H-shell. What follows in the star's evolution is a phase that is called **subgiant phase** (Section 1.2.1).

© 2004 Thomson - Brooks Cole

Proton-proton cycle

$$^1_1H + {}^1_1H \rightarrow {}^2_1H + e^+ + \nu$$
$$^1_1H + {}^2_1H \rightarrow {}^3_2He + \gamma$$
$$^3_2He + {}^3_2He \rightarrow {}^4_2He + {}^1_1H + {}^1_1H$$
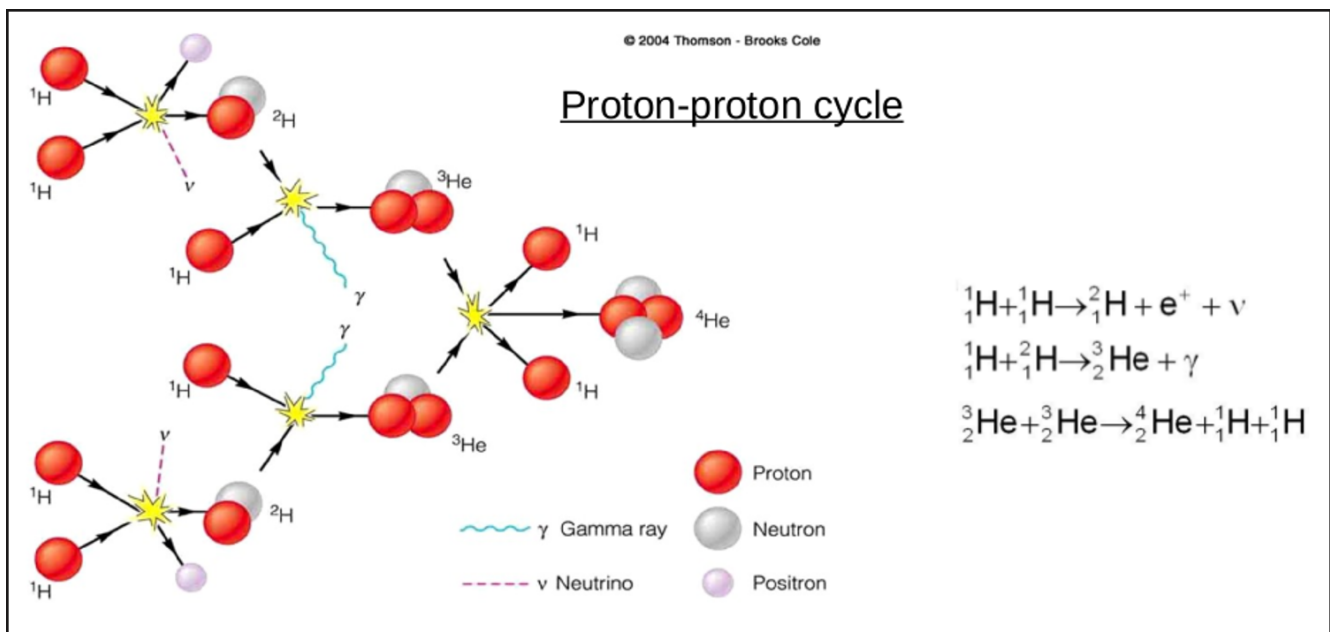
Figure 1.3: The proton-proton chain nuclear reaction: 4 H nuclei (protons) are combined to form 1 He nucleus (alpha particle). This reaction takes place at the core of low-mass stars (0.4 $M_\odot \leq M \leq 8\ M_\odot$) while they are still in the MS phase.

1.2.1 Subgiant

At the end of the MS phase, the produced energy at the core of the star is transferred to its surface through radiation. The difference between the produced luminosity at the core and that which eventually escapes from the star's photosphere is consumed in the heating of the intermediate layers of the star forcing them to dilate, which means increase in the star's radius

R. Assuming that the mass of the star stays constant (i.e. no mass loss at this point through stellar winds), Eq. 1.1 indicates that the surface luminosity L also remains practically constant. So, according to the following equation about luminosity:

$$L = 4\pi R^2 \sigma T_{eff}^4 \left[ergs^{-1} \right] \qquad (1.4)$$

where R is the radius of the star, $\sigma = 5.67 \times 10^{-8}$ W m^{-2} K^{-4} is the Stefan-Boltzmann constant and T is the effective temperature[3], T will decrease making the star to appear red in colour. That means that the star is moving horizontally to the right in the HR diagram converted into a **red subgiant** (Fig. 1.4). At the end of the subgiant phase, the temperature inside the core is $\sim 10^7$ K, which is hot enough for the H nuclear fusion as we saw, but not hot enough for He to start its fusing reactions in the core of the star (the needed temperature for this would be $\sim 10^8$ K). The temperature outside of the core is cooler (less gravitational pulling means less pressure on the gaseous layers) therefore the H-shell around the He core cannot burned. As no nuclear reactions can take place, there is no energy production to compensate for the inwards gravitational forces. The core begins to shrink and – due to its contraction – its temperature rises, heating up the H-shell which surrounds the He core. At this point, the **Hydrogen–shell burning** begins (Fig. 1.4, phase 1)[4].

Although the nuclear energy is high, the produced photons in the H-shell cannot escape yet due to the H that surrounds the H-shell (we say that the stellar matter is very *opaque* to radiation). These photons of the H-shell "push" outwards on the outer layers of the star (radiation pressure), forcing its photosphere to expand and, subsequently, to cool down. The star's radius increases by a large factor (for example: if the core radius is 10^{-2} R$_\odot$, the star radius reaches 50 R$_\odot$), its luminosity also increases ($L = 4\pi R^2 \sigma T^4$) while its temperature decreases, making the star to appear even redder. Now, the ever-growing luminosity cannot be transferred to the surface of the star through the stable radiation process, resulting in the unstable transfer of energy through convection (Fig. 1.2b). The star has now entered the **Red Giant phase** (Red Giant Branch - RGB) (Section 1.2.2).

1.2.2 Red Giant (RGB)

As we mentioned in the previous paragraph, in the RGB phase the envelope expands because of increased energy production, and it cools because of increased surface area. Fig. 1.5

---

[3]T_{eff} is defined as the temperature of a black body with the same energy flux at the surface of the star, and constitutes a good measure for the temperature of the photosphere.

[4]This is a repeatable pattern in the evolutionary course of a star: each time the core depletes the element it is fusing, it shrinks until it becomes hot enough for other fusion reactions. A new type of shell burning ignites between the core and the overlying shells of fusion.
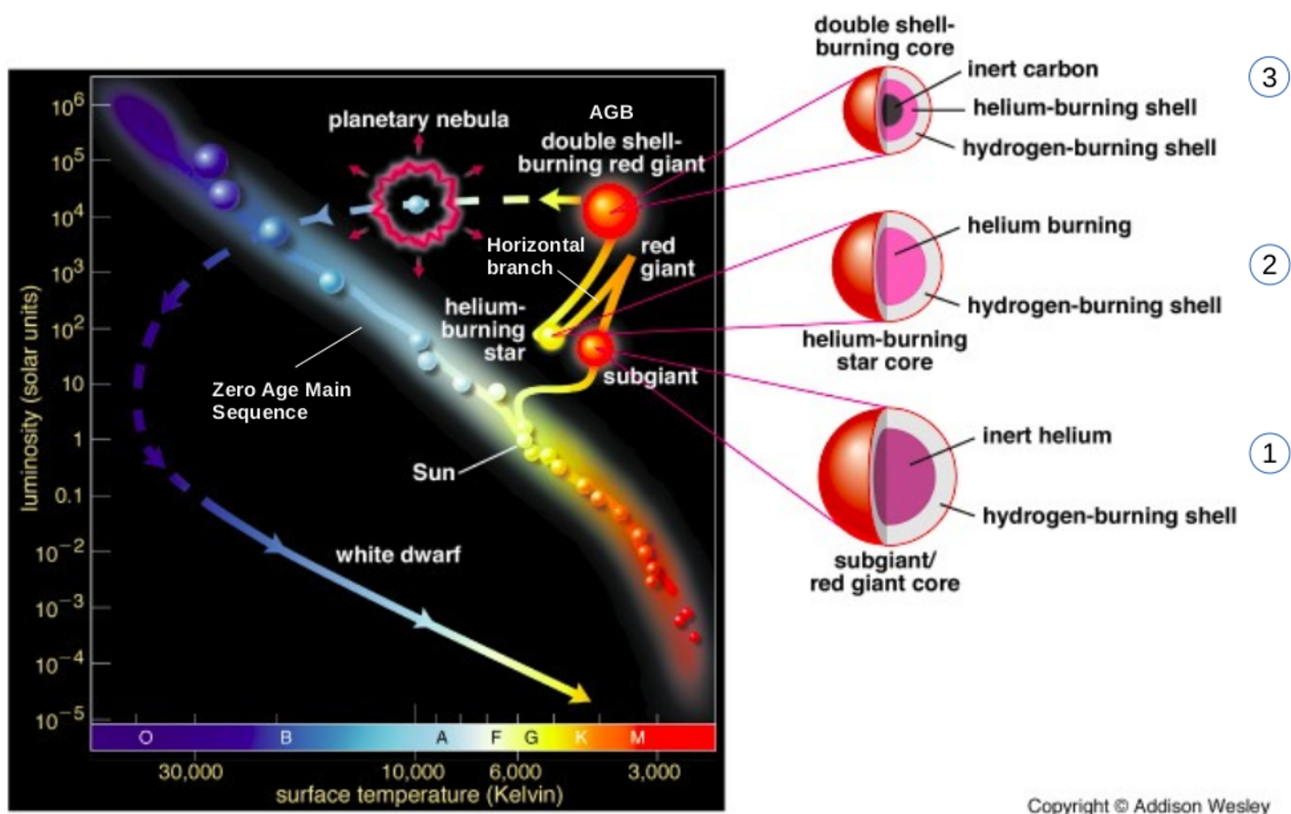
Figure 1.4: *On the left*: evolutionary track of a low/intermediate-mass star from the ZAMS phase to its transformation into a White Dwarf. *On the right*: the core layers of the star during its evolution from the subgiant phase up to the AGB phase (see Section 1.2.4) in the HR diagram.

illustrates the size of various stars, in order to get an idea of the enormous size that a Red Giant can reach. At its outer atmosphere, the star is characterized by dense stellar winds (Section 1.9.1) with mass loss rate 10^{-6} - 10^{-4} $M_{\odot}$ yr^{-1} (Mauron and Josselin 2011). On the other hand, in the inner part of the star, an explosion known as **Helium flash** will take place (Section 7.1), the outcome of which will be the creation of Carbon (C), and perhaps Oxygen (O) as well.

1.2.3 Horizontal Branch

After the He flash at the end of the Red Giant phase, in which He burns into C (and/or O) in the core of the star, the released energy is so strong that the resulted increased temperature causes the ending of the degeneracy pressure in the core (for *degeneracy pressure* see Section 7.1). The gas turns into an ideal gas and the thermal pressure (pressure due to the random movement of the particles) dominates now over the degeneracy pressure. The core expands depleting the gravitational pull exerted onto the H-shell that surrounds the core, leading to the decrease (but not the cease) of the H burning in that shell.

Hence, at this stage there are two sources of energy present in the star: a) H fuses into He
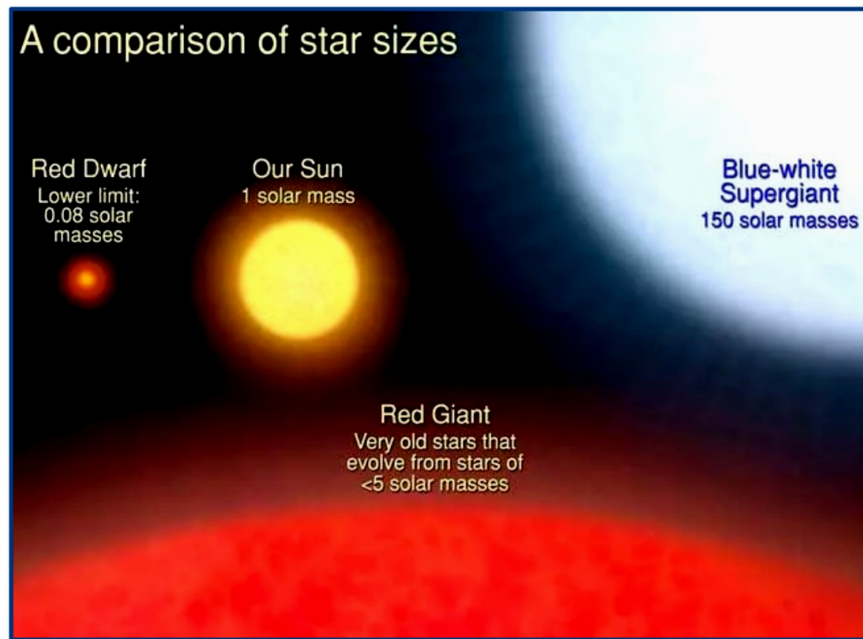
Figure 1.5: A comparison of star sizes, where we can see the enormous size a Red Giant can reach during its evolution.

in the shell that surrounds the core and b) He fuses into C in the core (Fig.1.4, phase 2). Despite the two sources of energy production, the overall outwards radiation pressure is not enough to compensate for the inwards gravity, so the star eventually shrinks and becomes less luminous. Progressively due to the shrinking, the rise in the effective temperature and decrease in surface area are such that the luminosity remains roughly constant ($L = 4\pi\ R^2\ \sigma\ T^4$), forcing the star to move almost horizontally to the left in the HR diagram. This period in the evolution history of low/intermediate-mass stars is called the **Horizontal Branch** (Fig. 1.4). The exact position of a star in this branch depends on the initial mass of the star, its chemical composition in the MS, and the mass loss of its outer layers during its stay to the Red Giant branch.

After this stage, the star "climbs" up to the HR diagram for a second time (the first was during the RGB phase) following a path called **Asymptotic Giant Branch** (Section 1.2.4).

1.2.4   Asymptotic Giant Branch (AGB)

By the end of the Horizontal Branch, the He burning in the core of the star has left behind Carbon (and in some cases Oxygen too) "ashes". The picture we now have is a core full of Carbon, surrounded by a He-shell which in turn is surrounded by a H-shell (Fig. 1.4, phase 3). The nuclear reactions in the core have ceased and consequently there is no counterbalance for the inward push of gravity. Hence, once again, the core begins to shrink and heat up. But, what saves the core from total collapsing is the Electron Degeneracy pressure.

This contraction, to the point that exists, generates the heat rise in the core, which however is not enough to ignite the fusion of C (the temperature has to be even greater than 10^8 K needed for He fusion). Hence, this thermal energy that anyway exists in the core is transferred in the He-shell that surrounds the C-O core, fusing He into C. Subsequently, the produced energy in the He-shell is transferred in the H-shell that surrounds the former, causing the burning of H into He. These two nuclear reactions that take place in the double shell burning lead to the increase of the star's luminosity ($\sim 10^4$ $L_\odot$). But once again, the produced photons are trapped by the H layers which surround the H-shell, and thus radiation pressure is exerted onto the outer layers of the star. The star expands, cools down and becomes redder. This is the beginning of a second Red Giant phase, which is called **Asymptotic Giant Branch (AGB)** phase, during which the star is moving up and right in the HR diagram. The term "asymptotic" is because the star asymptotically approaches (almost) the same location in the HR diagram as an RGB star does. These type of stars are also categorized as Red Supergiants (RSG) due to their red colour and enormous size (their radius range from a few hundreds to thousands of $R_\odot$). Two very famous RSGs are Betelguese and Antares A, as shown in Fig. 1.6.

Mass loss due to stellar winds is also present at this phase. Here, the stellar winds are more tenuous (mass loss rate 10^{-8} - 10^{-5} $M_\odot$ yr^{-1}; Höfner and Olofsson (2018)) and faster (order of $10\,km\,sec^{-1}$) than in the RGB phase. As a result of the stellar wind activity, AGB stars are usually surrounded by large quantities of gas and dust which partially absorb the stellar radiation and therefore modify the spectral appearance of the star, something that also happens in the case of an RGB star.

C and O "ashes" from He shell ignition are continually deposited onto the C-O core, increasing its mass. The increasing strength of gravity that follows forces the free electrons of the degenerate core to squeeze together even more, in order to increase the electron degeneracy pressure and finally counteract the inwards gravity force (remember that nuclear fusions have ceased, so degeneracy pressure is the only mechanism available against gravity for the stability of the core). This electrons squeezing leads to the shrinking of the C-O core. In order for the core to manage to maintain its equilibrium state, its mass must not exceed 1.4 $M_\odot$. Above that limit, degeneracy pressure its not enough to balance the strong inwards gravity and the core will totally collapse leaving behind either a neutron star or a Black Hole (see Sections 1.3 and 1.5 respectively). When the mass is below that limit, then the C-O core is the progenitor of a very hot, small and compact object, known as a **White Dwarf (WD)** (see Section 1.2.7). This upper limit of 1.4 $M_\odot$ is known as the *Chandrasekhar limit* for White Dwarfs in honour of the Indian astrophysicist Subrahmanyan Chandrasekhar for his major contribution in the interpretation of the physics of White Dwarfs, neutron stars and other compact objects (Nobel Prize in Physics,

1983).
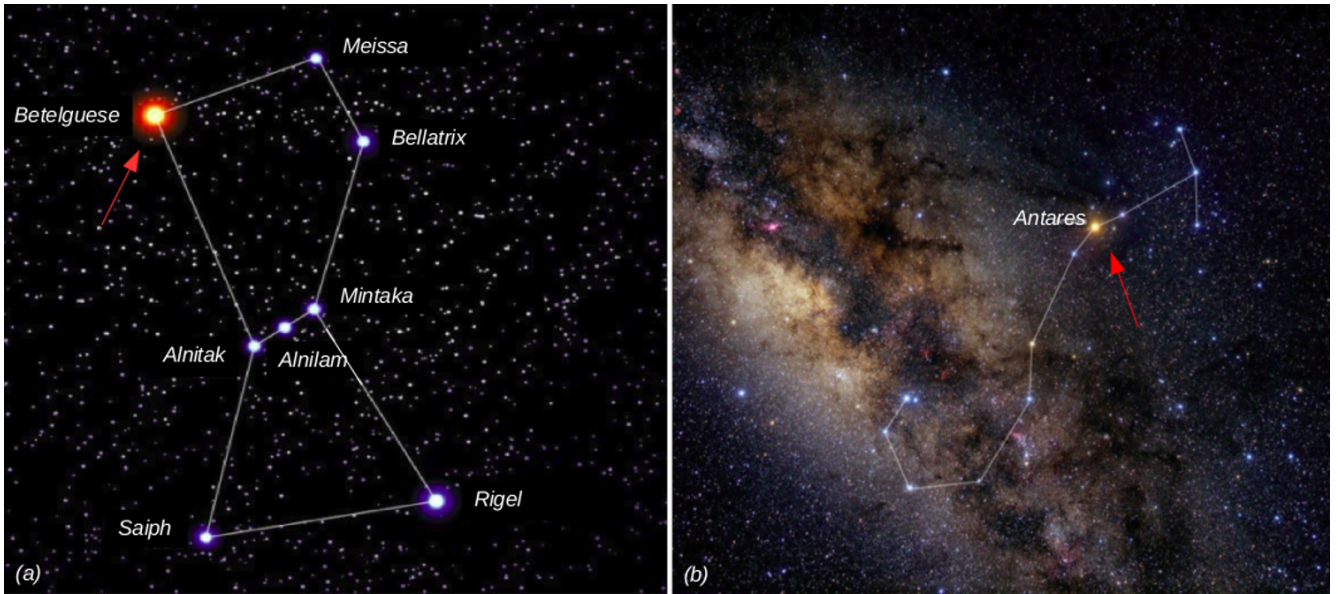
Figure 1.6: (a) The Red supergiant (RSG) Alpha Orionis in the constellation of Orion, also known as Betelgeuse ($R_{Betelguese}$ = 887±203 $R_\odot$). Ancient Greek Astronomer Ptolemeos as well as ancient Chinese astronomers mention Betelgeuse in their reports as a yellow star. Today we believe that Betelgeuse will explode as a Supernova (see Section 1.6) within the next thousands years. (b) The RSG Antaris A ($R_{Antares\ A}$ = 883 $R_\odot$) in the constellation of Scorpius. The Ancient Greeks named Antares "rival to Ares" (opponent to Mars), due to the similarity of its reddish hue to that of Mars. This comparison may have originated with early Mesopotamian astronomers.

1.2.5   Post AGB phase

At the end of the AGB phase, which is also known as Post-AGB phase, the star is characterized by strong mass loss (it can be as high as 10^{-4} $M_\odot$ yr^{-1}) which includes significant amount of dust grains, formed due to the star's low photosphere temperatures ($\sim$ 3000 K). There are several proposed mechanisms for the interpretation of the mass loss in Post-AGB stars: Helium shell flashes, periodic envelope pulsations (long period variables - LPVs), and/or low acceleration at their surface due to gravity that cannot hold any more their outer gaseous layers, according to the following equation:

$$g = \left(\frac{GM}{R^2}\right) \tag{1.5}$$

where g is the gravitational acceleration, G is the gravitational constant (6.674 $\times$ 10^{-11} N m^2 Kgr^2), M is the mass of the star and R is the radius of the star.

Whatever the mechanism, the result is the expulsion of the star's atmosphere, the latter basically consisted of H and He, leaving behind a hot and dense C-O core surrounded by thin layers of residual H and He. Gradually, since no outer layers are present any more to obscure the core, the high temperature of the exposed core is revealed and this is why the star is moving nearly horizontally to the left in the HR diagram as a Post-AGB star.

Remind that we examine the case of low-mass stars whose C-O core mass does not exceed 1.4 $M_\odot$. In this case, this hot, glowing material ejected through the mass loss of an AGB star is called **Planetary Nebula (PN)** (Fig. 1.4), and it is glowing due to the ionization it undergoes from the ultraviolet radiation emitted from the hot central star. In later evolutionary stage when the H and He expanding shells are completely diluted into space and extinguished, the luminosity of the star drops rapidly, and the revealing core cools off to become a White Dwarf. Planetary Nebulae and White Dwarfs are presented more thoroughly in Sections 1.2.6 and 1.2.7 respectively.

1.2.6   Planetary Nebulae

The term "Planetary Nebula" is obviously misleading. When these objects were first detected[5], they were thought to be planets due to their small, round shape and their greenish colours, the latter caused by an oxygen emission line present in the nebula (see for example the central region of the *Hourglass Nebula* in Fig. 1.8c).

Today, as we outlined above, it is believed that PNe are the expelled atmospheres of the central stars of post-AGB stars, photoionized by the latter, and also the progenitors of White Dwarfs (Shklovsky 1956; Paczyski 1971). Since the PN "birth", i.e. when the central star lost its outer shell that became the planetary nebula, the time span is about 3.5×10^4 years. This is much shorter than almost any other stellar evolution times, which shows that the PN phase is a relatively short-lived stage in the evolution of a star.

One evidence in favour of the idea that late-type low mass stars are the progenitors of PNe, is the presence of dust in the infrared and molecules in the mm wavelengths in the nebula. This indicates that the material in the nebula came from a cool stellar atmosphere (remember that in low temperatures material tends to get condensed, leading to the creation of dust and molecules in the cool atmospheres of the stars), something that strengthens the belief that the progenitors of PNe are Red Giants. Furthermore, the C-O cores of their central stars, suggest that we speak about Red Giants in the AGB phase, and not in the RGB phase where the star's core consists of He.

---

[5]First PN ever detected: Dumbbell nebula by Charles Messier in 1764.

With regards to the expansion velocities of PNe, observations show that they are of the order of $\sim 20-30$ km s^{-1}. This value is incomparable smaller than the escape velocities from current central stars of PN (White Dwarfs) which is about ~ 1000 km s^{-1}, which means that the shells of PNe have not been detached from a WD. On the contrary, their velocities match with the escape velocities of Red Giant stars which are about ~ 10 km s^{-1} (Kwok et al. 1978), but still are higher than these. Furthermore, their densities are higher than those in the circumstellar envelope of an AGB star. Therefore, it seems that the simple detachment of the atmosphere from an AGB star is not the case. A different mechanism is needed to compress, accelerate and form the circumstellar envelope into a PN.

The mechanism that is currently widely accepted was proposed by Kwok et al. (1978), and it is known as the model of Interactive Stellar Winds (ISW). According to this, the fast and tenuous stellar wind ejected from the core of the post-AGB star collides with the remnant of the slow and dense stellar wind previously ejected from the precursor Red Giant star, leading to the creation of the Planetary Nebula.

More analytically, the winds in the Red Giant phase have relatively low velocities (~ 10 km s^{-1}) but substantial mass-loss rates (10^{-5} M$_\odot$ yr^{-1}). This process produces a large, cool, neutral (mostly consisted of H), slowly-expanding shell around the star. On the other hand, the hot central core exposed after this envelope mass loss is characterized by a fast stellar wind ($\sim 10^3$ km s^{-1}), but its mass-loss rate is substantially lower (typically 10^{-8} M$_\odot$ yr^{-1}). When this rarefied, fast wind interacts with the more dense, slowly-moving outer envelope, it gets shocked and superheated (with T = 10^6 K), creating a "hot bubble" filled with coronal gas, i.e. very hot and sparse gas. This bubble is accelerated outwards from the central star, sweeps up the initially expelled AGB envelope (the dense and slow stellar wind) and constrains it into a cool (with T = 10^4 K), thin and dense shell that traces the bubble's perimeter. This shell is responsible for the optical and IR (due to dust grains) radiation detected in PNe, while the "hot bubble", which is fully contained within the bright optical rim/shell, emits the diffused hard X-ray emission (≥ 10 *keV*) present in PNe (Fig. 1.7). The bubble is separated from the outer, much cooler gas by a contact discontinuity.

Thus, at this point the structure consists of three main regions: i) the innermost fast wind from the core, ii) a region where the fast wind collides with the material previously lost from the cool star and iii) an outer layer of molecular gas.

The case of two interacting winds as a formation mechanism for PNe, is the simplest possible case. If, for various reasons, more discontinuities in velocities occur, then more than one shell may be produced, as we can see in Fig. 1.8 (a), (d) and (e).

With regards to the X-ray emission, the shocked fast stellar winds in the "hot bubble" model
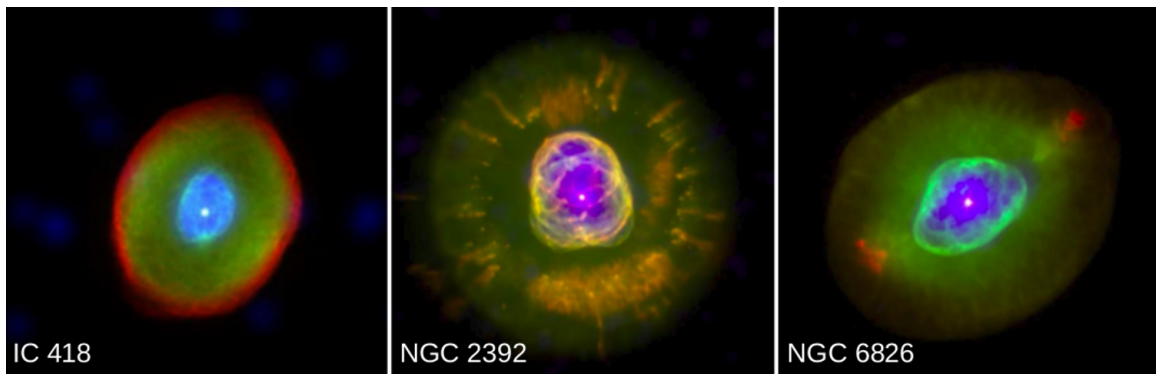
Figure 1.7: *Chandra* and *HST* (Hubble Space Telescope) composite pictures of the PNe IC 418, NGC 2392, and NGC 6826. X-ray emission from the "hot bubble" is shown in blue, and optical Hα 6563 Å and [N II] 6548, 6584 Å emission in green and red, respectively. Credits: Ruiz et al. (2013).

is not the only source of X-ray radiation in PNe. Softer X-rays (0.3-2.0 keV, luminosities L$\sim$ 10^{31} erg s^{-1}) may originate from the central stars of PNe, which can reach temperatures as high as $100.000 - 200.000$ K. They appear as point sources, contrary to the shocked winds which are expected to be extended sources emitting continuously out to the inner wall of the dense shell of the PNe. Finally, a point source centered on the PN nucleus with a hard X-ray spectrum or an extraordinarily high X-ray luminosity may indicate a different emission mechanism, such as an X-ray binary (Chu et al. 2000).

The various, beautiful colours in the optical waveband that PNe illustrate are attributed to the photoionization they undergo from the central star. While the hot, condensed central star remains in equilibrium state, the ultraviolet photons it emits are absorbed by the atoms of H, He (and possible heavier elements present in the nebula, transferred from the core to the surface through conduction) causing the atoms to excite (creation of ions) or ionized (creation of free electrons). When the electrons fall back to the lower energy levels, or free electrons reconnect with the atomic nuclei, they emit radiation in the visible range of spectrum, resulting in the colour palette we see in their images.

With regards to the observed morphology of PNe, the various structures they present are basically classified as spherical, bipolar and elliptical (Fig. 1.8), while it is quite common for their structure to be accompanied by halos, jets, collimated outflows and/or knots (clumps of material with dark cores and luminous cusps on the sides facing the star). The case of the PN Hb4 which is presented in this Thesis in Section 4, is a typical example of a Planetary nebula which expels pairs of knots on either side of its core star.

However, their apparent morphology depends strongly on i) the available resolution of the image, ii) the detected ionized/molecular emission lines and iii) the projection effect (viewing
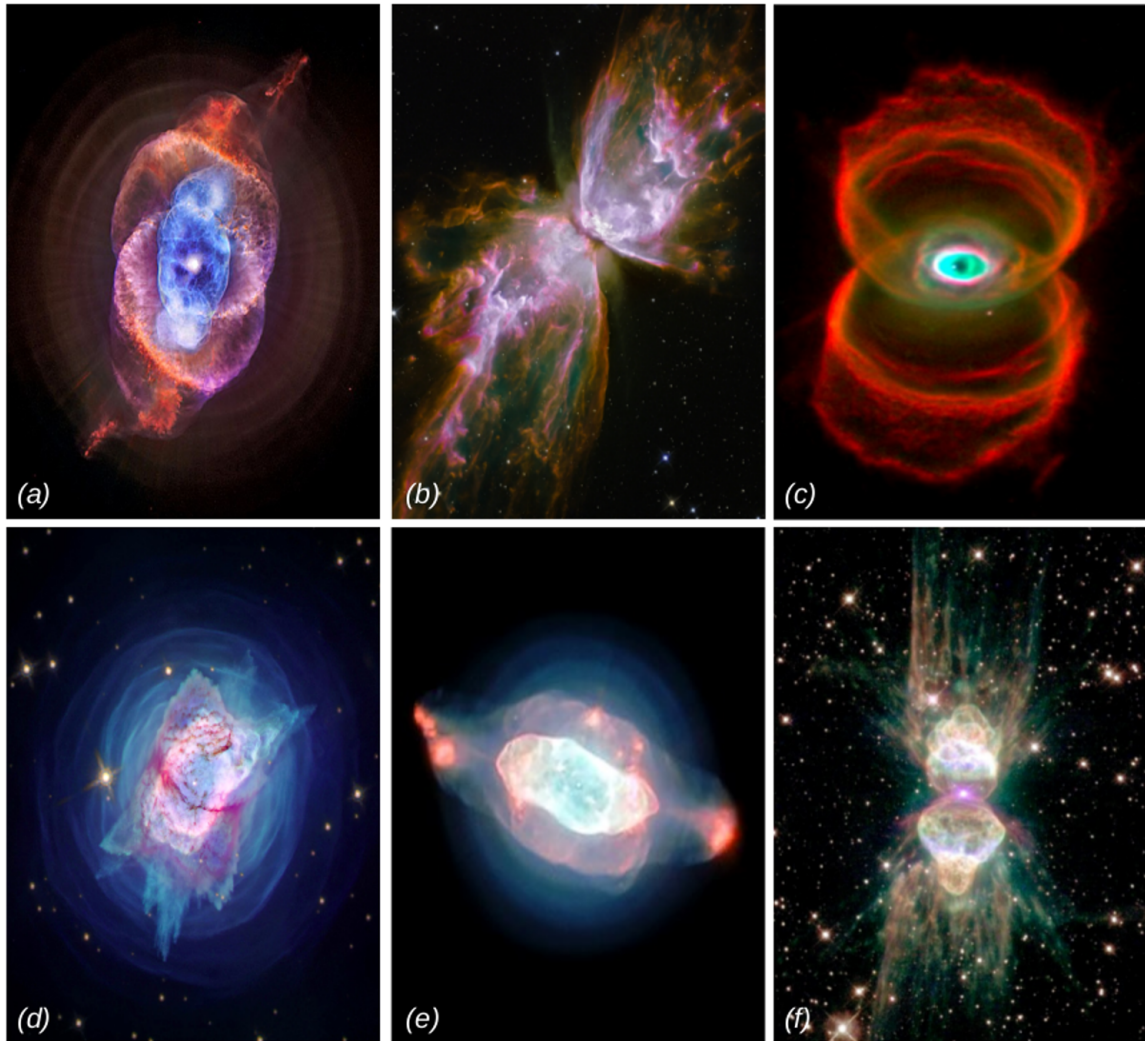
Figure 1.8: PNe of intriguing morphologies: (a) NGC 6543 or the *Cat's Eye* nebula, Image Credit: X-ray: NASA/CXC/SAO; Optical: NASA/STScI (b) NGC 6302 or the *Butterfly nebula*, Credits: NASA/Hubble Space Telescope (*HST*), (c) *HST* image of MyCn18 or the *Hourglass nebula*, Credit: NASA, R.Sahai, J.Trauger (JPL) and The WFPC2 Science Team (d) *HST* image of NGC 7027, or the "Jewel Bug" nebula. Image credit: NASA/ESA/J. Kastner, Rochester Institute of Technology, (e) NGC 7009 or the *Saturn nebula*, Credits: ESO/J.Walsh. (f) Menzel 3 (Mz3) or the *Ant nebula*, Credits: NASA/ESA, Hubble Space Telescope. From these, (a) and (d) are in the northern hemisphere, while the rest of them at the southern hemisphere.

angle under which the object is seen). Thus, observed morphology is not enough for the structural classification of a PN. In addition, the various components that a PN consists of (ionized, atomic, molecular, and dust components) do not necessarily have the same geometry. Multi-wavelength observations along with kinematic data are necessary to separate various components projected on the same positions in the sky. Furthermore, 3D modeling, e.g. *SHAPE* code (Steffen et al. 2011), can provide us the 3D structure of a PN. A very nice work on this has been presented by Clyne et al. (2015a). Through this thorough probe we would be able to constrain even more the classification criteria of a PNe.

An understanding of their real geometric structure is of vital importance as it is the first step toward understanding of their dynamical evolution. For example, spherical structure implies a smooth envelope ejection in a uniform ISM, while bipolar morphology may denote strong mass-loss through the poles of the central star. Multiple, fainter outer shells may be evidence for multiple ejections and/or interaction of multiple stellar winds, as mentioned above. For the variety in the morphology of the PNe, it is possible that various mechanisms may contribute such as ISW, pulsations, dynamical instabilities, multiple ejections of material from the stellar surface, the presence of one or more companion stars and presence of magnetic fields. These mechanisms may operate in the same object at different times resulting in the final PN formation.

1.2.7 White Dwarfs

At the final stage of a PN, the nebular shell expands and merges with the interstellar gas, while its central star becomes a White Dwarf (WD). WDs occupy the down-left region in the HR diagram (Fig. 1.4). A WD is about the size of the Earth (Earth radius ~ 6000 *km*) and contains approximately the same amount of mass as the Sun ($M_\odot \sim 10^{30}$ *kg*) (for the relationship between mass and radius in a WD, see Section 7.2). They are super dense objects, with density 10^6 gr cm^{-3} (for comparison, Sun's density = 1.4 gr cm^{-3}, Earth's density = 5.5 gr cm^{-3}). Its C-O core cannot undergo any nuclear fusion any more (this would demand temperatures even higher than 10^8 *K*). Since there is no nuclear energy produced to resist the inwards gravitational pull, the only mechanism that prevents this very dense core from collapsing is the outwards electron degeneracy pressure (note that the gas in the core now is not an ideal gas, but degenerate). In order for the WD to maintain its Hydrostatic equilibrium state, its mass must not exceed the *Chandrasekhar limit*. Above that limit, inwards gravitational force would be too strong to get balanced by the degeneracy pressure, and the WD would totally collapse.

While the core stays in this equilibrium state, it emits radiation in the region of soft, or lower-energy, X-rays, ionizing the previously expelled gaseous envelope of the star. The core

illuminates, not because it generates energy (nuclear reactions have stopped), but because it has trapped a large amount of heat which is gradually radiated away. Progressively, the core will cool off by radiating light, up to the point that it will no longer be visible. Then it will be transformed into a **brown dwarf**, a cold stellar corpse with the mass of a star and the size of a planet. It will be composed mostly of C, O and Ne, the products of the most advanced fusion reactions of which the star was capable. This procedure will be completed within the next billion years. A second possible scenario about the late stages of a WD, is the latter to belong to a binary system. In this case, the WD ends its life as a Nova or a Type Ia Supernova, which is analytically described in Section 1.6.2.

It is worth mentioning that, as a degenerate star -like a WD- cools, its atoms "solidify" and are lined up into a giant, highly compact lattice (just like in a crystal where we see organized rows of atoms). When carbon is compressed and crystallized in this way, then the star becomes a giant *diamond-like* star. Hence, we can say that WDs are *diamonds* scattered in space!

1.3   Evolution of high-mass stars, with 8 $M_\odot \leq$ M $\leq$ 20 $M_\odot$

As high-mass stars are considered these with 8 $M_\odot \leq$ M $\leq$ 20 $M_\odot$. They are created due to the very effective molecular gas accretion driven by gravity during the protostar formation. Due to their high mass, the inward gravitational forces are so strong that are able to compress the hydrogen core to much higher temperatures than in low-mass stars. Therefore, in the core of a MS high-mass star, hydrogen fusion also occurs, but now through the Carbon-Nitrogen-Oxygen (CNO) cycle (Bethe 1939), rather than through the proton-proton chain as in the case of low-mass stars. The released energy is proportional to $\sim T^{17}$, while in the proton-proton chain is $\sim T^4$. The end result of these two reactions is the same (He production), but the steps are different (Fig. 1.9).

Specifically, in CNO cycle, four protons are used in order to produce one He atom. During this procedure, Carbon, Nitrogen and Oxygen act as catalysts that speed up the reaction, without though being consumed. We have to note that, although the primary constituents in stars are H and He, however if in some cases (much) smaller amounts of heavier elements are present, such as C, N and O (possibly present in the vicinity of the protostar due to a previous explosion of a SN), they can participate in the reactions of the CNO cycle, and in the end to produce He in the core of the star. CNO cycle fuses H at a much higher rate than the proton-proton chain that occurs in low-mass stars. This is why massive stars have shorter lives with respect to low-mass stars (a 25 $M_\odot$ spends about 2.5 million years in the MS, while the Sun about 10 billion years).
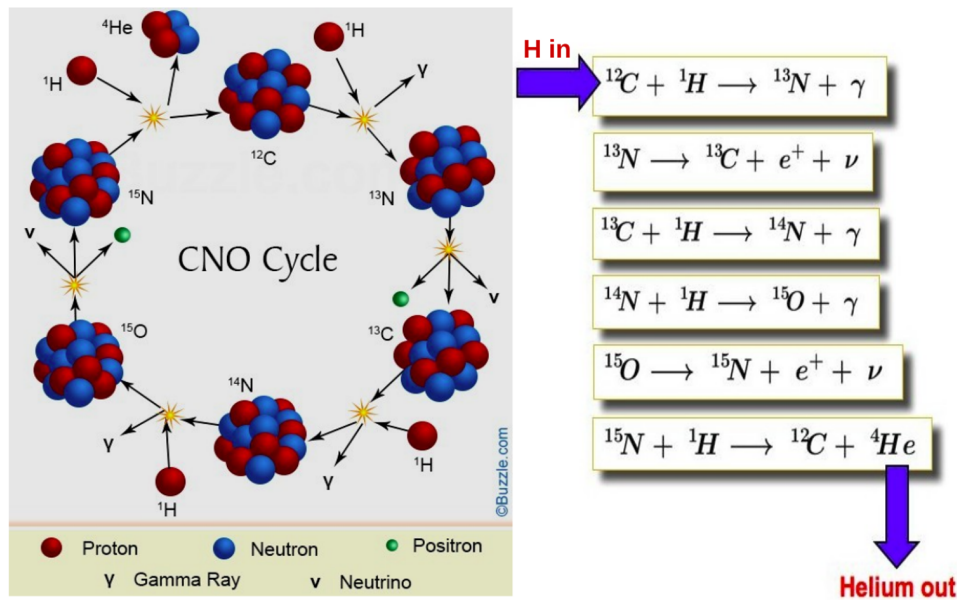
Figure 1.9: The Carbon-Nitrogen-Oxygen cycle, or CNO cycle in abbreviation. Here, four protons are used in order one He atom to be created. C, N and O "help" for the reaction to occur much faster, without however to get consumed through this.

After the He formation, He is burning into C and the rest fusion reactions continue to the point that Iron (Fe) is formed at the core of the star. These reactions take place when the star is at the AGB (or else Red Supergiant) phase. Detailed analysis from this point and on is presented in Section 1.6.3. Here we can say that what follows the Fe formation is a spectacular explosion called **Supernova (SN)**, which signals the death of the massive star. The expelled material from the star forms a nebula, called **Supernova Remnant (SNR)** (Section 1.6.4). On the supposition that the remaining star mass after the explosion is 1.4 $M_\odot \leq M \leq 3.2$ $M_\odot$, the stellar remnant is a neutron star (for details see Section 2.1.2). On the other hand, if $M \geq 3.2$ $M_\odot$, then the star collapses into a black hole, as we will see in Section 1.4.

1.4   Evolution of high-mass stars, with M$\geq$30 $M_\odot$- Wolf-Rayet stars

As we saw in the previous paragraph, stars with 8 $M_\odot \leq M \leq 20$ $M_\odot$, will explode as Supernova after they reach the Red Supergiant phase. However, the more massive stars, after their RSG phase and before they explode, they will pass through an additional evolutionary stage, becoming *Wolf-Rayet* (WR) stars. This is a special type of stars named after the astronomers Charles Wolf and Georges Rayet who first discovered them in 1867. These stars are very massive ($30-200$ $M_\odot$), very hot ($30.000-150.000$ K) and very luminous ($\sim 10^6$ $L_\odot$), with extremely fast stellar winds ($\sim 1000-2000$ $km\,sec^{-1}$) (see Section 1.9.1), while their attribute is their unusual spectra that will be described below. Their position in the HR diagram (Fig. 1.1)
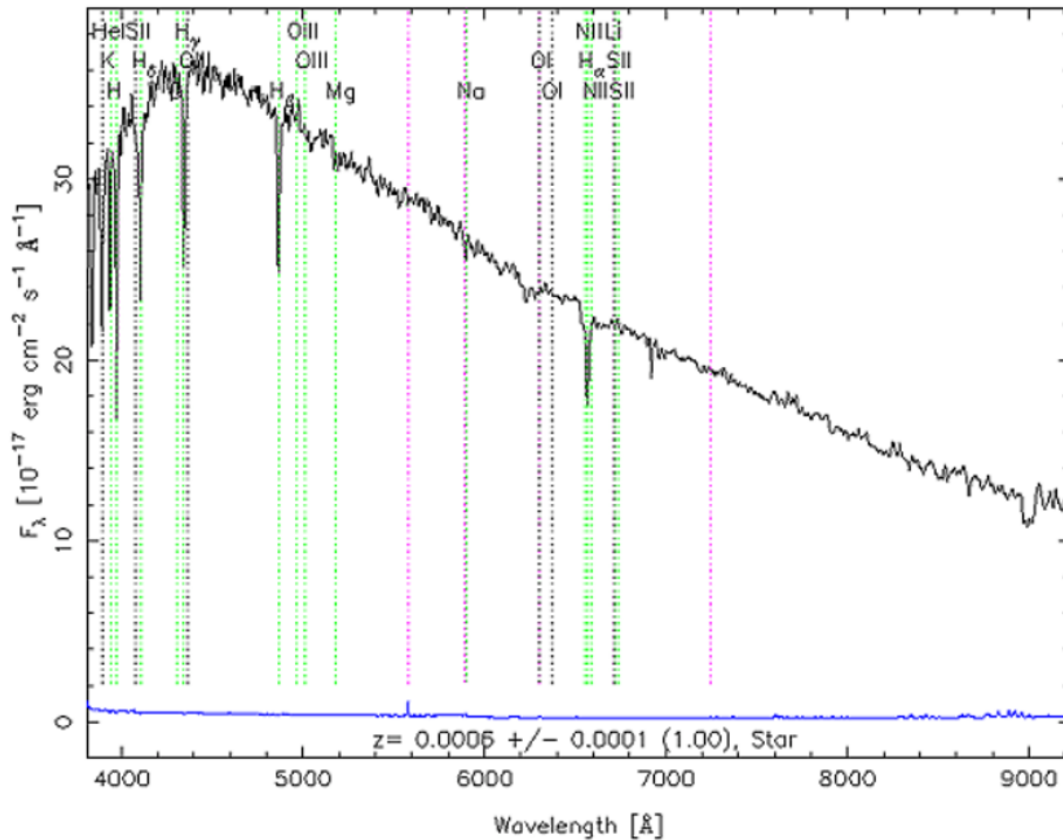
Figure 1.10: A typical spectrum of a MS star: continuum with absorption lines.

is at the upper left corner, while it is thought that their progenitors are O-type stars.

More specifically, during the RSG phase the star may lose a significant amount of mass from its outer envelopes through the stellar winds process, creating a gaseous shell around it. Therefore, as the H (or even He) envelope has been expelled, the exposed C-O hot core of the star emits copious amount of UV photons that ionize the expelled material, forming an optically bright, bubble-shaped nebula around it. The exposed core is called Wolf-Rayet star, while the discarded outer layers that surround it are referred to as Wolf-Rayet nebula (Fig. 1.11 a, c, d).

It took many years for the astronomers to figure out the nature of these objects they were observing, and this is because of their unusual spectra. Typically, Main Sequence stars show a continuum spectrum with absorption lines, as a result of light energy absorption at specific frequency form overlying elements (Fig. 1.10).

On the contrary, WR stars present continuum spectrum with broad emission lines (with equivalent widths up to 1000 Å!), similar to a nebular spectrum (Fig. 1.11b). Specifically, their spectrum contains almost no Hydrogen, but illustrates prominent, broad emission lines of ionized Helium, and highly ionized Nitrogen or Carbon. By decoding their spectra we can elicit the following

conclusions about their physical characteristics:
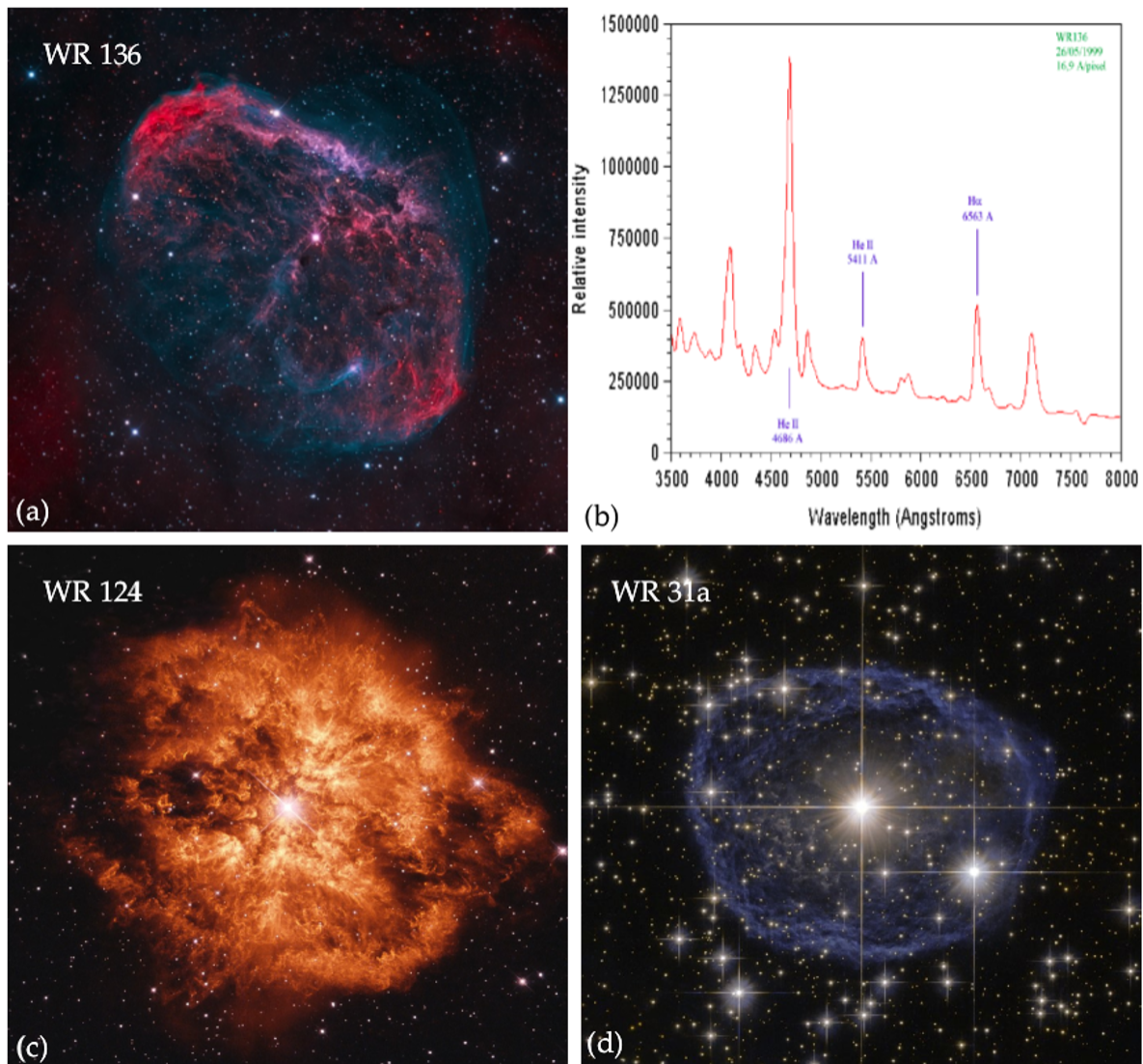
Figure 1.11: (a) The Galactic Wolf-Rayet star WR 136 and the Crescent nebula (NGC 6888) that surrounds it. In red is the Hα and in blue the [O III] emission line. Credit: Miller, Walker. (b) The spectrum of the Galactic WR 136 star with prominent the emission lines of ionized Helium. Also present is the Hα line, which indicates that the star must still have an outer layer of Hydrogen. (c) The WR nebula M1-67, mainly glowing in Hα, surrounds the Galactic exploding star WR 124. Credits: Hubble Legacy Archive. (d) The Galactic WR 31a star surrounded by this WR blue bubble consisted of dust, Hydrogen, Helium and other gases. Credit: NASA/ESA Hubble Space Telescope.

    - the lack of Hydrogen indicates that these stars are indeed in later evolutionary stage, where they have lost their Hydrogen envelope, allowing the already formed C-O core to be revealed.

    - the high degree of element ionization dictates photons of high energy which are expelled from the inner layers of the star of high temperature (and ionize its outer layers). This justifies

the formation (and the presence in their spectra) of heavier elements too, as N and C.

- the large width of their emission lines (which present both blue and red shift) implies that WR stars have strong stellar winds ejected towards all directions. They are driven by the radiation pressure on the star's gas (mechanical pressure forced onto the gas by the highly energetic emitted photons). As we said, their velocity is of the order of $\sim 1000 - 2000$ km sec^{-1}, while the stellar mass they eject is about $\sim 10^{-5}$ M$_\odot$ yr^{-1}. These extremely fast stellar winds interact with the outer layers of H (or He) previously ejected by the star in the RSG phase, creating an emission nebula around the WR star.

WR stars are very massive and therefore short-lived, that's why they are rare. In our Galaxy, there are about 220 known WR stars. It is assumed that there are much more, but not easily detectable due to dust. We can argue that Wolf-Rayet is not exactly a "type" of star but rather the last stage of evolution of very massive stars of O-type before they turn into a Supernova. In particular, they are thought to end their lives as Type Ib or Type Ic Supernova explosions (see Section 1.6.3).

1.5 Evolution of very massive stars, with M$\geq$200 M$_\odot$

In the previous paragraph we saw that massive stars tend to end their lives with a spectacular explosion (Supernova), leaving behind a neutron star. However, there is an upper limit in the mass of a neutron star, and this is 3.2 M$_\odot$, over which neutron degeneracy pressure in the core (not *electron* degeneracy any more) cannot balance gravity. Very massive stars, with M$\geq$200 M$_\odot$, create neutron stars with masses that exceed the critical mass of 3.2 M$_\odot$. The result is the star to collapse under its own gravity and all of its matter to be now compressed into a very small place, which is called **black hole**. Due to the high concentration of matter in this tiny region in space, the pulling force of gravity is so strong that even light is not able to escape. An "anatomy" of a black hole is given in Fig. 1.12.

*Comment on mass and evolution of a star:

We have already mentioned that low-mass stars tend to end their lives as White Dwarfs (through the Planetary Nebulae stage), while massive stars end as neutron stars or black holes through a Supernova explosion. We need to clarify that the factor that determines the star's fate is not only the initial mass that the star has in the MS, but also the mass the star possesses in its middle and old age, after the mass-loss that has undergone during its lifetime, basically through the stellar-wind mechanism. This will eventually define the mass of the star's core.
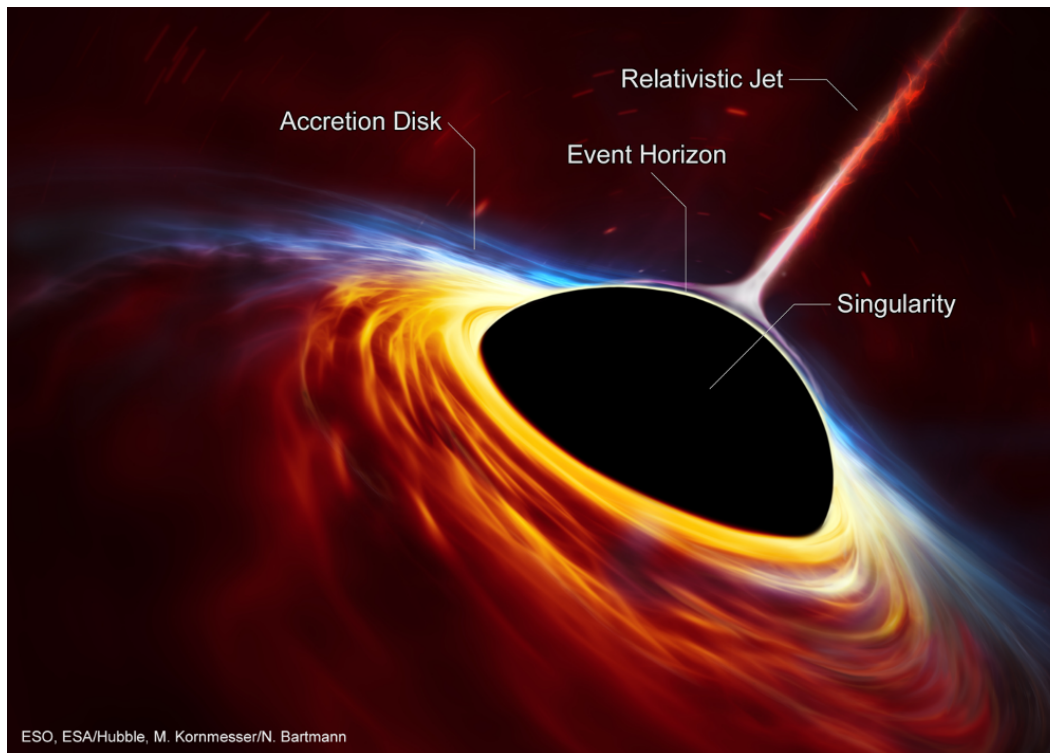
Figure 1.12: This artist's impression depicts a rapidly spinning supermassive black hole surrounded by an accretion disc. This thin disc of rotating material consists of the leftovers of a Sun-like star which was ripped apart by the tidal forces of the black hole. The black hole is labelled, showing the anatomy of this fascinating object. Credits: ESO

So, if for some reasons (*e.g.* strong stellar winds, or interaction in a binary system) a massive star loses important amount of mass, it will not necessarily end as a SN, but rather as a WD.

1.6 Supernova (SN) – Supernova Remnants (SNRs)

As **Supernova (SN)** is characterized the massive explosion which occurs at the end state of a star's lifetime. This progenitor star can be either a massive star (M $\geq$ 8 M$_\odot$) or a C-O White Dwarf in a close binary system, as we will see in the following Sections. During this massive explosion, the produced shock wave gives a huge push to the star's expelled material, forcing the latter to move supersonically into the interstellar medium (ISM), interact with it and enrich it with the heavier elements produced during the explosion. What remains after this interaction is a luminous expanding nebula, the **Supernova Remnant (SNR)**, which contains the stellar matter ejected during the explosion and also the interstellar matter swept up by the star's propagating shock wave. SNRs usually illustrate complex morphologies, while their radiation emission covers almost all the waveband, from γ-rays to radio lines.

1.6.1 Classification of Supernovae

Spectroscopically, Supernovae are divided into two main types (Fig. 1.13): Type I which have (almost) no Hydrogen in their spectra, and Type II which do exhibit H emission lines. With regards to the explosion mechanism, they are broadly classified as thermonuclear (Type Ia / low-mass progenitor stars) and core-collapse (Type II, Type IIb, Type IIL, Type IIP, Type Ib and Type Ic / massive progenitor stars) . Below we outline the explosion mechanism for each type.

1.6.2 Type Ia Supernova – Thermonuclear explosion

The fact that Type Ia SNe show no H lines in their spectra indicates that the progenitor star (the star that exploded) had no H envelope any more at the time of the explosion. A candidate stellar object for this could be a White Dwarf. On the other hand, in order for a WD to explode, its mass must have exceed the *Chandrasekhar limit*, i.e. 1.4 M$_\odot$, which means that somehow the WD managed to increase its mass. The latter can happen if this star "steals" matter from a companion star. These clues lead to the scenario of a close binary system for a Type Ia SN, the one component of which is a WD while the nature of the second component is still strongly debated. So far, two are the most accepted scenarios for the progenitor system of Type Ia SN (Fig. 1.14):

i) **Single degenerate system:**

In this binary system we want a companion star that maintains its H-envelope, so a candidate can be a MS star or a Red Giant. Also, it has to be at a close distance to the WD, in order for the
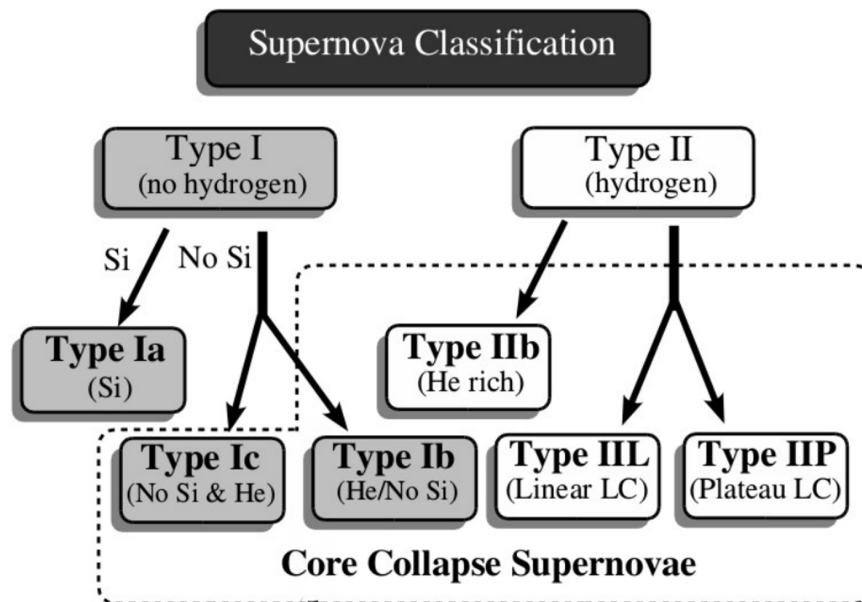
Figure 1.13: The Supernova classification scheme based on optical spectroscopy and light curve (LC) shape. Credits: Vink (2004).

extremely dense WD to exert strong gravitational pull onto the H-atmosphere of its companion star, accreting matter from it. Progressively, the WD's mass increases over the critical limit of 1.4 $M_\odot$ (WD's density reaches $2 \times 10^9 \, \mathrm{gr \, cm^{-3}}$), which means that the electron degenerate pressure in its core can no more withstand the increasing gravity. The core gets compressed and its temperature increases to the point that fusion reactions turn on again. An explosive burning flame starts to propagate outwards, behind which material undergoes explosive nuclear burning. The composition of the ashes depends on the maximum temperature reached behind the flame, which decreases as the burning front crosses layers of lower and lower densities (although still degenerate). The composition is mainly ^{56}Ni in the central parts which in turn decays into Fe, with progressively lighter elements (Ca, S, Si, etc) in more external layers. This is in agreement with the elemental stratification presented in the spectra of Type Ia, with an inner ejecta layer consisting of Fe and the outer ejecta of mid-Z (atomic number) elements (Vink 2004).

Finally, the WD explodes as a carbon-detonation supernova (thermonuclear explosion). The total energy released by nuclear burning is of order 10^{51} erg, which is sufficient to overcome the binding energy of the White Dwarf in the explosion. Therefore, the progenitor star gets completely disintegrated, no stellar remnant remains, while its companion star is pushed away due to the explosion and is now called a "runaway star". So, the nebulae from Type Ia SN host no star in their interior, in contrast to the Type II (Core Collapse SN) where the progenitor star

is still there, transformed either to a neutron star or a black hole (see Section 1.6.3).

Although the WD accretes H (and perhaps He too, if it is present) from its partner star, its spectra after the explosion shows almost no H at all. The reason is that the strong gravity at the WD's surface (where the new arrived H is deposited on) compresses H to densities and temperatures high enough to fuse it into C and O. However, the main product of the fusion is Fe which is dumping into the ISM through the explosion.

ii) **Double degenerate system:**

In this scenario, the companion star is also a C-O White Dwarf, and the two WDs are orbiting one another. Due to a process called *common envelope evolution*, the two WDs merge together, the mass of the system exceeds the *Chandrasekhar limit* and the system explodes, following the thermonuclear explosion described in the "Single degenerate system" mechanism. However, there is a main doubt about this scenario with regards to whether the C-burning initiated by the WD merger leads to the required burning and explosion of the merged White Dwarf, or proceeds quiescently and results in a core collapse SN.

Type Ia SNe occur in galaxies of all types, including elliptical galaxies which only contain old stellar populations, indicating that SNe Ia can have long-lived, low-mass progenitors. They are also used as "standard candles", i.e. objects of known, absolute brightness used for distance indicators. Because the exploded stars are C-O White Dwarfs and their explosion is triggered near the *Chandrasekhar limit*, they are characterized - more or less- by the same luminosity. Their consistent peak luminosity indicates their distance from Earth and subsequently the distance of their host galaxy.

Nova: In the case of a close binary system with a White Dwarf as the one component, there is the possibility the amount of the accreting H mass onto the surface of the WD from its partner star not to be enough for the limit of 1.4 $M_\odot$ to be exceed. In this case, the layer of H created on the WD's surface is squeezed more and more by the continually added H and by the strong gravity of the WD, its temperature and density rise and finally H becomes degenerate. Eventually, conditions of pressure and temperature become extreme enough that hydrogen burning begins, resulting in a powerful nuclear fusion explosion on the surface of the WD, during which almost all the H mass that has been accreted is thrown off. After a while the WD calms down, and additional explosions can occur when H mass transfer begins again. The difference with the Type Ia SN is that now the WD is not destroyed, but follows an accretion-explosion cycle, a phenomenon called **recurrent nova** (e.g. Harvey et al. 2020).

Type Ia Supernova
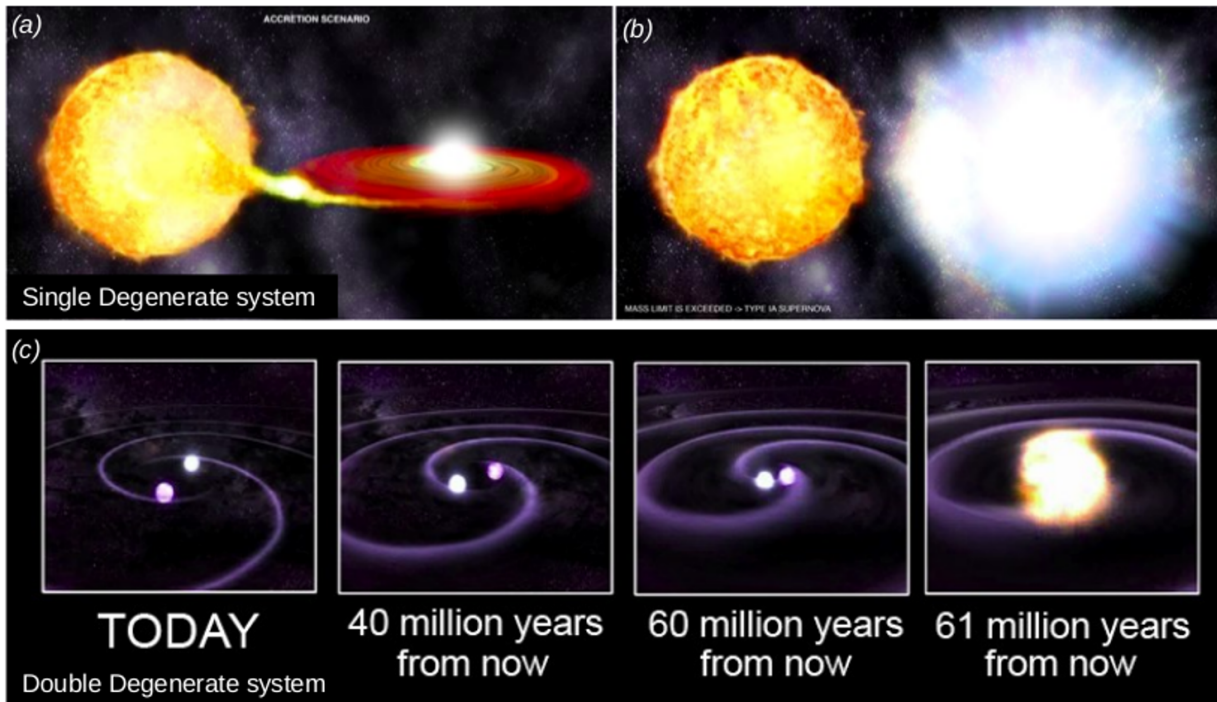
Figure 1.14: (a) Single Degenerate scenario: A white dwarf (on the right) fed by a normal star (on the left) reaches the critical mass of 1.4 $M_\odot$ and (b) explodes as a Type Ia supernova. Image Credit: NASA/CXC/M Weiss. (c) Double degenerate scenario: Two white dwarfs orbiting one another. In the future, their orbits will get smaller and smaller, and faster and faster, until someday they merge and explode as Type Ia SN too. Image Credit: NASA/GSFC/D.Berry

1.6.3   Type II Supernova – Core Collapse explosion

In Section 1.3 we were at the stage of evolution of a massive star (8 $M_\odot \leq$ M $\leq$ 20 $M_\odot$) where He has been burned into C at its core. After this phase (point 2 in Fig. 1.15), the weight of the outer layers of the massive star is sufficient to force the C core to contract until it becomes hot enough to fuse C into O, Ne, Na and Mg (point 3 in Fig. 1.15) (remember that in low-mass stars the nuclear burning ceases at the point of C or C–O formation, due to the much lower gravity that the star exerts on its core, which leads to much lower temperatures).

This conversion into heavier elements occurs through the *alpha process* in which each heavier element is created from the reaction of He with the product of the previous reaction[6].

---

[6]Remember that in the beginning, He fuses into C through the *triple alpha process* - see Section 7.1, Fig. 7.1.

For example:

$$\ce{^{12}_{6}C + ^{4}_{2}He -> ^{16}_{8}O + \gamma} \tag{1.6}$$

$$\ce{^{16}_{8}O + ^{4}_{2}He -> ^{20}_{10}Ne + \gamma} \tag{1.7}$$

$$\ce{^{20}_{10}Ne + ^{4}_{2}He -> ^{24}_{12}Mg + \gamma} \tag{1.8}$$

What follows is a cycle of core contraction, heating of the lighter elements in shells around the core, ignition of these elements, exhaustion of each nuclear fuel in the core and transformation into heavier elements, new core contraction until it reaches a new temperature high enough to fuse the even heavier produced nuclei, and so on. This procedure halts, when Iron (Fe) is formed. Over time, the internal structure of a massive star resembles that of an onion consisting by an Iron core, and layers of elements layered over each other. As we move from the center and outwards, fusion reactions are still taking place in these layers/shells of decreasing temperature, where we meet nuclei of progressively lower mass, i.e. silicon and sulphur, oxygen, neon, carbon, helium, and finally, hydrogen (point 4 in Fig. 1.15).

A detailed analysis with respect to the Fe-burning at the center of the star, is presented in Section 7.3. For now we can say that the Fe-burning, which is an endothermic chemical reaction, leads in the end to the collapse of the inner core of the star under its own gravity, producing a massive explosion which is called a **Core Collapse /CC** SN explosion or **Type II Supernova**. This explosion signals the end of the life of a massive star that collapses under its own gravity leaving behind a neutron star, on condition that the mass of the star after the explosion is $1.4 \, M_\odot \leq M \leq 3.2 \, M_\odot$. (if $M > 3.2 \, M_\odot$, a black hole is created - see Section 1.5). The energy released during the explosion is of magnitude $\sim 10^{51} erg$, and is so strong that in some cases can overshadow a whole galaxy. In Fig. 1.16, one case of Type II and two of Type Ia SN are illustrated where clearly the SNe events are distinguished with respect to the rest galaxy due to their extreme brightness.

Type II SNe occur in the spiral arms of spiral and irregular galaxies. These are regions where star formation takes place, massive stars exist and young stars of Population I[7] usually live. They are not found in elliptical galaxies though.

Fig. 1.17 illustrates the two mechanisms of SN explosions, Type Ia (thermonuclear explosion of a White Dwarf, see Section 1.6.2) and Type II which was discussed in this subsection.

---

[7]Population I: Young stars formed during the later stage of the universe when the heavier elements were already abundant in space. This is why they are metal-rich. They are more commonly found in the spiral arms of the Milky Way galaxy. Population II: Older stars formed during an earlier time of the universe when heavier elements had not yet been formed. This is why they are metal-poor. They can be found in the galactic halo and in Globular clusters too (classification by Baade 1944).

The table on the right of the figure:
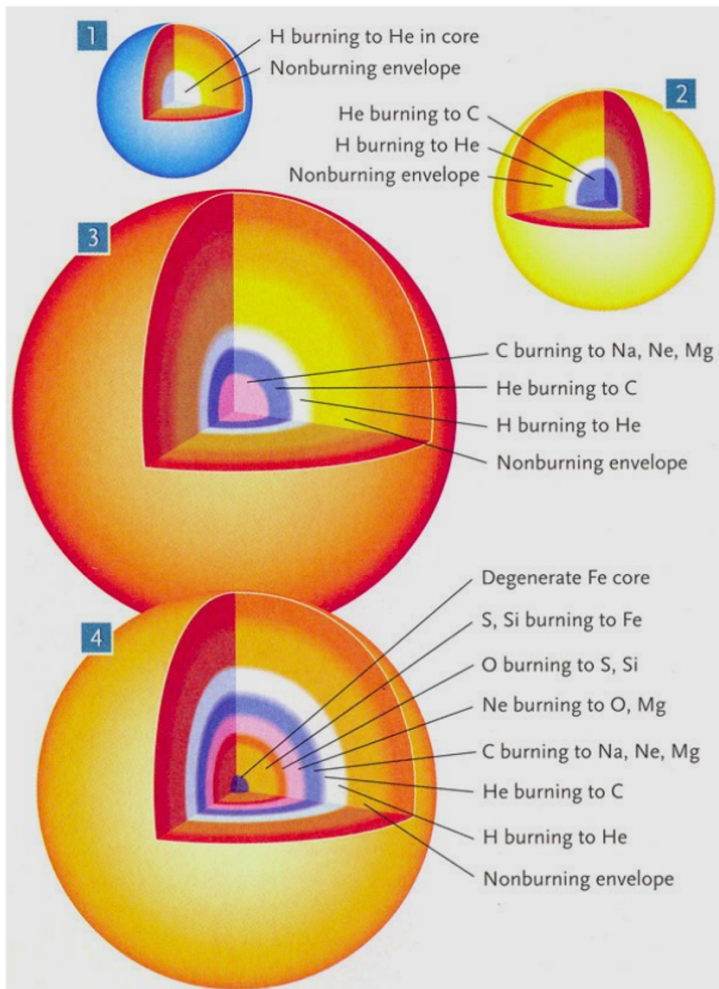
Stage	Duration
H → He	7×10^6 years
He → C	7×10^5 years
C → O	600 years
O → Si	6 months
Si → Fe	1 day
Core Collapse	¼ second

For a 25 solar mass star:

H shell: $T = 2 \times 10^7$ K, $\rho = 10^2$ gr/cm^3

Si shell: $T = 4 \times 10^9$ K, $\rho = 10^7$ gr/cm^3

Image credit: S&T: Casey Reed
Source: J.Hester & others

Figure 1.15: *On the left*: Stratification of the chemical elements in the inner structure of a massive star, starting from the H fusion (1) and ending with the Fe formation (4). *On the right*: Time duration for some of the intermediate phases of elements transformation. Also, an example for temperature and density in two shells in the interior of a 25 $M_\odot$ star.

Sub-classification of Type II SNe:

Although the explosion mechanism for Type II SNe is common and is based on the gravitational collapse of the massive progenitor star, Type II are classified in the following subcategories:

i) On the basis on the presence or absence of the outer hydrogen and helium shells before the explosion (Fig. 1.18):

Type II: H and He emission lines are both present in their spectra, which indicates that SNII retain both their hydrogen and helium shells prior to the explosion.

Type IIb: They present a weak H line in their initial spectrum. Later on, H line becomes undetectable and their spectrum closely resembles that of a Type Ib supernova, i.e. no H, but He lines present in the spectrum. The progenitor could have been a massive star that lost a major fraction of its H envelope before exploding, either due to ejection or due to interactions
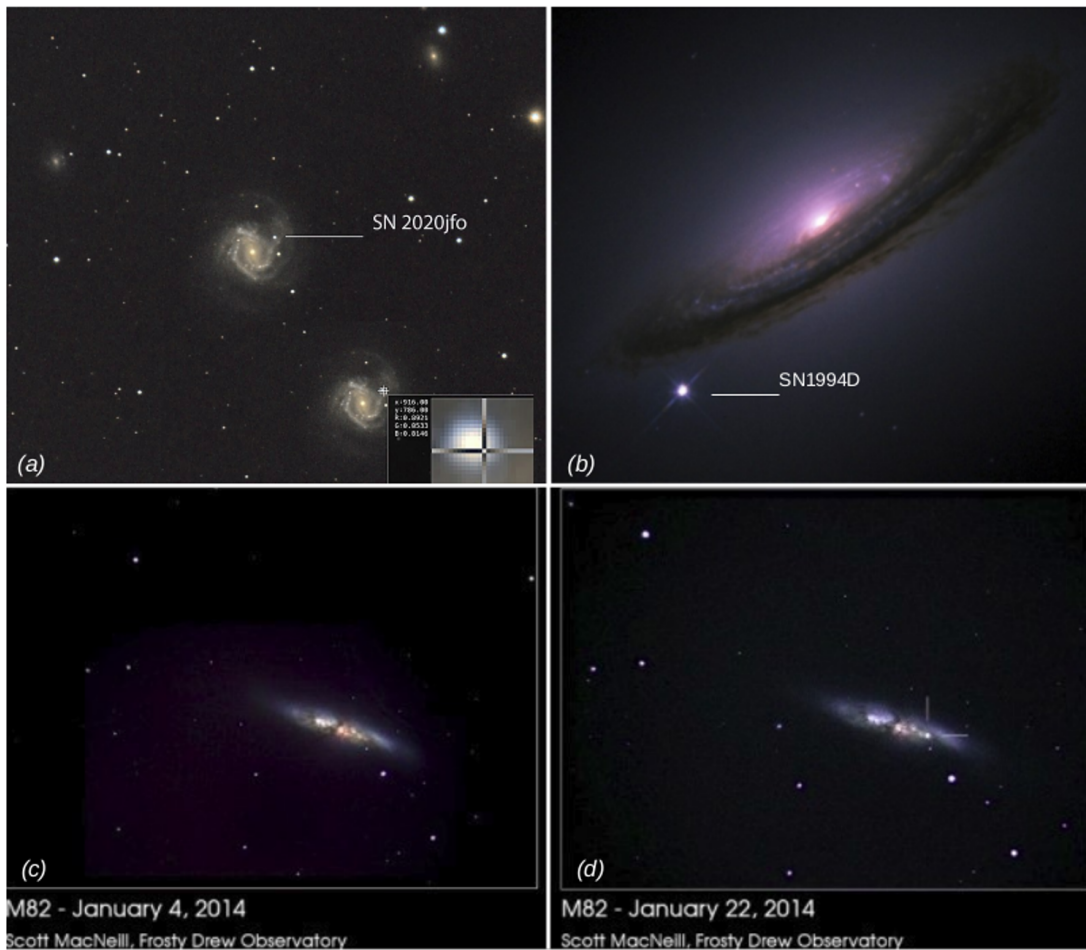
Figure 1.16: a) The very bright Type II supernova SN2020jfo in the galaxy Messier 61 (bright spot marked in the image), observed on May 15, 2020 as recorded by Raman Madhira from Ray's Astrophotography Observatory. A 11 inches RASA telescope plus a colour CMOS was used. b) Hubble Space Telescope-Image of the Type Ia SN 1994D (SN1994D) in galaxy NGC 4526 (SN 1994D is the bright spot on the lower left). c) Cigar Galaxy (M82) on January 4, 2014, and d) M82 a few days later when the Type Ia SN designated as PSN J09554214+6940260 exploded (the SN is marked with two vertical lines).

with a companion in a binary system, leaving behind the core that consisted almost entirely of helium. As the ejecta of a Type IIb expands, the hydrogen layer quickly becomes more transparent and reveals the deeper layers. The IIb class was first introduced (as a theoretical concept) by Woosley et al. (1987).

Type Ib: Their spectra show neither Si 6347, 6371Å absorption lines (typical of Type Ia spectra), nor H lines too, but there is obvious presence of He absorption. So, it is believed that they result from the core-collapse of a massive star, which appears to have lost its hydrogen envelope prior to the explosion but managed to retain its helium envelope. The envelope loss can be attributed to strong stellar winds, to a mass transfer in a close a binary system, or a combination of both.
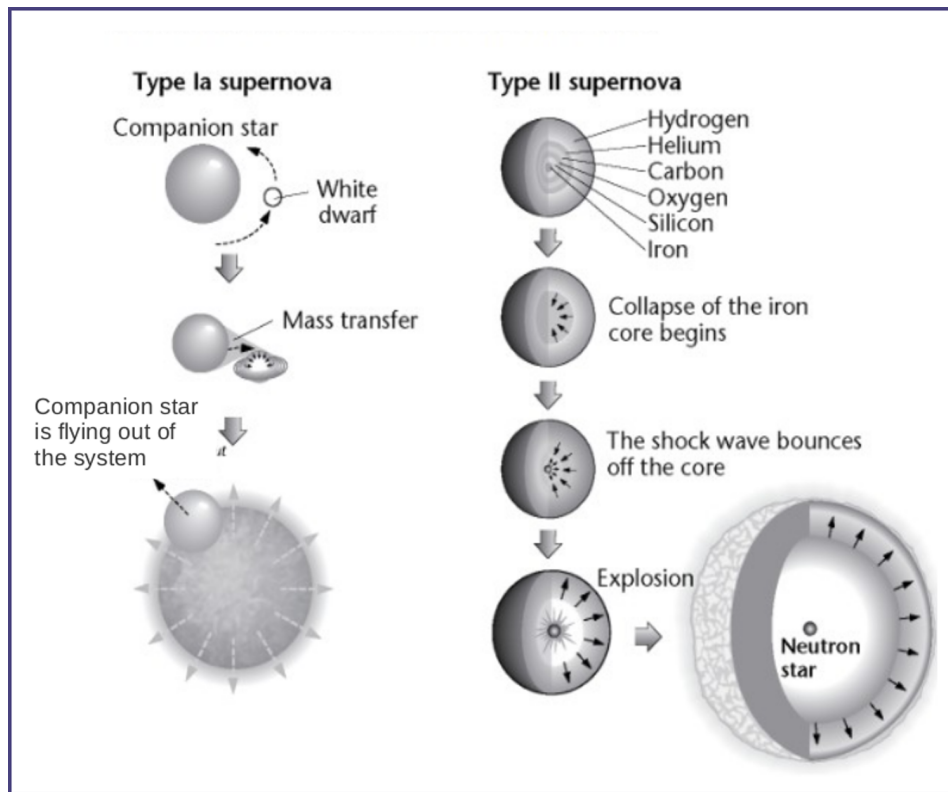
Figure 1.17: The two different mechanisms leading to a SN explosion. *On the left*: Type Ia SN caused by the explosion of a C-O white dwarf following a mass transfer event. *On the right*: A Type II SN develops at the end of the life of a massive star whose core collapses, thereby triggering the explosion (Source: Peter Palm).

Type Ic: This type appears no H nor He absorption lines in their spectra. It seems they have lost both their hydrogen and helium envelopes through some mechanism prior to the explosion.

ii) With respect to the shape of their light curves after the maximum brightness (Fig. 1.19):

Type IIP: The light curve presents a distinctive flat stretch or plateau (P stands for the "plateau") during the decline after the maximum brightness, representing a period where the visual luminosity stays relatively constant for several months before the decline, and decays at a slower rate.

Type IIL: The light curve for a Type II-L supernova shows a steady, linear (L stands for "linear") decline following the peak brightness.

Core-Collapse progenitors

Type II	Type Ib	Type Ic
H and He shells	He shell only, no H shell	no H nor He shells
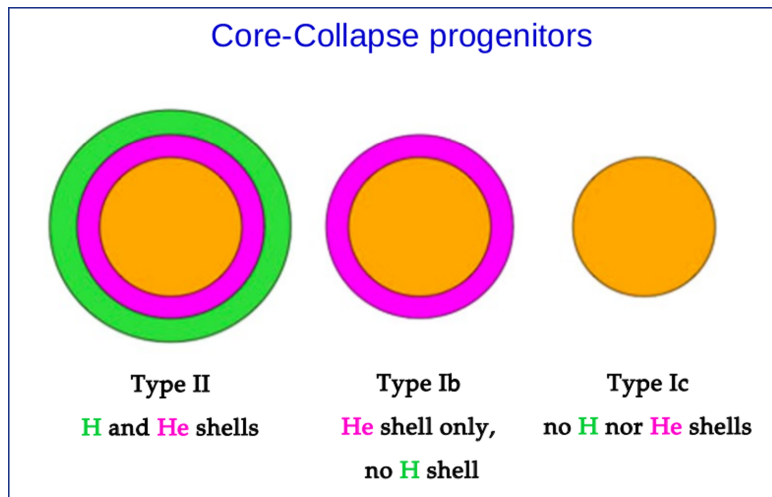
Figure 1.18: SNe of Type II, Ib and Ic, all result from a core collapse of a massive star. The differences arise depending on whether the progenitor has lost or retains its H and He shells before the explosion. Image Credits: © Swinburne University of Technology.

1.6.4 Supernova Remnants (SNRs) – Dynamical evolution

We present the basic evolutionary stages of a Supernova remnant (SNR) generated from a Core-Collapse SN. A general guideline has been given by Woltjer (1972), where SNR's evolution is divided in the following 4 phases:

1. *Free expansion* or *ejecta dominated phase*, which lasts for a few hundreds years after the explosion

2. *Adiabatic* or *Sedov-Taylor phase*, for the next $\sim$ 20.000 years

3. *Radiative* or *"snow-plough" phase*, up to 500.000 years

4. *Merging phase*

We assume the most simple case, that is a non-rotated progenitor star, which undergoes a symmetric explosion, and whose stellar debris expand equally and isotropically into a homogeneous and uniform ISM (i.e. no clouds or density gradients). We also neglect the effects of relativistic particles (cosmic-ray acceleration) and magnetic fields.

1.6.5 Phase I: Free expansion phase or ejecta driven evolution ($M_{ej} > M_{sw}$)

This phase is characterized by the free propagation in the CSM/ISM of the stellar material expelled from the star after its Supernova explosion. The released energy, $E_o = 10^{51}$ erg, is consumed into kinetic and thermal energy of the stellar ejecta. The radiation emission in the optical at this phase is negligible, therefore it can be termed as adiabatic (Reynolds 2017)

© 2017 University of Iowa
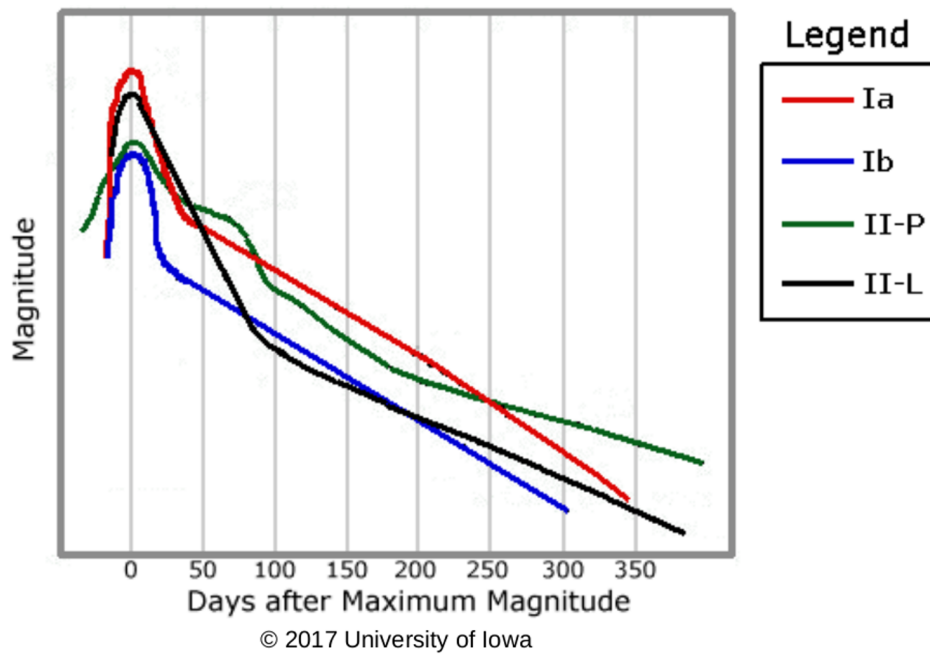
Figure 1.19: Light curves of Type Ia SN (White Dwarf supernova) and Type Ib, IIP and IIL (massive star supernova).

(adiabatic → no energy loses through radiation). The propagation velocity of the expanded gas-shell, which is of the order of $V_s \sim 10^4$ km s^{-1}, is incomparable higher to the sound speed in the local ISM[8]. Therefore, between the front of the stellar ejecta and the ISM, a shock wave is created (*forward shock* or *blast wave*) which drives the propagation of the expelled gas-shell into the surrounding ISM (Fig. 1.20). A shock front constitutes an interface through which mass flow can occur (in contrast to a contact discontinuity where no mass transfer happens). So, as the shock wave travels through the ISM, the gas-shell sweeps up / absorbs the ISM that meets on its way, without however getting involved with this material. This material, hereafter called "shocked ISM" (region 2 in Fig. 1.20), is now compressed and heated, moving to the same direction as the forward shock front, but at a velocity V_1 lower than the latter. In particular, $V_1 = \left(\frac{3}{4}\right)V_s$ (see description below, about Rankine-Hugoniot equations).

At this stage, the mass swept up by the shock wave (M_{sw}) is negligible compared to the mass ejected from the star (M_{ej}) ($M_{ej} \gg M_{sw}$), and this is why the expansion moves on at a constant velocity without deceleration (free expansion phase).

If there was no interstellar material in the vicinity of the star, then the expelled gas would continue its free propagation at velocities as high as $V_s = 3 \times 10^4$ km s^{-1}. But ISM is present (with a typical value of density $\rho = 1.7 \times 10^{-24}$ gr cm^{-3}[9]) forcing the stellar ejecta to propagate

---

[8]Remember that ISM mainly consists of neutral (H I) or ionized (H II) Hydrogen. Typical values for the sound speed in these regions are: $\alpha_{HI} \sim 1.2$ km s^1 and $\alpha_{HII} \sim 17$ km s^{-1}.

[9]ISM density $\rho = no \times m_H = 1.7 \times 10^{-24}$ gr cm^{-3}, where $no = 1$ cm^{-3} is the arithmetic density of H in space and
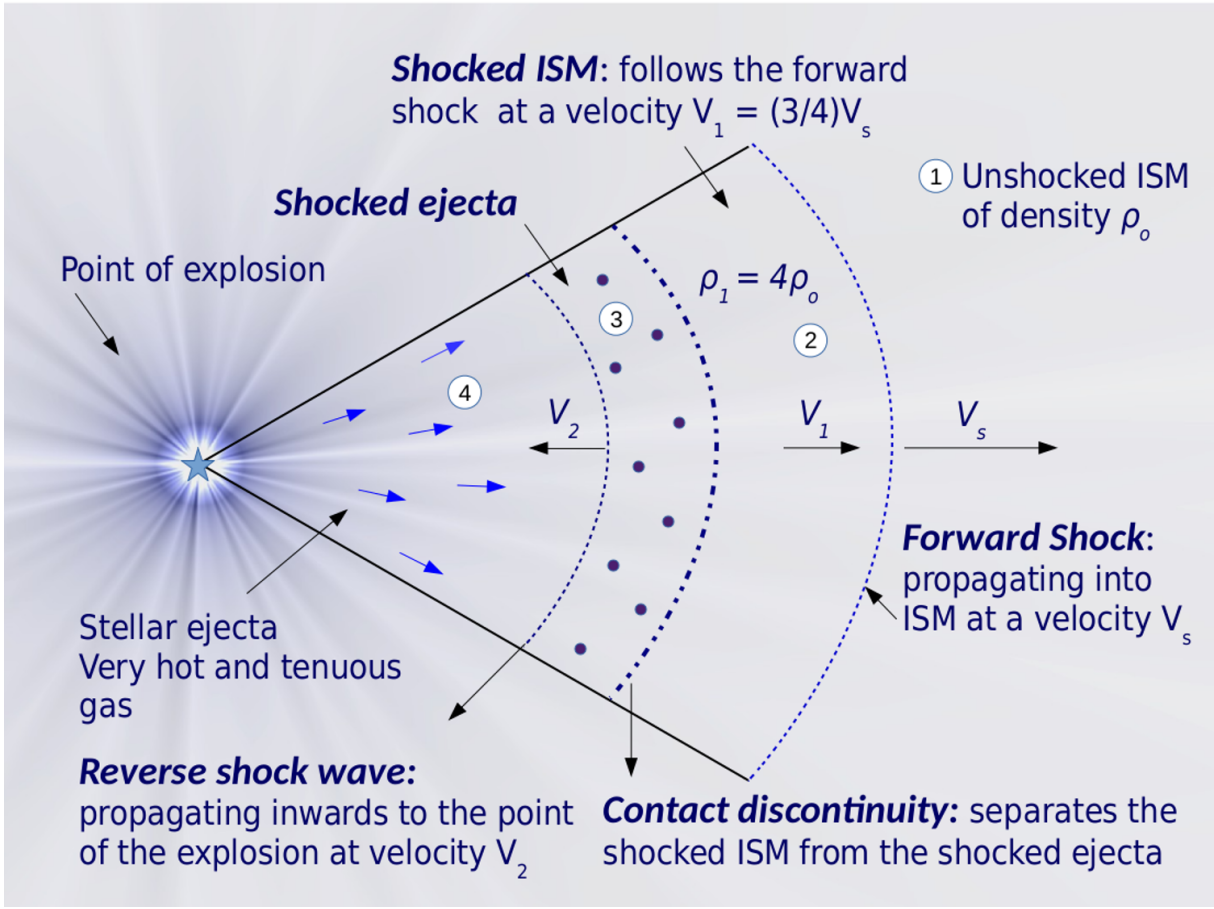
Figure 1.20: Stratification of the expanding shell of a SNR, from the point of explosion up to the outer forward shock wave front. For description of the regions 1 to 4, see Section 1.6.4.

at lower velocities. In particular, we meet average velocities of 10.000 km s^{-1} for Type Ia events and 5.000 km s^{-1} for CC explosions (Reynolds 2017).

The radius R_s of the remnant (which is the distance of the shock front from the explosion center) and its age at this phase (which, in practise, is the time of evolution of phase I), can be calculated by the following equations:

$$\rho = \left(\frac{M_{sw}}{V} \right) \tag{1.9}$$

$$V = \left(\frac{4}{3} \right) \pi R_s^3 \tag{1.10}$$

$$R_s = V_s t \tag{1.11}$$

where ρ is the ISM density, M_{sw} is the mass of the shocked ISM at the end of phase I, V is the volume occupied by the SNR when its radius is R_s, V_s is the velocity of the shock wave and t is the time duration of phase I, i.e. the age of the remnant at the end of phase I.

To set an example: if we consider $M_{sw} = M_{ej} = 5$ M$_\odot$, $\rho = 1.7 \times 10^{-24}$ gr cm^{-3} and $V_s = 10^4$ km sec^{-1}, the above equations give: $R_s \sim 3.6$ pc and $t_s \sim 350$ yr. In other words, this phase

---

m$_H$ is the mass of H atom.

58

will end after 350 yr from the explosion, when the gas-shell will be at a distance of 3.6 pc from the exploded star. In general, the free expansion phase lasts about $\sim 100 - 1000$ yr. An example of a SNR which is at this evolutionary phase, is the Galactic SNR Tycho (the remnant of the supernova SN 1572) with an estimated age of ~ 450 yrs.

When the mass swept up by the shock wave (M_{sw}) is equal to the ejected mass (M_{ej}) from the star, then the stellar ejecta begins to decelerate and this signals the end of the free expansion phase. Phase I ends after time:

$$t = 200 \left(\frac{M_{ej}}{M_\odot} \right)^{\left(\frac{1}{3}\right)} \left(\frac{n_o}{cm^{-3}} \right)^{\left(\frac{-1}{3}\right)} (yr) \tag{1.12}$$

while the radius R of the remnant after the end of Phase I is given by the equation:

$$R = 2 \left(\frac{M_{ej}}{M_\odot} \right)^{\left(\frac{1}{3}\right)} \left(\frac{n_o}{cm^{-3}} \right)^{\left(\frac{-1}{3}\right)} (pc) \tag{1.13}$$

1.6.6   Phase II: Sedov-Taylor or adiabatic phase ($M_{sw} > M_{ej}$)

After the end of the free expansion phase, the gas-shell continues to expand absorbing more and more ISM (shocked ISM in region 2 of Fig. 1.20). At the point of which the shocked ISM begins to exceed the stellar ejecta ($M_{sw} > M_{ej}$), the deceleration of the expelled shell begins. However, its velocity still remains higher than the local sound speed of the ISM, which means that the forward shock wave described in Phase I is still present, acting like a spherical, supersonically moving piston which drives the expansion of the gas-shell. If we assume that the mass of the ISM before the explosion was initially "contained" in a sphere of radius R (at the center of which the star was located) and had a density ρ_0, now this material has all been absorbed by the shock wave and compressed into a thin and dense shell of thickness $\sim 0.1R$ and density $\rho_1 = 4\rho_0$. This is exactly the shocked ISM described in Phase I, but now located in a thin shell behind the shock front (region 2 in Fig. 1.20, not in scale).

The radius and the velocity of the forward shock, which in practice are the same as these of the expanding shell, are given by the Sedov-Taylor equations:

Sedov-Taylor equations: Taylor (1950) and Sedov (1959), independently presented the mathematical approach of a point explosion in a uniform medium of density ρ, and studied the propagation of the produced adiabatic shock wave into this ambient medium. This analysis can be applied for a massive explosion (Supernova) in a very small place ($R = 0$) within a very short time scale ($t = 0$), in the limit where the swept-up mass (M_{sw}) exceeds the SN ejecta

mass (M_{ej}). According to their analytical self-similar solutions (i.e. later time solutions which depend on both r and t, are a scaled-up version of the system at an earlier time), the general equations that can describe the radius and the velocity of a SNR which propagates spherically in a homogeneous ISM, are:

$$R_s = \alpha t^m \tag{1.14}$$

$$V_s = \frac{\partial R_s}{\partial t} = m\alpha t^{m-1} \tag{1.15}$$

where m is a constant number (expansion parameter), while α is a constant depending on the physical parameters of the system, i.e. energy E_0 and density ρ_0.

In phase II, constant $\alpha = \left(\frac{2E_o}{\rho_o}\right)^{\frac{1}{5}}$ while constant $m = \frac{2}{5}$. Therefore, equations 1.14 and 1.15 give:

$$R_s = \left(\frac{2E_o}{\rho_o}\right)^{\frac{1}{5}} t^{\frac{2}{5}} \tag{1.16}$$

$$V_s = \frac{\partial R_s}{\partial t} = \left(\frac{2}{5}\right) \left(\frac{2E_o}{\rho_o}\right)^{\frac{1}{5}} t^{\left(\frac{-3}{5}\right)} \tag{1.17}$$

On both sides of the forward shock (regions 1 and 2 in Fig. 1.20), mass, momentum and energy are conserved (law of Hydrodynamics), which implies that there is no mass, momentum or energy accumulation inside the shock wave. The shock is assumed to be infinitely thin, and this is why a more appropriate term for it would be *shock front* instead of "shock wave". However, both terms are used equally. Rankine-Hugoniot equations are based on the conservations law of Hydrodynamics mentioned above, and provide the density, pressure and temperature of the two gases on either side of the shock front, i.e. the undisturbed ISM and the shocked ISM. Finally, from Rankine-Hugoniot relations, we derive the following equations (derived for monoatomic gas where $\gamma = \frac{C_p}{C_v} = \frac{5}{3} =$ the ratio of the specific heats of air):

$$\rho_1 = 4\rho_o \tag{1.18}$$

$$V_1 = \left(\frac{3}{4}\right) V_s \tag{1.19}$$

$$P_1 = \left(\frac{3}{4}\right) \rho_0 V_s^2 \tag{1.20}$$

$$T_1 = \left(\frac{3}{16}\right) \left(\frac{\mu m_H}{k}\right) V_s^2 \Rightarrow T_1 = \left(\frac{3}{32}\right) \left(\frac{m_H}{k}\right) V_s^2 \tag{1.21}$$

where ρ is the density, V_s is the velocity of the forward shock wave (shock front), P is the pressure and T is the temperature (note that the shock velocity defines the temperature of the post-shocked gas). The pre-shock gas is labelled with the subscript 0, while the post-shock gas with the subscript 1. k is Boltzmann constant ($k = 1.38 \times 10^{-23}\ JK^{-1}$), m_H is the mass of H
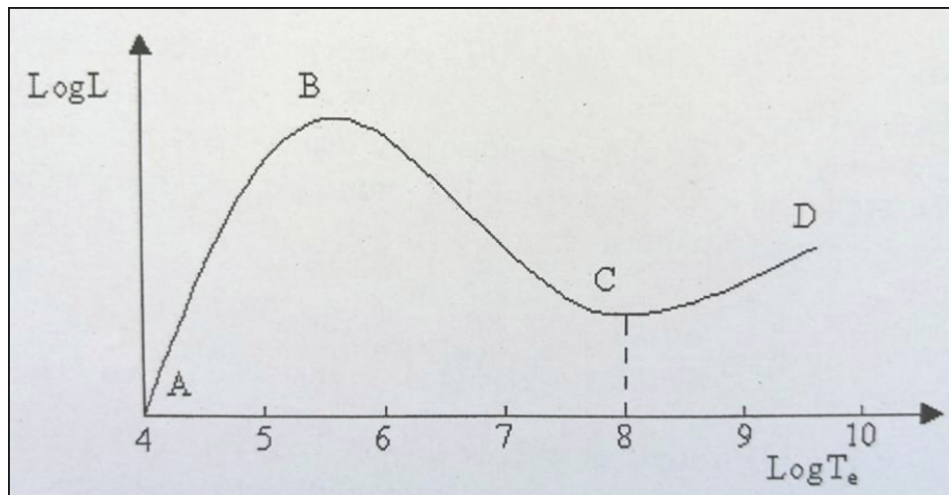
Figure 1.21: Interstellar cooling curve: it illustrates the cooling rate L, i.e. the energy loss due to radiation (per volume and per time) with respect to the temperature T (Goudis, Shock waves, 2007).

atom ($m_H = 1.7 \times 10^{-24} gr$), while μ is the mean molecular weight of the gas. We assumed that the shocked ISM is fully ionized (H II gas), therefore $\mu = \frac{1}{2}$.

Why is called "adiabatic phase": The temperature of the shocked ISM is $T_1 > 10^6$ K (from 10^4 K in the ionized undisturbed ISM). In such high temperatures, recombination between free electrons and ions is very rare to happen due to the high kinetic energy of the particles. This recombination would have produced optical radiation, which constitutes one of the cooling mechanisms for the SNR, as this radiation energy finally escapes from the remnant. Consequently, the cooling rate at this stage is very low (see Fig. 1.21) and there is almost no optically emitted radiation from the shocked ISM. This is why Phase II is also characterized as adiabatic (Phase I is adiabatic as well), while the forward shock here is termed as "adiabatic" or "non-radiative". But, to be more rightful, non-radiative shocks do radiate (at this phase in the X-ray band), but little of the energy dissipated in the shock is converted into radiation. Therefore, non-radiative shocks are faint compared to the radiative shocks. So, as practically no energy is lost in radiation, all the initially released energy ($E_o = 10^{51}$ erg) of the explosion is partially used as kinetic energy for the shell expansion ($E_{kin} = 40\%E_o$), while the rest of it is consumed as thermal energy of the gas of the expanding shell ($E_{therm} = 60\%E_o$). Therefore, in Phase II energy is preserved.

Reverse shock formation: In the meanwhile, the star keeps ejecting material from its center. This stellar ejecta falls onto the decelerated, dense shocked ISM shell, it is reflected from this obstacle-shell and a second **reverse shock** is formed (McKee 1974) which is moving accelerated towards the center of the explosion, as it meets regions of lower and lower density (Fig. 1.20). Now, the ejecta that is still coming from the star, meets the reverse shock front, passes through it, it gets absorbed and compressed by it, and finally decelerated in a zone which is called "shocked ejecta" zone (region 3 in Fig. 1.20). As time progresses, the reverse shock continues to move towards the center, heating the gas in region 4 of Fig. 1.20 at temperatures $T = 10^7 - 10^8$ K. The cooling rate of this gas is very low (Fig. 1.21), and the radiation emitted from this very hot and tenuous gas (coronal gas) is in the soft X-ray band (<10 keV). This is the only kind of radiation observed in Phase II. However, this radiation emission is not significant with respect to the total explosion energy, and this is why we consider no energy loss at this stage.

1.6.7 Phase III: Radiative phase (Snow-plough phase)

Transition from Phase II to Phase III:

Over time, the temperature of the shocked ISM decreases. We can see this by substituting Eq. 1.17 into Eq. 1.21, from which we derive a relationship of the temperature T_s of the post-shock

gas (region 2 in Fig. 1.20) with respect to the time t of evolution:

$$T_s = const. \times t^{\frac{-6}{5}} \tag{1.22}$$

We see that as evolution time t progresses, T_s reduces, which means that the cooling rate becomes important (according to the cooling curve of Fig. 1.21) and optical radiation can now be emitted from the shocked ISM. Generally speaking, radiation losses begin when temperature T_s falls below $\sim 10^5$ K, in which case Oxygen emission line becomes an important coolant.

In order to have a sense of the time scaling of this procedure, it would be useful to compare the cooling time t_c with the evolution time t of the remnant. The cooling time t_c of the post-shock gas is related with its temperature T_s by the equation:

$$t_c = \left(\frac{3k}{4n_o \lambda} \right) T_s^{\frac{3}{2}} \tag{1.23}$$

where n_o is the arithmetic density of the unshocked ISM, and λ a parameter related to the cooling function $\Lambda(T)$. By substituting Eq. 1.22 into Eq. 1.23, we derive a relationship between the cooling time t_c and the evolution time t, i.e. the age of the remnant, or else its expansion time:

$$t_c = const. \times t^{\left(\frac{-9}{5} \right)} \tag{1.24}$$

Eq. 1.24 implies that as evolution time t passes, the time t_c in which the post-shock gas cools down, reduces. In other words, progressively, the shocked ISM will cool down faster than the shell will expand and, due to its cooling, this post-shock gas will begin to emit radiation. But, before that, there will be a moment at which the cooling time will be equal to the age of the remnant, and that would be:

$$t_c = t_{age} = const. \times Eo^{\frac{3}{14}} \rho_o^{\left(\frac{-8}{14} \right)} \tag{1.25}$$

For this critical moment when t_c equals t_{age}, the expansion velocity of the shell V_s and the radius R_s of the forward shock (i.e. the radius of the remnant) are given by the Sedov-Taylor equations:

$$V_s = const. \times Eo^{\frac{1}{14}} \rho_o^{\frac{1}{7}} \tag{1.26}$$

$$R_s = const. \times Eo^{\frac{2}{7}} \rho_o^{\left(\frac{-3}{7} \right)} \tag{1.27}$$

Typically, for explosion energy $E_o = 10^{51}$ erg and ISM density $\rho_o = 10^{-24}$ gr cm^{-3}, adiabatic phase lasts for about 3×10^4 yr, at the end of which the velocity of the forward shock wave drops at the value of $V_s = 250$ km s^{-1}, while it's radius is about $R_s = 20$ pc. From this point and on, the previously adiabatic shock wave of Phase II is now becoming a radiative (or luminous)

shock in Phase III. This signals the end of Phase II (energy conservation) and the beginning of Phase III (energy loss due to radiation / momentum conservation), which is also called Radiative Phase or Snow-plough phase.

Phase III:

This cooling stage can roughly be described by two successive phases: i) Pressure-driven phase and ii) Momentum-driven phase, depending on when the shocked ejecta radiates (or not) during the evolution, something that is related to its velocity.

Pressure-driven phase or snow-plough phase or Energy-driven model:

Between the shocked ISM and the shocked ejecta (regions 2 and 3 respectively in Fig. 1.20), a contact discontinuity is formed. This is a surface between materials of different composition and entropy, on both sides of which pressure remains relatively constant, but no mass flow occurs.

If the velocity of the shocked ejecta is greater than a critical value ($V_{sh.ej} > V_{critical}$) (Goudis, Dynamic Interstellar Phenomena, 2007)

$$V_{critical} = 100 n_o \times \left(\frac{M*}{10^{-6} \ M_\odot \ yr^{-1}} \right)^{\frac{1}{9}} km \, s^{-1} \qquad (1.28)$$

then it's temperature is so high ($T \sim V_s{}^2$) that the gas cannot cool down due to radiation emission, but only through energy flux from region 3 to region 2 due to adiabatic expansion of the former. In other words, the shocked ejecta acts like a thermal, adiabatically expanding piston (no energy losses), whose thermal pressure exerts force onto the shell of the shocked ISM, pushing the latter to move outwards like a snow-plough mechanism does (Fig. 1.22), always keeping constant the relative pressure between the shocked ejecta and the shocked ISM (*pressure-driven* or *snow-plough phase*).

At the same time, the density in the shocked ISM region increases due to the continuously incoming unshocked interstellar material. This, in conjunction with the temperature decrease over time in the shocked ISM (Eq. 1.22), leads to the decrease of the cooling timescale, as Eq. 1.23 implies. As the post-shock gas cools down, the recombinations between free electrons and ions are allowed, and the gas-shell loses energy through optical radiation emission[10] (radiation loss in the shocked ejecta is considered negligible). Therefore, the adiabatic shock wave of Phase II turns now into a radiative shock.

It is worth mentioning that the high temperature in the adiabatic waves of Phase II is responsible for the high thermal energy of their free electrons, i.e. their high mobility, which resists to the compression of the shocked gas. On the other hand, the gas in the radiative

---

[10]For further description of the radiation mechanisms in SNRs, see Section 1.8.
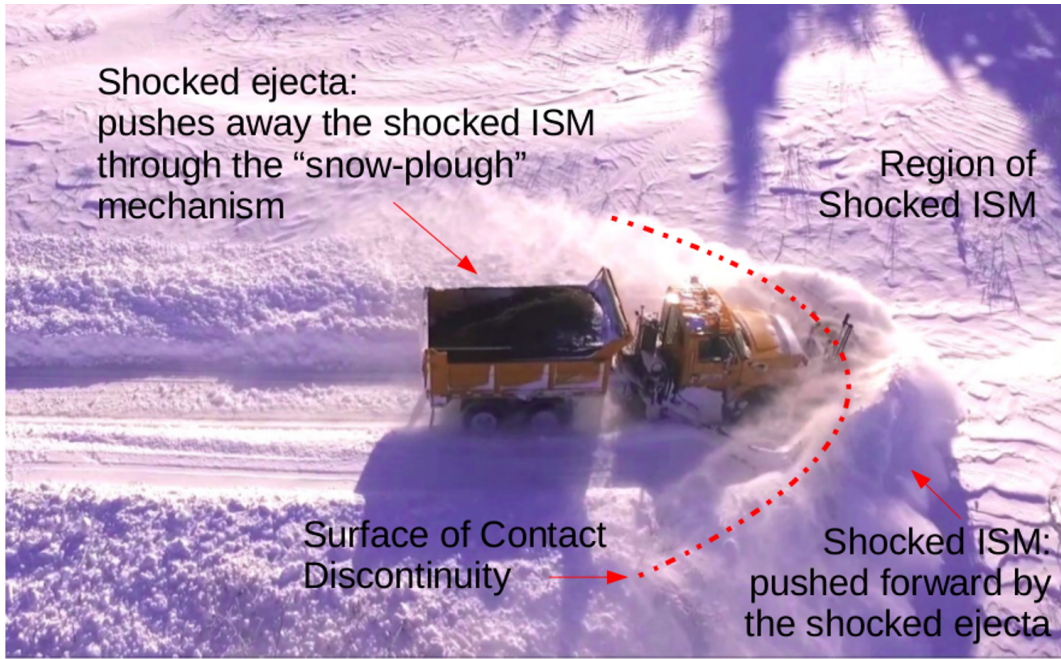
Figure 1.22: The "Snow-plough" model of Phase III in SNRs evolution. The shocked ejecta pushes forward the shocked ISM in the same way as the snow-plough vehicle pushes away the snow. The contact discontinuity separates the two regions of shocked ISM and shocked ejecta.

shocks of Phase III is now dense (compressed), due to the energy loss through radiation which enables its compression (Goudis, Shock waves, 2007).

Finally, in order for the shocked ISM to retain the pressure balance with the shocked ejecta that pushes the former outwards, this dense shell of the post-shock gas collapses in a very thin layer that moves along with the shock front. At this stage, the radius of the expanding shell is given by the equation (Goudis, Dynamical Interstellar Phenomena, 2007):

$$R(t) = 19pc \left[\frac{E_o}{10^{51}erg}\right]^{0.23} \left[\frac{n_o}{cm^{-3}}\right]^{-0.26} \left[\frac{t}{10^4yr}\right]^{\frac{2}{7}} \tag{1.29}$$

However, Cioffi et al. (1988) argued that the above expression $R \sim t^{\frac{2}{7}}$ does not accurately describe the expansion in radiative phase. Therefore, they presented an improved offset power-law analytic solution for the pressure-driven expansion, according to which the radius of the remnant is given by the equation:

$$R(t) \sim t^{\frac{3}{10}} \tag{1.30}$$

The pressure-driven phase comes to an end when the internal driving pressure vanishes due to radiative cooling. After this point, the SNR enters the second part of Phase III, called the Momentum-driven phase, which is described below.

Momentum driven model:

As time progresses and the whole remnant expands radially, there will be a point at which the velocity of the shocked ejecta will be lower than the critical value ($V_{sh.ej} < V_{critical}$). As a result, its temperature is also reduced, and the shocked ejecta cools down and loses energy due to the emission in the optical[11]. Consequently, there is no pressure any more of the thermal energy of the shocked ejecta over the shocked ISM (it is lost due to radiation emission). In this case, the shocked ejecta and the shocked ISM are pushed forward due to the momentum of the unshocked ejecta that is transported on them through its incidence on the reverse shock front. This is called "momentum-driven model", and the radius and velocity of the remnant are given by the equations (Oort 1951):

$$R(t) \sim t^{\frac{1}{4}} \tag{1.31}$$

$$V(t) \sim t^{\frac{-3}{4}} \tag{1.32}$$

We can note that the exponent 0.3 in the Eq. 1.30 given by Cioffi et al. (1988), is included in the general expression or the remnant's radius:

$$R(t) \sim t^n \text{ where } \frac{1}{4} \leq n \leq \frac{2}{5} \tag{1.33}$$

We see that the exponent n which defines the time dependence of the shell expansion, is between the value $\frac{2}{5}$ in the adiabatic Phase II during which the energy is preserved, and the value $\frac{1}{4}$ in the radiative Phase III during which the momentum is preserved.

1.6.8 Phase IV: Merging – Dissipation phase

As the SNR ages, it loses energy through radiation and it's expansion rate slows down. When the speed of the expanding shell drops to the values of local sound speed of the ISM, i.e. ~ 10 $km\,sec^{-1}$, then the pressure of the gas in the interior of the shell equals the pressure of the ISM outside of the remnant. Consequently, no further shell-expansion can occur, the shell falls apart, cold ISM gas intrudes into it and fills the SNR's cavity for the next $\sim 10^6$ yr. Progressively, the remnant merges with the ISM up to the point that totally dissipates in space. All the elements produced during the SN, are now mixed with the ISM (chemical enrichment of the local environment).

Fig. 1.23 illustrates the 4 evolutionary phases of a SNR, summarizing the values for the parameters of radius, explosion time and velocity.

---

[11]A general conclusion from this analysis is that interstellar shocks with $V_s > 250$ km s^{-1} do not radiate efficiently, while when $V_s < 250$ km s^{-1} are in practise radiative shocks (Goudis, Dynamical Interstellar Phenomena, 2007).
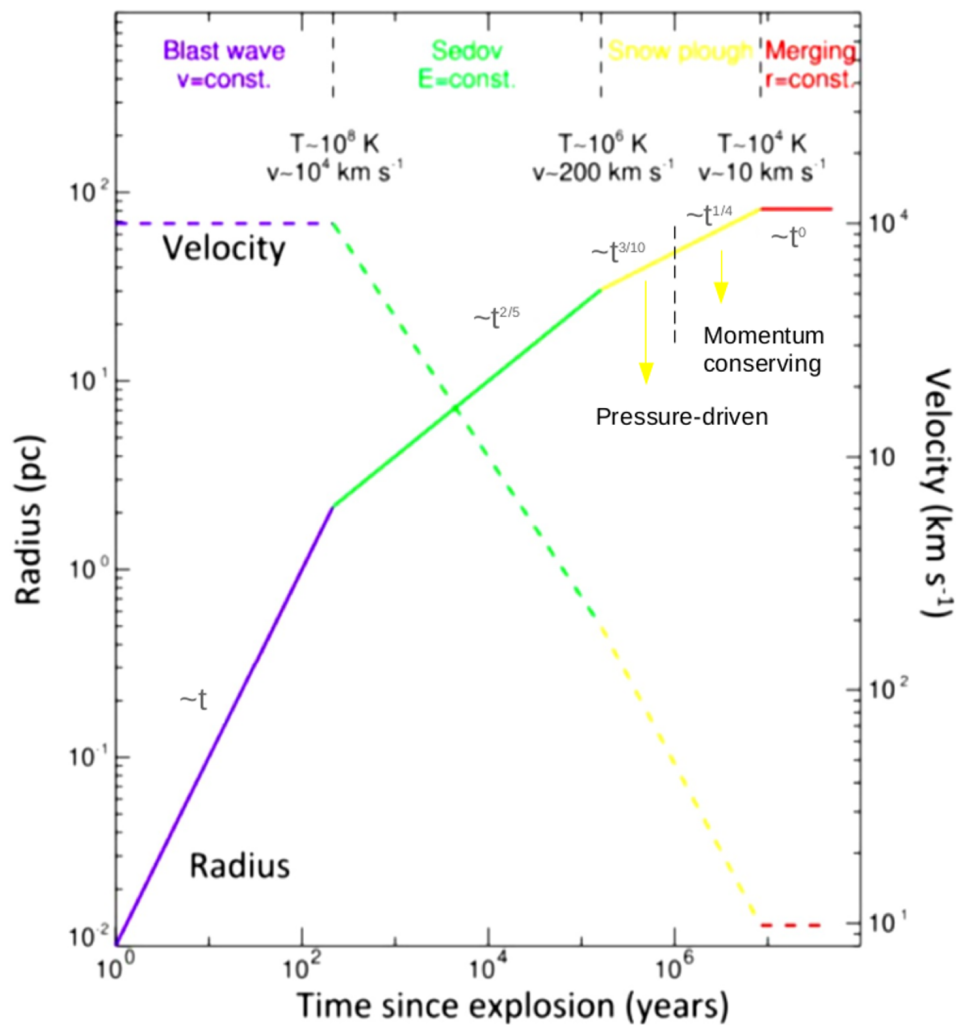
Figure 1.23: The four phases of the evolution of a SNR. We see that, as the radius of the remnant increases with time, its expansion velocity decreases. Credits: Padmanabhan (2001), Wilms (2012).

1.7 Classification of SNRs

SNRs are classified with regards to their morphology and their spectra. Both are strongly depended on the properties of the progenitor star whose explosion gave birth to the remnant, and on the environment in which this massive explosion took place. Wind-bubbles around the star (cavities formed from the strong stellar winds of the progenitor - Section 1.9), magnetic fields, molecular clouds and density variations in the CSM/ISM are some of the factors that can influence the shaping of a SNR. On the other hand, their spectra, i.e. the emission line in which they emit radiation, depends strongly on the above factors, but also on the evolutionary stage at which the SNRs are observed. A general "rule" is that young SNRs show strong X-ray emission, while evolved SNRs emit strongly in the optical band. However, there are some exceptions, as we will see below.

Despite the great morphological and spectral variety they present, SNRs have broadly been

classified in the following categories:

1. **Shell-type:** As the shock wave of the SNR propagates into space, it heats up the local ISM creating a shell filled with hot gas. In three dimensions, they are spherical shells, but to us they seem like bright ring-structures. That's because, along the line of sight, almost all of their shocked material is gathered at their edges rather than in their central region (*limb brightening* phenomenon). An example of a shell-type SNR is E0102-72 in the Small Magellanic cloud (Fig. 1.24a).

2. **Crab-type:** They are named after the famous Crab-nebula SNR (Fig. 1.24b), and are also known as Filled-center SNRs, "plerions" or Pulsar Wind Nebulae (PWNe). The term "plerion" originates from the greek word pleris ($\pi\lambda\eta\rho\eta\varsigma$) which means filled. They are filled by non-thermal emission powered by a pulsar star (highly magnetized rotating neutron star) located at their center. This is why they appear as a filled region of emission rather than a bright ring as Shell-type do (Fig. 1.24b). They are observed from radio to the highest-energy γ-rays. Their X-ray size is generally shorter than their radio and optical size due to the smaller synchrotron lifetimes of their higher energy photons (Safi-Harb 2012).

3. **Composite remnants:** They are a cross between Shell-like and Crab-like nebulae. They are subclassified as:

   Mixed-Morphology (MM): Also known as thermal Composites. They are characterized by a shell-like morphology in the radio, and a centrally filled thermal emission in the X-rays (with little or no limb-brightening). Their emission arises primarily from swept-up interstellar material, not ejecta (Rho and Petre 1998). An example of a MM SNR is the IC443 (Fig. 1.24c).

   Plerionic Composites: They show shell structures with a central region filled both with radio and X-ray emission. An example in this category is G21.5-0.9 SNR (Matheson and Safi-Harb 2010) (Fig. 1.24d).

4. **Balmer-dominated SNRs:** The optical spectrum of a SNR exhibits forbidden lines ([N II], [O III], [S II]) as well as the H Balmer series (Section 1.8.5). However, there are some SNRs that they are characterized by the presence of strong Balmer lines emission (e.g. Hα, Hβ, Hγ), along with Lyman series, He I and He II lines, and lines from more massive elements in the UV, but show little or no evidence of forbidden lines seen in radiative shock spectra. Chevalier & Raymond (1978) proposed that these lines are emitted when the shock front sweeps up the neutral H and the other neutral elements that are present in the proximity
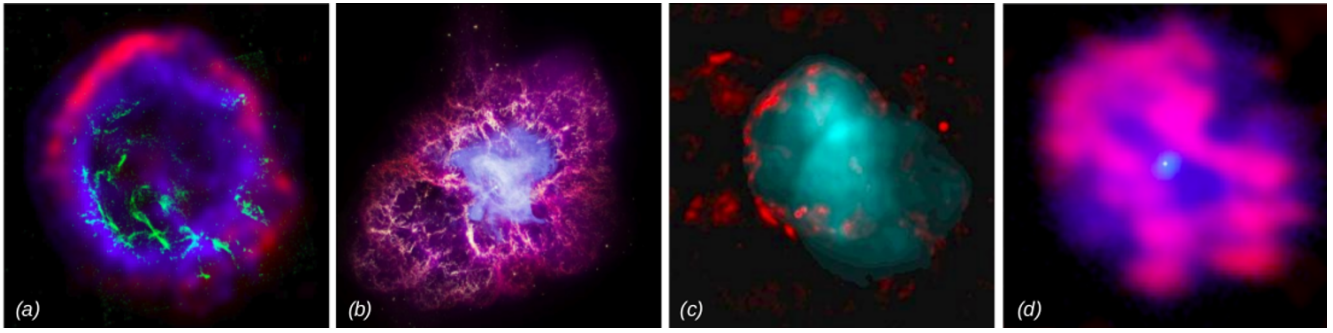
Figure 1.24: a) Colour composite of the shell-type SNR E0102-72: X-ray in blue (NASA/CXC/SAO), optical filamentary structures in green (NASA/HST), and radio in red (ACTA). b) Crab nebula with the pulsar at its center: the Chandra X-ray image is shown in blue (NASA/CXC/SAO/F.Seward), the Hubble Space Telescope optical image is in red and yellow (NASA/ESA/ASU/J.Hester and A.Loll), and the Spitzer Space Telescope's infrared image is in purple (NASA/JPL-Caltech/Univ. Minn./R.Gehrz). c) MM SNR IC443: red shows radio emission and blue shows X-ray emission. The radio emission is distributed in a shell while the X-ray emission is center-filled (image credits: Jonathan Keohane). d) The Plerionic SNR G21.5-0.9: the 22.3 GHz radio data are here shown in red and overlaid with the 0.2-10.0 keV X-ray data shown in blue. The cross indicates the position of the pulsar PSR J1833-1034 (Matheson and Safi-Harb (2010)).

of the SNR, in front of the shock (upstream region). In order to have neutral regions around a SNR, its progenitor star cannot be of Type II, for they cause strong ionization of the region. Therefore, it is believed that the progenitors for these SNRs are of Type Ia, because they don't produce so much energy, so neutral elements can survive. Two typical examples of this classification are the SNRs Tycho and N103B (Fig. 1.25).

SNRs of irregular morphologies:

The SNRs categories mentioned above are the basics ones, and of course they cannot cover the whole range of morphologies observed in these objects. The morphology and the kinematics of a SNR may be influenced from a variety of factors. Some of them may be related to the CSM formed from the progenitor star during the pre-explosion era (stellar winds and wind-bubbles, rotation of the star, supersonic movement of the star). Some others are attributed to the physical properties of the ISM the SNR is propagating into after the SN explosion (density and/or temperature variation, molecular clouds, dust grains). SNRs of peculiar morphologies and with a complex velocity field are of great scientific interest for they carry crucial information, the decoding of which provides valuable clues about the progenitor star and its environment. The MM SNR VRO 42.05.01 belongs to this category, and this is why it was chosen as a case study for this Thesis (see Section 5).
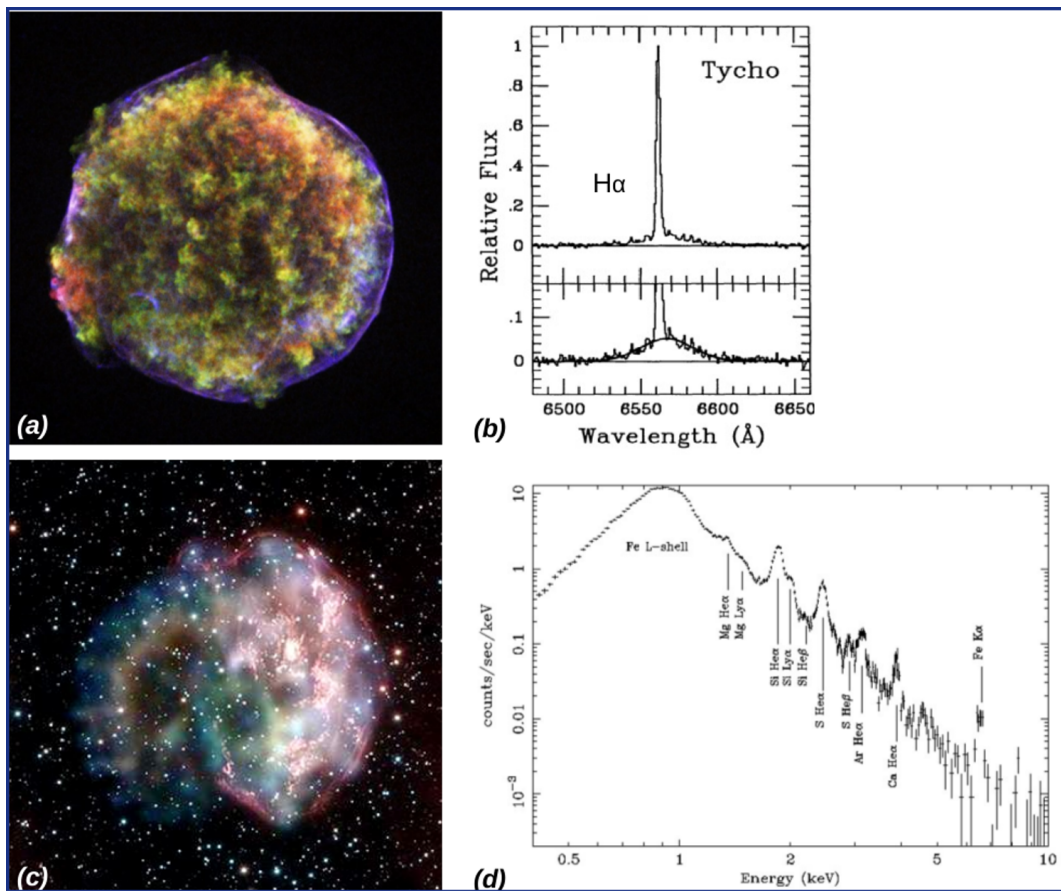
Figure 1.25: Image (a) shows the Tycho SNR (Chandra X-ray Observatory), while in (b) its spectrum is illustrated with dominant the Hα emission line (Smith et al. 1991). Image (c) shows the SNR N103B (Chandra archive Collection), while in (d) its spectrum is presented, where the highly ionized lines of Mg, Si, S, Ar, Ca, and Fe are labelled (Lewis et al. 2003).

1.8 Radiative emission of SNRs

SNRs are multiwavelength phenomena, whose emitted radiation covers almost all the range of the E/M spectrum. Traditionally, they are detected as radio sources, but they can present strong emission in the infrared (IR), optical, X-ray and γ-ray wavebands as well, in the form of both linear and continuum radiation. More specifically:

1.8.1 Radio synchrotron emission

It is emitted from a SNR during its whole lifetime and it was the traditional way that a SNR detection was based on (Dubner and Giacani 2015 and references therein). Although in the beginning it was thought that it was thermal radiation, its observed spectrum was not like the one that H II regions present (thermal black-body). Alfvén and Herlofson (1950) and independently Kiepenheuer (1950), both suggested that it should be non-thermal synchrotron

radiation, i.e. relativistic electrons which emit radiation (linearly polarized and continuum) when they are accelerated along the spiral lines of force of the magnetic filed of the remnant. This was later confirmed observationally by the detection of polarization in the Crab Nebula by Mayer et al. (1957).

The electrons responsible for this radiation can be accelerated at relativistic speeds by two ways, depending on the SNR type they belong:

1) **In Crab-type SNRs:** through a pulsar (rapidly spinning neutron star) at the center of the SNR, which supplies the SNR with electrons over its full lifetime[12]. These electrons are accelerated in the dynamical lines of the pulsar's magnetic field, and therefore they emit radiation.

2) **In Shell-type SNRs:** if there is no pulsar, electrons are accelerated through the diffuse shock acceleration (DSA) mechanism (Fermi (1949); Bell (1978a); Bell (1978b); Blandford and Ostriker (1978)). According to DSA, electrons undergo multiple crossings back and forth through the shocked and unshocked ISM. Due to the velocity difference between the two gases on either side of the shock, electrons will gain in momentum each time they cross the shock, and will be accelerated in the turbulent magnetic field of it. Because this procedure takes place at the region of the shock front, it is obvious that -in this case- the detection of the radio emission marks the outer edges of the SNR.

In both cases, in order for these electrons to produce radio synchrotron, their initial energy must be of the order $\sim GeV$. If it is of the order of $\sim TeV$, then the produced radiation falls into the X-ray synchrotron range, as we will see in Section 1.8.3 below.

1.8.2 Infrared (IR) emission

IR radiation in SNRs is related to the dust grains, either present in the ISM or produced during the SN ejecta (Williams and Temim 2017 and references therein). These are sub-micron sized ($\leq 1\mu m$) solid particles composed of C, Mg, Si and Fe. Because their size coincides with the wavelength of blue light, dust grains can be heated by absorbing and scattering UV and optical blue light (much more efficiently than red light). A second way of dust heating is by direct collision with energetic particles. In both cases, grains are heated in equilibrium temperatures of $30 - 50$ K or more, which means that when they cool down they radiate predominantly in the mid-far IR ($50 - 100\mu m$), either as linear emission or continuum emission as we will see below (remember that $E = \left(\frac{3}{2}\right) kT = h\nu\,(J)$).

There is also the case of relativistic electrons in shock waves, whose acceleration produces non-thermal synchrotron IR radiation.

---

[12]although a neutron star consists mainly of neutrons, it contains protons and electrons as well.

Young SNRs: As we saw, their post-shock waves emit mostly in the X-rays (high temperatures $\rightarrow$ no recombinations $\rightarrow$ non-radiative shocks). But since dust grains are not efficient absorbers of X-rays, their heating now is dominated by collisions with hot electrons and ions in the post-shock gas. As dust cools down, it re-emits significant IR emission as **thermal continuum**.

Older SNRs: Here, the slow shocks ($\leq 200 \ \mathrm{km\,s^{-1}}$) can emit significant amounts of optical/UV radiation due to the rapidly cooling gas in the post-shock environment (radiative shocks). This radiation is absorbed by the dust and re-emitted as **line thermal emission** from atomic gas (Fe, O, Si and Ne) and shocked molecular gas (mostly H_2). Virtually all of the IR emission from older remnants is dominated by swept-up ISM dust.

Most remnants show a mix of continuum and line emission sources, as we can see in the case of Kepler SNR (Fig. 1.26).
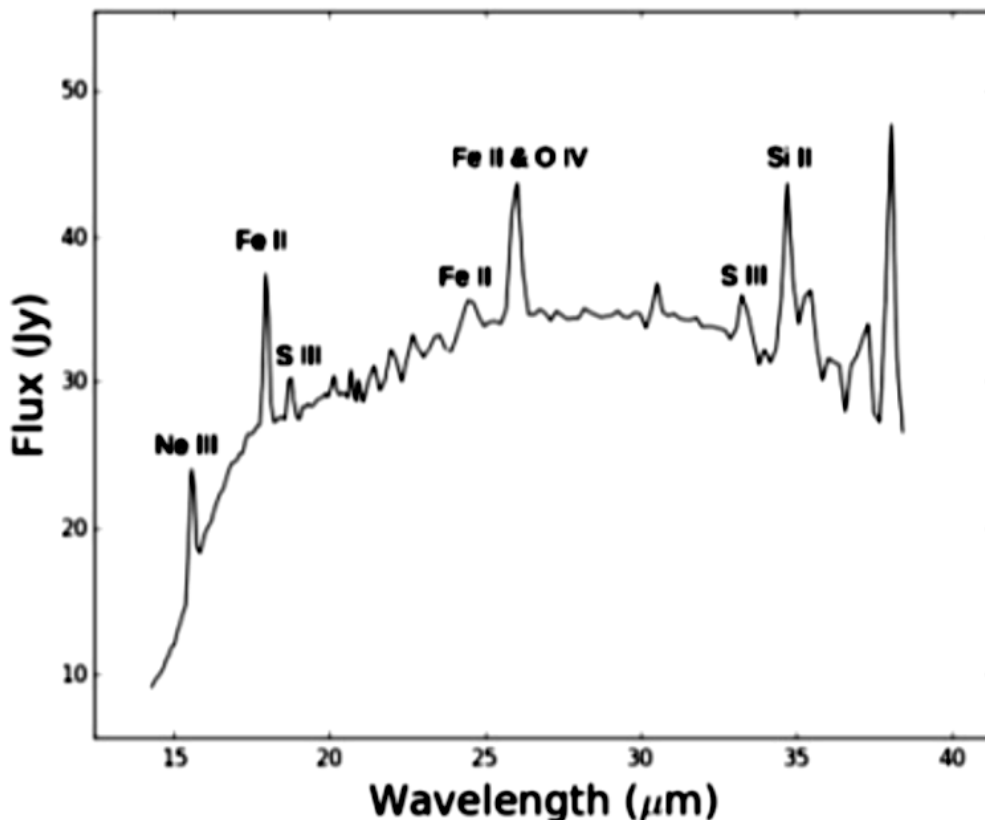
Figure 1.26: Spitzer mid-IR spectrum of Kepler's SNR. The continuum results from warm dust at ~ 100 K. Several emission lines from low-ionization state ions are also visible (Williams and Temim 2017).

1.8.3 X-ray emission

X-ray radiation in SNRs is observed in the regions where the gas temperature is $\sim 10^8\ K$ and/or high energy electrons are spiralling in the magnetic field of the SNR. It is broadly divided into thermal and non-thermal emission. Below we present the basic mechanisms that produce this radiation, while detailed description can be found in Vink (2012), Vink (2017) and Reynolds (2017).

Non-thermal X-ray emission It is produced from synchrotron radiation, observed in both Crab-type and Shell-type SNRs (and their composition types). It is the same mechanism discussed in Section 1.8.1, with the basic difference that now electrons are of much higher energy and therefore they produce X-ray synchrotron instead of radio-synchrotron radiation. More specifically:

Crab-type SNRs: Relativistic electrons of $\sim TeV$ are expelled from the central pulsar star and accelerated through its magnetic field lines. The result is linearly polarized continuum radiation in the hard X-ray band ($\geq 10\ keV$) (non-thermal synchrotron radiation).

Shell types SNRs: As there is no pulsar to generate relativistic electrons, X-ray synchrotron here reveals the location of active particle acceleration, which is the region of the forward shock front. So, in shell-type remnants, electrons are accelerated in $\sim TeV$ energies, through a back and forth movement into the turbulent magnetic field of the shock front (DSA mechanism described above in Section 1.8.1), obtaining by this way the proper energy in order to produce X-ray synchrotron radiation.

In Fig. 1.27 on the left part, the SNR G 1.9+0.3 is illustrated, where is clearly shown the X-ray radiation from the shell (in orange), and the radio emission from its central part (in blue).

Thermal X-ray emission It is observed in the post-shock heated ISM, and is composed of a continuum radiation along with linear emission (Fig. 1.27, right part). These are generated through the following mechanisms:

Thermal continuum emission:

1) **recombination continuum (free-bound emission):** a free electron is directly captured in an energy state n of an ion, while a photon is emitted. If the recombination happens in a ground level, the energy of the released photon is the ionization energy of the recombined ion. For recombination in higher levels, the energy of the emitted photon is that of the excited state.

2) **thermal bremsstrahlung (free-free emission):** a free electron inserts into the Coulomb field of a positive ion and "collides" with the ion (passes too close from it). The electron

decelerates without being captured by the ion, and due to its deceleration it emits radiation.

3) **two-quantum or two-photon emission:** In H atom, the energy level $n = 2$ is in reality a double state composed of $2s$ (meta-stable quantum level, i.e. transitions from upper to lower states are forbidden, that's why it's lifetime is very big, of the order of msec) and $2p$ state. Electrons from $2p$ may de-excite to the ground state $1s$ by direct emission of an Lα photon. On the other hand, electrons from $2s$ may arrive at $1s$, not directly, but by a simultaneous emission of two photons of random frequency (continuous radiation), the sum of which equals to the frequency of Lα line.

Thermal Line emission:

The observed emission lines come from the chemical elements released through the SN explosion. These are alpha-elements (O, Ne, Mg, Si, S, Ar, Ca) and iron-group elements (chiefly Fe and Ni and some trace elements with $20 \leq Z \leq 28$). These lines are in the band $0.5 - 10\ keV$ for temperatures between $0.2 - 5\ keV$, which is the typical temperature for plasma heated by SNR shocks, that's why they are observed in these regions of the remnant. They result from the classical mechanisms of direct excitation and de-excitation, and/or through ionization and recombination. Also possible is the case of fluorescence emission. Here, an electron of an inner quantum state is moving to a higher energy level by a photon absorption. Subsequently, when this electron is de-excited to an intermediate state, the emitted photon has less energy with respect to the initially absorbed photon.

1.8.4 Gamma-ray emission

An important source of γ-ray (but X-ray too) radiation, is the *inverse Compton* mechanism. According to this, an electron travelling at close the speed of light, collides with a lower-energy photon (from radio to UV). The electron loses energy, while the photon gains energy reaching a higher frequency and becomes a γ-ray photon.

1.8.5 Optical emission

SNRs emit in the optical band, when the adiabatic shock front loses energy, cools down and finally turns into a radiative shock. This optical spectrum consists of linear emission of Balmer and forbidden lines, in conjunction with a weak continuum component that extends in all the E/M spectrum. It basically contains H lines, from the H atoms present in the initially unshocked ISM which subsequently was swept up by the forward shock, and also emission lines from heavier elements (mostly O, S and N) which were in the ISM too, or were ejected during the
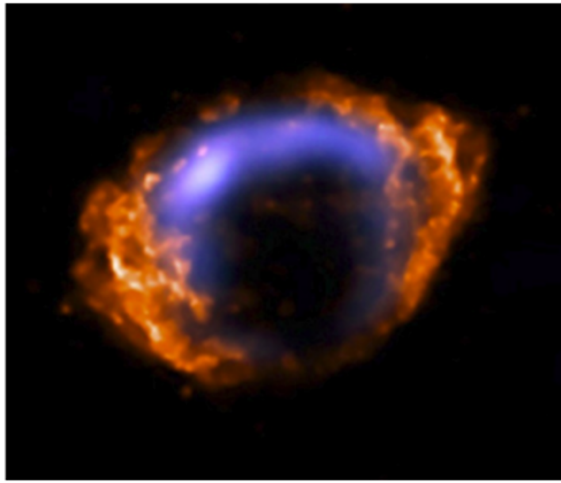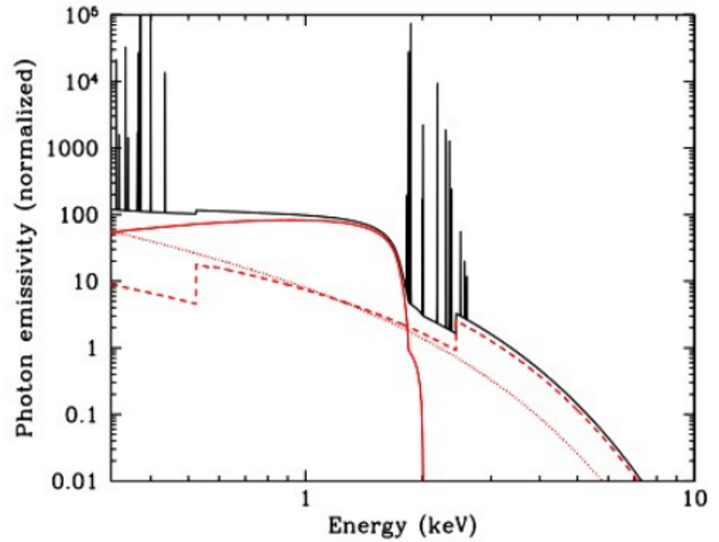
Figure 1.27: *On the left*: the youngest known SNR in the Milky Way (110 years old), G 1.9 + 0.3, brightening at both radio (blue) at its center and X-rays (orange) at its edges. Image Credit: X-ray (NASA/CXC/NCSU/S.Reynolds et al.); Radio (NSF/NRAO/VLA/Cambridge/D.Green et al.2019). *On the right*: Emissivity of a pure Si plasma ($kT = 1keV$). Continuum contribution is due to two-photon emission (red solid line), free-bound continuum (red dashed line), and bremsstrahlung (free-free emission, red dotted line). Also shown are the Si-L and Si-K shell line emission (Vink 2012).

SN explosion.

The temperature of the post-shocked gas (hot plasma) in the radiative shock front has now been reduced to $\sim 10^4$ K. Therefore recombinations between free electrons and ions are permitted, resulting in the optical emission from the radiative shock region. Below we present the mechanisms which produce this radiation.

Balmer emission lines and continuum radiation: Balmer lines (the most common of which are Hα and Hβ) are produced through the "fluorescence mechanism" according to which radiation of low wavelength is transported into radiation of larger wavelength. As an example we present -one of the ways for- the creation of Hα emission line. A free electron is pulled from a H ion and we assume that is directly captured in the energy level $n = 3$ (recombination). Due to this recombination, a photon is emitted in the form of *continuous radiation* (Paschen series / Infrared), with energy equal to the energy of this quantum state (up to now is the case of *free-bound emission* mentioned in Section). The electron of level $n = 3$ wants to end up in the ground state of minimum energy $n = 1$ and manages this through successive jumps from one level to the next. At each jump, a photon of specific frequency is emitted (*linear radiation*). Transition $n = 3 \rightarrow 2$ produces the Hα Balmer emission line in the optical. Finally, the transition $n = 2 \rightarrow 1$ produces an Lα photon (Lyman series / UV band). In the case of the direct transition
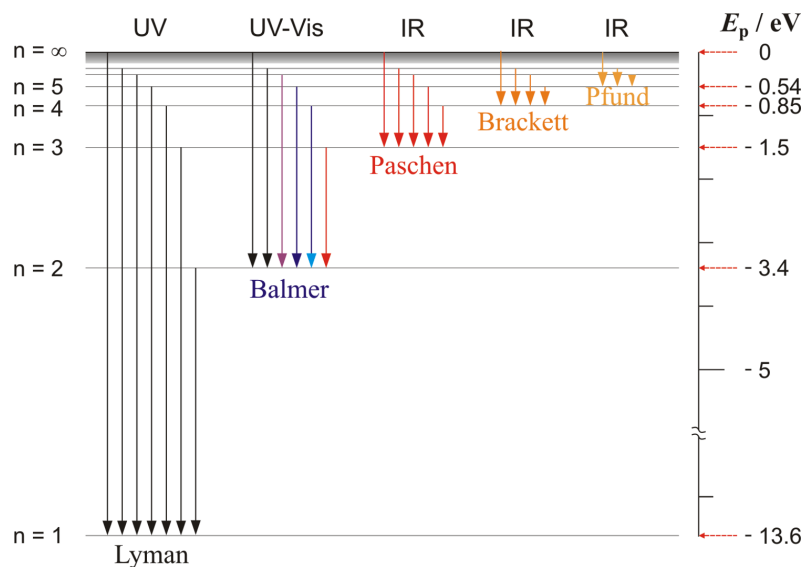
Figure 1.28: Electron transitions between the energy levels for the H atom, and the emitted waveband for its transition.

of the electron $n = 3 \rightarrow 1$, a Lβ photon is emitted, which is about to get absorbed by a neutral H atom, stimulate it in the $n = 3$ level and so on. Following the same pattern we can see that the direct transition $n = 4 \rightarrow 2$ finally produces the Hβ emission line (Fig.1.28).

Forbidden lines of [O II], [O III], [N II], [S II]:

The emission of these forbidden lines results from the collisional excitation and spontaneous de-excitation of the already ionized atoms of oxygen, nitrogen and sulphur (O^+, O^{++}, N^+, S^+).

More specifically, these ions were formed through the photoionization mechanism in a previous evolutionary stage of the remnant at which the temperature was very high (10^7 - 10^8 K). The cross section of these ions in their collisions with the free electrons of the nebula is much higher with respect to the equivalent cross section of the H ions (protons). In other words, these ions constitute a bigger target for the free electrons to fall onto them, in contrast with the protons of the nebula, although the latter are much more in quantity.

The fact that, in the current radiative phase, the temperature of the nebula has fallen to $\sim$ 10^4-10^5 K, implies that the energy of the free electrons is lower than 10 eV. Therefore, no H and/or He atoms can get stimulated in their first energy level[13]. The energy distribution of the free electrons is Maxwellian and it is shown in the left part of Fig. 1.29. In this plot we can see that, at temperature 10^4 K, there are electrons with energy $2 - 5$ eV. This amount of electron energy is adequate for the excitation of the already ionized atoms (O^+, O^{++}, N^+, S^+) in states

---

[13]Remember that the needed energy for the stimulation of an electron in the first energy level, is 13.6 eV for H atom and 24.5 eV for He atom.

near to their ground state (Fig. 1.29 *on the right*). These states are metastable which means that their de-excitation time is not 10^{-8} sec, but they are characterized by an extremely long spontaneous de-excitation time of the order of $\Delta t \sim 1$ sec.

Their de-excitation can be achieved by two ways: i) by collision of the electron which is trapped in the metastable state, with a free electron and ii) by spontaneous decay of the stimulated electron, in a lower energy level. The first way leads to no radiation emission, but to rearrangement of the electrons energy. This happens because the free electron that escapes after the collision, receives the energy of the electron which was in the metastable state. On the other hand, the spontaneous de-excitation leads to the emission of what is called *forbidden line*. This kind of radiation (forbidden lines) is emitted in regions of low density, where the de-excitation through collisions is very rare to happen. In our laboratories, even the best achieved vacuum is still dense (10^{11} cm^{-3}), so the de-excitation happens through collisions in the end. The photons which are produced through the spontaneous de-excitation are not bounded from these ions again, because of the low cross section of these ions in the photon absorption (in contrast with their high cross section in electron absorption). On the contrary, these produced photons finally escape from the nebula, rendering this procedure an important cooling mechanism in the post-shock gas of evolved SNRs.

Comment on a SNR's spectrum:

At this point we need to clarify that the composition of a SNR spectrum, apart from its state of evolution, it can also indicate the physical properties of the CSM/ISM the SNR is evolving into. For example, if at some ambient region the remnant encounters a dense molecular cloud, its expansion through this area will be hindered and decelerated, contrary to its rest parts which will properly continue their evolution. This will be depicted on its spectrum as its shock velocity, the temperature of the shocked region and hence the emitted radiation will be accordingly affected. Therefore, it is quite common in a SNR to see many wavebands simultaneously, as for example in the case of the Crab nebula (Fig. 1.30) or CasA (Fig. 1.31). Decoding a spectra is in the same logic as decoding a peculiar morphology a SNR may present, as it was discussed in Section 1.7 - Classification of SNRs.

1.8.6 Information from Optical emission

As was mentioned above, optical radiation is emitted when the radiative shock front begins to cool down. The gas in this post shock region is practically the ISM medium, swept up and heated up by the shock front. Consequently, the emission lines it presents reflect the com-
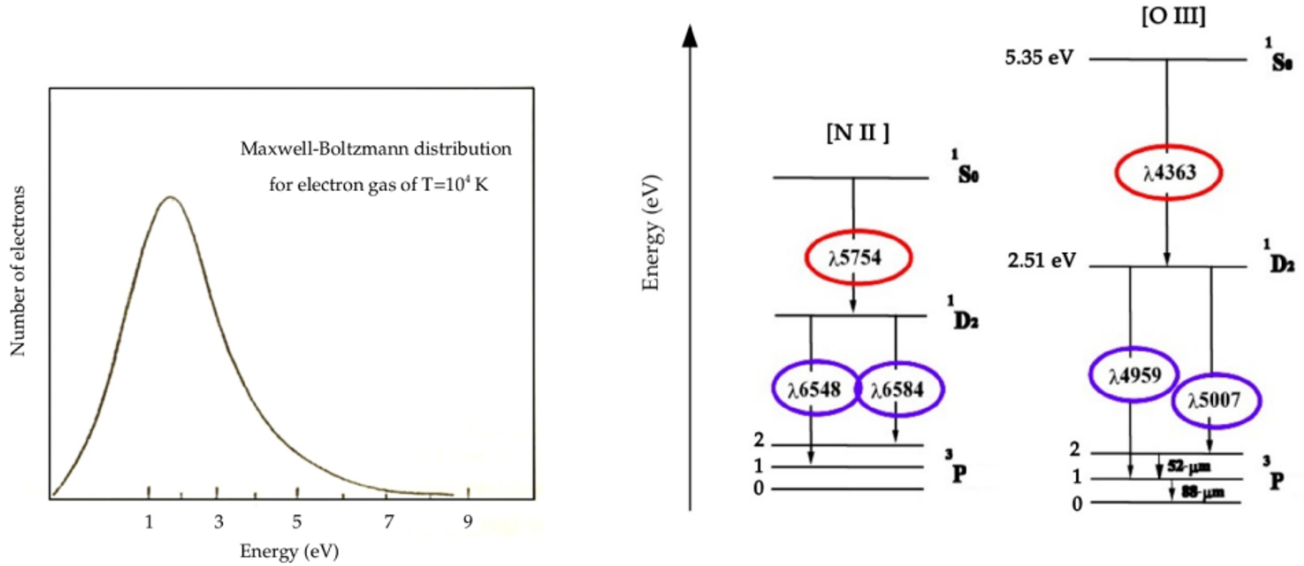
Figure 1.29: *On the left:* The Maxwell-Boltzmann energy distribution of a cloud of free electrons at temperature $T = 10^4$ *K. On the right:* Electron transitions for N and O, producing forbidden emission lines. [N II] 6548, 6584 Å and [O III] 5007 Å are optical, while [O III] 52, 88 μm are infrared forbidden lines. For description of the emission process, see in the text.
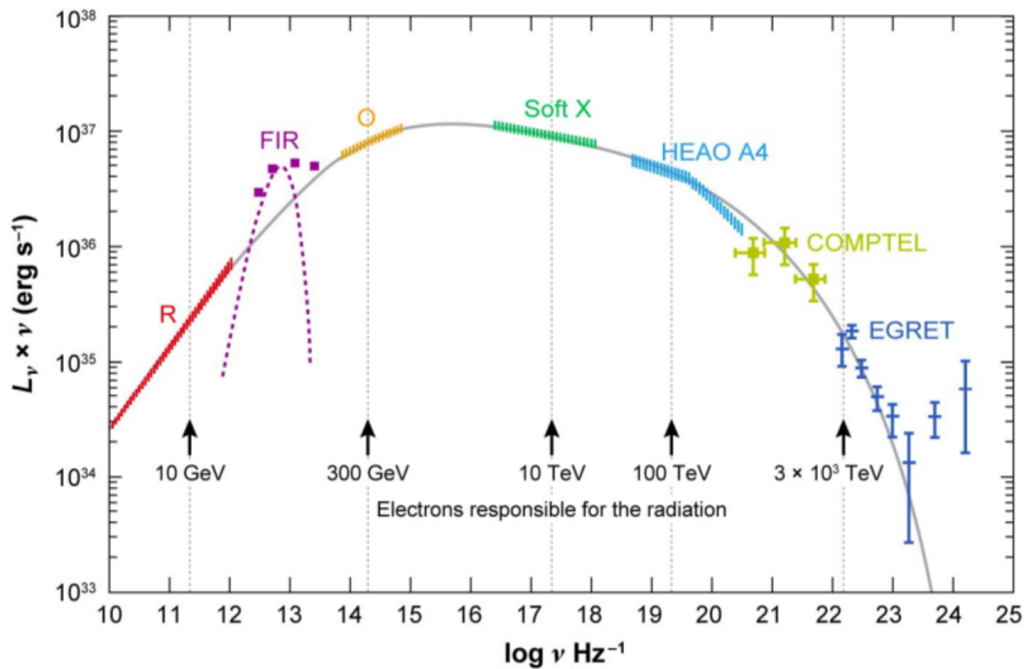
Figure 1.30: The spectra of the SNR Crab nebula. As we can see, its emission covers all the waveband, from radio to γ-rays. Credits: Hester (2008).
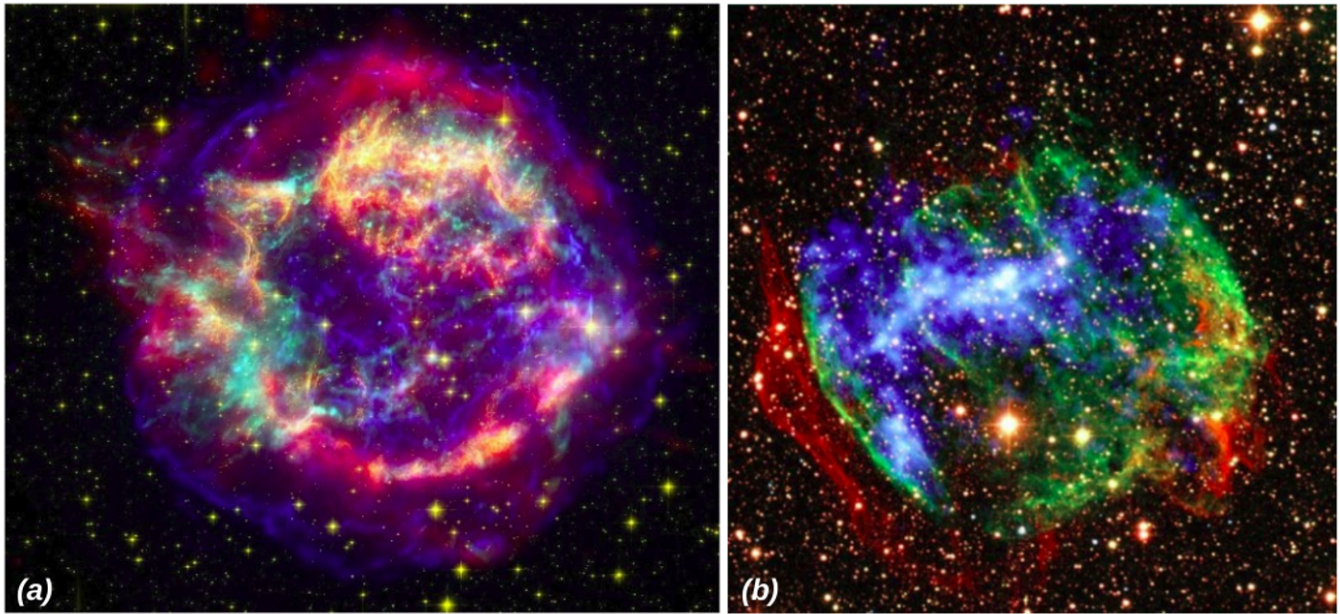
Figure 1.31: a) This image of the SNR CasA is a combination of three different wavebands of light. Infrared data from the Spitzer Space Telescope are colored red; visible data from the Hubble Space Telescope are yellow; and X-ray data from the Chandra X-ray Observatory are green and blue. Credits: NASA/JPL-Caltech/STScI/CXC/SAO Animation: NASA/JPL-Caltech/Univ. of Ariz./STScI/CXC/SAO. b) An image of the Galactic supernova remnant W49B, composed from images taken in the shocked molecular H_2 (infrared), here shown in red), [Fe II] emission (green), and X-rays (blue) (Credit: NASA/CXC/SSC/J. Keohane et al. 2007). It is suggested that W49B is evolving in a wind-blown bubble, confined by a molecular shell of H_2, which is responsible for the infrared emission we observe.

position of the ambient ISM. Therefore, through imaging and spectroscopic data in the optical we can derive important information about the SNR itself and its environment as well, such as electron temperature, electron density, metallicity, ionization state and velocity of the shock waves. Details can be found in Osterbrock and Ferland (2006). Here we mention the importance of specific forbidden lines in SNRs' detection.

Detection of SNRs: A classical diagnostic (but not the only one) for the SNRs detection, is the quantity of [S II] present in a nebula. A nebula is traditionally characterized as SNR when [S II] 6716, 6731 Å/Hα 6563 Å > 0.4, while when [S II] 6716, 6731 Å/Hα 6563 Å < 0.4 then it's about an H II region (Mathewson and Clarke 1973). Below we present a short explanation of this:

In order for sulphur (S) to get single ionized (S$^+$), energy of 10.4 eV is demanded which commensurate with temperature 10^5 K and more. This means that S$^+$ had already been formed in the post-shock, stimulated through photoionization by the X-rays of that region. In later times, when the temperature in the post-shock reduces and the wave becomes radiative, there are

no more electrons of high enough energy to photoionize S^+ into S^{++} , neither photons can be absorbed by S^+ due to the very low cross-section of the later in photon absorption. Therefore, S^+ is now excited in higher energy levels, only through collisions with the free electrons of the gas. These higher levels are metastable, the decay of which leads to the emission of [S II] forbidden lines, as was described above in Section 1.8.5. As we said, the photons of the forbidden lines cannot be absorbed by the sulphur ions, and this is why this photon-radiation escapes from the SNR, resulting in the further cooling of the post-shock region. On the other hand, in an H II region, the quantity of double ionized S (S^{++}), is much more with respect to that of S^+, due to the high energy UV photons provided from the hot star that ionizes this region. This is why in an H II region we expect the ratio [S II] / Hα to be less that 0.4.

1.9   Modified Circumstellar Medium – Stellar Winds and Wind bubbles

An assumption that was clearly adopted from the beginning, is that the SN explosion evolves into a homogeneous environment. In reality things are much more complicated, since mass outflows from the progenitor star during the pre-explosion era, in the form of continuous stellar winds or irregular mass loss outbursts, can create a "wind-bubble" (or wind cavity) around the star, significantly modifying its CSM. The blast wave subsequently generated from the SN explosion interacts with this modified medium, altering the SNRs' "typical" evolutionary path as this was described in Section 1.6.4, and modifying its structure. Below, we give a brief description of stellar winds, and we outline the basic structure of a wind bubble.

1.9.1   Stellar Winds (SW)

As "stellar wind" (SW) is defined the continuous, radial supersonic outflow of gas ejected from the upper atmosphere of a star (Fig. 1.32).

The two most important parameters regarding a stellar wind, is its mass loss rate (by convection, is the amount of solar masses the star loses per year) and its terminal velocity, which is the velocity of the SW at a large distance from the star. They can be driven by various mechanisms, specified by the main force that is responsible for the wind. Detailed anaysis can be found in Crowley (2006) and Espey and Crowley (2008).

However, two main factors that can define their strength, are the mass and the radius of the star at each specific evolutionary stage. To set an example, the SWs in Red Giants are dense (mass loss rate 10^{-6} M$_\odot$ yr^{-1}to 10^{-4} M$_\odot$ yr^{-1}; Mauron and Josselin 2011) and slow ($10-30$ km s^{-1}) (Ohio, Chapter 12). Their density is attributed to their low surface temperature, where a cool stellar atmosphere favours the formation of dense material. On the other hand

their low velocities are justified through the escape velocity equation:

$$V_{esc.} = \sqrt{\frac{2GM}{R}} \tag{1.34}$$

where G is the gravitational constant, M is the mass of the star and R is its radius at the Red Giant Branch. (typical radius of RGB stars $500 - 1500$ $R_\odot$; Mauron and Josselin 2011). As we can see, the bigger the radius, the lower the escape velocity of the outer stellar gas.

Another factor that must be taken into account is the binarity (or not) of the stellar system. That is because, in the case of a binary system, the interaction with the companion star may modify the shape of the wind (not be simply spherical any more) and also alter its mass-loss rate (Decin et al. 2020). Finally, although it was assumed that these stellar outflows are basically homogeneous, recent works report their clumpy nature in some cases too (Pradhan et al. 2019).

Stellar winds play an important role in the evolution of a star for two main reasons: i) they define how much material is lost by the star per unit of time (stars with high mass-loss rates will evolve differently from those with low mass-loss rates), and ii) the ejected material forms a nebula around the star, called "wind-bubble" or "wind-cavity" which modifies the -otherwise-uniform CSM. A possible Supernova explosion inside this bubble would have a serious impact on the evolution of the formed SNR.

Below we describe as an example of SW, the case of dust driven winds which is manifested in luminous and cool stars (AGB/RSG stars).

Dust driven winds: It is a widely accepted scenario about the mass loss through stellar winds generation in both AGB and RSG stars. According to this mechanism, pulsations lift gas out to distances above the photosphere, where the temperature becomes low enough for dust formation to occur. The photons emitted by the star (radiation pressure) collide with the dust grains, transferring to the latter their momentum ($\frac{h\nu}{c}$). Subsequently, as the dust grains are accelerated outwards, they drag the gas along with them through mutual collisions, resulting in the stellar wind formation. From the above it seems rational that the mass-loss rate depends both on the stellar luminosity (radiation pressure) and temperature (to allow dust to form) (Kwok 1975; van Loon et al. 2005).

1.9.2 Structure of a Wind-bubble

The steady injection of mass in the form of stellar winds at different evolutionary stages of a star, sweeps up the material of the ambient medium, excavating by this way a wind-blown cavity (or "bubble") around the progenitor star. This bubble is bordered by a thin, dense, cold
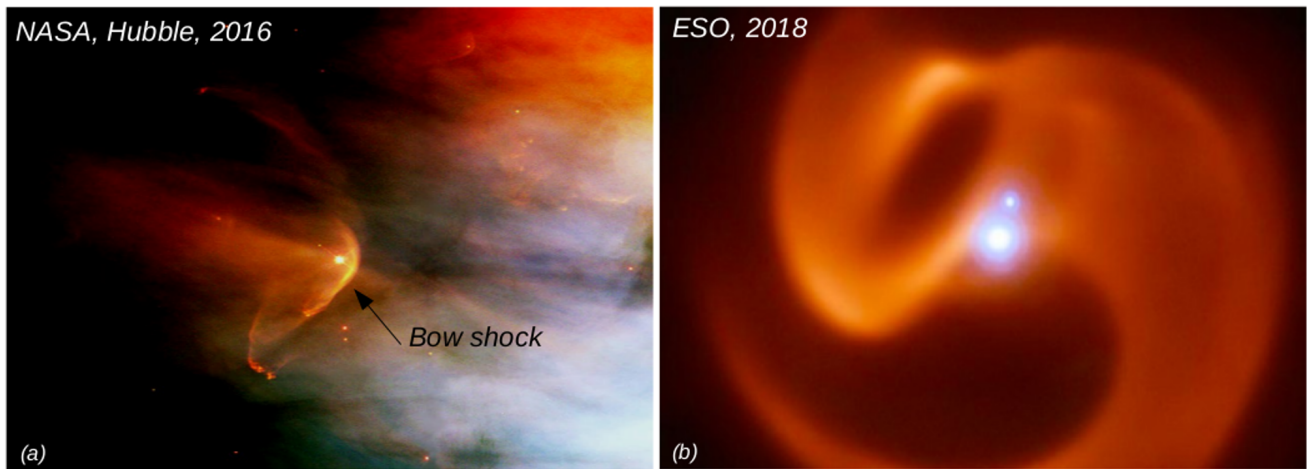
Figure 1.32: Two observational images that depict (and verify) the presence of stellar winds in stars. (a) Variable star LL Orionis in the Orion Nebula. While the star (bright dot) is moving to the right in the image, its ejected fast stellar wind is moving into the slow surrounding material of the Orion Nebula, creating a bow shock at the front part of its movement. This bow shock is analogous with the waves created at the prow of a ship moving through water. Credits: Hubble Heritage Team (AURA / STScI), C. R. O'Dell (Vanderbilt U.), NASA, (b) Dust cloud surrounding the triple star system 2XMM J160050.7-514245 (informally called Apep). The pinwheel structure is generated by the collision of stellar winds from two Wolf-Rayet stars. Credit: ESO/Callingham et al.

shell of swept-up interstellar material (practically Hydrogen, ionized from the UV radiation of the star) and contains most of the low-density swept-up shocked stellar wind at high temperature ($T \geq 10^6$ K) (Castor et al. 1975; Weaver et al. 1977).

The stratification of a circumstellar (CS) bubble can be described in much the same manner as is done for a Supernova remnant shell, as the latter is illustrated in Fig. 1.20. However, a main difference is that in a SNR there is a sudden ejection of stellar matter during the SN explosion, while in a wind-bubble we see a continuous injection of energy (stellar wind) into the bubble until the wind stops. A simplified, schematic illustration of a circumstellar (CS) shell is given in Fig. 1.33 and concerns the case of a SW generated by a Wolf-Rayet star, which is described in the next paragraph.

1.9.3   Case of a Wolf-Rayet (WR) stellar wind

We assume the case of a Wolf-Rayet star immersed in a H II region. These stars are typically characterized by strong stellar winds of ~ 2000 km sec^{-1} (region 4 in Fig. 1.33). This velocity is considered hypersonic with respect to the sound speed of the ambient H II gas (~ 10 km sec^{-1}) that surrounds the star (region 1 in Fig. 1.33). Therefore, stellar wind acts like a spherically expanding piston, whose forward shock front that is created in front of it pushes the ionized
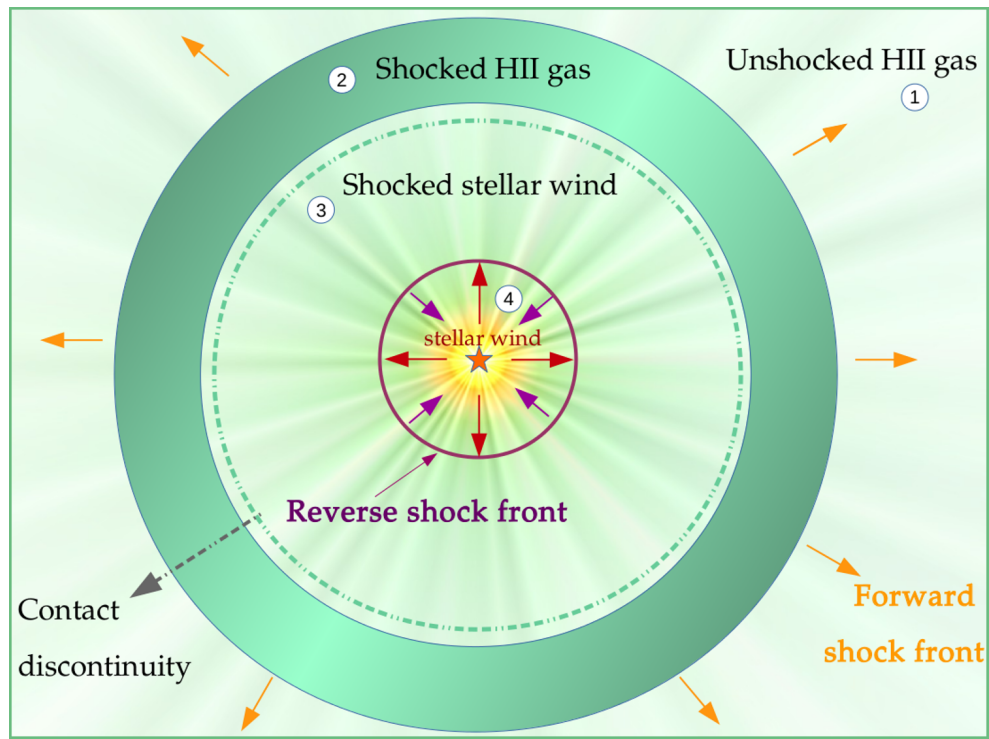
Figure 1.33: Structure of a stellar wind cavity (or else a circumstellar shell) excavated due to the stellar-wind activity of a Wolf-Rayet star into the ambient circumstellar medium. For further description, see in the text.

hydrogen away from the star. The sequel is pretty much the same as in the SNRs case. The expanding forward shock sweeps and swallows the H II gas, which is now collapsed as shocked H II gas into a cold ($\sim 10^4\ K$) and dense shell behind the shock front, as a result of radiative cooling (region 2 in Fig. 1.33). The continuously coming stellar wind falls onto this dense shell, is reflected by its inner surface forming by this way the reverse shock we see in Fig. 1.33, which is propagating towards the stellar wind. The stellar wind that passes through the reverse shock is absorbed by it, compressed, heated and decelerated in the region 3 of Fig. 1.33. Its temperature is of the order of $\sim 10^7\ K$ which allows the emission in UV and soft X-rays. Between the shocked stellar wind and the shocked H II gas, a contact discontinuity is formed that separates the two regions.

1.9.4   SNe explosions inside Wind-bubbles

When the star explodes inside a wind-blown cavity, its shock wave interacts with this modified CSM (Weaver et al. 1977; Franco et al. 1991). In this case, the evolution of the SNR deviates from the classical model described in Section 1.6.4, where the SN was directly evolving into a homogeneous ambient ISM. Now, the structure and properties of the pre-existing wind-blown bubble shape the dynamics, kinematics and morphology of the resulted SNR. A significant

parameter that can influence this evolution, is the ratio of the mass of the CS shell to the mass of the ejected SN (Franco et al. 1991, Dwarkadas 2005).

If the CM shell mass is lower than the SN ejecta mass, then the CM shell does not play an important role in the evolution of the SNR. But, in the opposite case, the impact of the SN ejecta on a much massive and dense CM shell results in the creation of a number of shock waves moving back and forth inside the bubble. More specifically, when the SNR shock interacts with the dense circumstellar shell, a part of the shock is transmitted through the dense CM shell and expands slowly into this denser medium, while the rest shock is reflected onto the dense CM shell and travels back into the already-shocked lower-density medium.

Regarding the reflection of the shock, this procedure can be very complicated. Although the SN shock starts off as a spherical structure, due to the pressure fluctuations that exists inside the turbulent bubble, it ends up to propagate towards the CM shell as a rippled shock. Therefore, when every piece of this non-uniform shock collides with the inner boundary of the bubble, each collision results in a reflected shock in that region that continues to travel inward and eventually passes the reverse shock of the SN ejecta. Consequently, there are many reflected shocks that arise from various interactions with the dense CM shell, that reach the central region of the star at different times in consequence of their different velocities.

Taking into account that the emission/luminosity is proportional to the square of the density, these fluctuations in the pressure and the density implied due to the presence of the successive shock waves can define the luminosity of the remnant and alter the emission it would have if it was propagating directly into the local ISM.

Chapter 2

2 Instrumentation and data reduction

For the data acquisition in imaging and spectroscopy, three different telescopes were used. In particular, wide filed images were obtained using Skinakas telescope (Crete, Greece), high-resolution imaging were obtained with "Aristarchos" telescope (Helmos, Greece), while the spectroscopic data were obtained with the SPM telescope (San Pedro Martir Observatory, Mexico). Below, the characteristics of each telescope are presented.

2.1 Telescopes

Skinakas Observatory – 0.3m optical telescope:

Skinakas Observatory is located on top of the Ida mountain in Central Crete (Greece) at an altitude of 1750m. The 0.3m optical telescope was employed for the acquisition of wide field images needed for the VRO project (Fig. 2.1). This telescope is of Schmidt-Cassegrain type, with focal ratio f/3.2, The observations were performed in 2000 and 2001.

Helmos Observatory – "Aristarchos" telescope:

Helmos Observatory is located on mount Helmos (Aroania) in the Northern Peloponnese (Greece) at an altitude of 2340m. It hosts the optical telescope "Aristarchos" (Fig. 2.2) which was used in order to obtain high resolution images for the VRO project. It is of Ritchey-Chretien type, with a primary mirror diameter 2.3m and focal ratio f/8. The observations were performed between the years 2011 and 2019.

San Pedro Martir (SPM) Observatory – 2.1m telescope:

Figure 2.1: a) Skinakas Observatory in Crete, Greece. b) The 0.3m telescope used for the obtained wide field images of the VRO project.

The San Pedro Martir National Astronomical Observatory it is located in the homonymous mountain range, located in Ensenada, Baja California, Mexico at a height of 2.800m. For our observations we employed the 2.1m optical telescope, which is of Ritchey-Chretien type, with focal ratio f/7.5 (Fig. 2.3). The observations were performed in the years 2010, 2011, 2012, 2016 and 2019.

2.2 Instrumentations

2.2.1 Imaging

For the wide-field and high resolution imaging data, we used the CCD cameras mounted on the telescopes of Skinakas and Helmos Observatory respectively. Below we present the characteristics of each camera, while the function of a CCD camera is described in Section 7.4.

1. **Camera and used filters for Wide field imaging:** The camera was a 1024×1024 pixel^2 Thomson CCD, with pixel size 19μm, image scale 4 arcsec pixel $^{-1}$ and Field of View (FOV/covered surface on the sky) 70×70 arcmin ^{2}. The images were taken in the narrow band filters Hα+[N II] 6548, 6584 Å, [O III] 5007 Å and [S II] 6716, 6731 Å. Furthermore, broad band filters of continuum red (Cont red) and blue (Cont blue) were used for the background stellar subtraction in the images Hα+[N II] 6548, 6584 Å and [O III] 5007 Å respectively (Table 2.1).
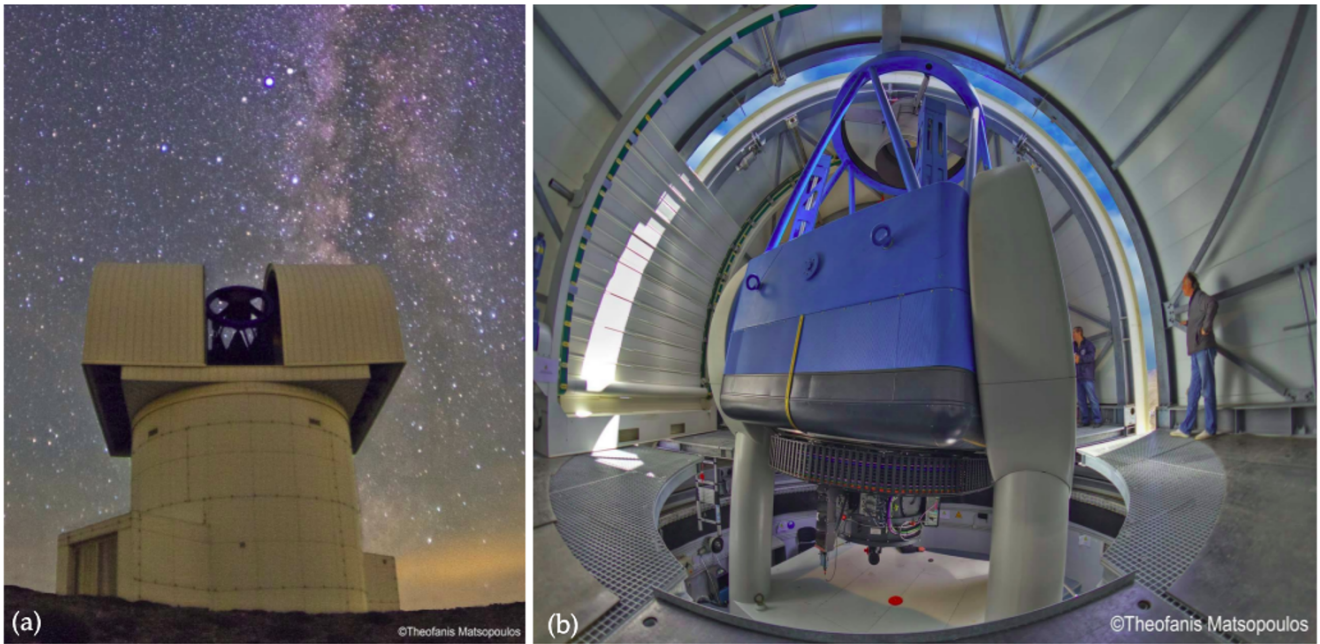
Figure 2.2: a) 2.3m "Aristarchos" telescope in Helmos Observatory (Greece). b) The telescope at the interior of the dome (Credits: Theofanis Matsopoulos).

2. **Camera and used filters for High-resolution imaging:**

High-resolution images where obtained by the use of two CCD cameras (Fig.2.4), both in "Aristarchos" telescope: 1) the 1024×1024 pixel^2 LN CCD camera, with pixel size 24μm, image scale 0.28 arcsec pixel^{-1} and FOV 4.8×4.8 arcmin^2, and 2) the 2048×2048 pixel^2 LN2 CCD camera, with pixel size 13.5μm, image scale 0.16 arcsec pixel^{-1}, and FOV 5.5×5.5 arcmin^2. "LN" stands for Liquid Nitrogen, which is the cooling mechanism of these cameras in order for their temperature to maintain at -120 °C during the observations, reducing by this way the thermal noise (for this, see Section 2.3.1).

The images were taken in the narrow band filters Hα+[N II] 6548, 6584 Å, [O III] 5007 Å and [S II] 6716, 6731 Å. Furthermore, broad band filters of continuum red (Cont R) and blue (Cont B) were used for the background stellar subtraction in the images Hα+[N II] 6548, 6584 Å and [O III] 5007 Å respectively (Table 2.2).

WIDE-FIELD IMAGING			
Filter	Central Wavelength λ (Å)	Bandwidth $\Delta\lambda$ (Å)	Exposure time (sec)
Hα+[N II] 6548, 6584 Å	6560	75	2400
[O III] 5007 Å	5005	28	2400
[S II] 6716, 6731 Å	6708	20	2400
Cont red	6096	134	180
Cont blue	5470	230	180

Table 2.1: Used filters for wide-field imaging in Skinakas Observatory (Crete, Greece).

HIGH RESOLUTION IMAGING			
Filter	Central Wavelength λ (Å)	Bandwidth $\Delta\lambda$ (Å)	Exposure time (sec)
Hα+[N II] 6548, 6584 Å	6580	100	1800
[O III] 5007 Å	5011	30	1800
[S II] 6716, 6731 Å	6727	40	1800
Cont red	6680	100	100
Cont blue	5700	70	100

Table 2.2: Used filters for high-resolution imaging in "Aristarchos" telescope (Helmos, Greece).
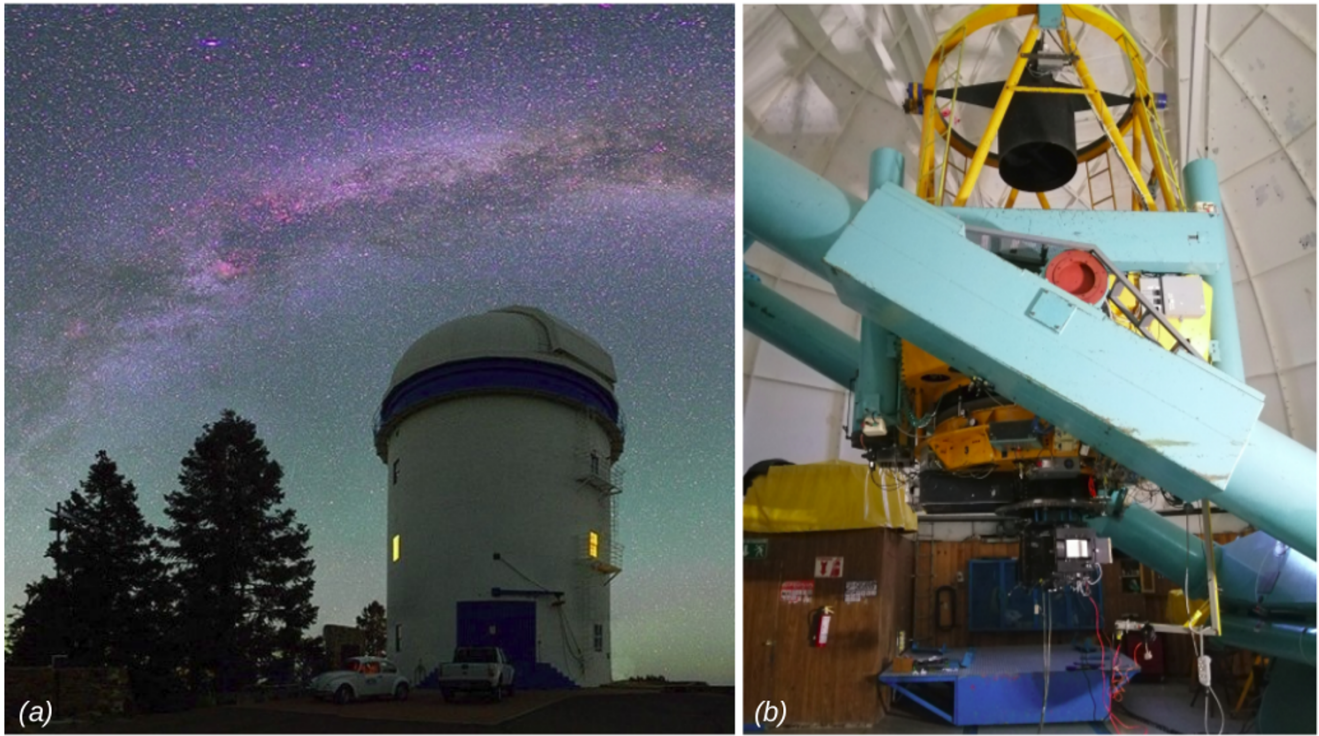
Figure 2.3: a) The dome of the 2.1m San Pedro Martir (SPM) telescope in Baja California state, Northwestern Mexico. b) The 2.1m SPM telescope at the interior of the dome (Credits: Sophia Derlopa).

2.2.2 Manchester Echelle Spectrometer (MES – SPM)

The Manchester Echelle Spectrometer (MES -SPM: Meaburn et al. 2003), currently mounted on the 2.1 m telescope of the San Pedro Martir (SPM) Observatory in Mexico, was employed for the needs of this work. Its primary use is to obtain spatially-resolved profiles of individual emission lines from faint extended sources emitting in the range $3900 - 9000$ Å with a spectral resolving power of $R = \lambda/\Delta\lambda \leq 10^5$. The "grooves per mm" parameter is $G = 1/d = 31.6$ / mm.

Its optical layout is shown in Fig. 2.5, where the light enters through the slit and the interference filter to the lens which collimates the beam. After its diffraction and reflection from the echelle grating, it is refocused on the detector where the data are stored. The spectrometer shows no cross-dispersion (no overlapping of emission lines from adjacent spectral orders). It can also be used for obtaining a direct image of the field (FOV image), by isolating the grating putting a mirror in front of it.

In Fig. 2.6(a) we see the MES-SPM spectrograph mounted on the 2.1m telescope at SPM Observatory, while Fig. 2.6(b) shows the dimensions of the used slit. A more detailed description of an echelle spectrograph is presented in Section 7.5.
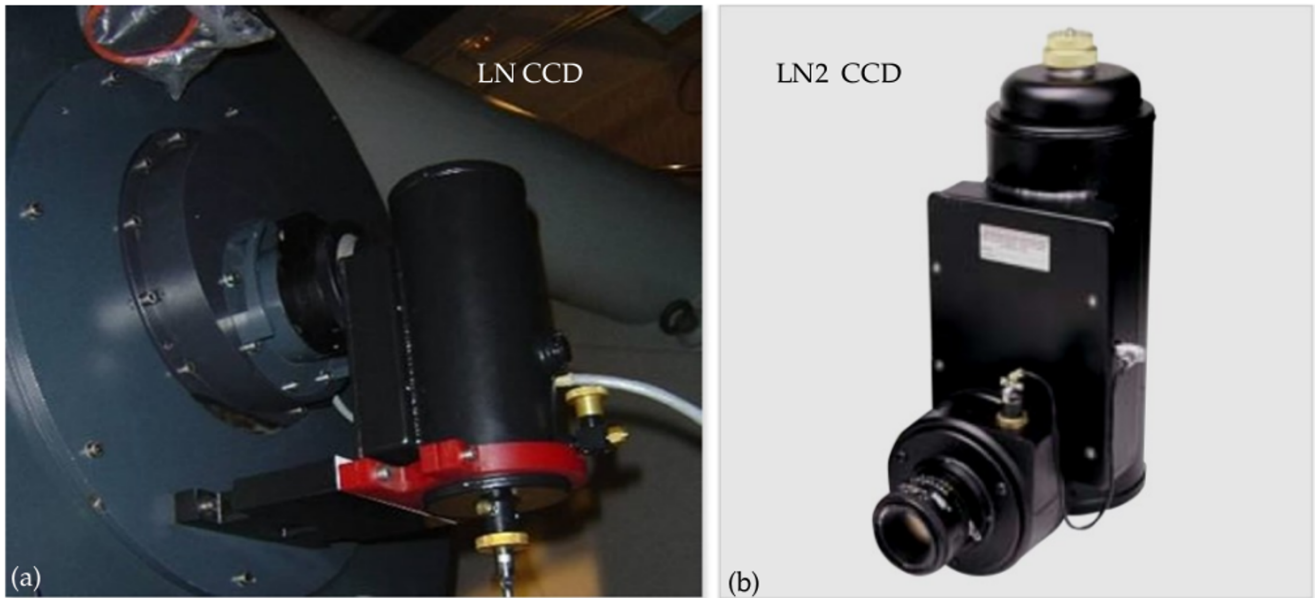
Figure 2.4: a) The LN CCD camera mounted on "Aristarchos" telescope at the focal plane of the telescope and b) The LN2 CCD camera. Both cameras were used for high-resolution imaging in "Aristarchos" telescope. For description, see in the text.

2.3 Data analysis

Imaging and spectroscopic data obtained with the telescopes, are not completely "clean" images. Electronic noise, dust on the optics, low efficiency in some of the camera's pixels and burned pixels are some of the factors that can influence the quality of the obtained images. Therefore, some extra images are needed to be obtained with the telescope, named *bias* and *flats*, which help to eliminate the aforementioned factors during the *data analysis* process. Below we present the usage of bias and flat images. In Sections 2.3.2 and 2.3.3 we present the IRAF commands for each step of the imaging and spectra analysis respectively.

2.3.1 Bias and flat

–**Bias images**: The function of a CCD camera is based on the photoelectric phenomenon. According to this, bounded electrons are detached from a semi-conductor (the chip of the CCD), when photons of appropriate frequency incident on its surface, transport their energy in these electrons, making the latter to escape from the pulling force of their atoms. These photoelectrons consist the counts we collect in the end from the object's emitted radiation (in our case, from the SNR).

However, even though the CCD camera operates at very low temperatures (about -120 °C) there are always some free electrons in the chips of the CCD moving randomly at high speeds
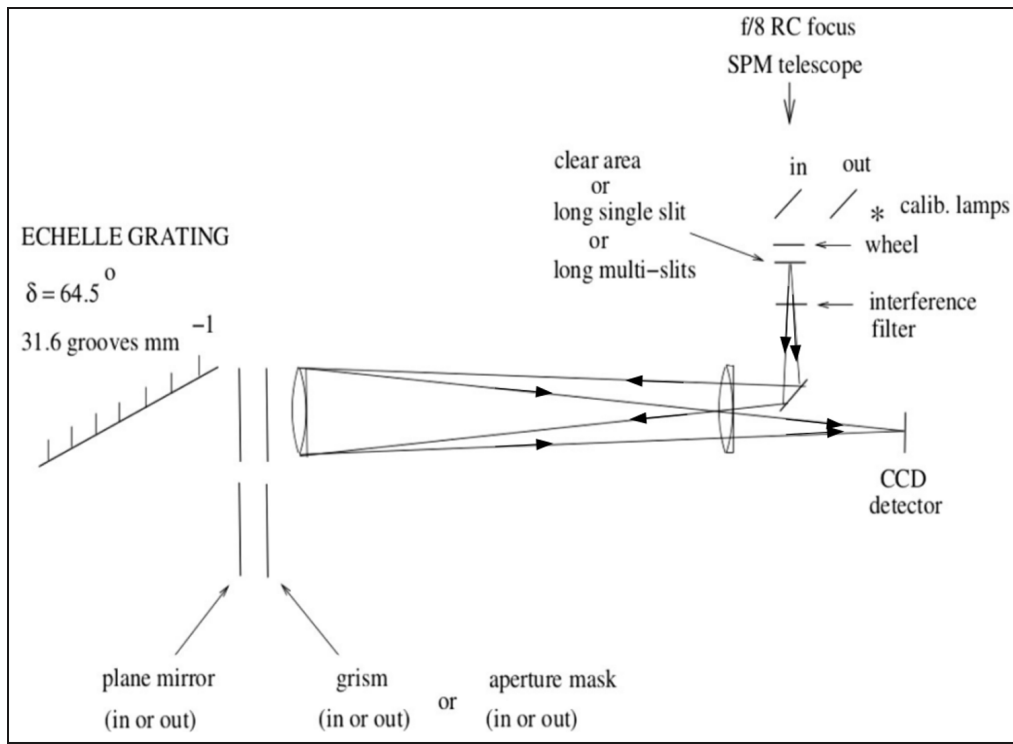
Figure 2.5: Schematic layout of the MES-SPM where the light path can be seen. When the slit is removed and the mirror is placed in front of the grating, MES can be used to obtain a direct image of the field.

(thermal electrons), which are recorded from the camera as photoelectrons and are inserted in every image we obtain. Of course, these photoelectrons have nothing to do with the real radiation we want to collect from the object we observe, and this is why these counts need to be removed from all the data images.

Therefore, in order to isolate and record this thermal "noise" we take images with zero exposure time and the shutter of the camera closed (if the shutter of the camera were open, then we would collect photoelectrons due to the photons of the object too). These images are called *bias*. During the night, we take many bias images before and after an exposure. Later, in the data analysis, we combine these bias images to create a median bias, or master bias as it is called (Fig. 2.7a). This master bias is then subtracted from every single image we have obtained during that night.

-**Flat images**: For the same intensity of radiation that incidents on the chips of the camera, each pixel produces a different number of photoelectrons, i.e. it has a different efficiency. The result is, the obtained image to present non-uniformity in its lighting. That is, the image is brighter in some regions and darker in some others, but this fluctuation is not due to the radiation emitted from the object. If all the pixels had the same response, how many counts each pixel would eventually produce?

A second point is that, until the light reaches the camera (detector) it is reflected onto
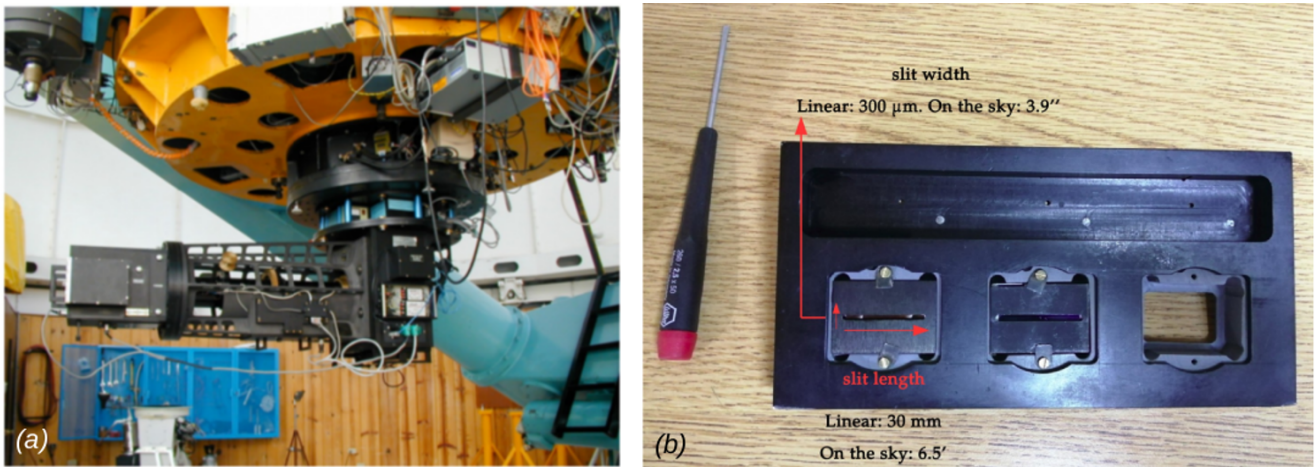
Figure 2.6: a) The MES-SPM spectrometer mounted on the 2.1m telescope at the SPM Observatory. b) The case where the slits for the MES-SPM spectrometer are kept at the SPM telescope. The image shows the slit (width and length) used for the performance of the observations for the project of VRO.

the mirrors and passes through optical devices (filters, slits) on which dust may have been deposited. Light is scattered on these dust grains, so these photons are not recorded from the detector. This dust is depicted on the images as "donuts-ring" structures, and again is not due to the radiation of the object we observe.

In order to eliminate these errors, we take *flat* images. Flat images must be taken when there are no stars at all on the sky at the moment of the exposure, i.e. just before or just after the sunset, or right after the sunrise. Therefore, any non-uniformities and dust presence are revealed in the obtained flat images, and subsequently removed form the data images. We take at least three flat images in each filter (because pixels have different response to each wavelength), with exposure times $\Delta t > 3$ sec (if $\Delta t < 3$ sec, then the shutter of the camera may not have fully closed yet - shutter effect).

The image data is divided by the normalized flat of the same filter (Fig.2.7b), the latter deduced after the data analysis the flat has undergone as this is described in Section 2.3.2. By this way, the image data is discharged from the errors mentioned above.

2.3.2 Imaging

For the data reduction, the IRAF software package was employed. In our project, the wide field images as well as the majority of the high-resolution images had already been analysed. However, below we present the data analysis procedure which was applied for the rest obtained high-resolution images and - up to a point- it is the same for the spectrum analysis as well, as will be shown in the next Sections.

In order to proceed in any process between images (e.g. addition, subtraction, division), the images have to be of the same dimensions, i.e. to have the same number of pixels between them in x and y axis. That's because the operations between images are in practise operations between the counts of the pixels located at the same position in every image.
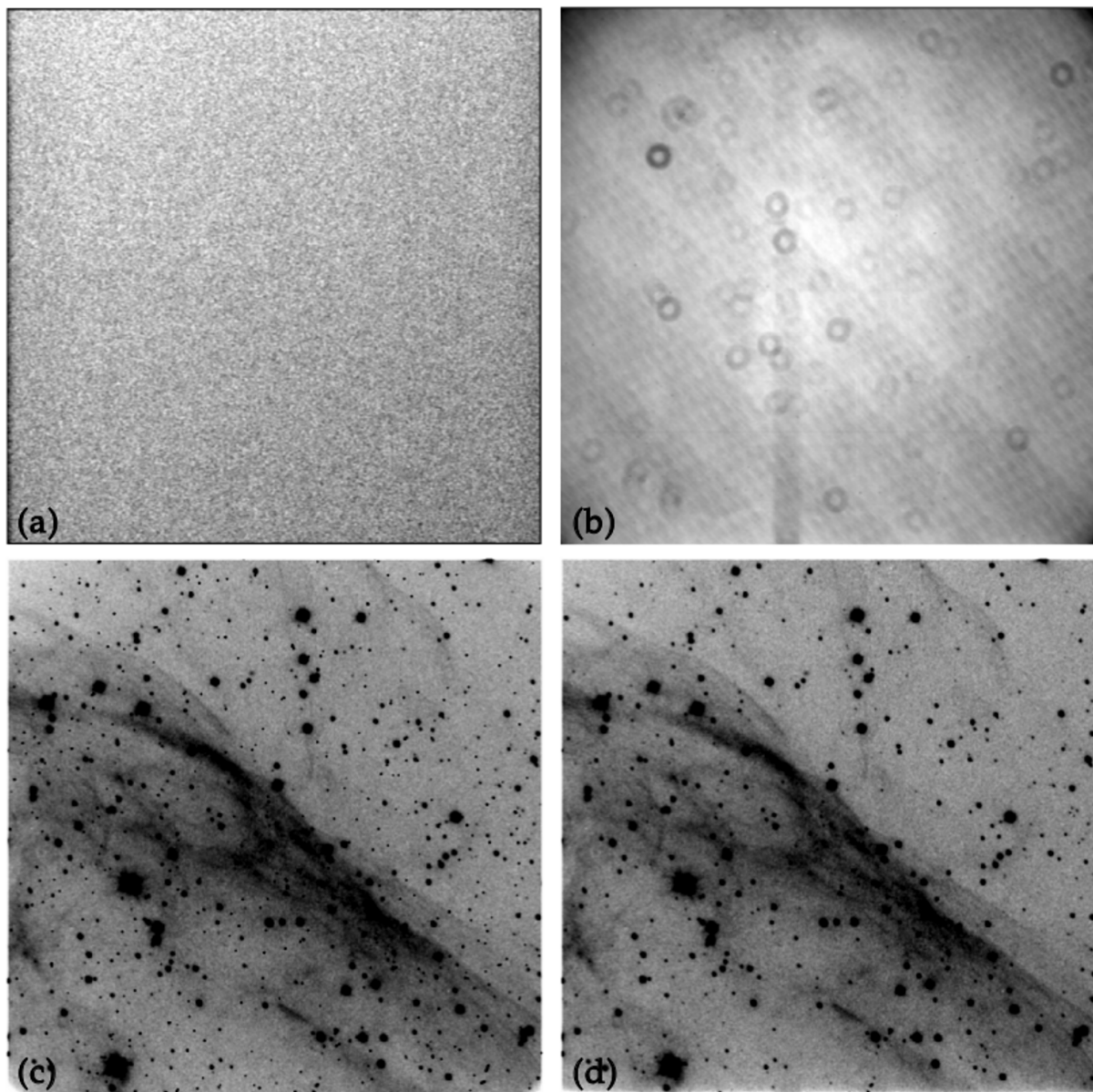
Figure 2.7: a) Master bias: it is subtracted from all the data. b) Normalized flat: it reveals the fluctuation in the lighting that is inserted into the image data. The "donuts-rings" structures seen in this image, are due to the dust grains on the optics. c) Image data, after master bias subtraction and normalized flat division. d) The same image data after the cosmic rays removal.

Data analysis and IRAF commands for imaging:

1. **Creation of master bias image:**

We combine all the bias images in order to create the "masterbias" image (Fig. 2.7a) (command: *zerocombine*).

2. **Creation of medianflat and normalized flat <u>in each filter</u>:**

   We combine all the flat images of the same filter (command: *flatcombine*) in order to create the medianflat image. From the median flat, we subtract the master bias (created before) (command: *imarith*). Subsequently, we normalize the deduced image (commands: *imstat* and *imarith*) in order to create the normalized flat. In the end, every pixel of the normalized flat should have a value around unity $(0.99 - 1.01)$ (Fig. 2.7b). Practically, this provides the response of each pixel at the same intensity of incident light, i.e. if the intensity of the incident light on the camera was 100 %, it shows us what the efficiency in photoelectrons of each pixel would be.

3. **Cosmic rays removal from flat images:**

   In case there are cosmic rays in the flat images, we remove them either in the medianflat, or in the normalized flat step (command: *crutil* → *cosmic rays*). In general, cosmic rays are inserted in all data which are obtained with the shutter of the telescope opened (image and spectral data, flat and arc) and should be removed from these images. The longer the exposure time in each image, the more amount of cosmic rays that hit on the detector. Consequently, we won't see cosmic rays in bias images, for they are obtained with the shutter of the camera closed and their exposure time is zero.

4. **Subtraction of master bias from each image data**: We use the command *imarith*.

5. **Division of each image data with the normalized flat <u>of the same filter</u>**: We use the command *imarith* (the deduced image is shown in Fig. 2.7c).

6. **Cosmic ray removal from the image data**: We use the command *crutil* → *cosmic rays* (the deduced image is shown in Fig. 2.7d).

   Comment on the colours in telescope images: At this point it would be useful to note that the observational images obtained with telescopes are not colourful, but are always in black and white colours, despite the use of certain optical filters each time. What the detector records, is the amount of counts (photoelectrons) in each pixel, and of course electrons have no colour. The spectroscopic analysis allows us to know which element is present in which region of the nebula. For example, detection of Hβ 4861 Å emission line implies that this part of the nebula should be blue, detection of the forbidden lines of [O III] 5007 Å indicate blue-green
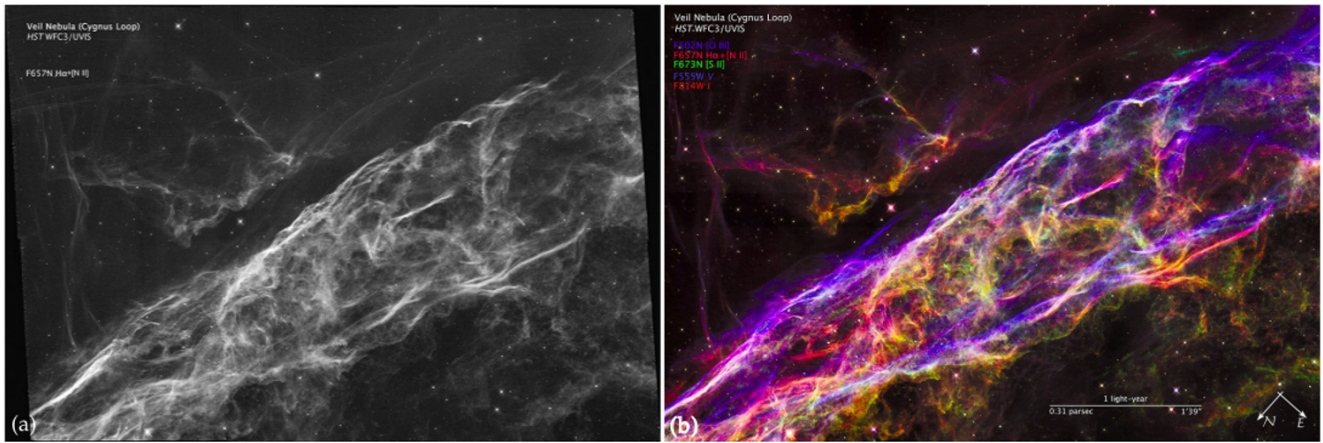
Figure 2.8: A Hubble WFC3 six-field mosaic of a small portion of the western limb of the Cygnus Loop, the Veil nebula. On the left, the grey-scale image in Hα+[N II] 6548, 6584 Å emission lines as obtained from the telescope. On the right, the produced image after the colours assignment. The filters and ions representing each colour are indicated on the figure.

colour, while Hα 6563 Å and [N II] 6548, 6584 Å indicate red colour for the nebula. Subsequently, the colour of the chemical element that emits radiation in the specific wavelength is assigned to the image creating a comprehensive colour image (red, blue and so on). An example of this is illustrated in Fig. 2.8.

2.3.3 Spectroscopy

The obtained spectroscopic data (which are also called 2D spectra) were also analysed in the typical way using the IRAF software package. The first steps of spectrum analysis are exactly the same as for the imaging process, i.e. master bias subtraction, division by the normalized flat and cosmic rays elimination. The difference is that now we do not proceed with astrometry, but in wavelength and velocity calibration of the spectrum, as will be shown in Sections and , with the purpose to finally extract the Position Velocity (PV) diagram of the spectrum.

–**Comment on the flats data:**

Regarding the flats data obtained with the MES-SPM telescope, apart from the commands presented in Section 2.3.2, we also needed to apply two more commands in order to eliminate the light differences:

i) *response*: makes the pixels to have the same efficiency in all λ along the dispersion axis

ii) *illumination*: corrects the light fluctuations along the spatial axis.

We can see the result in Fig. 2.9c along with the rest analysed data from the MES-SPM telescope, apart from the spectra data which are presented in Fig.2.10.

Next, we present the data analysis and IRAF commands from the point of cosmic rays

removal (Section 2.3.2) and on.

2D specrtum wavelength calibration –**Arc image:** For the λ calibration of a 2D specrtum we use the *arc* image. This is a reference 2D spectrum we obtain with the spectrometer in order to calibrate a spectrum of the object in wavelength. In the case of echelle spectrometry, an arc spectrum should be taken right after the spectrum data, in order to ensure that the grating will be exactly at the same position for the spectra and arc data.

An arc spectrum is produced by the discharge of a specific ionized gas contained in a lamp, whose emission lines are very well defined. In our case, the gas was ThAr (Thorium/Argon), and the spectrum it produces is shown in Fig. 2.9d. Each vertical, black line corresponds to a specific λ. Through the data analysis we eliminate the line's curvature, as each line can take only one value, the one of the λ. By this way, the arc is perfectly calibrated and, as we said, it can be used as reference image for the λ calibration of the specrtum data too.

Below we present the data analysis process and the IRAF commands at each step of this procedure.

1. **Arc calibration in** λ: Median bias subtraction, and subsequent division by the normalized flat (command: *imarith*). If there are any cosmic rays, they must be removed (command: *crutil $\rightarrow$ cosmic rays*).

   – We identify basic emission lines in the 2D spectrum of the arc ThAr lamp (black lines), through their matching with the already known 1-dimensional (1D) spectrum of the same gas-lamp (Fig. 2.11) (command: *identify*). The purpose is to match a wavelength value at each pixel of the arc image along the dispersion axis (this is the axis vertical to the spectrum of the emission lines). This is actually the *arc calibration* that later will be used for the λ calibration of the SNR spectrum.

   – IRAF takes as reference point the wavelength matching of the previous step and is now going through every row of the arc spectrum, calibrating the whole dispersion axis in λ (command: *reidentify*).

   – We assign a pixel value to every column, and a wavelength λ to every line of the arc spectrum (command: *fitcoords*).

2. **2D data spectrum calibration in** λ: We apply the calibrated arc spectrum of the previous step to the data spectrum, and the data image is now λ calibrated too (command: *transform*). Furthermore, the curving initially present in the image, has now been eliminated (Fig. 2.10c).
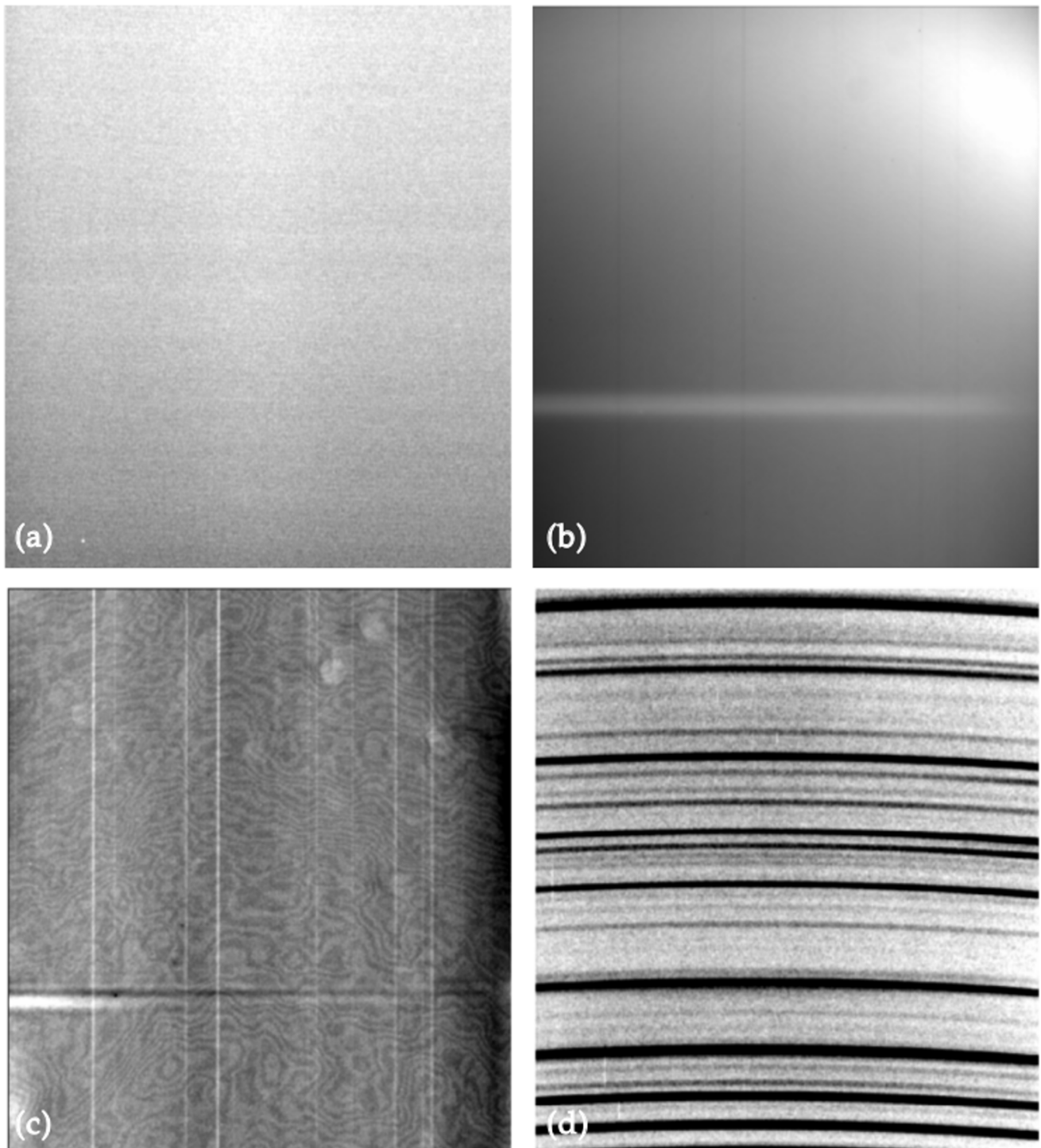
Figure 2.9: Analysed data from the MES-SPM telescope: a) Master bias, b) Median flat, c) Normalized flat, c) Arc spectrum. For data spectrum images, see Fig. 2.10.
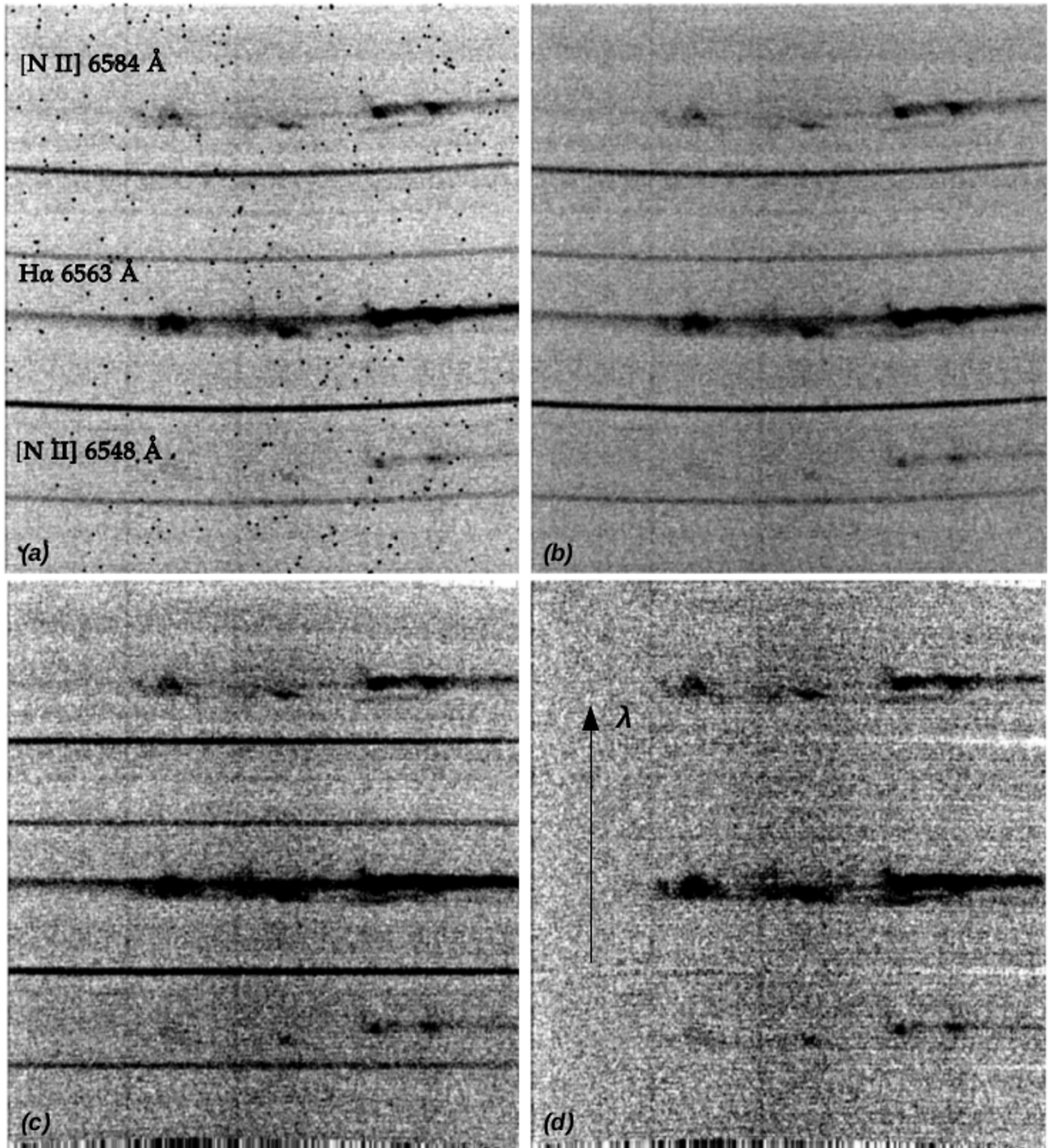
Figure 2.10: 2D data spectrum of Hα+[N II] 6548, 6584 Å emission lines of a region of the SNR VRO 42.05.01, in four steps of data analysis. a) the image has been master bias subtracted and divided by the normalized flat. b) Cosmic rays elimination. c) Wavelength calibration along the vertical axis through ThAr arc-lamp (elimination of the image curvature). d) Sky background removal. In the end, the continuous, black horizontal lines (sky emission lines) have been removed. The remained three black, horizontal stripes correspond to the spectrum of the Hα+[N II] 6548, 6584 Å emission lines of the object, with the 6548Å line at the bottom of the image to be the weaker one.
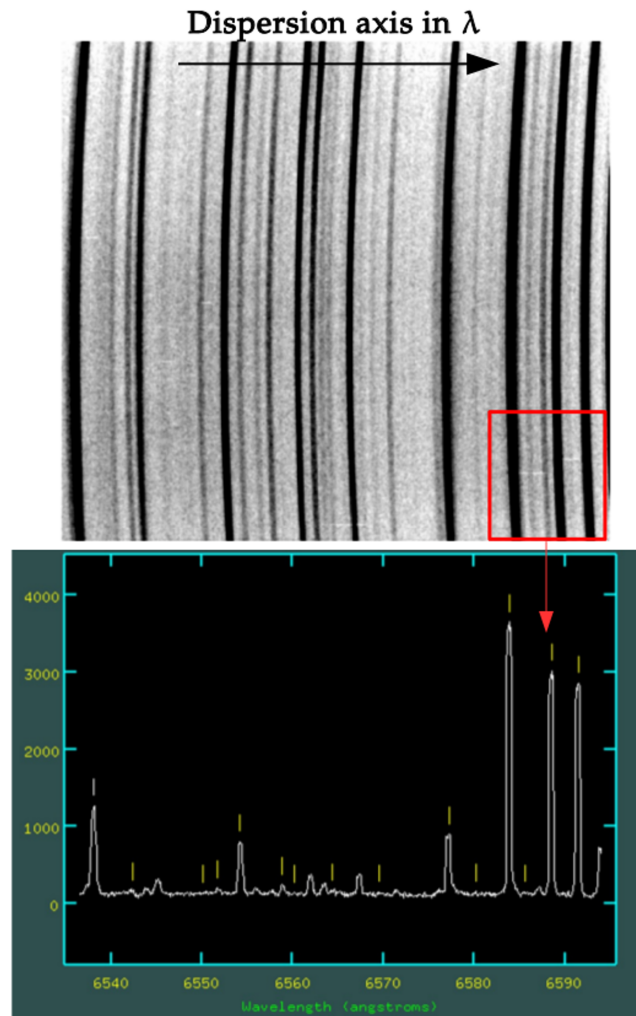
Figure 2.11: On the top of the image, the 2D spectrum of the ThAr lamp is presented (arc spectrum). It is the same arc as that in Fig. 2.9d, but rotated by 90 deg. Each line, is an emission line of the ThAr gas of the lamp. At the bottom, the 1D spectrum of the same gas-lamp. We use the well known 1D spectrum of the lamp in order to identify the emission lines in the 2D spectrum and calibrate its dispersion axis. In this case, representative are the last three strong emission lines, marked with the red frame.

3. **Sky background removal**: Apart from the remnant's emission lines, also present in a spectrum are the sky continuum emission lines, shown as continuous horizontal black lines in the image. These have to be removed from the data spectrum in order to keep only the radiation from the SNR (command: *background*). The result is shown in Fig. 2.10d.

 2D spectrum: What we see in Fig. 2.10d is called 2D spectrum λ calibrated. The vertical axis (the axis of wavelength) is called dispersion axis, while the horizontal is called spatial axis. In our example, the spectrum was extracted for an Hα+[N II] 6548, 6584 Å emission line image. We followed the same procedure for all the images in every filter. If the emission line has no Doppler effect, then it is located exactly at the position of the thoretical λ value. But, if the

Doppler effect is present, then the emission line is shifted with respect to the theoretical λ, as we will discuss in Section .

The next step is to transform the calibration in wavelength to velocity in the dispersion axis, and also calibrate the spatial axis from pixels that it is now, in arcmin. By this way, we will be able to obtain the Position-Velocity (PV) diagrams we need in order to apply them in SHAPE code for the 3D MK model.

2D spectrum velocity (V_{helio}) calibrated In Section we saw how we extracted a 2D spectrum calibrated in wavelength. In this Section we move on to the calibration of the same 2D spectrum in heliocentric velocity (V_{helio}), by transforming the wavelength λ of the dispersion axis of the 2D spectrum in its equivalent velocity.

$V_{Doppler}$ and V_{helio}: As it is known, due to the relative movement of an object with respect to an observer on Earth, the observed spectrum in an emission line of it ($\lambda_{obs.}$) is shifted with respect to the theoretical value of this emission line ($\lambda_{theor.}$). This is called *Doppler effect* and is depicted on the radial velocity of the object (velocity along the line of sight) according to the equation:

$$V_{Doppler} = c\frac{\left(\lambda_{obs.} - \lambda_{theor.}\right)}{\lambda_{theor.}} \tag{2.1}$$

where c is the speed of light in vacuum ~ 300.000 km sec^{-1}. Specifically, if the observed radial velocity of the object is $V_{Doppler} > 0$ then it is receding from us, if $V_{Doppler} < 0$ the object is moving toward us, while when $V_{Doppler} = 0$ then the object is moving, keeping though a constant distance relative to us.

Apart from the relative movement of the object and the observer on Earth, there is also the movement of the observer due to the Earth's rotation and evolution around the Sun. These motions have to be eliminated from the radial velocity of the object. This reduction is called *heliocentric correction*. In practise, through this correction, the 2D spectrum will be calibrated in velocity with respect to the frame in which the Sun is at rest (i.e. assuming that the Sun is at the center of the reference system of movement).

Data analysis: Regarding the spectrum data analysis, at first we insert the value of V_{helio} in the header of the image (command: *astutil $\rightarrow$ rvcorrect*). In our example (2D spectrum of Hα+[N II] 6548, 6584 Å in Fig. 2.10d), $V_{helio} = 11.53$ km sec^{-1} for this specific image, with respect to the Hα 6563 Å emission line. The shifted observed radial velocity of the SNR includes both Doppler and heliocentric effect:

$$\vec{V} = \vec{V}_{Doppler} + \vec{V}_{helio} \tag{2.2}$$

100

Remember that what we want to do is to correspond a radial velocity value to each λ value in the dispersion axis of the 2D spectrum. As an example, the calibration is performed with respect to Hα 6563 Å emission line. When $\lambda = 6562.82$ Å (theoretical value for Hα 6563 Å), Eq. 2.1 gives $V_{\text{Doppler}} = 0$ km sec^{-1} and from Eq. 2.2 is derived that $V = V_{\text{helio}} = 11.53$ km sec^{-1}. Therefore, in the 2D spectrum we will assign the velocity $V_{\text{helio}} = 11.53$ km sec^{-1} to the wavelength $\lambda = 6562.82$ Å. The whole calibration in the dispersion axis will be done based on this velocity value and the produced 2D spectrum will be in the end heliocentric calibrated (command: *wcsedit*). The result is shown in Fig. 2.12, where apart from the velocities in the dispersion axis, we also inserted arcmin calibration in the spatial axis.

The same procedure was repeated for all the emission lines of the spectrum respectively, i.e. in our example, for the [N II] 6584 Å and 6548 Å lines too, resulting in spectra calibrated in heliocentric velocity, with respect to each one of these emission lines.
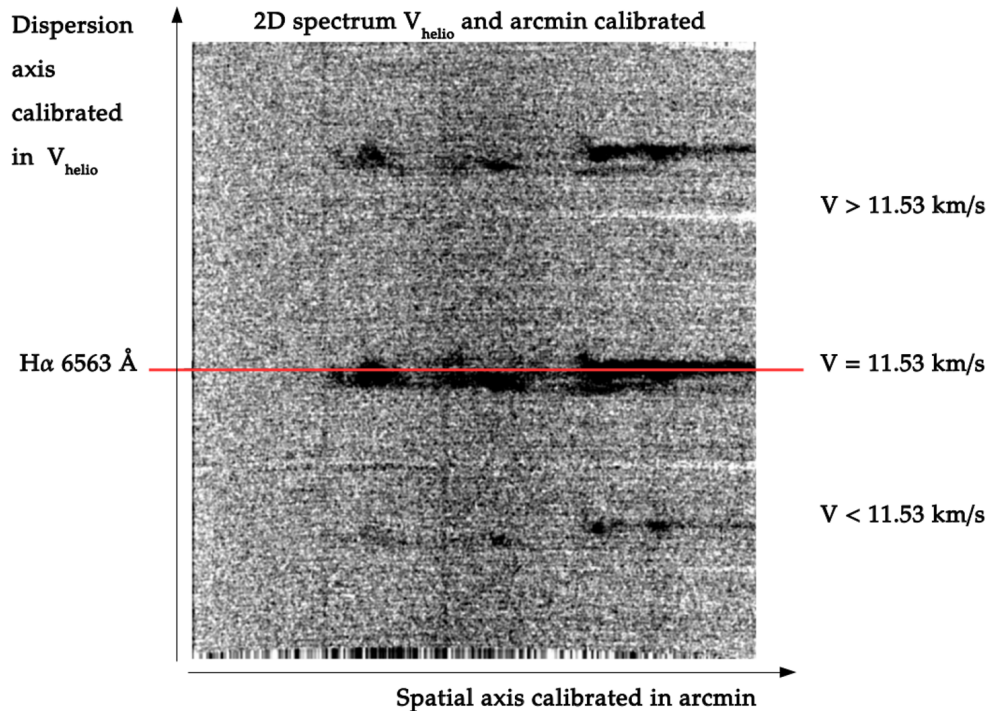
Figure 2.12: 2D spectrum calibrated in arcmin, and heliocentric velocity with respect to the Hα 6563 Å emission line. The part of the nebula whose Hα 6563 Å emission line has $V_{\text{helio}} > 11.53$ km sec^{-1} is receding from us, while the part that shows $V_{\text{helio}} < 11.53$ km sec^{-1} is coming toward us. For further description see in the text.

Position-Velocity (PV) diagrams   The next step is to deduce the Position-Velocity (PV) diagrams. Very simply, these are produced from a 2D spectrum calibrated in velocity and arcmin (see Section), by "cutting" that region of the spectrum which contains the emission line
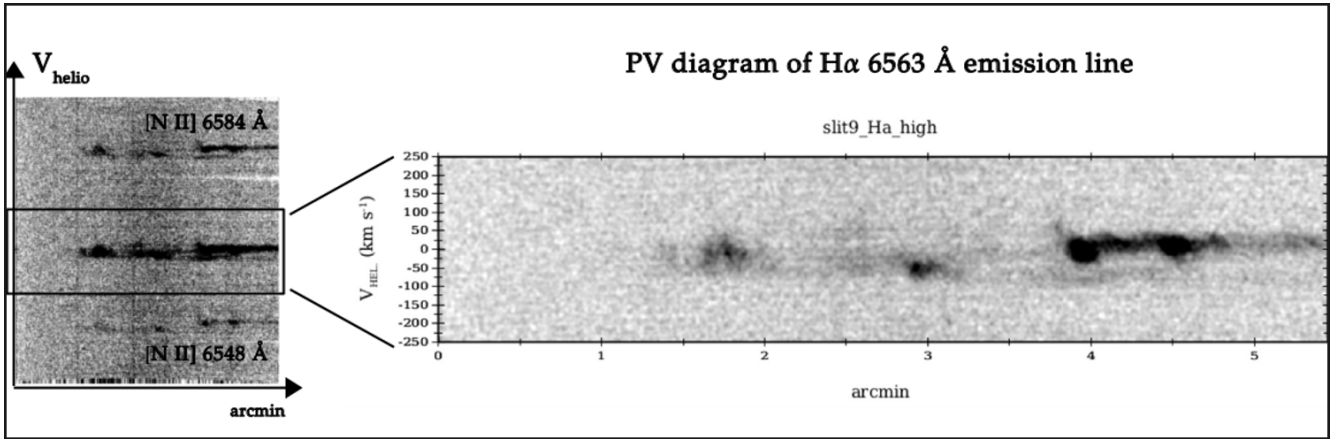
Figure 2.13: *Left:* 2D spectrum calibrated in V_{helio} and arcmin with respect to the Hα 6563 Å emission line. *Right:* The PV diagram of Hα 6563 Å in high contrast, deduced from the corresponding 2D spectrum. For further description see in the text.

we are interested in. In the example of Fig. 2.12, the image is calibrated according to the Hα 6563 Å emission line, so this is the line we are going to isolate and create the PV diagram. In order for the velocity axis to be easier readable, at the pixel where $V_{helio} = 11.53$ km sec^{-1} (see description in Section) we placed $V = 0$ km sec^{-1}. Based on this, the velocity range of each produced PV is ± 250 km sec^{-1} (Fig. 2.13). The spatial (horizontal) axis has a length of 5.5 arcmin, which basically is the length of the slit through which the radiation of the SNR has passed.

These PV diagrams were applied to the SHAPE code for the creation of the 3D MK model.

1D spectrum λ and velocity calibrated   From a λ calibrated 2D spectrum we can proceed to the extraction of its equivalent 1D spectrum, or else its *profile*. The IRAF command is *apextract* $\rightarrow$ *apall*, it has as input image the 2D λ calibrated spectrum and it produces a plot of the spectrum with respect to the wavelength λ in the horizontal axis (Fig. 2.14a). Subsequently, having as an input in the command *dopcor* the previously extracted profile, we deduce the same plot f(λ), but with the heliocentric correction inserted (Fig. 2.14b). Finally, we input the latter profile in the command *disptrans* and we end with the 1D spectrum which is Doppler and heliocentric corrected, and finally calibrated in V_{helio} (Fig. 2.14c).
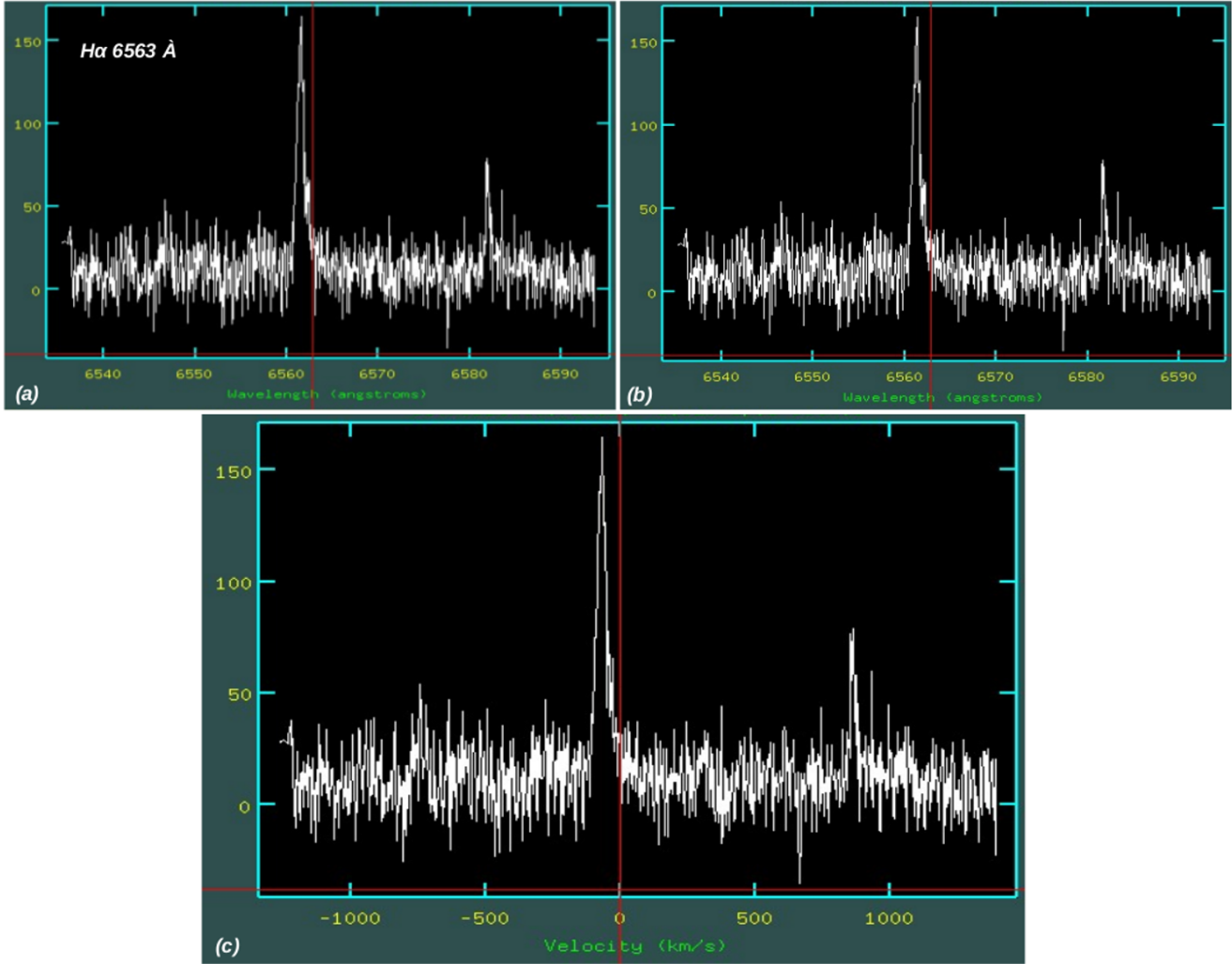
Figure 2.14: a) The λ calibrated 1D spectrum, extracted from the 2D spectrum of Fig. 2.10d. b) The same plot λ calibrated with heliocentric correction. c) The same plot calibrated in V_{helio}. The red lines indicate the position of $\lambda_{theor.} = 6562.82$ Å and $V_{\text{helio}} = 0$ km sec^{-1} respectively. We see that the deduced spectrum is shifted to the left with respect to the reference point of $\lambda_{theor.}$ or $V_{\text{helio}} = 0$ km sec^{-1}.

Chapter 3

3   3D Morpho-kinematic (MK) model

3.1   SHAPE code

Why 3D modeling:

Regardless the state-of-the-art astronomical instruments used in imaging and spectroscopy for the study of celestial objects, the fact that the obtained data are two-dimensional (2D) restricts the range of our knowledge for these objects, due to the absence of the information in the third dimension along the light of sight. Therefore, the step of the scientific research in the third dimension came as a necessity, since the benefits from a 3D study of an object will significantly contribute to a deeper interpretation of the collected observational data.

Current tools for 3D modeling in SNRs:

Regarding SNRs, up to date two were the most important tools for gaining information on the missing third dimension: i) the 3D (magneto) hydrodynamic (MHD) models which reproduce the 3D physical properties by comparing the 2D projection of the models with the observational data, and ii) the 3D velocity-maps which are created by the proper motion and Doppler shifted velocities of different parts of the nebula .

New entry in 3D SNRs - SHAPE code:

What we introduced in the field of 3D SNRs, is called *3D Morpho-kinematic (MK)* model. This is a snapshot in time which illustrates the morphology and the velocity field of an object in three dimensions. For this modeling, the astronomical software SHAPE was employed (Steffen and Koning 2017) in which imaging and high-resolution spectroscopic data of the object are applied as guiding data to the modeling process. Subsequently, using a list of tools (structural or

physical) that SHAPE provides, we manually reconstruct the 3D morphology and produce the synthetic spectra, i.e. the PV diagrams, that match the structure of the observational data of the object. Therefore, the synthetic output image and PV diagrams generated by our model are qualitatively compared with the observational data. The modification of the model structure continues until the synthetic image and PV diagrams reproduce adequately the observed images and PV diagrams, respectively. SHAPE has already been extensively used in order to study the 3D MK structure of Planetary Nebulae. However, up to date, no similar work for SNRs had ever been performed.

Why SHAPE had not been applied to SNRs before:

The reasons for this are: i) SNRs are usually very extended sources, which means that, apart from the imaging data, a great amount of spectroscopic data is also required for a full coverage of the remnant and ii) the asymmetries that SNRs usually display in their shape denote a great complexity in morphology and kinematics which is an additional factor of difficulty in the 3D visualization. The lack of such a 3D model in the field of SNRs was our motivation to proceed in the creation of the first 3D Morpho-Kinematical (MK) model of a SNR, using as a case study the Galactic SNR VRO 42.05.01.

SHAPE application in the current Thesis:

Due to the fact that SHAPE code has already been employed for numerous cases of PNe, while no similar project had ever been performed in SNRs, it was reasonable to learn the code by applying it to PNe before attempting its application in such a complicated object as VRO. The selected object was the PN Hb4, and the outline of its 3D reconstruction with SHAPE are presented in Section 3.2. The application of SHAPE to VRO 42.05.01 is presented in Section 3.3, where we also describe the basic steps of the code, directly applied to this object. In Sections 4 and 5 the scientific results of these projects are presented.

3.2 SHAPE code in the PN Hb4

Our motivation in order to create the MK model of the PN Hb4 is the pair of bipolar collimated outflows (knots) protruded from both sides of the main plane of the nebula (Fig. 3.1). These outflows present an unusual decrease of their expansion velocity as a function of distance from the core of the PN, i.e. the most distant parts of the outflows seem to move outward more slowly than the closer ones with respect to the main core of the PN. The goal was, through the 3D MK model, to give answers about the origin of these outflows, and subsequently for the mass loss mechanism during the evolution of the nebula that produced them. As observational data we used high dispersion long-slit echelle spectra along with high resolution images from

Hubble Space Telescope (*HST*). These were used in the SHAPE software, following the method that will be explained below, in order to construct the 3D morphology and reproduce the kinematic structure of the torus and the knots of the PN as well.

Figure 3.1: *HST* image of the Planetary Nebula Hb4 in [N II] 6584 Å emission line. The central region consitutes the core of the PN, from which two bipolar outflows are expelled, towards its northern and southern region respectively. The characteristic of these bipolar structures is the unusual decrease of their expansion velocity as a function of distance from the core of the PN. Their classification and the interpretation of their kinematics was the motivation for the 3D MK reconstruction of this object with SHAPE code.
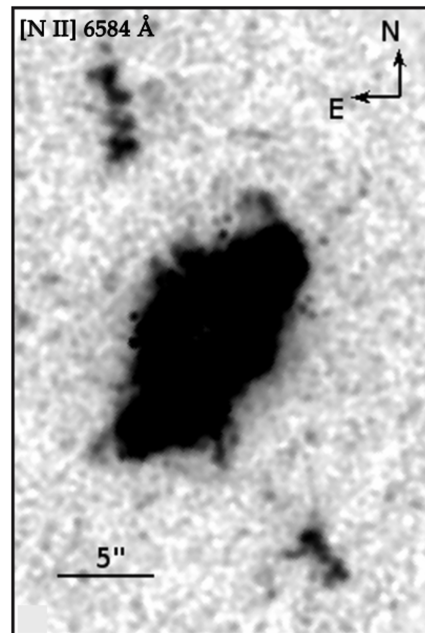
Step 1: Imaging and PV as data for the modeling process, for the core of the PN

At first, we started with the reconstruction of the main core of the nebula, in order for the latter to constitute the reference point for the distances of the knots from the central star that we were about to reconstruct afterwards.

In Fig. 3.2 we see the SHAPE software and the two input images which are displayed as backgrounds in the Renderer window in SHAPE to guide the modeling. As imaging data we applied the [N II] 6584 Å image from *HST* telescope, 42.7 arcsec in size (Fig. 3.2a). The two parallel white lines demarcate the position of the spectrograph slit which passes through the core and the two bipolar outflows of the PN. Its dimensions of width (1.9 arcsec) and length (42.7 arcsec) were inserted in SHAPE through the *Parameters → Group*. In Fig. 3.2b, the PV diagram of the core of Hb4 in the same emission line as the 2D image is displayed. In the next paragraph is explained, how this specific PV diagram had been extracted for the needs of the model.

Calibrating and isolating the PV diagram of the core: Although the PV deduced from the data analysis was calibrated in V_{helio}, the PV we applied in SHAPE (Fig. 3.2b) was calibrated in expansion velocity: $V_{\text{exp}} = V_{\text{helio}} - V_{\text{sys}}$. This is the radial velocity at which every part of the nebula is moving with respect to the center of the PN, where we assumed $V = 0 \ \text{km sec}^{-1}$. We
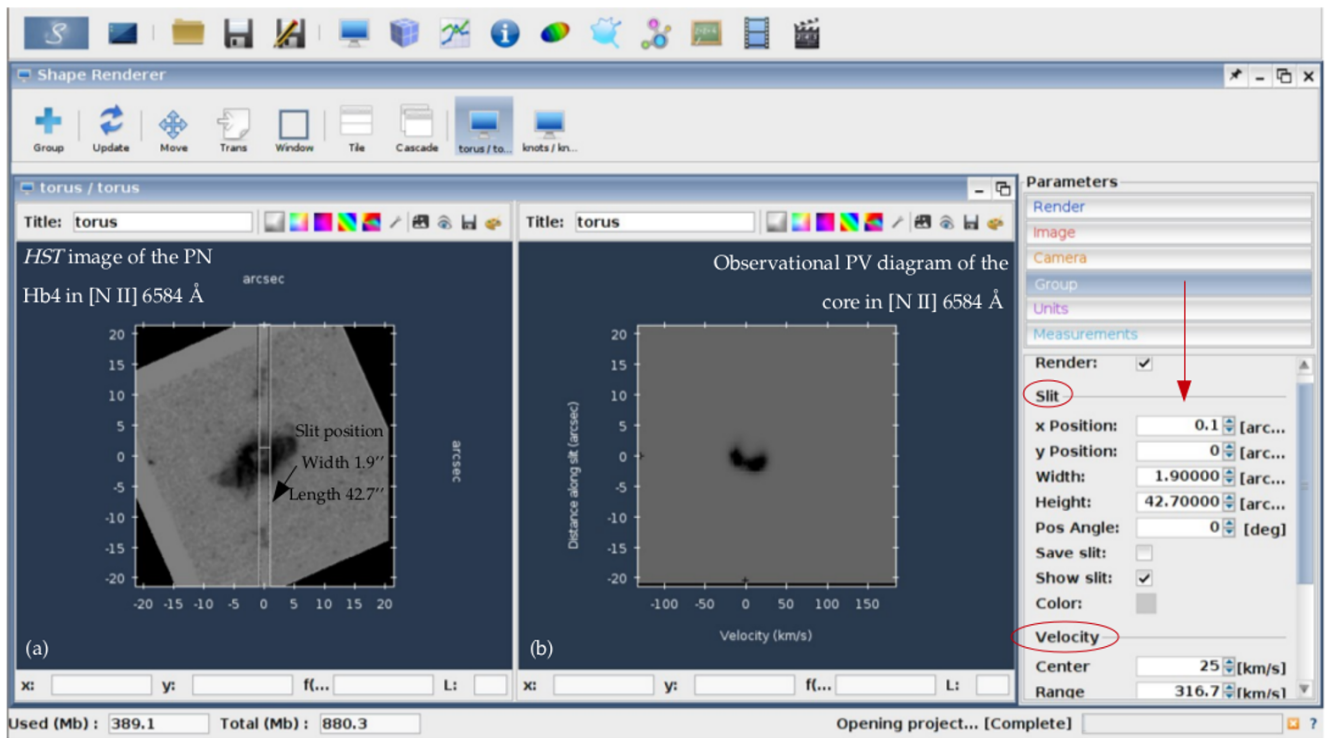
Figure 3.2: Two input images in the SHAPE Renderer window. a) the 2D image of the PN Hb4 overlaid with the slit position. b) the PV diagram of the core of the PN –in the same emission line– calibrated in $V_{\exp}$. The slit's position and dimensions along with the velocity range of the PV diagram, were used in the *Group* window.

did this, because we wanted to calculate at which outflow velocity each knot had been expelled from the core of the PN (the radial velocity deduced from the observations is the projection of the outflow velocity deduced from the model, as will be explained below). Fig. 3.3a shows the PV diagram of Hb4 deduced from the analysis. We can distinguish the part of the core (at the center) and the two groups of knots in the form of bipolar outflows at either side of the core. In order to "reveal" the core and be able to apply its PV in SHAPE for its 3D reconstruction, we applied high-contrast scale in this image, deducing the Fig. 3.3b. Furthermore, in order for the latter to be applied in SHAPE, it was rotated by 90 deg clockwise so as the velocity axis to be horizontal, and also match with the slit's orientation. It's velocity range in SHAPE was inserted through the *Group* window.

Step 2: Reconstructing the core

Geometrical structure:

Fig. 3.4 shows the SHAPE 3D window, in which the 2D image of the PN of the SHAPE Renderer is displayed, along with the slit position. In this window we choose the proper geometrical structure in order to create the 3D morphology of the object, and modify it accordingly
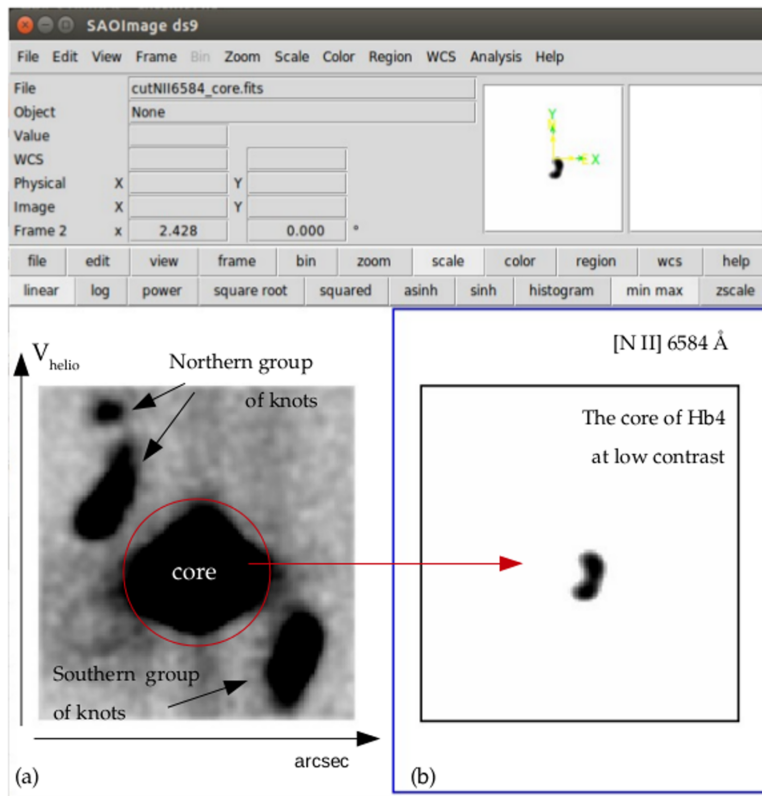
Figure 3.3: a) The PV diagram of the PN Hb4 in [N II] 6584 Å. We can discern the central region of the core along with the regions of the knots. b) The same diagram in low-contrast scale for the "isolation" of the core. The latter was applied in SHAPE for the 3D reconstruction of the core of the PN.

through the set of *Modifiers* (physical and geometrical) that SHAPE provides us with.

The final model deduced from SHAPE reproduces the core of Hb4 as a toroidal component, with inner radius 3.2 arcsec and outer radius 3.5 arcsec. The *Modifiers* we used were Displacement, Size, Shell and Position Angle/Inclination (the later for the rotation of the torus). The resulting torus is overlaid on the 2D image of the PN, as shown in Fig. 3.4.

Velocity law for the core:

In the *Modifier* → Velocity we set the velocity field for the torus (Fig. 3.5). We applied a homologous expansion law, that is radial expansion with the velocity increasing linearly with distance ($\vec{V} \propto \vec{r}$). The equation is $\vec{V} = B\left(\frac{\vec{r}}{r_0}\right)$, where B is the outflow velocity (whose projection is the radial $V_{\exp}$ along the line of sight), r is the distance in arcsec of a given point from the center of the field, and r_0 is the distance in arcsec from the center at which (r_0) the velocity is equal to B. In the case of the torus, $r_0 = 3.5$ arcsec, equal to its outer radius, while its outflow velocity was found to be $B = 15$ km sec^{-1}.

Step 3: Synthetic PV diagram of the core

The defined geometrical structure of the torus and its velocity field, generated its synthetic
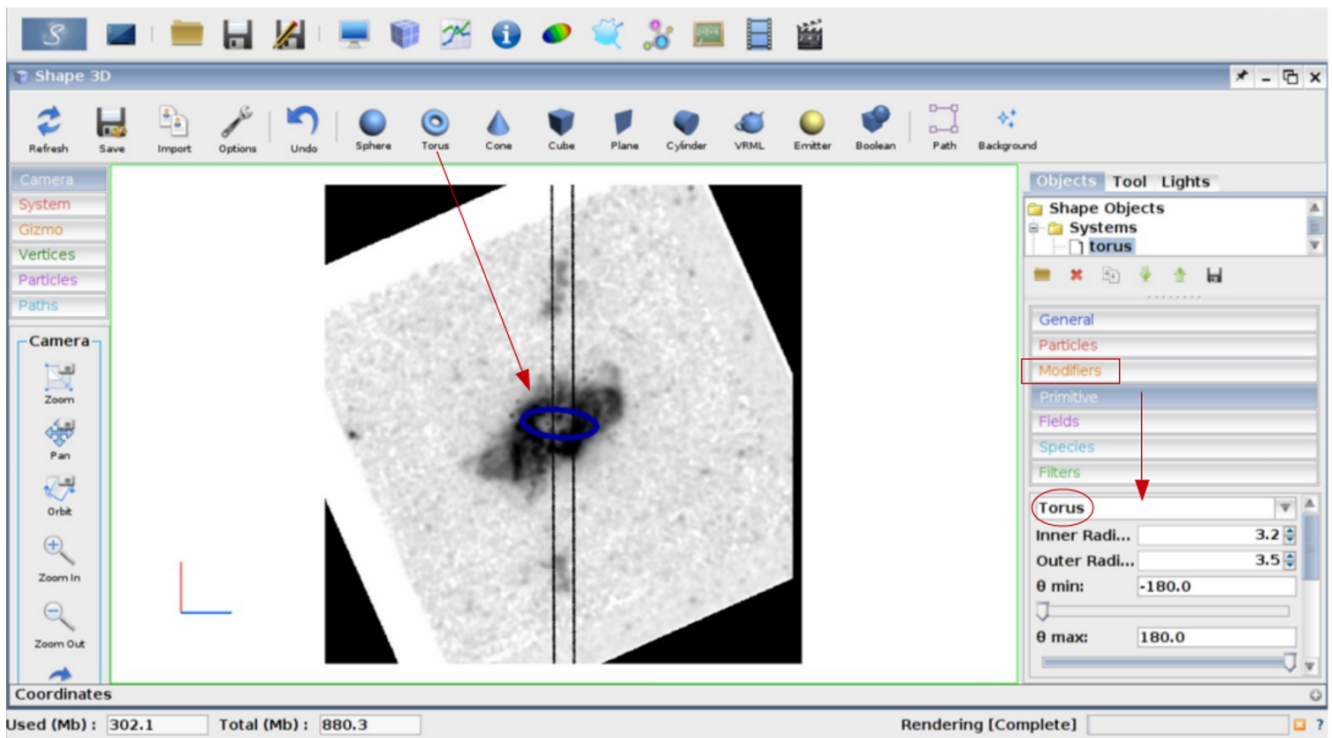
Figure 3.4: SHAPE 3D window: for the core reconstruction we chose a torus which was given its shape through the selected *Modifiers* in order to match with the torus of the PN shown in its 2D image. In *Primitive* we inserted its inner and outer radius.

PV (blue-red coloured) in the SHAPE Renderer window, overlaid on the observational PV (black coloured), as shown in Fig. 3.6b. In blue is the part of the torus that approaches us, while in red is the part that recedes from us. The agreement between the observational and synthetic PVs, in conjunction with the geometrical fitting of the structure with that shown in the 2D image, is the criterion for accepting the model. Therefore, while modeling, we keep modifying the structure and/or the velocity field to the point that an acceptable fitting between observations and modeling is accomplished.
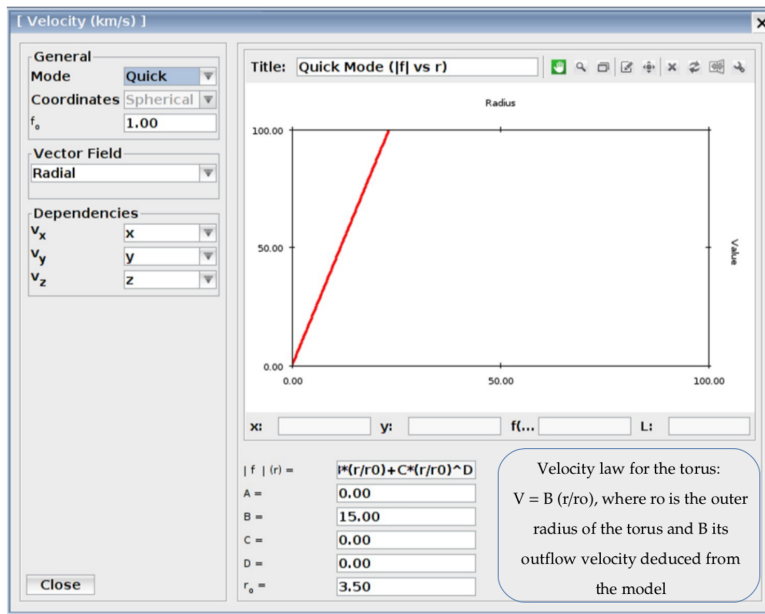
Figure 3.5: The window of the *Modifier* → Velocity in SHAPE, in which the velocity law of an object (or a substructure of it) is defined. r_o is the distance from the center of the structure up to its outer geometrical limit, and *B* is the outflow velocity deduced from the model. In this example, the velocity law for the core of Hb4 is shown.

After having defined the core's position, we proceeded to the 3D reconstruction of the knots. The purpose was to identify their morphology and, through their outflow velocity produced with SHAPE, to interpret their overall kinematic behaviour. The method continues as follows:

Step 4: PV for the knots as input image

Fig. 3.7 illustrates the SHAPE Renderer window, where the 2D image remains the same as in the core reconstruction, while in the PV diagram a low-contrast image of the high-resolution spectrum has been applied in order for the regions of knots to be distinguished. The red boxes include the northern knots, while the blue boxes the southern knots. It is important to understand that what we see in Fig. 3.7b are the knots that were included in the slit, and were distinguishable according to the available resolution of the spectrograph. Again, in order to reproduce the PV of each knot, we had to know its position (with respect to the center of the torus) and its velocity law.

Step 5: Reconstruction of the knots

As an example we will use knot 1 and we will describe how we defined its position and velocity field. The procedure is exactly the same for the other knots too.
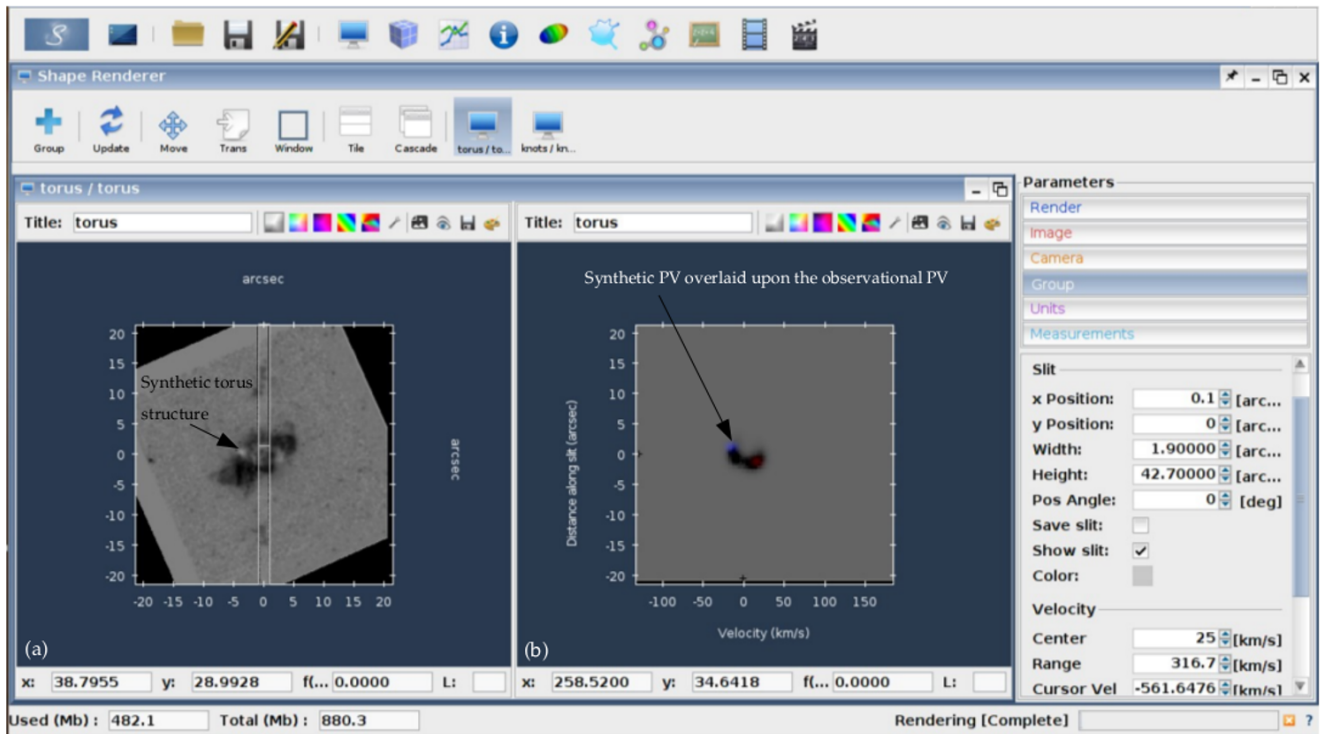
Figure 3.6: a) The synthetic torus structure (in white) overlaid on the 2D image of the PV. b) The synthetic PV (coloured) overlaid on the observational PV (in black). In blue is the part of the torus that approaches us, while in red the part that recedes from us.
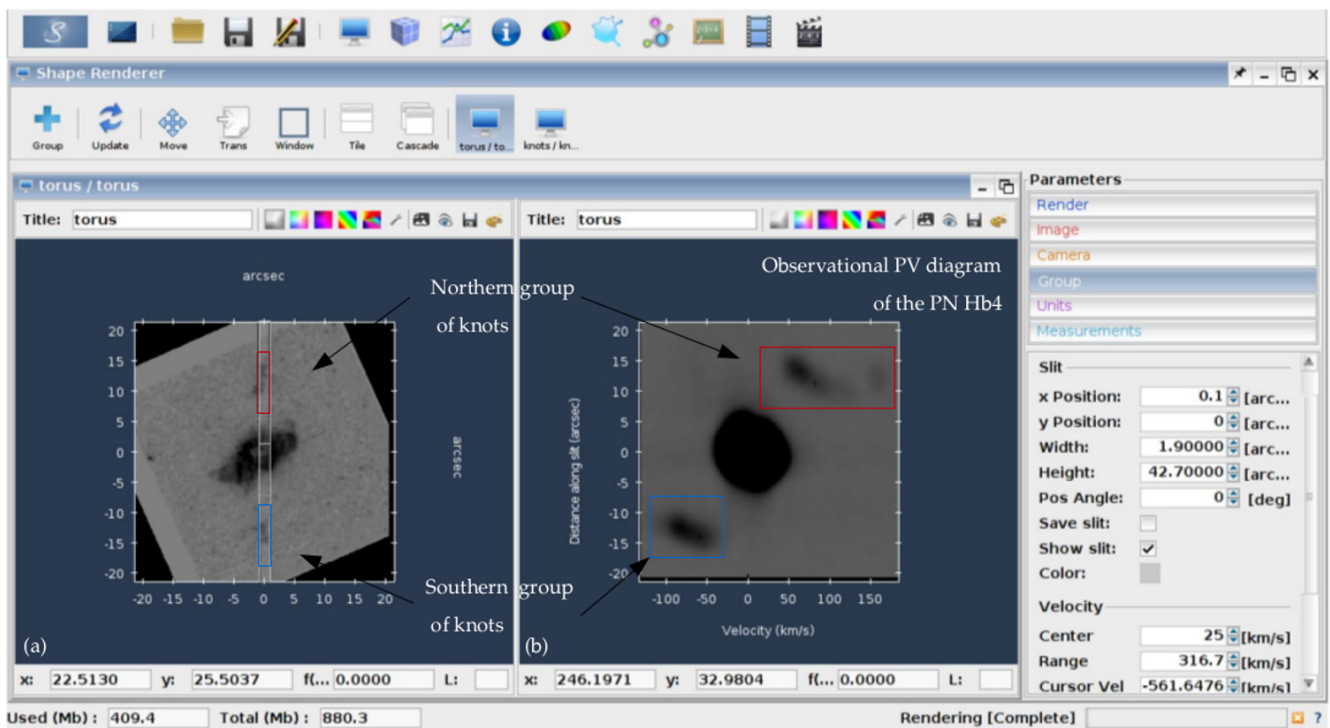
Figure 3.7: a) The same 2D image of Hb4 in [N II] 6584 Å as in the core reconstruction. b) The PV diagram of Hb4 is in low-contrast, in order for the regions of the group of knots to be noticeable. In both images, the red boxes include the northern knots, while the blue boxes the southern knots.
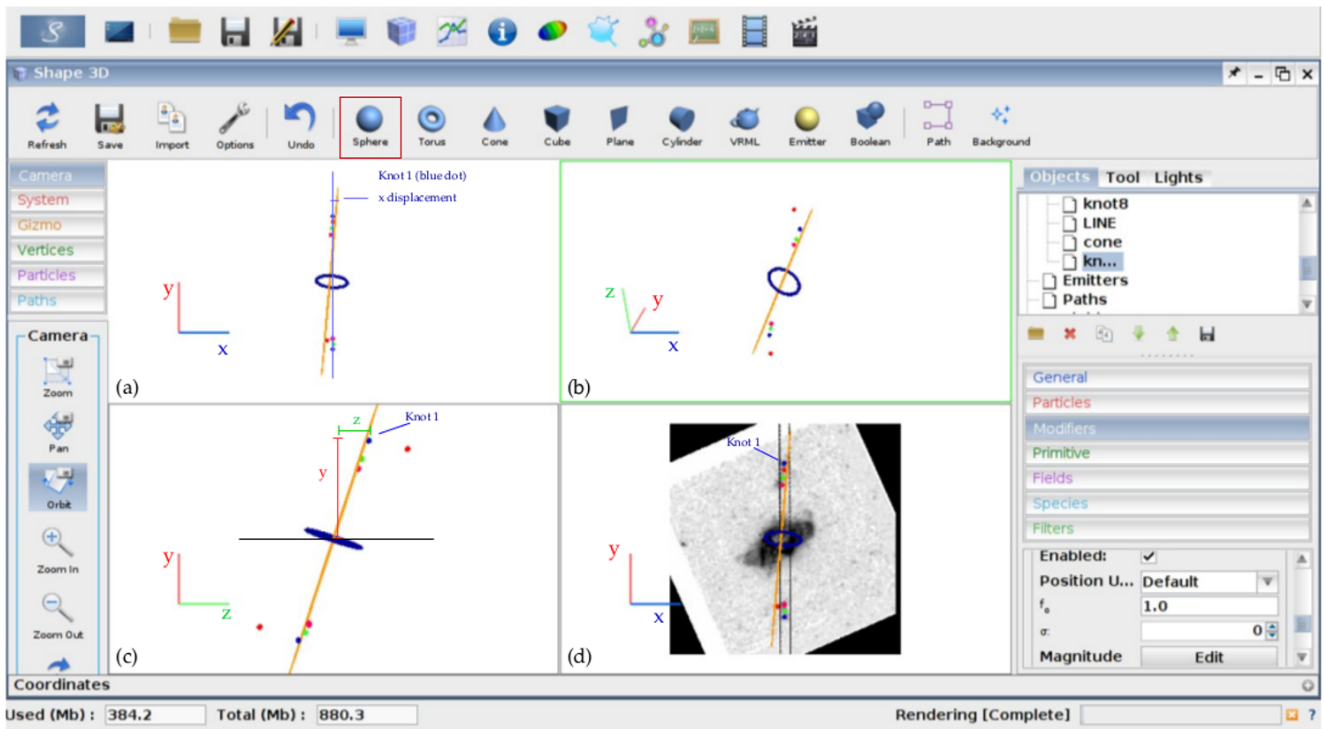
Figure 3.8: The 3D model of Hb4 as viewed from different angles. The blue ellipse is the torus of the PN, the coloured dots are the knots on either side of the core and the orange line is the symmetry axis perpendicular to the plane of the core. In (a) and (c), the x, y and z distances of knot 1 from the center of the core are displayed, which were defined through the *Modifier* → Displacement. Images (a) and (d) show the model from the same angle, with the difference that in (d), the model is overlaid on the 2D image of Hb4.

Geometrical structure for knot:

In order to create a knot, in the SHAPE 3D window we select a sphere and, through the *Modifier* → Size, we define its size in x, y and z axis (Fig. 3.8). Next, we overlaid this sphere (knot 1) on the 2D image in the position where we see knot 1, using the *Modifier* → Displacement. This *Modifier*, "moves" the structure in x, y and z axis of the 2D image with respect to the center of the image. In the PN model, the Displacement of each knot was considered with respect to the center of the torus (which coincides with the image center). Regarding the x and y axis, these displacements were easily defined from the image. What we had to constrain was the displacement in z dimension, i.e. how far from the torus was a knot in the direction along the line of sight. In this, the synthetic PV diagram would help us, through the velocity law that we applied for the knot.

Velocity law for knot:

In the velocity equation $\vec{V} = B\left(\frac{\vec{r}}{r_0}\right)$, the parameter $r_0 = \sqrt{x^2 + y^2 + z^2}$, where x, y and z are the values from the Displacement *Modifier* for knot 1. (Fig. 3.9). In the beginning we chose an

113
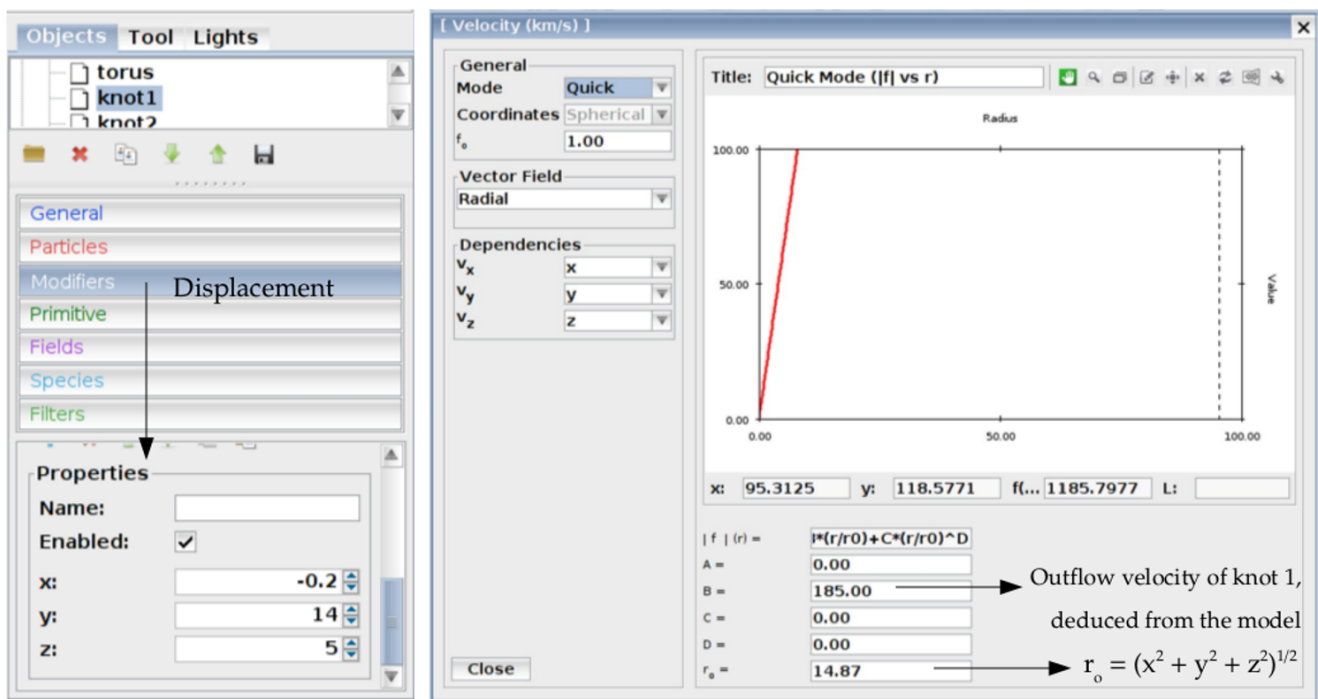
Figure 3.9: *On the left*: The *x*, *y* and *z* values for knot 1 of the *Modifier* → Displacement. *On the right*: the velocity law for knot 1. For description see in the text.

arbitrary *z* value, and checked the synthetic PV diagram produced from this velocity law. As we have already said, the produced PV has to match with the observational PV. After several tests, we achieved the best fitting between the observational and the synthetic PVs, and therefore we constrained the distance from the torus of knot 1 in the *z* direction. We repeated the same procedure for the other knots that we were able to identify in the 2D image and in the high-resolution spectrum of Hb4. The produced synthetic PVs for all the knots (blue-red shifted) are shown in Fig. 3.10b, overlaid on the observational (black coloured) PV.

The scientific results of this project are presented in Section 4.

114
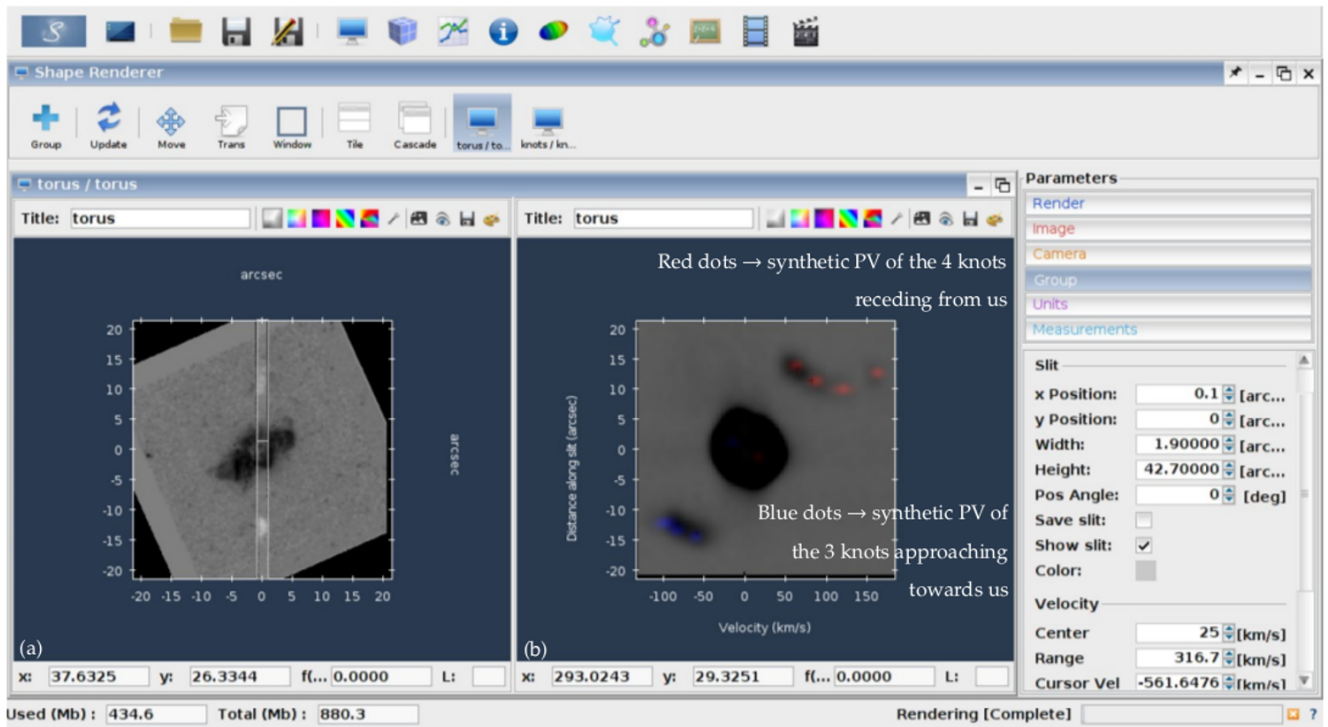
Figure 3.10: (a) The 2D image of the PN Hb4 overlaid with the 3D knots reconstructed with SHAPE (white dots inside the slit). (b) The synthetic PV for each knot (blue-red shifted) overlaid on the observational PV of Hb4.

3.3 SHAPE code in the SNR VRO 42.05.01

In this Section we present the basic steps of the followed method for the construction of the 3D MK model of the SNR VRO 42.05.01.

Step 1: Imaging and PV as inputs

Fig. 3.11 illustrates the SHAPE environment and the two observational images we displayed as background in the render window of SHAPE. The first input is the wide field image of VRO in Hα+[N II] 6548, 6584 Å emission lines, overlaid with the 26 slits positions at the areas where spectrum was obtained (blue lines). From these, 21 spectra were obtained with slit Position Angle (P.A.) of 45 deg with respect to the North and the remaining five at a P.A. of 90 deg, with the purpose to cover the whole area of the remnant.

In the same image, the red line represents the synthetic slit that the code creates at the position of each observational slit. Its length and width in the code are the same as these of the observational slit, i.e. 5.5 arcmin and 3.9 arcsec respectively. The presence of the synthetic slit indicates the reproduction of the equivalent synthetic PV with the code, in analogy to the observational slits that "provide" us the observational PVs (Section). Therefore, the second
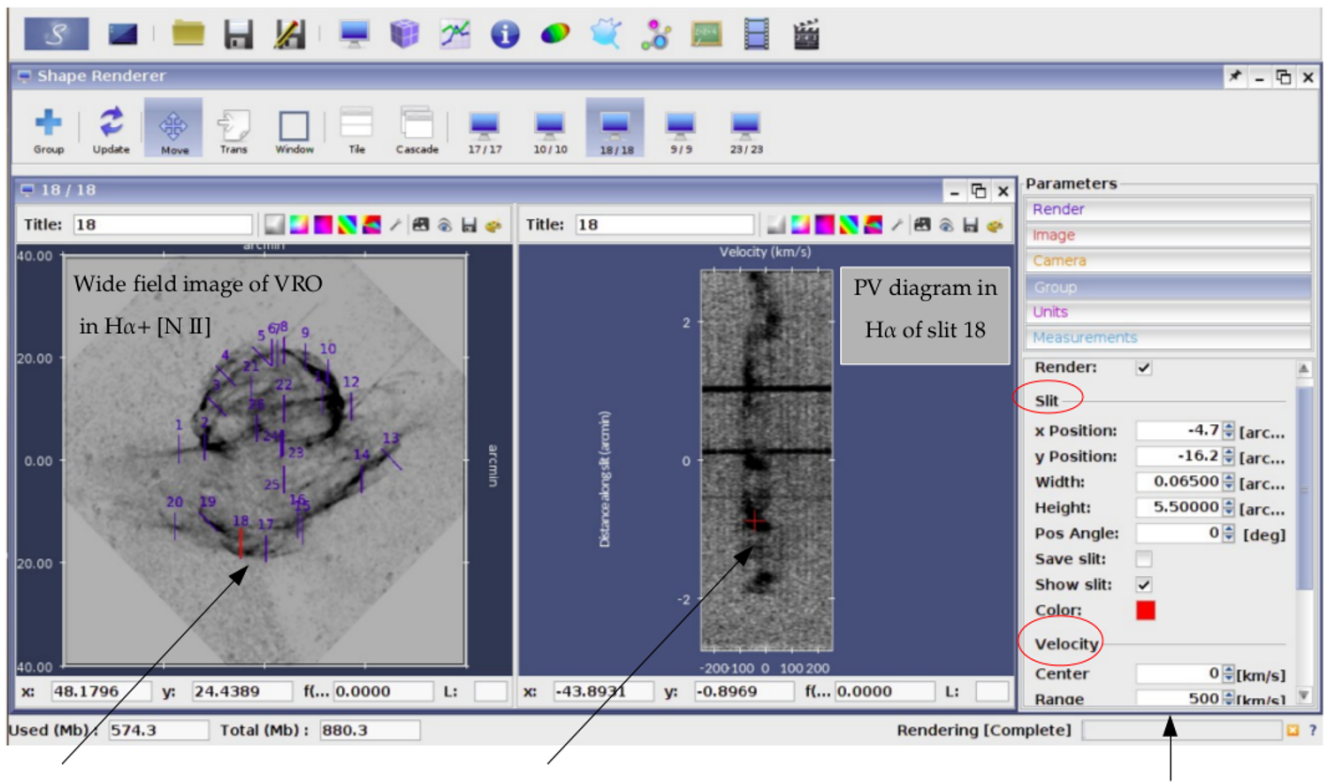
Figure 3.11: SHAPE environment: The 2D image of the object (on the left) and the PV diagram of each slit (on the right) that were used in SHAPE.

used image is the PV diagram in Hα 6563 Å emission line that corresponds to the equivalent observational slit (in our example, slit 18). Always, the 2D image and the observational PVs are of the same emission line.

Step 2: Define the scaling

Before we proceed to the construction of a 3D structure with SHAPE, it is of crucial importance to define the correct scaling between the 2D projection of the remnant in the input image and the structure we are about to create. No matter how complicated morphologies we are capable of creating with SHAPE, if the scaling is not correct the produced model will not have any physical meaning.

In literature, VRO had two components: a *shell* and a *wing*. So, the idea was to initially create two spherical shells that subsequently would be modified with the code accordingly, in order to match with the structures we see in the input 2D image. In order to define the scaling, we used the input 2D image of VRO, and with ds9 we measured the radius of each circle that
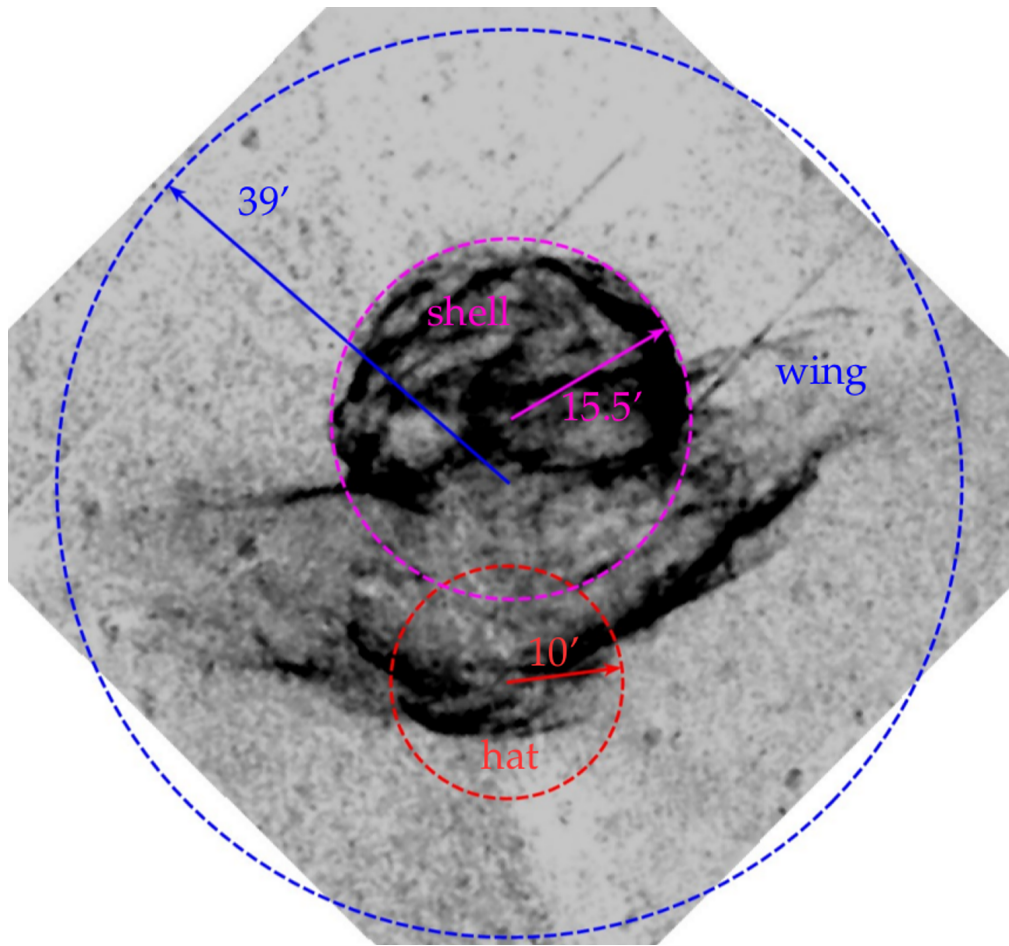
Figure 3.12: Wide field image of VRO in Hα+[N II] 6548, 6584 Å. Each one of the circles contains one component of VRO (*shell*, *wing* and *hat*). The measured radius of each circle was used for the scaling of the construction of these components with SHAPE, and for the velocity field of VRO.

contains the *shell* and the *wing* (Fig. 3.12). While creating the model, we saw that the lower part of the wing was separated from the rest wing (due to different kinematic behaviour - explained below in Section 5). This is why in Fig. 3.12 there is a third component, named *hat*, contained in a circle too. The measured radius r_0 of each circle was the radius of each spherical shell created with SHAPE. The parameter r_0 would be inserted in the velocity field too, as will be described in Step 4.

Step 3: 3D structure through "Modifiers" / Filaments

After defining the radius of the spherical shell, we started building the *wing* component in SHAPE by gradually deforming the spherical shell (see Fig. 3.13 and description in the caption) applying a number of geometric tools (size, squeeze, bump) that SHAPE provides through the "Modifiers" application (Fig. 3.14, on the left). Subsequently, we followed the same method for the *shell* and the *hat* components as well.

With respect to its morphology, a special characteristic of VRO is the filamentary structures

117
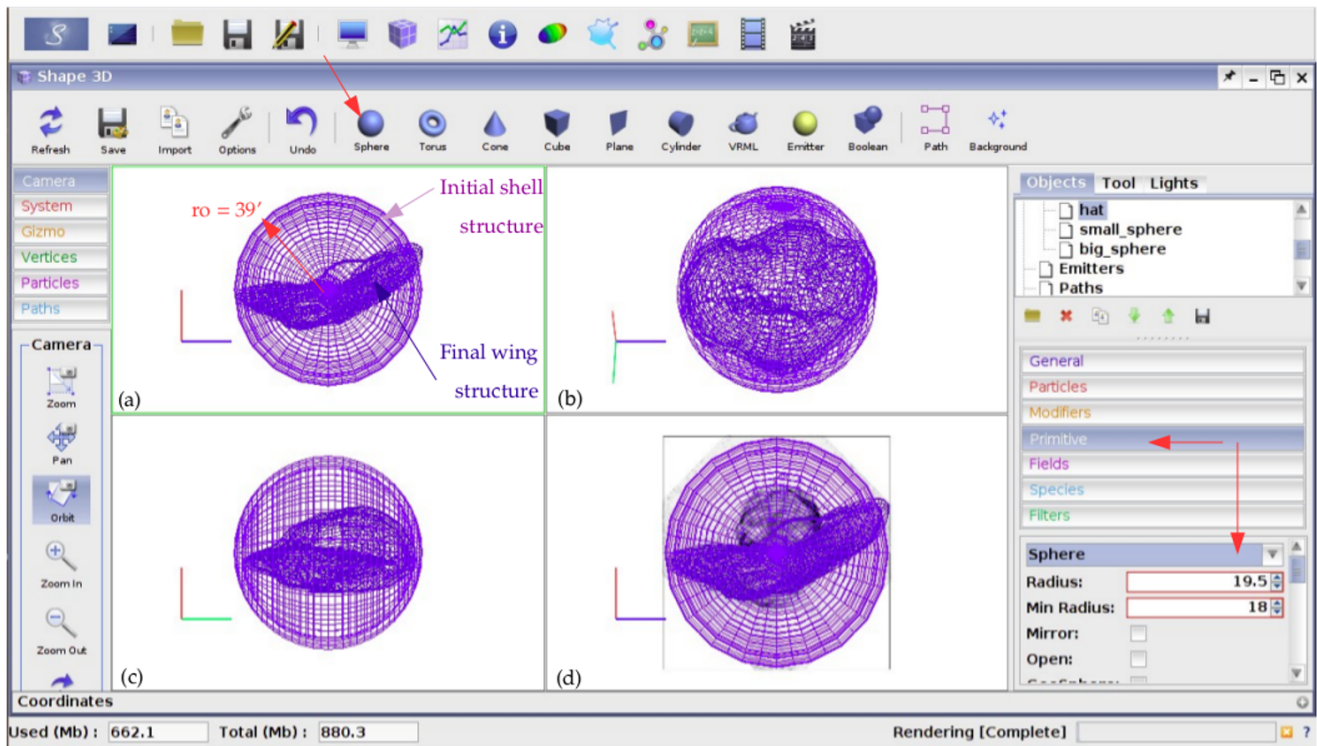
Figure 3.13: SHAPE environment: from the upper line we choose the 3D shape we want to create. For a shell construction, we choose a sphere, and then through "Primitive" we insert an outer and an inner radius, forming a shell. We see that the shell has a radius of 39 arcmin, while in "Primitive" we have 19.5 arcmin. This is why we used the Modifier *size* where we doubled the radius of "Primitive" in order to take the value we wanted. Also displayed is the final *wing* structure, formed after the modification of the initial spherical shell. Windows (a), (b) and (c) illustrate the 3D structures as viewed from different angles, while in window (d) the 3D structures are displayed overlaid upon the 2D input image of VRO at the background.

that it presents, almost all over its area. Especially in the *shell* there is a network of filaments, crossing the entire surface. The most intense of them were reproduced as indentations on the surface of the component through the *bump* Modifier. In this case the visual appearance of a filament comes from the fact that the indentations are seen more tangential, and therefore the path through them is longer and hence the image appears brighter in these regions.

Step 4: Velocity field

A key assumption for a 3D MK modeling is the velocity field of each component. This is a function of the radius r of the created structure (Fig. 3.14 on the right), while the center of the field is at the geometrical center of the structure.

More specifically about the velocity law of VRO:

VRO is at evolved phase, so we assume that the acceleration phase has ended and now it

118
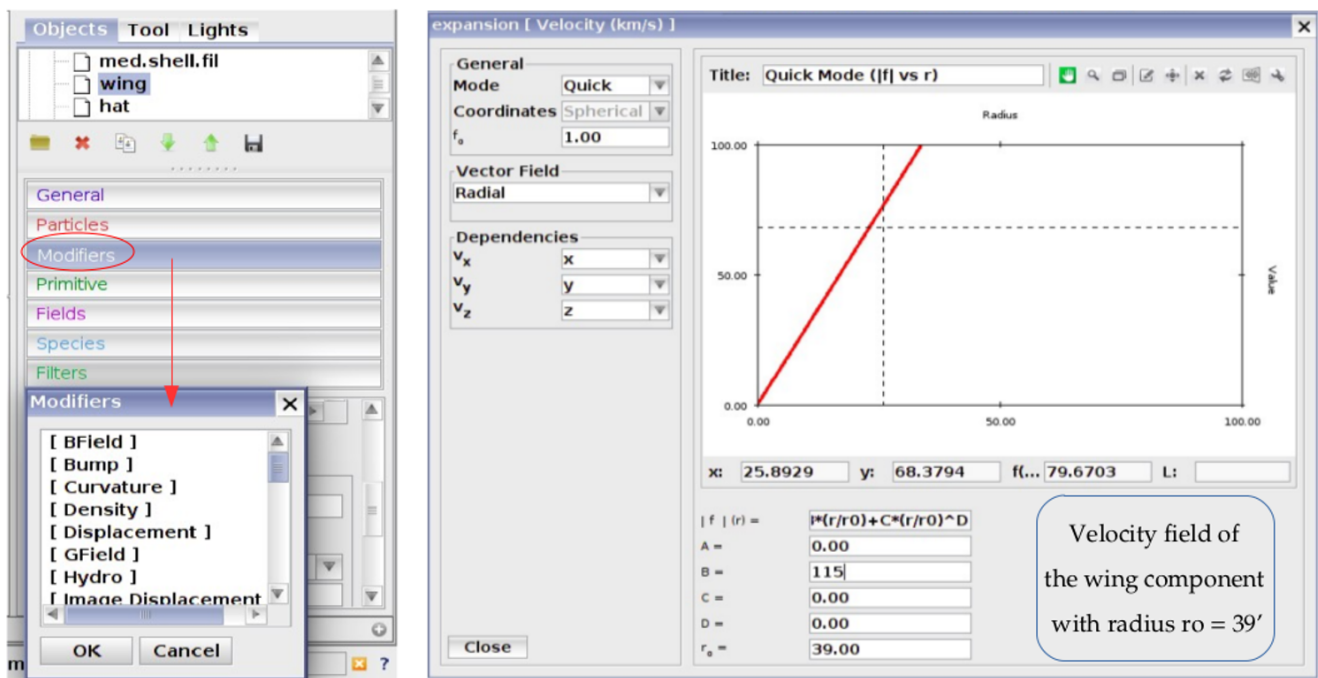
Figure 3.14: SHAPE environment: *On the left*: the list of the Modifiers that SHAPE provides for the modification of the created geometrical structures. *On the right*: the window where we can choose the parameters for the velocity field of each component.

is expanding at a steady velocity. For all the components of VRO, we applied the homologous expansion law $\vec{V} = B\left(\frac{\vec{r}}{r_0}\right)$, where B is the expansion velocity (whose projection is the radial V_{helio}, along the line of sight), r is the distance in arcmin of a given point from the center of the field, and r_0 is the distance in arcmin from the center at which the velocity is equal to B. Given that VRO has three components and its expansion center is uncertain, we assumed that the expansion velocity field center of each component coincides with its geometrical center.

Among the three components, the most complex component to constrain was the *wing*, for it doesn't show the spherical (or hemispherical) geometry that the other two components illustrate. Therefore, the assumption we made for the *wing*, was that its sizes in the two vertical axis (width, and along the line of sight) are equal. Subsequently, the modification of its structure was made according to its spectra, as it is described below in Step 5. Therefore the expansion centers for the *shell* and the *hat* were offset from that of the *wing* and with different B coefficients.

Step 5: Synthetic PV diagrams

As soon as the 3D structures were set up and their velocity field had been applied to the code, we moved on to the last step that is the reproduction of the synthetic PV diagrams, as shown in Fig. 3.15. It is the same SHAPE environment as in Fig. 3.11 (example of slit 18) with the difference that now the 3D model of VRO (in white) is overlaid on the 2D image of VRO (on

the left), and the synthetic PV (blue-red lines) is overlaid on the observational PV (black lines) (on the right). The blue lines represent the part of the region of the nebula (captured in the slit) that approaches us, while the red lines the part of the nebula the recedes from us.
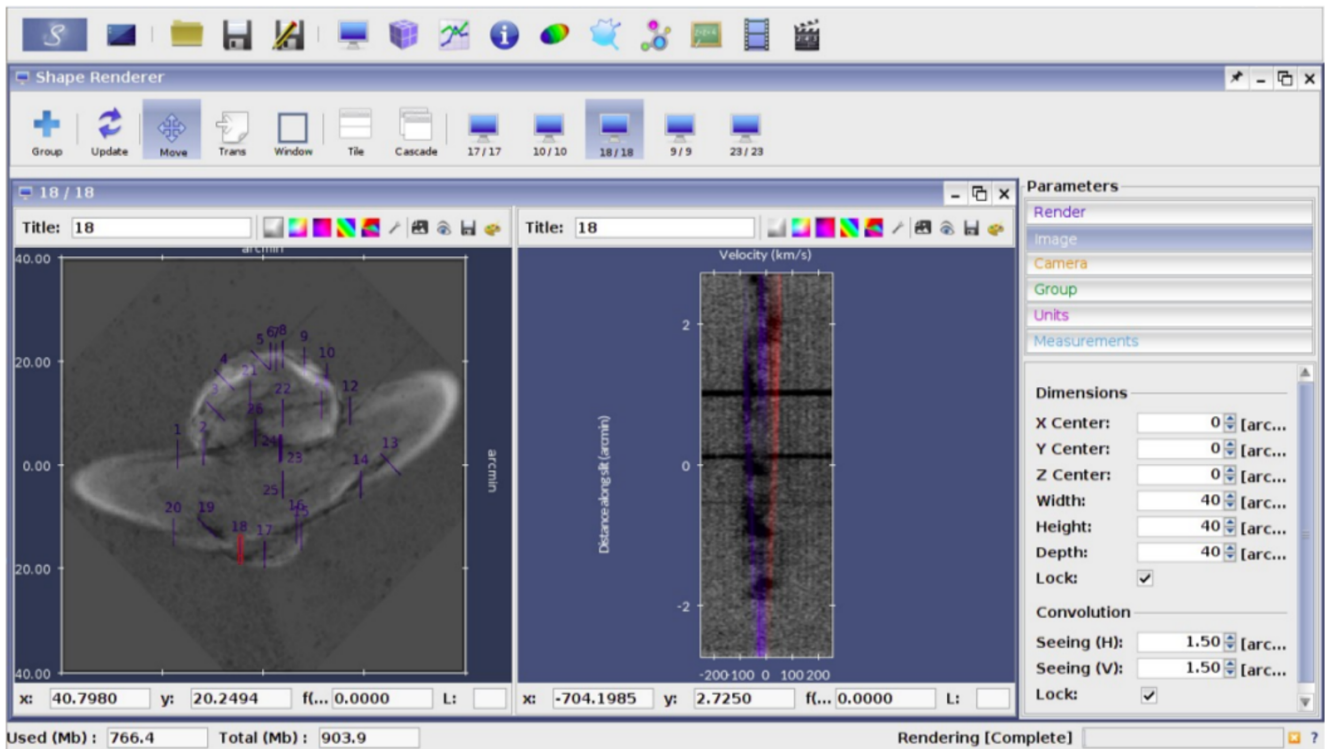
Figure 3.15: *On the left*: the 3D morphology of VRO overlaid on the 2D image. *On the right*: The synthetic PV produced with SHAPE (coloured lines) overlaid on the observational PV of slit 18 (black lines).

Synthetic PVs depend both on the created 3D structure and on the applied velocity law for each component. To put it differently, even if the morphology seems to match with that of the 2D image, if the deduced PV is not correct then the 3D structure and/or the velocity law need to be altered, depending on the slit position too. This is of crucial importance for the decoding of the SNR's morphology along the line of sight. A successful model in SHAPE code is the one that reproduces the morphology and the all PV diagrams of the object, in order for the model results to be consistent with the observations in both imaging and spectroscopic data.

Chapter 4

4 PN Hb4

The scientific results of the Hb4 project which are presented below, were published in the scientific journal Monthly Notices of the Royal Astronomical Society (MNRAS), Volume 484, Issue 3, p.3746-3754 (Derlopa et al. 2019).

4.1 Introduction

Using a general description, a Planetary Nebula (PN) is an emission nebula consisted of an expanding bright shell of gas ionized by the strong ultraviolet (UV) radiation field of the central white dwarf. It is formed when an evolved, low-to-intermediate mass star (1-8 $M_\odot$) expels its outer layers in the Asymptotic Giant Branch (AGB) phase, in the form of a slow (10 $\mathrm{km\,s^{-1}}$) and dense stellar wind (10^{-4} $M_\odot$) at a high mass-loss rate. Then, this material interacts with a fast ($\sim1000\,\mathrm{km\,s^{-1}}$) and tenuous stellar wind, resulting in the formation of spherical PNe, based on the assumption that both stellar winds are spherically symmetric (Interacting Stellar Wind Model - ISWM; Kwok et al. 1978).

However, the majority of PNe exhibit a diversity of aspherical structures (e.g. elliptical, bipolar; Schwarz et al. 1992; Boumis et al. 2003, 2006; Sahai et al. 2011; Weidmann et al. 2016). The interaction between an AGB wind, which has a high-density difference between the poles and the equator, and a spherically symmetric fast wind can explain the formation of aspherical PNe (Generalized ISWM; Balick 1987; Icke 1988). Common envelopes around binary systems provide the necessary density difference between the polar and equatorial directions on the AGB wind (e.g. Livio and Soker 1988), ensuing the formation of bipolar PNe (e.g. Frank et al. 2018; García-Segura et al. 2018).

An interesting case of PN due to its peculiar morphology and kinematical properties is Hb4 (G 003.1+02.9; α_{2000}: $17^h41^m52.7^s$, δ_{2000}: $-24°42'08.0''$). It is located in the Galactic Disk, with an estimated distance of 2.88 ±0.86 kpc (Frew et al., 2016). *Gaia* Data Release 2 (DR2) gives a parallax of 0.435±0.189 mas[1] (Gaia Collaboration 2018). Using a statistical approach, Bailer-Jones et al. (2018) estimate its geometric distance to 2.55 kpc with 1σ minimum and maximum bounds of 1.57 and 5.29 kpc, respectively.

Sahai et al. (2011) classify Hb4 as a multipolar nebula with an irregular structure and a barrel inner region. At the outer parts, it also shows a pair of collimated, detached jets or elongated knots moving with a velocity of $\sim150\,km\,s^{-1}$ (López et al. 1997). Rabaça et al. (2003) (see their, figure 1) reported a faint secondary bipolar structure, close to the central part, aligned with the minor axis, a feature that, in the end, implies poly-polarity for this nebula.

Hb4 is also identified as Type I PN in Peimbert's scheme because of its high N/O abundance ratio (Peña et al. 2017). The abundance discrepancy factor of singly ionized oxygen is found to be equal to 3.7 (García-Rojas et al. 2013), which might be indicative of a binary central star (Corradi et al. 2015). Its nucleus is classified as hydrogen-deficient star of WO3 class by Acker and Neiner (2003) and of WC4 class by Górny et al. (2004). A possible link between jets and knots with binary systems or Wolf-Rayet (WR) central stars in PNe has also been proposed (Miszalski et al. 2009).

The most striking characteristic of Hb4 on which this paper focuses, is the pair of bipolar collimated outflows (López et al. 1997; Hajian et al. 1997), protruding from both sides of the main plane of the nebula, which display a spectrum of low-ionization structures (LISs; Gonçalves et al. 2001, Akras and Gonçalves 2016) relative to the rest of the nebula (Corradi et al. 1996). These two outflows exhibit Hα/[N II] 6584 Å line ratio of ~1.10 (northern) and ~1.20 (southern), in contrast with the value of 3.29 of the core (López et al., 1997). This is expected, because this ratio is much stronger in the outflows than in the core, as has already been mentioned in low-ionization structures (LISs) (Akras et al. 2017). According to López et al. (1997), the systemic heliocentric radial velocity is $V_{sys} = -58.9\ km\,s^{-1}$, while the expanding velocity of the shell that surrounds the core of Hb4 is $V_{exp} \simeq 21.5\ km\,s^{-1}$. This is in good agreement with the calculated values of $V_{exp} = 23\pm2\ km\,s^{-1}$ (Robinson et al., 1982) and $V_{exp} = 23\pm4\ km\,s^{-1}$ (Danehkar, 2014).

In their kinematic analysis on Hb4, López et al. (1997) modelled the outflows as bow-shocks, whereas Danehkar (2014) defined these structures as "point-symmetric thin knots". Hajian et al. (1997) suggested that the southern outflow of Hb4 could be defined as jet, while for the northern structure they proposed the term "fast, low-ionization emission regions" (FLIERS;

---

[1] the *astrometric excess noise* is lower than 1 which implies a reliable parallax measure, but because of the high fractional parallax error, the inverse parallax does not provide a reliable distance estimate.

Balick et al. 1993) because of the knots' sizes, peculiar velocities and almost symmetric placement on opposite sides of the central star.

FLIERS are low ionization microscopic structures (~1 arcsec) within PNe in the shape of knots, jets, filaments, etc. They are usually found in pairs, and they exhibit equal but opposite velocities with respect to the nebula's systemic velocity. According to Gonçalves et al. (2001), FLIERS fall into the general category of LISs, that is, small scale, low-ionization structures that cover a wide range of expansion velocities from few tens to hundreds of $\mathrm{km\,s^{-1}}$. Therefore, considering their kinematical behaviour, LISs can be separated into FLIERS as mentioned above, bipolar rotation episodic jets (BRETS; Lopez et al. 1995), and slow moving, low ionization emitting regions (SLOWERs; Perinotto 2000). The nature of LISs is still an open question. They exhibit very similar morphologies, kinematics and emission line spectra to many Herbig-Haro (HH) objects, which are primarily heated and excited by collisions (Balick et al., 1993, 1998). It has been recently shown that a combination of photo-ionization by the strong UV radiation of the central stars and shock interactions of the LISs with the surrounding nebular material can explain their spectral characteristics (e.g. Raga et al. 2008; Akras and Gonçalves 2016; Akras et al. 2017).

In this project new spectroscopic data of Hb4 along with high resolution *Hubble Space Telescope HST* optical images are applied in the astronomical code SHAPE with the aim of clarifying the morphology and kinematic behaviour of the two bipolar outbursts in question, through the three-dimensional (3D) model of the core and the outflows of Hb4. Our focus on the outflows is motivated by the observational spectrum in which an unusual decrease of the expansion velocity is observed as a function of distance from the core. This analysis can give feedback for the origin of these outflows, and subsequently for the mass-loss mechanism during the evolution of the nebula that produced them.

We describe the observations in Section 4.2. The SHAPE modeling and the results of the morpho-kinematic models are presented in Section 4.3 and 4.4 respectively. We discuss the results in Section 4.5, and we conclude in Section 4.5.

4.2   Observations

4.2.1   High resolution imaging

The optical image used (Fig. 4.1) was obtained from the Mikulski Archive for Space Telescopes, from observations made with the Hubble Space Telescope (*HST*) on 1996 October 28 (Borkowski, 1996). The detector was the Wide Field Planetary Camera 2 (WFPC2) with

800×800 pixel^2, each 15 μm in size. The field of view was 2.5$\times$ 2.5 arcmin^2 and the image scale 0.1 arcsec pixel^{-1}. For the needs of the presented probe we used the narrow-band filter F658N (λc = 6591 Å) with an exposure time of 400 sec.

4.2.2   High-dispersion long slit spectroscopy

The observed long slit echelle spectra were obtained in 2015 March at the 2.1 m telescope in San Pedro Martir National Observatory, Mexico, with the Manchester Echelle Spectrometer (MES-SPM; Meaburn et al. 2003). This spectrometer has no cross dispersion. Hα 6563 Å and [N II] 6548, 6584 Å nebular emission lines were isolated by the 87th echelle order. Because the Hα emission line features have similar morphology to that of the [N II] 6584 Å, here we present only the latter for comparison with the data of López et al. (1997).

The Marconi E2V 42-40 camera, with 2048×2048 pixel^2, each 13 μm in size, was the detector. Two times binning was used in both the spatial and spectral dimensions which resulted in a 0.35 arcsec pixel^{-1} spatial scale. The 1076 increments gave a total projected slit length of 5.12 arcmin on the sky. The slit width used was 150 μm (10 km s^{-1} and 1.9 arcsec wide), and was oriented at Position Angle (PA) of 22° along the axis that connects two outflows, as seen in Fig. 4.1(a) (slit S4). The exposure time for each spectrum in each filter was 1800 sec. The data were analysed in the typical way using the IRAF software package. The spectra were calibrated in heliocentric radial velocity (V_{hel}) to $\pm$2.6 km s^{-1} accuracy against spectra of a thorium/argon lamp. The atmospheric seeing was varying from 1 to 1.5 arcsec during the observations.

4.3   SHAPE modeling

Most morphological information of PNe comes from imaging observations, but it can be complemented with kinematics that is obtained from the spectrum through the Position-Velocity (PV) diagrams. For the three-dimentional visualization of Hb4, we used the code SHAPE (Steffen and López 2006; Steffen et al. 2011) which has been extensively used to study the morpho-kinematic structure of planetary nebulae (e.g. Akras and Steffen 2012; Clyne et al. 2015a; Akras et al. 2016). The following method for the 3D modeling of Hb4 was presented in Section 3.2. Here, we remind that SHAPE provides a list of tools (structural or physical) that allow us to construct the 3D morphology and reproduce the kinematic structure of an extended object, in this case a PN. The synthetic output image and PV diagram generated by our model are qualitatively compared with the observational data. The modification of the model structure continues until the synthetic image and PV diagram reproduce adequately the observed images and PV diagrams, respectively.

4.4 Results

The *HST* [N II] 6584 Å image in Fig. 4.1 displays the morphology of Hb4. Fig. 4.1(a) clearly shows the central bright ring of the nebula, the fainter roughly elliptical structure that surrounds that annular core, as well as a number of filaments and low-ionization structures. The three parallel slits positions of López et al. (1997) (S1-S3) oriented in the east-west direction and that of our observations at a PA of 22° (i.e. S4) are also displayed. Fig. 4.1(b) emphasizes the collimated outflows which, in Section 4.4.3, are characterized as "knots".
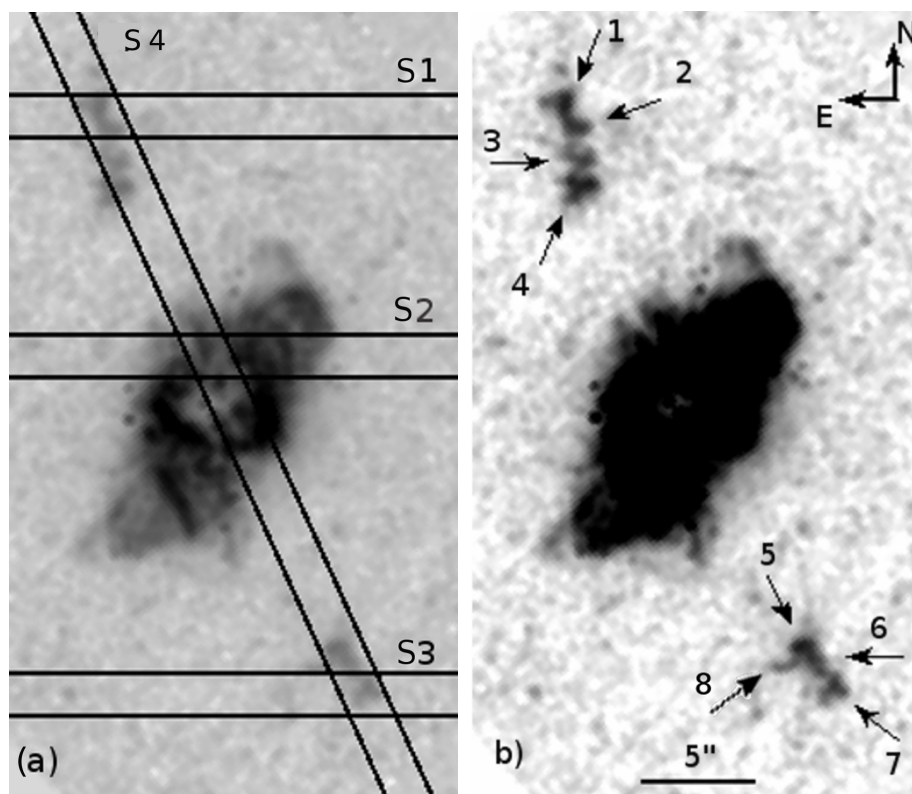
Figure 4.1: *HST* image of Hb4 in [N II] 6584 Å emission line in low and high greyscale representation (logarithmic scale). a) Emphasis is given to the central main ring and the elliptical structure around it. Also displayed are the three parallel slits of López et al. (1997), S1-S3, along with the slit position of our observations, S4. b) The image shows labelled knots on both sides of the central PN included within the slit S4, apart from knot 8 (see Section 4.5).

The elliptical structure, inside which the main core is located, consists of a major and a minor axis, with projected lengths of approximately 15 and 6 arcsec, respectively. This structure in the periphery of the main ring has a non-uniform shape, which might indicate either the interaction of strong stellar winds with the interstellar/circumstellar medium, or an explosion preceded the final ejection of the gaseous shell.

The bipolar outflows, which are the main subject of this project, are ejected on both sides

125

of the nebula, and are not perfectly aligned with respect to each other. The direction away from the central star of the northern outflows is tilted by approximately $\sim 5°$ with respect to that of the southern outflows, in agreement with López et al. (1997).

For the classification of the fast moving outflows two cases are considered: (i) jets; (ii) string of knots. In both assumptions, we consider the same model for the core of the nebula, which we present directly in the following subsection.

4.4.1 Modeling the Hb4 core

In order to represent the outflows of Hb4 using the code SHAPE, it was necessary also to reconstruct the main core of the nebula, so that the core would constitute the point reference for the distances of the knots from the central star.

The overall structure of the core was adequately modelled with a torus. Fig. 4.2(a) displays the mesh structure of the synthetic torus positioned on the *HST* image along with the observational slit position (two vertical lines of 1.9 arcsec width between them). The image scale is the same as that in Fig. 4.1(b). Two groups of knots are also displayed, which are described in Section 4.4.3, along with the symmetry axis perpendicular to the plane of the core (orange line). The slit is at a PA of 22° with respect to the North, while, as derived from our SHAPE model, the major axis of the torus is at an angle of 107° relative to the north, the angular size of the torus is 7 arcsec and its mean expansion velocity is $14 \pm 5\,\mathrm{km\,s^{-1}}$.

Fig. 4.3(a) displays the observational PV diagram of Hb4 in the [N II] 6584 Å emission line, in a low contrast that features the core's spectrum. Fig. 4.3(b) illustrates the synthetic PV diagram of the torus obtained with SHAPE, which reproduces the key structure of the observational PV. The coloured areas in the synthetic spectrum represent the northern and southern parts of the core which are redshifted and blueshifted, respectively.

Having the representation of the nebula's core, we continue with the two scenarios for the clarification of the outflows.

4.4.2 Outflows as jets

What makes Hb4 intriguing is that, according to the observational PV diagram (Fig. 4.4(b), grey-scale representation), the most distant parts of the outflows seem to move outward more slowly than the closer ones with respect to the main core of the PN. This does not agree with previous findings for PNe (e.g. Riera et al. 2002; Vaytet et al. 2009) or for jets (e.g. Corradi et al. 1999; García-Segura et al. 1999).

Nevertheless, a similar "abnormal" behaviour is reported in Devine et al. (1997) where the observed outflows are eventually described as a chain of Herbig-Haro objects of complex morphologies and radial velocities, which systematically decline with increasing distance from the core of HH34 IRS. A similar expansion law – exponentially decrease with the distance from the central star – has been reported in IRAS 18113-2503 (Orosz et al. 2018) and it is attributed to the interaction between the outflow and the circumstellar envelope decelerating the gas.

Therefore, in the case of Hb4, the first scenario of uniform jets with a linear increase of velocity with the distance from the main core fails to reproduce the observations. This result reinforces the second scenario that the outflows are likely to be separated substructures, each one of which has emerged from the core with its own velocity at different explosion events.

4.4.3   Outflows as knots

The second hypothesis for the morphology of the outflows, is to consider them as string of separated knots.

The first indication for this, was the difference between the substructures that were captured in our slit position from the observations of 2015, and those that were present in the slit positions in López et al. (1997) (see Fig. 4.1a). We noticed that the microstructures presented in our observations, were absent from López et al. (1997). This suggests that the outflows are likely not uniform structures. Depending on the slit position and orientation, different fragments are able to be detected.

The second indication, which was quite unambiguous, came from the high resolution *HST* optical image. In Fig. 4.1(b), where Hb4 is illustrated in the [N II] 6584 Å emission line, the fragmented nature of the outflows seems to be obvious. From that image -and from the echelle spectra, as explained in the following paragraph- the knots contained in slit S4 which were identified according to the available resolution, are knots 1-4 in the north-eastern outflow and knots 5-7 in the south-western outflow. Knot 8 which is also labelled on the image, is not included in slit S4, and it is explained in Section 4.5.

The third indication came from the contours in the observational PV diagrams. In Fig. 4.4(a) the PV diagram of Hb4 is illustrated in the [N II] 6584 Å emission line, along with the contour map. The contours parameters were chosen according to the counts of the knots, not of the core, which explains the difference in the contour curves we see in the plot. The formed contours on the outflows are an indirect but adequate proof that these outflows are not an undivided structure, but they consist of many individual substructures in different distances relative to the main star, and with different velocities. Again, the labelled vectors indicate the

position of each knot -included in slit S4- in the observational PV diagram.
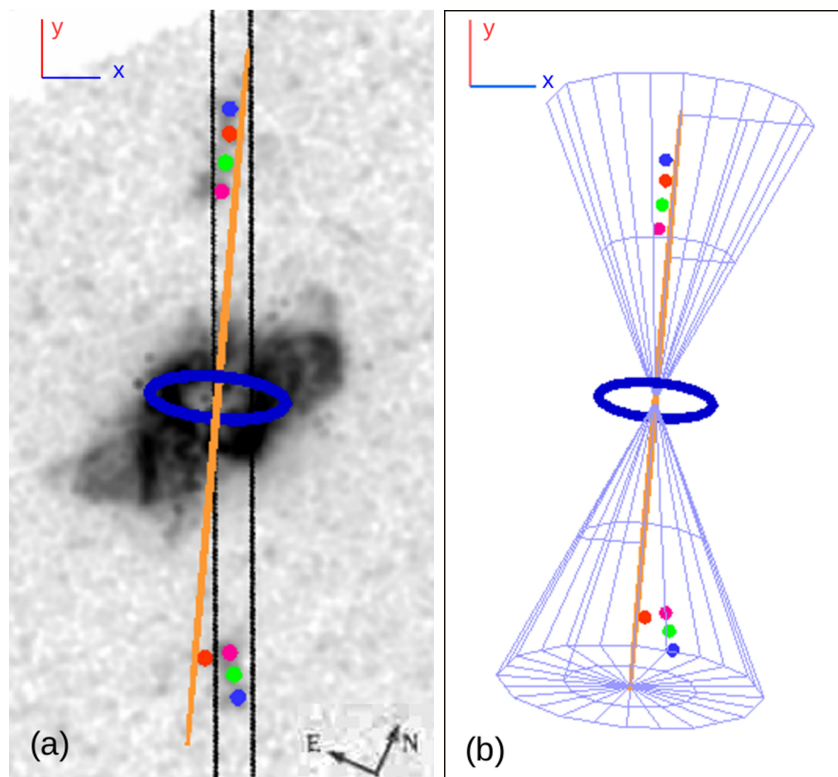
Figure 4.2: a) Superposition of *HST* [N II] 6584 Å image along with the slit position and the SHAPE model of the core, the knots for Hb4 and the symmetry axis perpendicular to the plane of the core (orange line). The scale is the same as in Fig. 4.1(b). b) The same model without the *HST* image, and with the two cones which define the region of the knots' emission from the core.

Taking into account the above indications, the scenario of a string of knots is favoured. Therefore, having as a fact that the collimated outflows in Hb4 are fast moving detached knots receding on both sides of the core of the PN, we proceeded to the representation of the knots with SHAPE as small spheres that follow a linearly decreasing velocity law towards the distance from the central star.

Fig. 4.2(a) illustrates the superposition of the *HST* [N II] 6584 Å image along with the 3D mesh of the final model of Hb4, where the outflows are considered as group of separated knots. Furthermore, it displays the axis of symmetry of the system perpendicular to the plane of the torus (orange line), as well as the model for the torus, as this was described in Section 4.4.1. All of these structures were produced with the SHAPE code. Information about the knots' position derived from the SHAPE model (distance from the nuclear center and projected angle of ejection with respect to the main axis) along with the velocities for the knots and torus, are presented in Table 4.1. In this table, the expansion velocity $V_{exp} = V_{hel} - V_{sys}$, is derived from the observational data and is the velocity with which every structure of the PN is moving
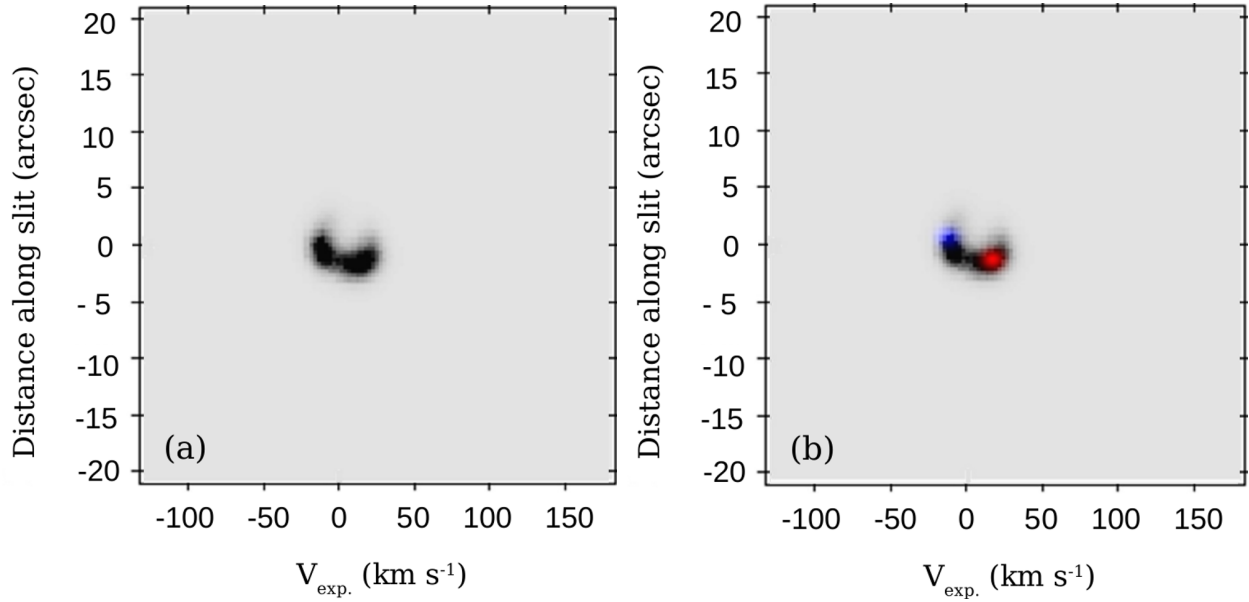
Figure 4.3: (a) Observational PV diagram of the core of Hb4 in the [N II] 6584 Å emission line (slit S4). (b) The synthetic PV diagram of the core obtained with SHAPE, overlaid on the observational diagram. The redshifted and blueshifted regions of the core indicate the radial expansion of the core of Hb4.
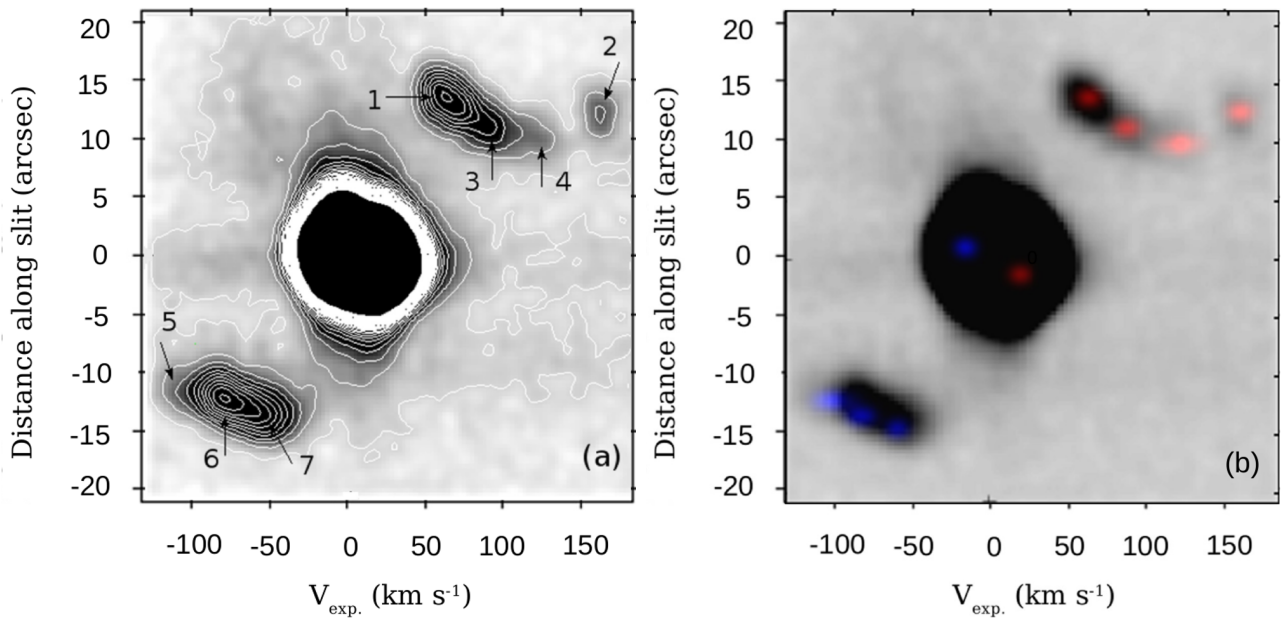
Figure 4.4: (a) Observational PV diagram in the [N II] 6584 Å emission line of Hb4 along with the contours lines and the positions of the knots included into the slit S4 (in linear scale). (b) Superposition of the observational PV diagram and the synthetic PV diagram, produced with SHAPE.
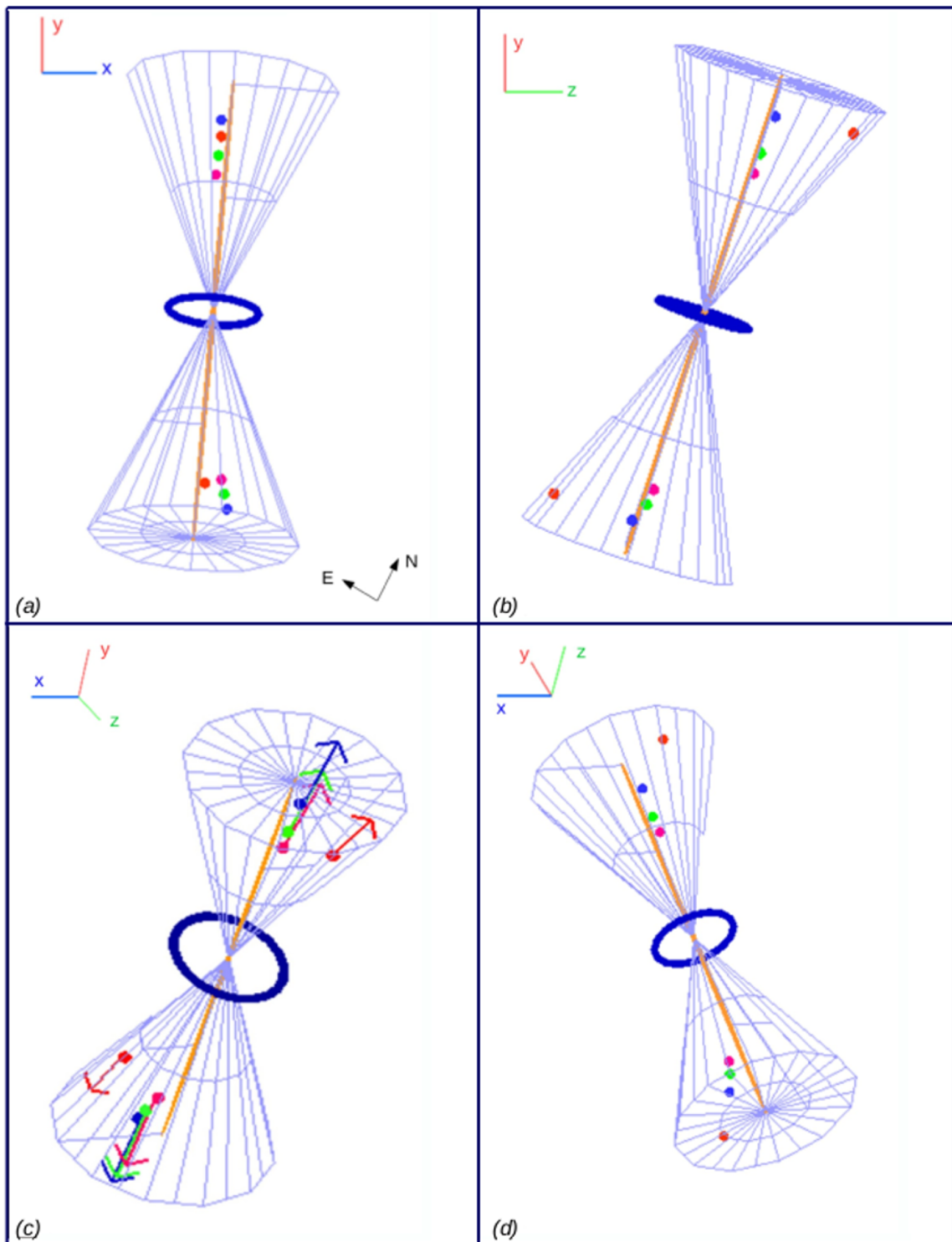
Figure 4.5: The produced SHAPE model of the core and the knots for Hb4, as it is displaced from four different angles. The orange line is the symmetry axis of the PN, perpendicular to the plane of the torus. The two cones demarcate the areas within which the knots are assumed to have been expelled from the core. In panel (c), the coloured vectors represent the direction of V_{out} for each knot.
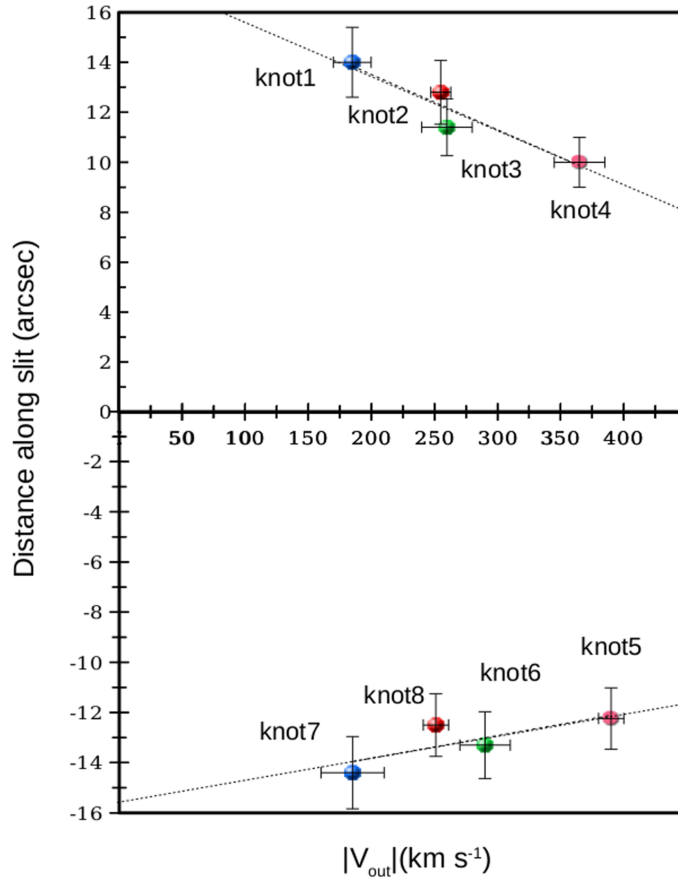
Figure 4.6: Plot of the absolute outflow velocity of each knot with respect to its distance along the slit, relative to the core of Hb4. The colours of the knots are the same as in the SHAPE model. Knots with the same color constitute a pair of knots, considered to have been expelled at the same time from the core of Hb4. The dotted lines represent the best-fitting lines obtained with the least-squares method.

relative to its center, where we consider the velocity equal to zero. The orientation of V_{exp} is along the line of sight (i.e. is pointing into the plane of the page along the z-axis; see Fig. 4.2). The velocity law in SHAPE is $V = B\frac{r}{ro}$, where r and ro are given in arcsec. B stands for the outflow velocity (V_{out}) in $km\,s^{-1}$ in Table 4.1, which is a velocity derived from the model and its direction is along the symmetry axis of the PN (see Fig. 4.5c). The projection of V_{out}, is the expansion velocity. In Fig. 4.2(b), the same SHAPE model for the whole system is displaced along with the two cones, each one of radius 7 arcsec and height 16.5 arcsec. These cones indicate the region within which the emission of the knots is assumed to have taken place.

For a better understanding of the knots' position in 3D space, four images are presented in Fig. 4.5, where our model is viewed from four different angles. In Fig. 4.5(a), Fig. 4.5(b) is displaced again for comparison reasons, and the z-axis points into the plane of the page. Fig. 4.5(b) is like seeing Fig. 4.5(a) from the right. Fig. 4.5(c) and 4.5(d) present our model in free-form angles. The knots with the same color are assumed to consist pairs of emitted knots,
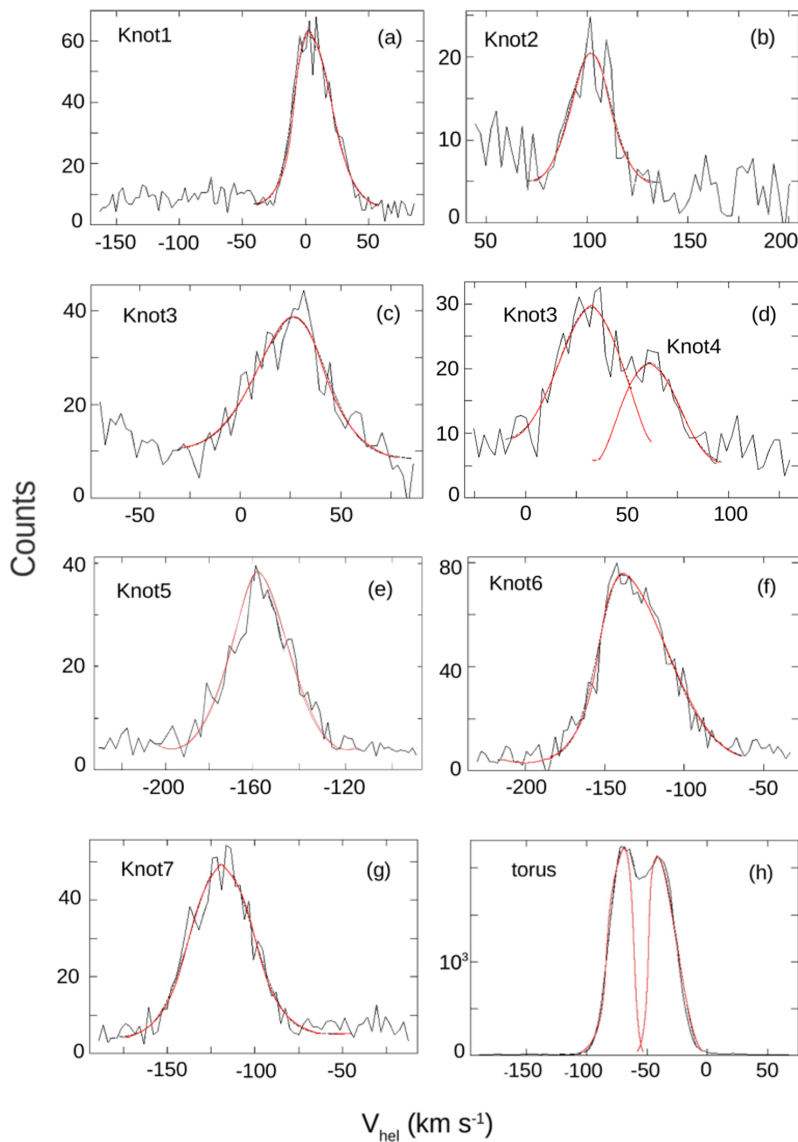
Figure 4.7: [N II] 6584 Å emission-line profiles of the knots identified in slit S4, along with the profile for the torus of the nebula. In panel (d) both knots 3 and 4 are presented as it is difficult to separate them because they are very close to each other.

as it is discussed in Section 4.5.

The synthetic PV diagram that corresponds to this final model is shown in Fig. 4.4(b) in colour scale, along with the observational PV in grayscale. Indeed, this model gives a synthetic PV which is in very good agreement with the observational diagram, as in the locations where there is a knot according to the contour map, there is also a knot in the produced PV diagram, too. This result clearly verifies the assumption for the "knots" model, this time from a spectrum-analysis perspective.

Component	Distance (arcsec)	Angle (degrees)	V_{hel} ($\mathrm{km\,sec^{-1}}$)	V_{exp} ($\mathrm{km\,sec^{-1}}$)	V_{out} ($\mathrm{km\,sec^{-1}}$)	Kinematic age (years)
torus			$-72, -44$	$-13, 15$	15 ± 2	3190 ± 1090
knot 1	14.87 ± 1.48	4.8	2.4	61	185 ± 15	1100 ± 390
knot 2	16.55 ± 1.66	2.3	101	160	255 ± 8	887 ± 305
knot 3	12.08 ± 1.21	3.0	26.4	85	260 ± 20	635 ± 224
knot 4	10.61 ± 1.06	4.0	62	121	365 ± 20	397 ± 140
knot 5	12.42 ± 1.24	8.0	-160	-101	-390 ± 10	434 ± 150
knot 6	13.88 ± 1.40	8.3	-140	-81	-290 ± 20	660 ± 232
knot 7	15.24 ± 1.52	7.5	-117	-58	-185 ± 25	1125 ± 417
knot 8	16.38 ± 1.64	2.0	-219	-160	-251 ± 10	890 ± 309

Table 4.1: Velocities and Kinematic ages of the torus and the different knots. The distance of each knot from the nebular center is also presented, as long as the projected angle of ejection of each knot with respect to the main axis, as derived from the SHAPE model. The systemic velocity is V_{sys} = -59 $\mathrm{km\,s^{-1}}$.

4.5 Discussion

In this work, we studied the morpho-kinematic structure of the PN Hb4 using new echelle spectroscopic data, high resolution *HST* images and the SHAPE code. Hb4 displays a complex, multi-polar inner structure with a pair of seemingly collimated outflows. A bright fragmented ring-like structure is apparent together with an ellipsoidal component in the direction north-west south-east (Fig. 4.1a).

In addition, a number of small scale features (knots) and filaments are also identified. We believe that they exhibit a low-ionization spectrum similar to LISs (Gonçalves et al. 2001; Akras and Gonçalves 2016). Similar types of fragmented equatorial rings and equatorial LISs have also been found in several other PNe, such as the Eskimo nebula (García-Díaz et al. 2012) and the Necklace nebula (Corradi et al. 2011). It has been proposed that the photo-ionization front at the later evolutionary stage of PNe is responsible for the fragmentation of the shells (García-Segura et al. 2006) as well as an interaction between a jet/collimated outflow with the circumstellar envelope (Akashi et al. 2015).

Using the morpho-kinematic code SHAPE, we managed to reproduce the central ring-like structure and its PV diagram assuming a toroidal component whose major axis is at an angle of 107 ° with respect to the north. We found that the torus expands with an absolute mean velocity of $14 \pm 5 \,\mathrm{km\,s^{-1}}$, comparable with the velocities found in toroidal structures in PNe

with a WR-type nucleus (between 15 and 30 $km\,sec^{-1}$); Akras and López 2012; Akras et al. 2015; Gómez et al. 2018) and in agreement within the errors to the velocity given by López et al. (1997). Taking into account its angular size derived from our SHAPE model of 7 arcsec and adopting the distance of 2.88 ±0.86 kpc, we found a kinematic age of 3190±1090 years for the torus (see Table 4.1).

Regarding the bipolar outflows, a decline in radial outflow velocity as a function of the distance from the nucleus was found, as can be seen in Fig. 4.6. This velocity law is uncommon in PNe given that most of jets or outflows show a linear increase of velocity with distance (e.g. Riera et al. 2002; Vaytet et al. 2009; Corradi et al. 1999; García-Segura et al. 1999). Nevertheless, behaviour related to a decline in velocity has been reported in HH34 (Devine et al. 1997) and IRAS 18113-2503 (Orosz et al. 2018) which is attributed to interaction of the outflows with the interstellar/circumstellar medium. This encouraged us to explore these bipolar outflows as a string of discrete knots rather than a jet. Making use of the *HST* [N II] 6584 Å image and the echelle PV diagram, four knots in the northern outflow and three knots in the southern were identified. The resolution of our data might prevented the identification of more knots in the outflows, while the current picture of knotty outflows is different from the scenario of two elongated knots presented by López et al. (1997).

The knots are moving outward with a range of expansion velocities along the line of sight from -101 $km\,s^{-1}$ to 160 $km\,s^{-1}$, and a range of outflow velocities from -390 $km\,s^{-1}$ to 365 $km\,s^{-1}$. The significant decline of outflow velocity with respect to the distance from the central star is also in conflict with the bow shock model presented by López et al. (1997). Knot 2 is moving outward with an expansion velocity of 160 $km\,s^{-1}$, considerably higher than the remaining three knots in the northern and southern outflows and, according to the model, at an ejection angle from the main axis also higher than those of the rest knots, as illustrated in Figs. 4.5(b), 4.5(c) and 4.5(d). This could be because of its ejection from the nebula during the rotation of the PN, as explained below. However, as it is shown in Fig. 4.6, the outflow velocity of knot 2 is consistent with the radial decline outflow velocity law, which indicates that it is likely travelling inside the same ISM as the rest of the knots and experiences the same deceleration. For the ambient ISM, a gradient in its composition (e.g. density gradient) is assumed which accounts for the slowing down of the knots from the moment of their ejection.

The kinematical age of each knot in both outflows was estimated for D = 2.88±0.86 kpc. From the results which are assembled in Table 4.1, two significant conclusions can be drawn. The first is that the knots in the pairs 1-7, 3-6, and 4-5 have the same kinematical age, which implies that the knots in each pair were expelled at the same time. Knot 2, which as mentioned above, presents a displacement relative to the positions of the rest of the knots, had no equivalent

component in the southern region included in slit S4 that could be considered its companion knot during the explosion from the core. So, we selected from the *HST* image a knot (knot 8). Because this knot was not included in slit S4, we could not have kinematical information about it. Thus, we assumed that knot 8 has the same V_{exp} and the same displacement parameter z as knot 2. Subsequently, the other two spatial parameters (x and y) of knot 8 were measured on the *HST* image and used in SHAPE. Using these assumptions and information we calculated its kinematical age. Indeed, its age was found to be very close to the age of knot 2, which allowed us to consider that knots 2 and 8 are a fourth pair of knots in Hb4. The second interesting comment regards a periodicity in the explosion events that the pairs of knots appear to have; according to the calculated kinematical ages, each pair of knots was expelled every $200 - 250$ years from the core of the PN. Given that the deceleration of the knots is present, the periodicity in the ejections could not have been perceptible if the composition of the ISM was irregularly inhomogeneous. Thus, the gradient in its composition mentioned above is supported which causes the deceleration of the knots, but also preserves the time interval between the motion of the knots (i.e. they undergo a similar deceleration). However, it should be taken into consideration that, the absolute values of the kinematical ages could be lower if there was no deceleration of the knots.

Fig. 4.7 shows the profiles of the seven knots found in slit S4 along with the profile of the torus of the PN. It should be noted that there is a possibility that some of the knots might consist of more than one subknots which cannot be clearly identified due to the spectroscopic resolution. A representative example of nearby knots presented in the same profile is that of knots 3 and 4, as shown in Fig. 4.7(d). A second common feature in these profiles is the different background, which is a clue for the inhomogeneity of the ISM that each knot encountered while travelling outwards the main core. This results in the various expansion velocities of the knots as presented in Table 4.1. In the torus profile, the two peaks correspond to the northern and southern part of the torus which is included in slit S4, as shown in Fig. 4.2(a). The heliocentric velocities of these parts are $-72 \ \mathrm{km\,sec^{-1}}$ and $-44 \ \mathrm{km\,sec^{-1}}$ respectively, while their expansion velocities are $-13 \ \mathrm{km\,sec^{-1}}$ and $15 \ \mathrm{km\,sec^{-1}}$, respectively (see Table 4.1). This difference in the velocities is justified due to the inclination of the torus relative to the line of sight. Thus, the absolute mean expansion velocity of the torus has been calculated at $14 \ \mathrm{km\,s^{-1}}$ along the line of sight.

The strong [N II] 6584 Å emission detected in these knots compared to the value of the central parts implies some shock interaction with the circumstellar envelope (e.g. Raga et al. 2008; Akras and Gonçalves 2016; Akras et al. 2016; Akashi et al. 2015). By examining the high resolution *HST* [N II] 6584 Å image of Hb4, a misalignment of ~ 5 degrees between the northern

and southern string of knots is found. One possible interpretation for this, could be the ejection from a compact disk around a star in a binary that received a "push" by the wind from the other (p)AGB star (Huarte-Espinosa et al., 2013), which eventually caused this misalignment in the emission of the knots. Another probable scenario could be a rotation mechanism present in its central stars. Very recently, García-Segura et al. (2014, 2016) have shown that surface rotational velocity could in principle produce considerable asymmetries in these stars. Hence, we suggest that each pair of knots was expelled from the core during the same outburst and, due to the above mentioned possible mechanisms, a few degrees of misalignment was created. Taking into account the periodicity in the emission of knots, the scenario of the rotating core is considered as most probable. This leads us to the suggestion that Hb4 is the case of a rotating central star which emits knots in an almost regular rate. Same mechanisms have been proposed to explain the knotty curved jets detected in NGC 6778 (Guerrero and Miranda 2012) or Fleming 1 (Boffin et al. 2012). Lopez et al. (1993) have shown that the north and south strings of ionized knots in Fleming 1 PN could be generated by globules of gas ejected from a bipolar, rotating source within the core of Fleming 1. The BRETs scenario (Lopez et al. 1995) provides plausible explanation for the formation of the knots in Hb4. All the above cases reinforce the hypothesis of a binary central system for this PN. However, we cannot yet rule out the possibility that the knots had been shed symmetrically in the beginning, but the different ISM they encountered altered their velocity and inclination with respect to the initial emission axis. Further kinematical observations and theoretical modeling are needed.

Besides the bipolar knots, the presence of the fragmented torus and the equatorial LISs might indicate a PN formed via the common-envelope channel (Miszalski et al. 2009; Jones et al. 2014; García-Segura et al. 2018). The fragmentation of the equatorial disk or torus into knots and filaments has been revealed from high-resolution H_2 images of the bipolar PN NGC 2346 with a binary central system (Manchado et al. 2015). Akras et al. (2017) have also confirmed the presence of H_2 gas in LISs embedded in NGC 7662 but there is no direct confirmation of a binary nucleus.

The classification of Hb4's central star as a hydrogen deficient WR-type[2] (Acker and Neiner 2003; Górny et al. 2004) makes it uncommon since there are only two more known post-common envelope binary systems in PNe with WR companion. The dual-dust chemistry reported for Hb4 (Perea-Calderón et al. 2009) is also one of expected outcomes for a binary nucleus with WR component. Hb4 also belongs to the group of PNe with high ADF(O^{+2}) (3.7; García-Rojas et al. 2013) which may also be related with the presence of a binary central sys-

---

[2]WR-type stars are also denoted as [WR]. Although they show the same emission lines as typical Wolf-Rayet stars do, they are not WR stars, but they are closely related to white dwarfs.

tem. Soker and Livio (1994) discuss the presence of an accretion disk in PNe with binary central systems as one possible mechanism for the formation of highly collimated outflows/jets. Jet interaction with circumstellar envelope can also lead to the formation of an equatorial torus as in Hb4 (Soker and Rappaport 2000; Akashi et al. 2015). Akashi and Soker (2008) confirmed that jets can be responsible of equatorial ring, but with a mass significantly less than the total mass of the nebula; otherwise an additional mechanism is necessary for the formation of the torus (e.g. common-envelope interaction). An interesting point is the finding that the jets appear to be younger than the torus in the hydrodynamic models despite they are formed by the same event (Akashi and Soker 2008). Indeed, the torus in Hb4 is found to be older than the knots (Table 4.1). For known post-common-envelope PNe with binary nuclei, the toroidal component is younger than the jets (e.g. Ethos 1, Miszalski et al. 2011). But, there are two more PNe (NGC 6337, NGC 6778; Tocknell et al. 2014) in which the torus seems to have been formed before the jets. The delay between the equatorial torus and jets in Hb4 is of the order of 2000 years, comparable with the delay measured in NGC 6778.

The multi-polarity of Hb4 is also a very interesting finding as well as the various features that can be clearly seen in Fig. 4.1. Rabaça et al. (2003) reported a faint secondary bipolar structure, close to the central part, aligned with the minor axis. Apart from that, Hb4 also displays two more bow-shaped filamentary structures in the north-west and south-east directions, formed probably from a different episodic event than those of the pair of knots. No kinematical information are available for these structures, so it is not possible to estimate the time they were formed. Other PNe like Hb4 with multi-polar inner structures and knotty outflows have also been found (i.e. Palmer et al. 1996; Harman et al. 2004). All these structures, their inclinations and morphologies imply that there have been a number of ejections during the lifetime of this PN.

However, further observations are needed (both high-resolution images and echelle spectra) in order to measure proper motions, velocities and the dynamical ages of these features and confirm how many different sequential ejections happened. This would provide valuable information about the formation and evolution of this PN with a possible binary nucleus.

4.6 Conclusion

In this project, we presented a morpho-kinematical interpretation of the structure of the PN Hb4. We conclude the following:

(i) The two bipolar outflows of Hb4 were classified as string of knots and characterized by the decline in their outflow velocity relative to their distance from the central star of the

nebula. This deceleration is probably a result of the interaction of the knots with either an interstellar medium, which presents a gradient in its composition, or nebular material in the vicinity of the nebula.

(ii) In the northern and southern outflows, four and three knots respectively were identified, each of which travels outwards from the nebula with its own expansion velocity, covering a range from -101 $\mathrm{km\,s^{-1}}$ up to 160 $\mathrm{km\,s^{-1}}$. The knots seem to have been expelled from the core in pairs, following a periodicity in the explosion events of $200 - 250$ years.

(iii) By the use of the code SHAPE, the central part of the PN was modelled as a torus, and was found to have an absolute mean expansion velocity of 14 $\mathrm{km\,s^{-1}}$, and an outflow velocity of 15 ± 2 $\mathrm{km\,s^{-1}}$. The low-ionization structures exhibited by the central part of the nebula, indicate a common-envelope PN evolution.

(iv) We proposed that the central part of the nebula consists of a binary system that has a WR companion evolved through the common-envelope channel.

Chapter 5

5   SNR VRO 42.05.01

The scientific results of the VRO project which are presented below, were published in the scientific journal Monthly Notices of the Royal Astronomical Society (MNRAS), Volume 499, Issue 4, pp. 5410-5415 (Derlopa et al. 2020).

5.1   Introduction

Massive stars (M $\geq$ 8 $M_\odot$) and carbon oxygen white dwarfs members of interacting binaries (i.e. Filippenko 1997) may undergo an explosively violent death (supernova explosion, SN). The SN ejecta expand and sweep up the ambient medium. The resulting structure is progressively transformed into a beautiful gaseous nebula which is called supernova remnant (SNR). SNRs chemically enrich the host galaxy, they influence its dynamics, while the shock waves generated after the explosion are efficient cosmic ray accelerators. Moreover, the large-scale of asymmetries and complex structures that SNRs usually display, reveal inhomogeneities present in the ambient medium where they evolve in, and provide clues about the progenitor star, since SNRs interact with the material expelled during the progenitor's evolution (McKee 1988; Chiotellis et al. 2012). The importance and utility of probing SNRs relies on providing answers for the above crucial astrophysical topics.

Valuable information about the physical processes that dominate in SNRs are gained through imaging and spectroscopic data. Nevertheless, regardless of the details that state-of-the-art astronomical instruments can depict, the fact that these data are two dimensional (2D) restricts the range of our knowledge for these objects, due to the absence of the information in the third

dimension along the light of sight. Consequently, the benefits from a three dimensional (3D) study of a SNR aim at a deeper interpretation of the collected observational data.

Up to date, two are the main tools for gaining information on the missing third dimension of SNRs: (a) the 3D (magneto) hydrodynamic (MHD) models (Toledo-Roy et al. 2014; Bolte et al. 2015; Abellán et al. 2017; Potter et al. 2014; Orlando et al. 2019), which reproduce the 3D physical properties by comparing the 2D projection of the models with the observational data, and (b) the 3D velocity-maps (DeLaney et al. 2010; Alarie et al. 2014; Milisavljevic and Fesen 2013; Williams et al. 2017) which are created by the proper motion and Doppler shifted velocities of different parts of the remnant.

In this project we take a third approach, the so-called "Morpho-Kinematic modeling" which, up to now, it has been applied successfully in Planetary Nebulae (Akras and López 2012; Akras and Steffen 2012; Clyne et al. 2015b; Akras et al. 2016; Fang et al. 2018; Derlopa et al. 2019; Gómez-Gordillo et al. 2020), but never in SNRs. This method reconstructs the 3D morphology of the object by using imaging and high-resolution spectroscopic data. The lack of such a 3D model in the field of SNRs was our motivation to proceed in the creation of the first 3D Morpho-Kinematical (MK) model of a SNR. For our 3D MK model the astrophysical software SHAPE was employed (Steffen and Koning, 2017), while as a case study we used the Galactic SNR VRO 42.05.01 (hereafter VRO) for which no 3D model has been constructed before.

The VRO properties are presented in Section 5.2. The observations are described in Section 5.3. The 3D MK modeling and its results are presented in Section 5.4 and 5.5, respectively. In Section 5.6 we discuss the interpretation of our results and we end with our conclusions in Section 5.7.

5.2   SNR VRO 42.05.01 – Properties

VRO 42.05.01 (also known by its Galactic coordinates as G 166.0+4.3; α_{2000}: $05^h26^m30^s$, δ_{2000}: $+42°56'00''$) is an extended Galactic SNR (55 arcmin × 35 arcmin; Green 2019), already well-studied in radio, optical, X-rays and γ-rays wavebands. It has been a subject of investigation for many decades now, especially due to its peculiar shape, as it will be explained below. It falls into the category of Mixed-morphology SNRs (Rho and Petre 1998, and also see Section 1.7) as it presents a shell-like, non-thermal emission in the radio waveband and a thermal, centrally-peaked one in the X-rays (Fig. 5.1).

Sharpless (1959), using the imprints of optical nebulae at the Palomar Sky Survey, initially classified VRO as an H II region. Subsequently, optical observations unveiled the filamentary structures of the source (van den Bergh 1960, van den Bergh et al. 1973) and helped emission line
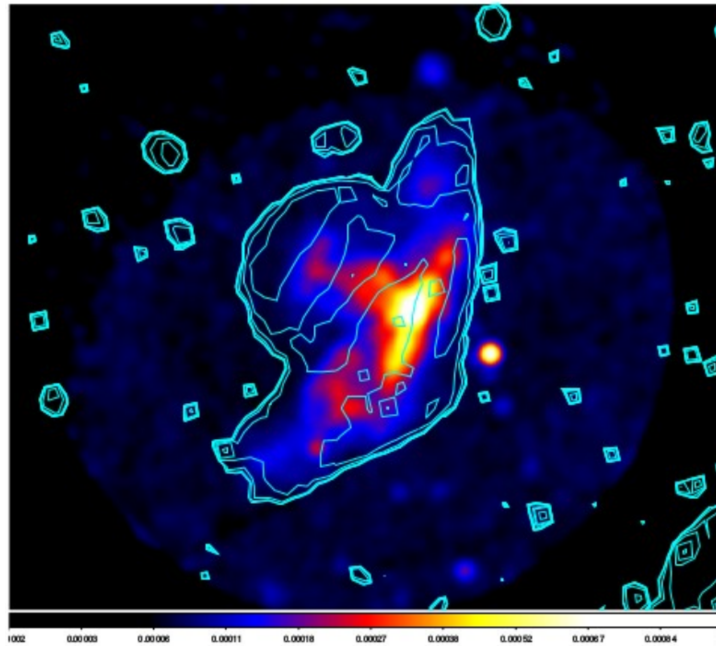
Figure 5.1: VRO 42.05.01 in radio and X-ray bands. The cyan contours correspond to CGPS radio observations at 1420 MHz. The X-ray mosaic is constructed from archival ROSAT PSPC observations in the 0.1 - 0.4 KeV band. We can see the central-peaked X-ray region, surrounded by a radio-shell structure, which is characteristic of Mixed-morphology SNRs. Image credits Arias et al. (2019b).

ratios to be measured (D'Odorico and Sabbadin 1977). Dickel et al. (1965) reported the detection of an extended radio source centered at the coordinates of VRO. Although this radio source had also been reported in 1962 by Hogg, it had not been previously catalogued. Therefore, it was given the name VRO (due to the Vermilion River Observatory where this radio detection occurred) and the number 42.05.01. By this way, this SNR was eventually named as VRO 42.05.01.

All the above observational data in conjunction with a non-thermal spectrum of spectral index = 0.4 (Haslam 1971), established VRO as a SNR.

Further proof reinforcing the SNR origin came from Lozinskaia (1979) (study in the optical) who revealed the presence of high-velocity gas ($\sim$140 $\mathrm{km\,sec^{-1}}$) corresponding to a shock-wave velocity of $\sim$200 $\mathrm{km\,sec^{-1}}$ and implying that the remnant is in its adiabatic phase with an age of 6×10^4 years.

Regarding other wavelengths, VRO has also been studied in the X-rays from Burrows and Guo (1994) and Guo and Burrows (1997), using ROSAT and ASCA observations respectively. The ROSAT image (at 0.5-2.0 keV) brought to light an X-ray shape similar to the radio morphology of VRO. What differs though is that the X-ray remnant is more centrally-peaked than the radio one. The derived X-ray spectrum (either from ROSAT or ASCA) is consistent with a ther-

mal remnant having an X-ray temperature of $\sim 8.5 \times 10^6$ K. The measured absorbing column density varies across the remnant and has values of a few times $\times 10^{21} cm^{-2}$. The authors note that taking into consideration the distance of the remnant which is $4.5 - 5$ kpc (Landecker et al. 1982, 1989), the column density appears to be rather low which implies a low mean density along the line of sight. Additional X-ray observations have been performed by Bocchino et al. (2009) with XXM-Newton and Matsumura et al. (2017) with Suzaku. The assumption that the central-peaked X-rays source is non-thermal is reinforced by the studies of Biggs and Lyne (1996) and Lorimer et al. (1998) who found no pulsar at the center of VRO.

VRO has also been studied in γ-rays by Araya (2013), who detected a GeV emission, attributed to leptonic origin. On the other hand, with respect to the HI observations, the surveys conducted by Braun and Strom (1986) and Landecker et al. (1989) aimed at investigating how neutral gas is associated with the remnant and distributed in its vicinity. It has been found that there is an intimate connection of HI with the radio/optical morphology. For example, many structures appear to coincide, post-shock HI has been identified while a prominent hole appears in the HI map where the hot, low-density cavity is. Furthermore, Landecker et al. (1989) estimated the systemic velocity of VRO at V_{sys} = -34$\pm$5 km s^{-1}, while its location was constrained at the Perseus spiral arm at a distance of 4.5$\pm$1.5 Kpc. With respect to its distance, new studies provide a much lower value of 1.0$\pm$0.4 Kpc (Arias et al. 2019a).

Regarding the conducted surveys in the optical band, the photographic plates of the Palomar Observatory Sky Survey (POSS) were the first to shed optical light to the whole remnant (Hα+[N II] 6548, 6584 Å, [S II] 6716, 6731 Å, [O III] 5007 Å images; van den Bergh et al. 1973; Parker et al. 1979). Since then only a handful of studies has been conducted, focusing rather on specific regions of the remnant, either photometrically (deep [O III] 5007 Å images; Fesen et al. 1983, Hα+[N II] 6548, 6584 Å, [S II] 6716, 6731 Å images; Pineault et al. 1985) or spectroscopically (Esipov et al. 1972, D'Odorico and Sabbadin 1977, Fesen et al. 1985).

After 30 years of inaction in the optical waveband, Boumis (2019) presented the most completed study of VRO that has been performed up to date, in imaging and spectroscopy. In particular, the continuum-subtracted, deep Hα+[N II] 6548, 6584 Å, [O III] 5007 Å and [S II] 6716, 6731 Å wide field images that were obtained depict the total area of VRO, while the Hα+[N II] 6548, 6584 Å and [O III] high resolution images which were also obtained for selected regions of the remnant, revealed the fine structures of the optical filaments. With respect to the spectroscopic data, the high resolution echelle spectra aimed at revealing the kinematics of VRO, while through the low resolution spectra and the extracted characteristic line ratios, the physical properties of the remnant (e.g. electron density) can be constrained. The new obtained observational data from Boumis (2019) were used in this Thesis in order to reconstruct the 3D

MK model of VRO with SHAPE software (see Section 5.3).

VRO was chosen for the 3D MK model due to its intriguing morphology which basically consists of two main parts: i) a hemisphere at the northeastern region called the "shell" and ii) a larger, bow-shaped shell at the southwestern region, called the "wing" (Landecker et al., 1982) (see Fig. 5.2). Due to its complex morphology, it has drawn the attention of the scientific community attempting to explain its overall shape. According to Pineault et al. (1987), the initial explosion of the VRO occurred in a region characterized by a density discontinuity. The part of the remnant that evolved into the denser region created the "shell" component, while the rest diffused into a hotter and tenuous medium and shaped the "wing" component. However, according to the recent results presented by Arias et al. (2019a), there is no physical proof of an interaction of the remnant with the surrounding molecular clouds and they attributed the almost triangular shape of the "wing" to a Mach cone cavity which was created by a supersonically moving progenitor star and was filled out by the SN ejecta. Finally, Chiotellis et al. (2019) modelled the observed morphology of VRO with 2D Hydrodynamic simulations, suggesting that the remnant is currently interacting with the density wall of a wind bubble sculptured by the equatorial confined mass outflows of a supersonically moving progenitor star.

The interpretation of the remnant's morphology still remains an open issue. Our aim is, using the physical results presented below that deduced from the 3D MK model, to contribute to the clarification of unanswered questions with respect to this intriguingly complicated SNR.

5.3   Observations

The observational data necessary for the implementation of the 3D MK model, are imaging and spectroscopic. Wide field imaging provide the overall morphology of the SNR, while high-resolution images reveal in detail the filamentary structures of specific regions of the remnant. On the other hand, through the high-resolution echelle spectra analysis we obtain the kinematic information for the part of the nebula for which we obtained spectrum. Wide-field images and echelle spectra are used as background images in the software SHAPE which was employed for the model, as analytically was discussed in Section 3.3. Below we present the information with respect to the imaging and spectroscopic data.

5.3.1   Wide Field imaging

The 0.3m telescope at Skinakas Observatory (Crete, Greece) was used in order to cover the whole area of the SNR VRO 42.05.01 (55×35 arcmin^2). The telescope is of Schmidt-Cassegrain

type, with focal ratio f/3.2. The observations were performed in 2000 and 2001. The used camera was a 1024×1024 pixel^2 Thomson CCD, with pixel size 19μm, image scale 4 arcsec pixel^{-1} and FOV 70×70 arcmin^2. The images were taken in the narrow band filters Hα+[N II] 6548, 6584 Å, [O III] 5007 Å and [S II] 6716, 6731 Å (Fig. 5.2), with exposure time E.T. = 2400 sec in each filter. Corresponding continuum images were also obtained with E.T.= 180 sec each, and were subtracted from those containing the emission lines to eliminate the confusing star field (Boumis et al. 2012, 2016).

For the needs of the presented 3D model, the Hα+[N II] image was used due to the high brightness of the remnant in this emission line in its total area (see Fig. 5.2a).

5.3.2 High-resolution imaging

High resolution images were taken with the 2.3m "Aristarchos" telescope (Ritchey-Chretien type, f/8 final focal ratio) in Helmos Observatory (Greece), between 2011 and 2019. For the needs of the project, two cameras were used: i) the 1024×1024 pixel^2 LNCCD camera, with pixel size 24 μm, image scale 0.28 arcsec and FOV 4.8×4.8 arcmin^2, and ii) the 2048×2048 pixel^2 LN2CCD camera, with pixel size 13.5 μm, image scale 0.16 arcsec, FOV 5.5×5.5 arcmin^2, and binning 2×2. The images were taken in the narrow band filters Hα+[N II] 6548, 6584 Å, [O III] 5007 Å and [S II] 6716, 6731 Å, with exposure time E.T. = 1800 sec in each filter.

Furthermore, broad band filters of continuum red and blue were used for the background stellar subtraction in the images Hα+[N II] 6548, 6584 Å and [O III] 5007 Å respectively. The used continuum red has a maximum efficiency of λ = 6680 Å and range $\Delta\lambda$ = 100 Å, while the maximum efficiency of continuum blue is at λ = 5700 Å with a range of $\Delta\lambda$ = 70 Å. Further information about the filters characteristic can be found in Helmos Obs. web-page: http://helmos.astro.noa.gr/. Finally, bias and flat images (in each filter) were also obtained, necessary for the data analysis.

The usage of high-resolution images was to imprint in detail the great filamentary structures scattered all over the area of VRO, in order to include them in its 3D representation. Both, the wide field Hα+[N II] 6548, 6584 Å image overlaid with the high-resolution images are shown in Fig. 5.3 (Boumis et al. 2021 in prep.).

5.3.3 Field of View images with the MES–SPM

MES–SPM has an additional operational mode of taking Field Of View (FOV) images overlaid with the slit position (Fig. 5.4a). We were taking a FOV - slit image right before and after each exposure (in the beginning before the spectra data, and in the end after the spectra and arc
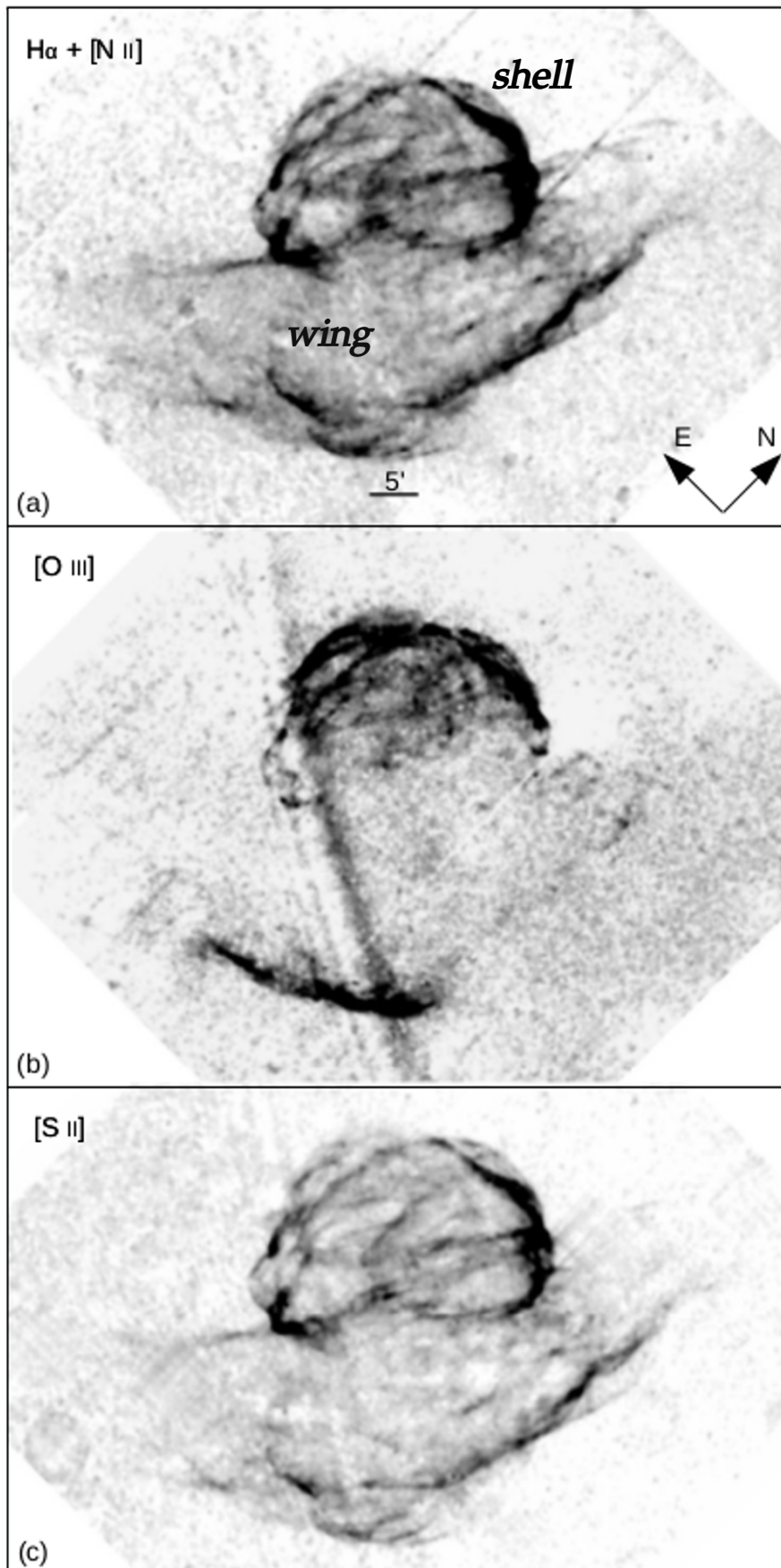
Figure 5.2: Wide field images of the SNR VRO 42.05.01 obtained at Skinakas Observatory (Crete, Greece) in filters Hα+[N II] 6548, 6584 Å, [O III] 5007 Å and [S II] 6716, 6731 Å. In image (a), the two basic components of VRO are also labelled, the "shell" and the "wing".
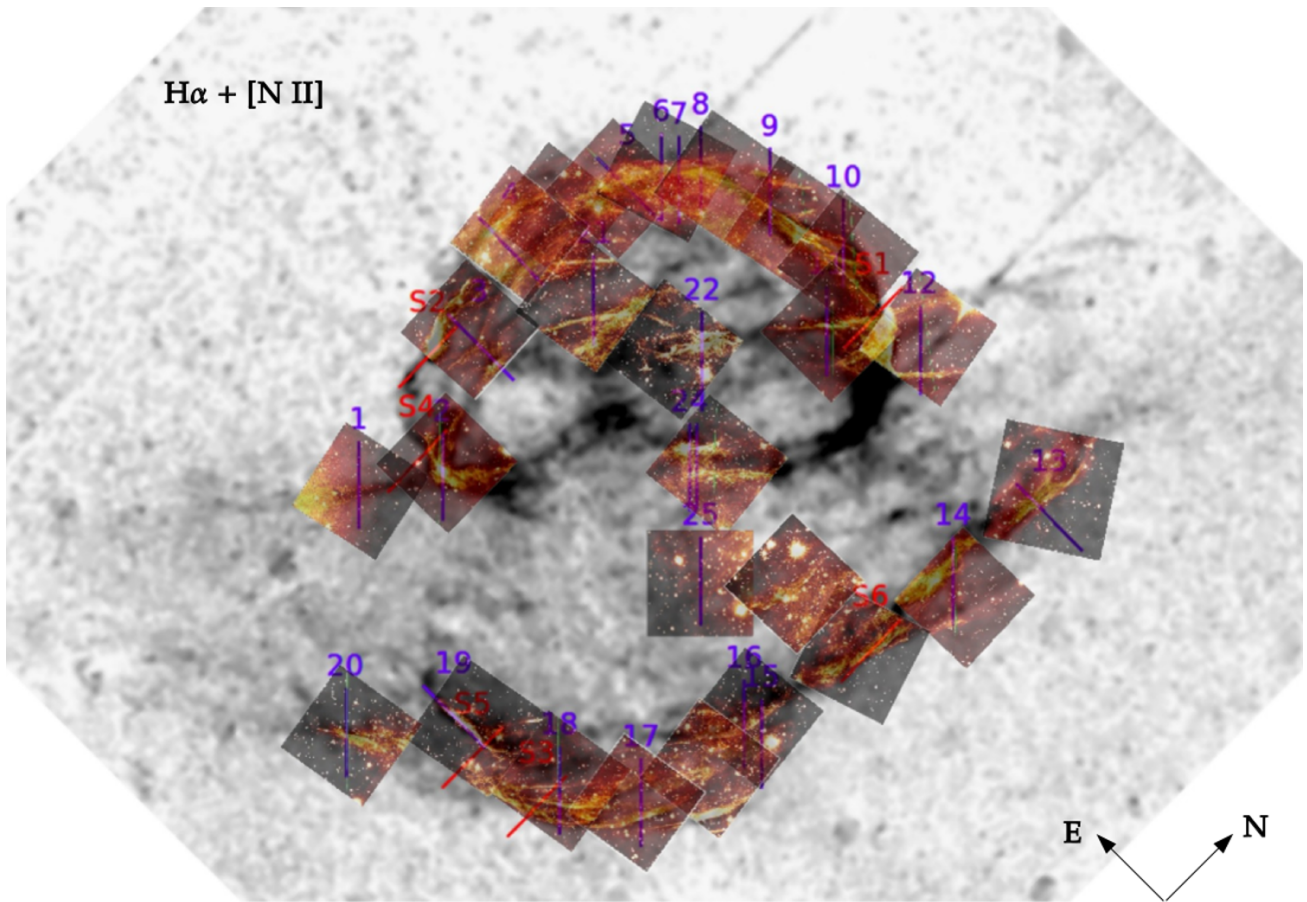
Figure 5.3: Wide field image of VRO 42.05.01 in Hα+[N II] 6548, 6584 Å from Skinakas telescope (Crete, Greece), along with the high-resolution images obtained with "Aristarchos" telescope (Helmos, Greece) (Boumis et al. 2021 in prep.).

data), in order to check any potential movements of the slit position. The exposure times were $80 - 240$ sec.

These images are very important in order to verify that we have put the slit in the correct region of the nebula where we want to obtain its spectrum. Furthermore, apart from the nebula, we seek to have some stars captured in the slit too, because their vertical emission lines in the obtained spectrum help us to specify the exact position of each part of the nebula along the slit. The bright star in Fig. 5.4 is a representative example. The stars should not be too faint, otherwise their emission lines will be faint too in the spectra and won't help us at all. Nor should they be too bright, because then there would be the danger of their brightness to "obscure" part of the nebula's spectrum we want to probe.

5.3.4   High-dispersion long-slit spectroscopy

High-resolution long-slit echelle spectra were obtained in Hα+[N II] 6548, 6584 Å, [O III] 5007 Å and [S II] 6716, 6731 Å between the years 2010 and 2019 (Boumis et al. 2021 in
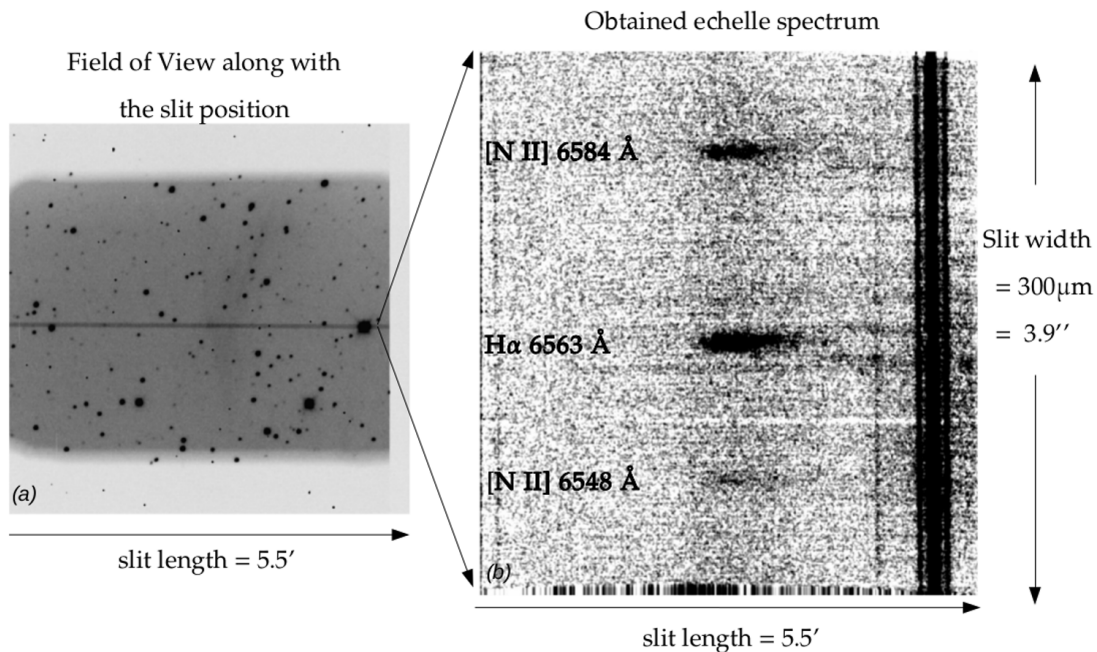
Figure 5.4: a) The FOV of a specific region of the SNR VRO 42.05.01, along with the slit position (horizontal line in the middle of the image). The slit has a length of 5.5 arcmin and a width of 300 μm, which corresponds to 3.9 arcsec in the sky. b) The obtained echelle spectrum which shows the emission lines of the part of the nebula that was captured inside the slit. We see that the spectral order $m = 87$ of the MES–SPM isolates these three emission lines. The bright, vertical line on the right of the spectrum is the emission from the big star captured on the right part of the slit in image (a) (big, black dot on the right).

prep.) at the 2.1m telescope in San Pedro Martir Observatory, Mexico, with the Manchester Echelle Spectrometer (MES–SPM; Meaburn et al. 2003). A 2048 × 2048 (13.5 μm pixel size) CCD was used with a two times binning in both the spatial and spectral dimensions, resulting in a 0.35 arcsec pixel^{-1} spatial scale. The slit length corresponds to 5.5 arcmin on the sky, while the slit width used was 300 μm, which corresponds to 20 km s^{-1} or 3.9 arcsec wide or 0.44 Å (Fig. 5.4). In total, 26 long-slit spectra were obtained with the purpose to cover the key areas of the remnant. From these, 21 spectra were obtained with slit Position Angle (PA) of 45° with respect to the North and the rest 5 at a PA of 90° (Fig. 5.6a). The spectra were finally calibrated in heliocentric radial velocity (V_{hel}) to $\pm$ 2.6 km s^{-1} accuracy against spectra of a Th–Ar lamp. The data were analyzed in the standard way using the IRAF software package. From the spectra analysis, the Position Velocity (PV) diagrams were deduced (see Fig. 5.5), from which the kinematical information was obtained which was necessary for the needs of the 3D model.
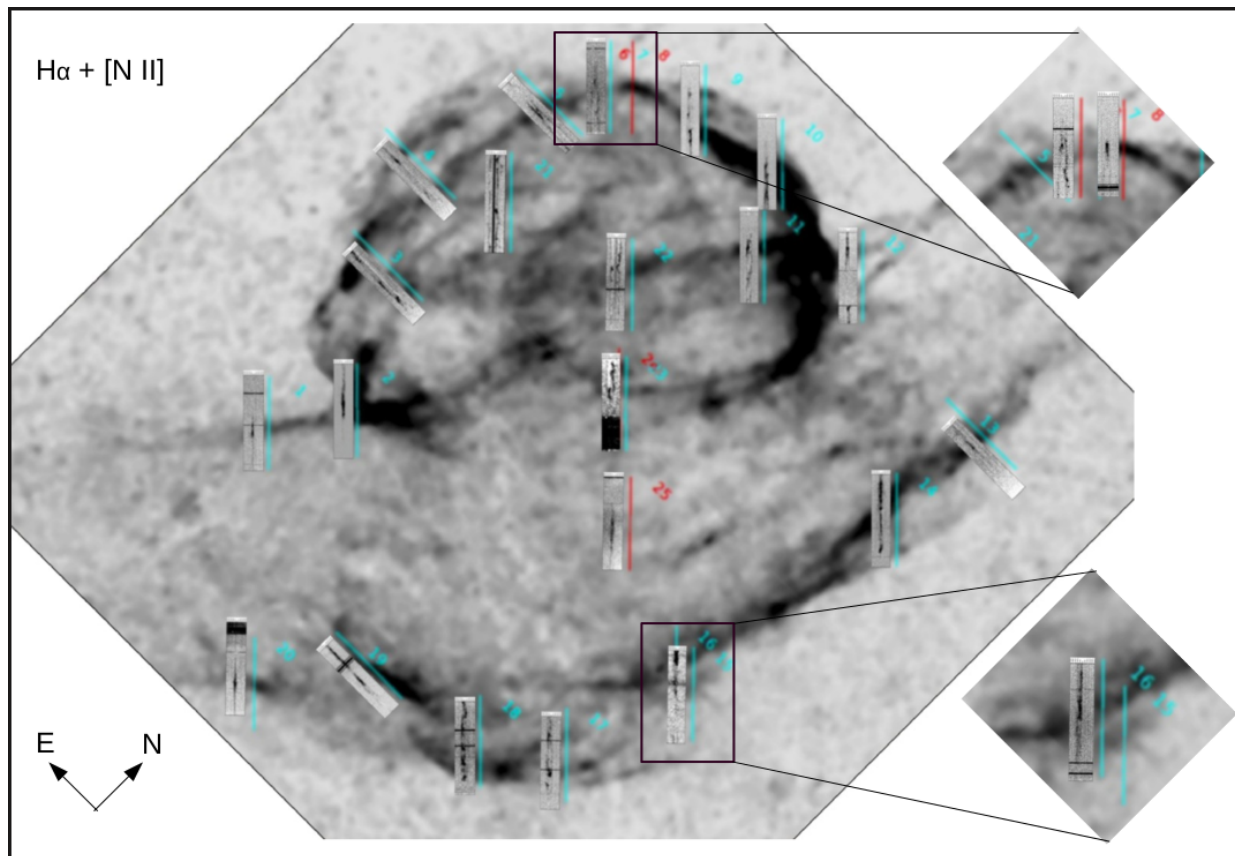
Figure 5.5: Wide field image of VRO in Hα 6563 Å emission line, overlaid with the PV diagrams at the equivalent positions where we have obtained echelle spectra. The slits positions are marked with the cyan and red labelled lines, while the PV diagrams are the plots seen on the left of the slits. In the subregions which are included in the two black boxes, the slits 6, 7, 8 and 15, 16 respectively were too close each other and therefore their PV diagrams were overlapping when illustrated simultaneously. This is why we present the PVs of slits 6, 8 and 16 separately in the magnified boxes.

5.4   SHAPE modeling

A 3D study of extended emission line sources like PNe, H II regions and SNRs is essential to provide new insights to their formation and evolution. Although PNe have been extensively studied via 3D MK modeling, there was no similar work for SNRs. The reasons for this were i) SNRs are usually very extended sources, which means that, apart from the imaging data, a great amount of spectroscopic data is also required for a full coverage of the remnant, ii) the asymmetries that SNRs usually display in their shape denote a great complexity in morphology and kinematics which is an additional factor of difficulty in the 3D modeling and iii) many SNRs are thin shells with low central emission along the line of sight, therefore most of the optical emission is tangent to the observer and hence radial velocities are close to zero. In this Thesis, we reconstructed the first 3D MK model for a SNR (VRO 42.05.01), using SHAPE software. The
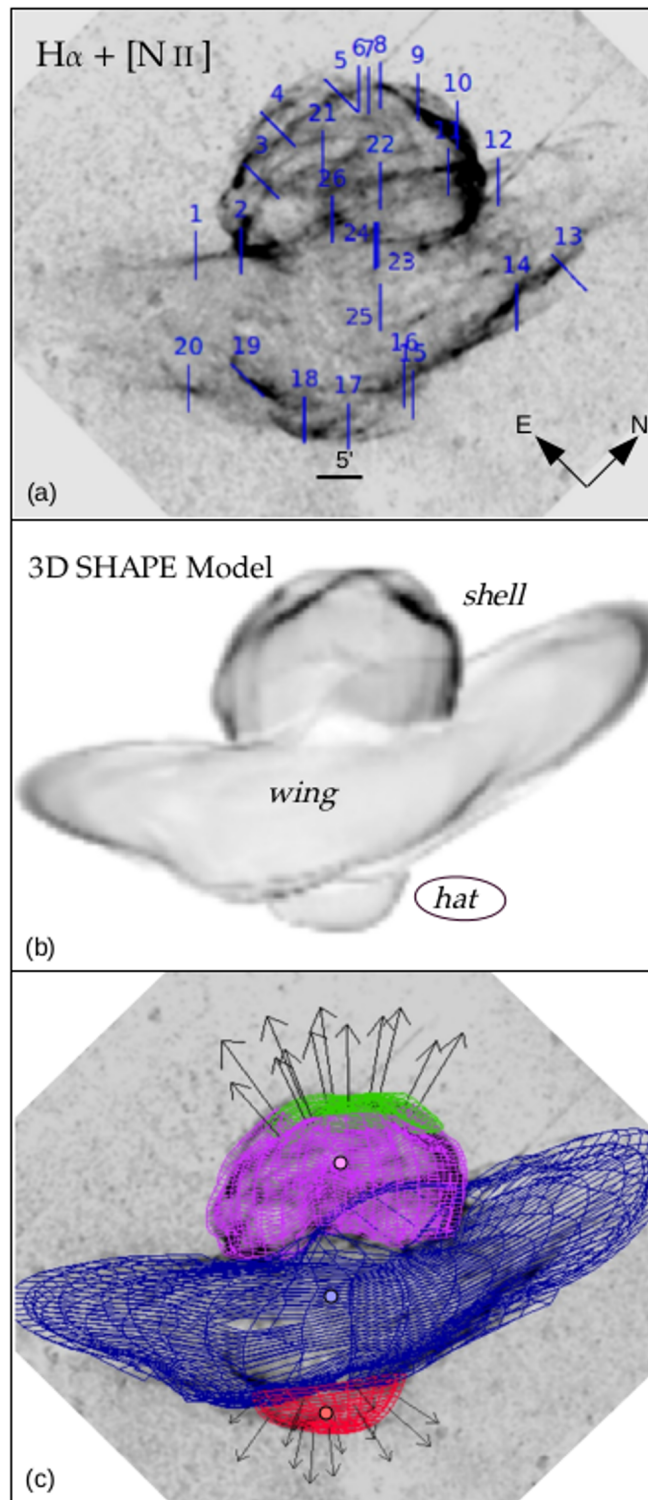
Figure 5.6: Fig. (a) shows the VRO in Hα+[N II] 6548, 6584 Å emission lines. The blue labelled lines represent the slits' positions where high resolution spectra were obtained. In Fig. (b) the 3D model of VRO is demonstrated, where its three components are labelled, and Fig. (c) illustrates the 3D model in mesh-grid representation overlaid on the Hα+[N II] image, without the slits' positions. The different colours correspond to the distinct components of the remnant with respect to their morphology and kinematics. The black arrows point to the direction of expansion of the green region and the "hat" component of VRO. The three coloured dots illustrate the geometrical center of each component, which coincides with the center of each component's velocity field too.
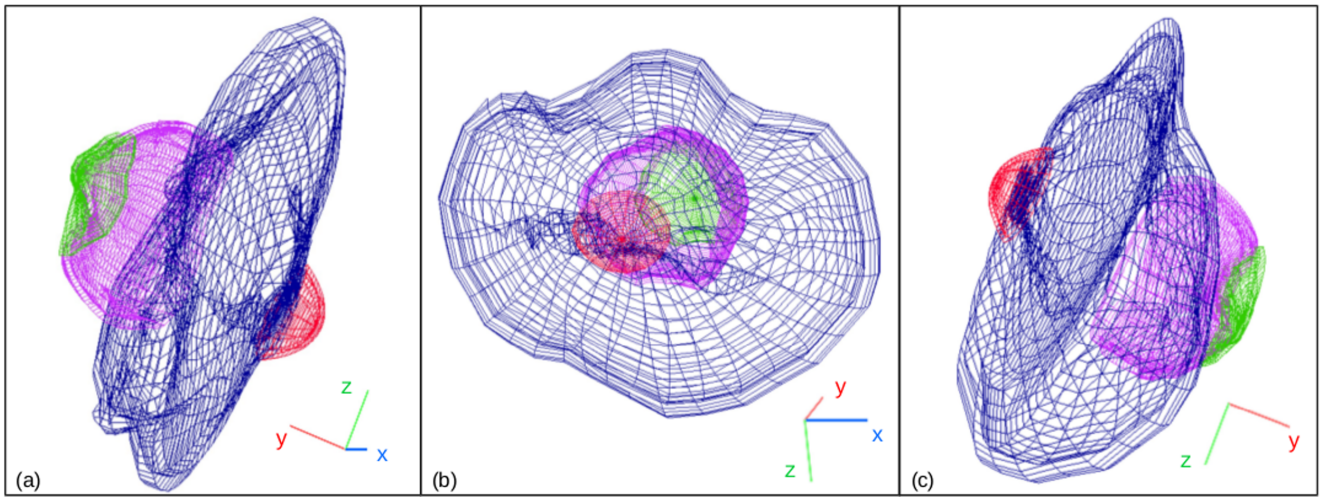
Figure 5.7: 3D model of VRO in mesh-grid representation, as seen from different angles rotated through x, y and z axis. For colour description *see* Fig. 5.6.

followed method for the creation of its 3D MK modeling, was extensively presented in Section 3.3. Below, we present the results of this study.

5.5 Results

Three components: Fig. 5.6a illustrates the observational Hα+[N II] image of VRO along with the slits' positions (blue, labelled lines) while in Fig. 5.6b the 3D model of VRO is presented. In the model we used the wing's outer edges as closed-ended, even though in Fig. 5.6a it seems that they are open-ended. A higher contrast version of this image, shows that even they are fainter and not continuous, they are closed, but the possibility of having shock break-out features there cannot be ruled out.

Apart from the "shell" and the "wing" components, a third component has also been added in the southwestern region of the remnant, that we term it as the "hat". The reason for representing this part as a separated structure was that, according to the observational data and the model, this lower part of the "wing" protrudes with respect to the rest "wing", and also shows a different kinematic behaviour. In Fig. 5.6c, the 3D visualization is illustrated but in a mesh representation, overlaid on Fig. 5.6a without the slits positions. The different colours correspond to the distinct components of the remnant, each one of which is characterized by its own morphology and velocity field. Fig. 5.7 also presents the mesh representation of VRO, as seen from different directions.

Morphologic attributes: We found that the whole remnant is tilted by approximately ~ 3-5

degrees with respect to the plane of the sky. That means that the "shell" goes inwards the page, while the "hat" component goes outwards from the page. Concerning the "wing" component, the model showed that its northern part is bent with respect to its eastern counterpart, implying a possible interaction with a denser ambient medium at this part of the remnant (see also Arias et al. 2019a). In addition, a part of the "wing" penetrates the central region of the "shell" at its front side (see Fig. 5.6a near slit 26), but also at its back side as well as shown by the model. Furthermore, the straight filament that crosses the shell in the positions of slits 11 and 22, is attributed – based on our model – to the northern back side of the "wing" component.

Velocity field in Hα 6563 Å emission line: The systemic velocity of the SNR was calculated to be V_{sys} = -17±3 km s^{-1}, lower than the value of V_{sys} = −34 km s^{-1} proposed by Landecker et al. (1989). With regards to the expansion velocities of each component, the model showed that VRO is not characterized by a uniform velocity law. The "shell" appears to expand at a velocity of V_{exp} = 115±5 km s^{-1}. However, the upper part of the "shell" (green region in Fig. 5.6c) presents an expansion velocity towards north-east of V_{exp} = 155±15 km s^{-1}, which is higher than that of the rest "shell", and also corresponds to the the highest velocity of the remnant in total, in this emission line. The "wing" appears to have an average velocity V_{exp} = 115±5 km s^{-1}, same as the "shell" counterpart. On the opposite side of the remnant in the south-west region, the "hat" was found to expand at a velocity of V_{exp} = 90±20 km s^{-1}, which is lower than that of the "wing" component. The black arrows in Fig. 5.6c point to the direction of the radial expansion of the green region and the "hat" of VRO.

In order to conclude for the expansion velocity of each part of the VRO, both the synthetic structure and the synthetic PV diagrams created with SHAPE should be in agreement with the equivalent observational data of VRO (imaging and spectroscopic). This is further explained in the next paragraph.

Position velocity (PV) diagrams in Hα: Apart from the morphological resemblance of the reproduced model with the observational image, our guide in order to check the validity of our model was the overall agreement between the observational PV and the synthetic PV diagrams produced with SHAPE. Therefore, we kept modifying the morphology and the velocities of each component, up to the point that we achieved the best agreement between all the 26 observational and produced spectra simultaneously. In Fig. 5.8, the 26 observational PV diagrams in Hα emission line are presented (black-coloured lines) overlaid with the synthetic coloured PVs reproduced with SHAPE. The blue and red lines correspond to the blue-and red-
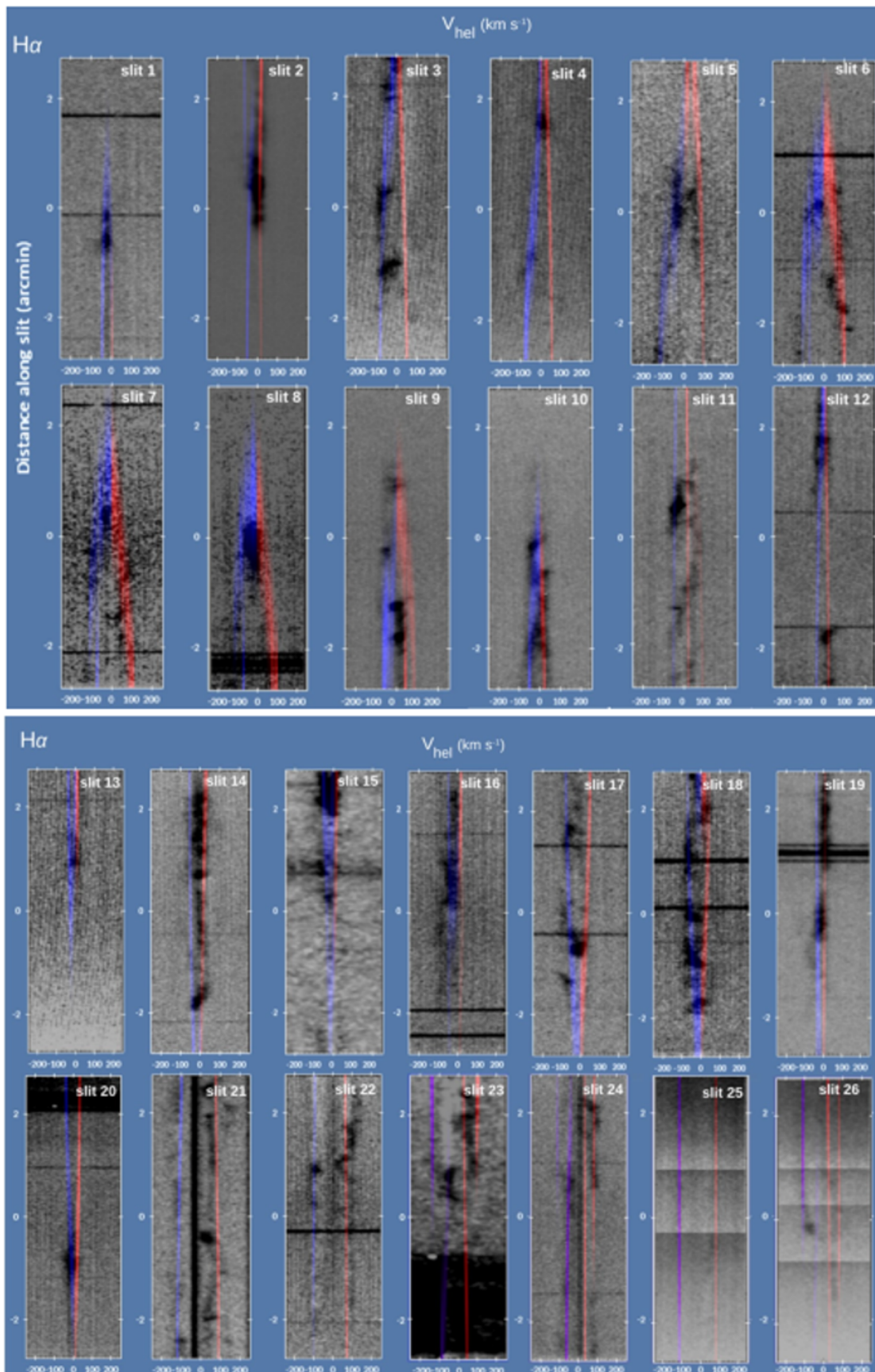
Figure 5.8: The 26 PV diagrams in Hα emission line extracted from the echelle spectra and used in the SHAPE code for the 3D modeling of VRO. In black-coloured are the observational PVs, while in blue-red coloured are the synthetic PVs produced with SHAPE, overlaid on the observational diagrams. For description see Section 5.5.

shifted part of the remnant, respectively.

A point that requires particular attention is that the synthetic PVs from the slits that located at contact regions of the remnant, present two pairs of blue-red lines. This is because the contribution in their synthetic spectra comes from both components. In particular, in slit 18 there is contribution from the "hat" and the "wing", in slits 24 and 26 from the "wing" and the "shell", while in slits 11 and 21 from the "shell" and the back side of the "wing". Similarly, in the synthetic PV of slit 26, both the "wing" and the back side of the "shell" contribute to the reproduced, synthetic PV diagram.

The matching between observational and synthetic PVs is quite sufficient, and it has been achieved for all the 26 spectra obtained for VRO. The goal was the overall fitting between observational and synthetic spectra, neglecting at this point individual substructures (blobs etc.) that the spectra may illustrate. Therefore, the model results are consistent with the observations in both imaging and spectroscopic data.

Velocity field in [O III] 5007 Å emission line: With respect to the [O III] 5007 Å emission line, VRO shows intense oxygen radiation in the regions which are shown in Fig. 5.9. These are the upper part of the "shell" component, the half northern "shell", and the "hat" component. In the "wing" there is almost no [O III] at all, apart from a linear filament at its lower-left edge.

In order to calculate the expansion velocity of VRO in [O III] 5007 Å with SHAPE, we obtained echelle spectra in the regions of the slits 2, 5, 8, 9, 10 and 18, as these are shown in Fig. 5.9, were the emission in this specific line is quite intense. Unfortunately, we do not have spectrum near the region of slit 20, i.e. the lower-left edge of the "wing" component, which is the only part of the "wing" that shows strong oxygen emission. Therefore, we do not have the equivalent kinematic information about its expansion velocity in [O III], as we do have for the rest slits positions.

According to the results of our model, the expansion velocity in [O III] of the upper "shell" (slits 5, 8 and 9) is $V_{exp} = 190\pm10$ km s^{-1}, the rest "shell" (slits 2 and 10) is expanding at a velocity of $V_{exp} = 130\pm10$ km s^{-1}, while the expansion velocity of the "hat" component (slit 18) is $V_{exp} = 110\pm20$ km s^{-1}. These expansion velocities are in good agreement with the equivalent velocities in Hα 6563 Å emission line deduced from our model, if we take into account the range or uncertainties in the calculation of the velocity for each component (Table 5.1).

With respect to the spatial distribution of [O III] and Hα 6563 Å in VRO, in Fig. 5.10 we present the wide field image of VRO in Hα 6563 Å overlaid with the [O III] 5007 Å, in order to directly compare the regions of each emission. Similarly, in Fig. 5.11, high-resolution images of Hα 6563 Å overlaid with the [O III] 5007 Å images are illustrated, for five out of six regions of
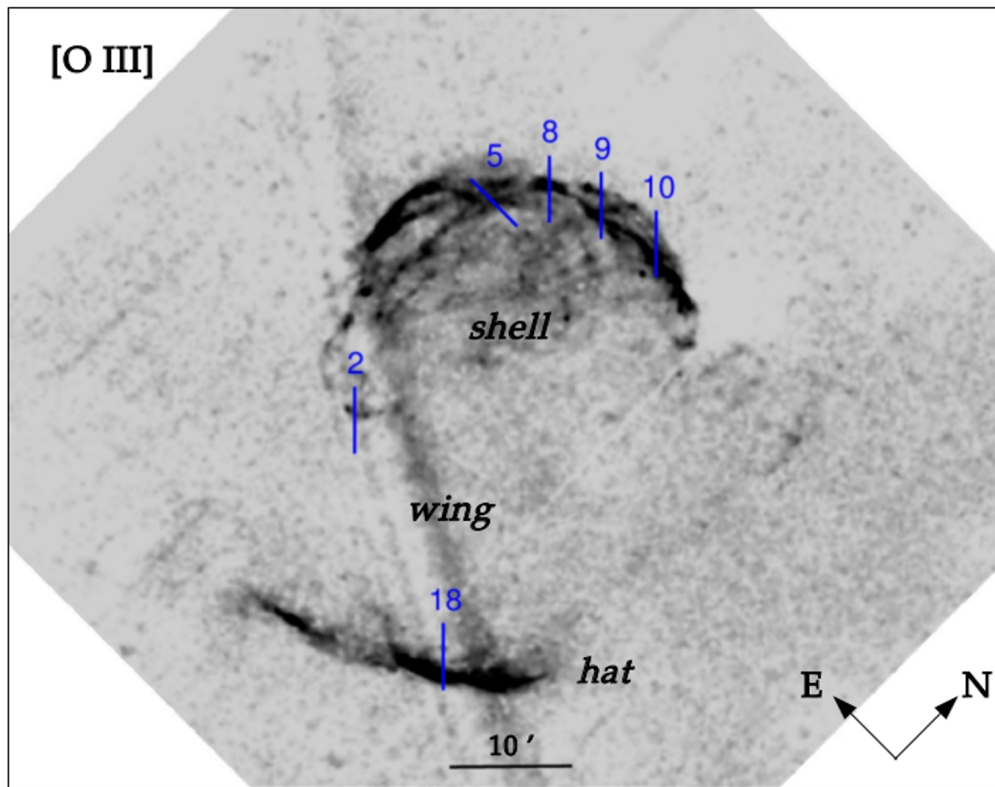
Figure 5.9: Wide field image of VRO in [O III] 5007 Å emission line. The overlaid labelled slits indicate the positions where we have obtained echelle spectra in [O III] 5007 Å line. The almost vertical diffuse line that crosses the remnant is a ghost.

VRO. In this regions we have also obtained echelle spectra, i.e. regions of slits 2, 5, 9, 10 and 18.

From the physical point of view, the emission of this specific forbidden line results from the collisional excitation and spontaneous de-excitation of the double ionized oxygen ions (see Section 1.8.5). To review the basics, [O III] is formed in regions where the gas temperature T < 10^4 K. In this -relatively- cold gas, the free electrons are of lower energy, but still their energy is adequate in order to excite the already double ionized oxygen atom into its metastable states, through the collision mechanism. Therefore, [O III] is present in the radiative phase of the remnant -when the temperature of the post shocked gas has been reduced- and, with respect to its spatial distribution, it is very often found behind the front shock itself. This is why [O III] constitutes a good indicator of the presence of hot, shocked material (see also Section 5.6, "Discussion").

Position-velocity (PV) diagrams in [O III]: Fig. 5.12 illustrates the observational PV diagrams (in black) calibrated in V_{helio}, overlaid with the synthetic PVs produced with SHAPE code (blue-red coloured). The later indicate the blue and red shifted regions of the nebula

Emission line	$V_{\exp(\text{upper shell})}$ $(\mathrm{km\,sec}^{-1})$	$V_{\exp(\text{shell})}$ $(\mathrm{km\,sec}^{-1})$	$V_{\exp(\text{wing})}$ $(\mathrm{km\,sec}^{-1})$	$V_{\exp(\text{hat})}$ $(\mathrm{km\,sec}^{-1})$
Hα 6563 Å	155 ± 15	115 ± 5	115 ± 5	90 ± 20
[O III] 5007 Å	190 ± 10	130 ± 10	–	110 ± 20

Table 5.1: This Table illustrates the expansion velocities of the components of VRO in Hα 6563 Å and [O III] 5007 Å emission lines, as these are deduced from the SHAPE model. In the "wing" component there was no spectrum available in the [O III] 5007 Å, so we do not have kinematic information about this component in this specific line. With regards with the rest parts, the velocities of the "shell" and the "hat" are of the same magnitude, within the range of errors for both emission lines, while for the "upper shell" we note that [O III] line is slightly faster that the Hα 6563 Å. For further discussion, see in the text.

respectively. As we noted in the equivalent PVs of the Hα emission line, the purpose was to reproduce with SHAPE code the overall shape of the observational PVs, neglecting at present individual, denser structures as blobs, knots etc that the remnant includes. We should note, however, that in some subregions of VRO, it seems that oxygen is spatially in front of hydrogen (Fig. 5.11, images for slits 5 and 10). These local, diffuse emissions of oxygen did not influenced the reconstruction of our 3D MK model using this specific line; the 3D representation was the same as that for the Hα line. To conclude, the synthetic PVs produced with SHAPE for the [O III] illustrate very good fitting with the equivalent observational PVs, similarly to the results of the Hα 6563 Å PVs. Therefore, the model is consistent with the observational data in this emission line as well.

Filamentary structures: Finally, an intriguing point of VRO which is related to its morphology, are the filamentary structures that it presents. As shown in Fig. 5.6a, the remnant shows a filamentary structure, but especially in the "shell" there is network of filaments, crossing the entire surface. The most intense of them were reproduced as indentations on the surface of the component (see Fig. 5.6b). Pineault et al. (1987) had also characterized the "shell" as "surface spherical in grand design but indented in detail". However, these filaments may also indicate higher densities in these regions of VRO.

A network of filaments is also present in the "hat" component. They can be clearly seen in Fig. 5.3, covering the area from slit 16 to slit 18. The extended filaments of the "shell" were obvious in the wide field image of VRO which was used in SHAPE, and this is why they could be reproduced. On the contrary, the filaments of the "hat" are of much smaller scale, much
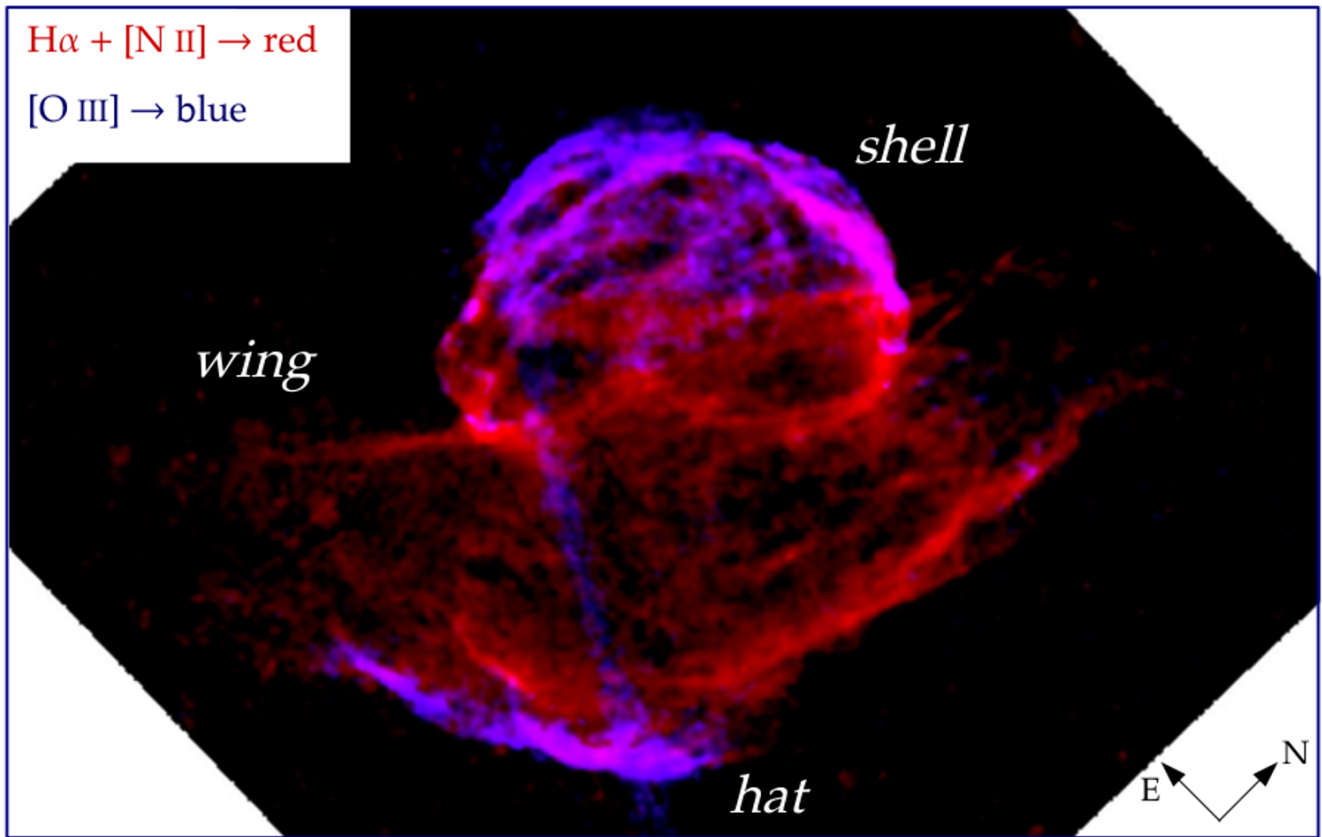
Figure 5.10: Wide field image of VRO in Hα 6563 Å emission line (red) overlaid with the [O III] emission line (blue). The blue, almost vertical line that crosses the nebula is a ghost. It is clearly shown that the only parts of the remnant where strong [O III] 5007 Å is present, are its half-upper "shell", the "hat" and the down-left part of the "wing " next to the "hat" component. This indicates the presence of strong front shock wave (see "Discussion" Section 5.6.)

closer to each other, and therefore they weren't obvious in the wide field image, but only on the high resolution images of VRO. This is why their reconstruction with SHAPE wasn't possible.

5.6   Discussion

Due to its peculiar morphology, VRO has become the subject of investigation for many years, in an attempt for its morphology to be correctly interpreted. The 3D visualization of VRO presented in this Thesis, managed to reveal its overall morphology for the first time. This, in conjunction with VRO's extracted velocity field, shed light into its evolutionary history along with the properties of the ambient medium that contributed to VRO's current general shape.

According to our model, VRO consists of three basic components: a "shell", a "wing" and a "hat". This distinction is on the basis of their morphology and kinematics. The first two structures were adopted from the already known literature and proved to have the same velocities range (V_{exp} = 115±5 km s^{-1}), while the third structure was added in the model due to

156
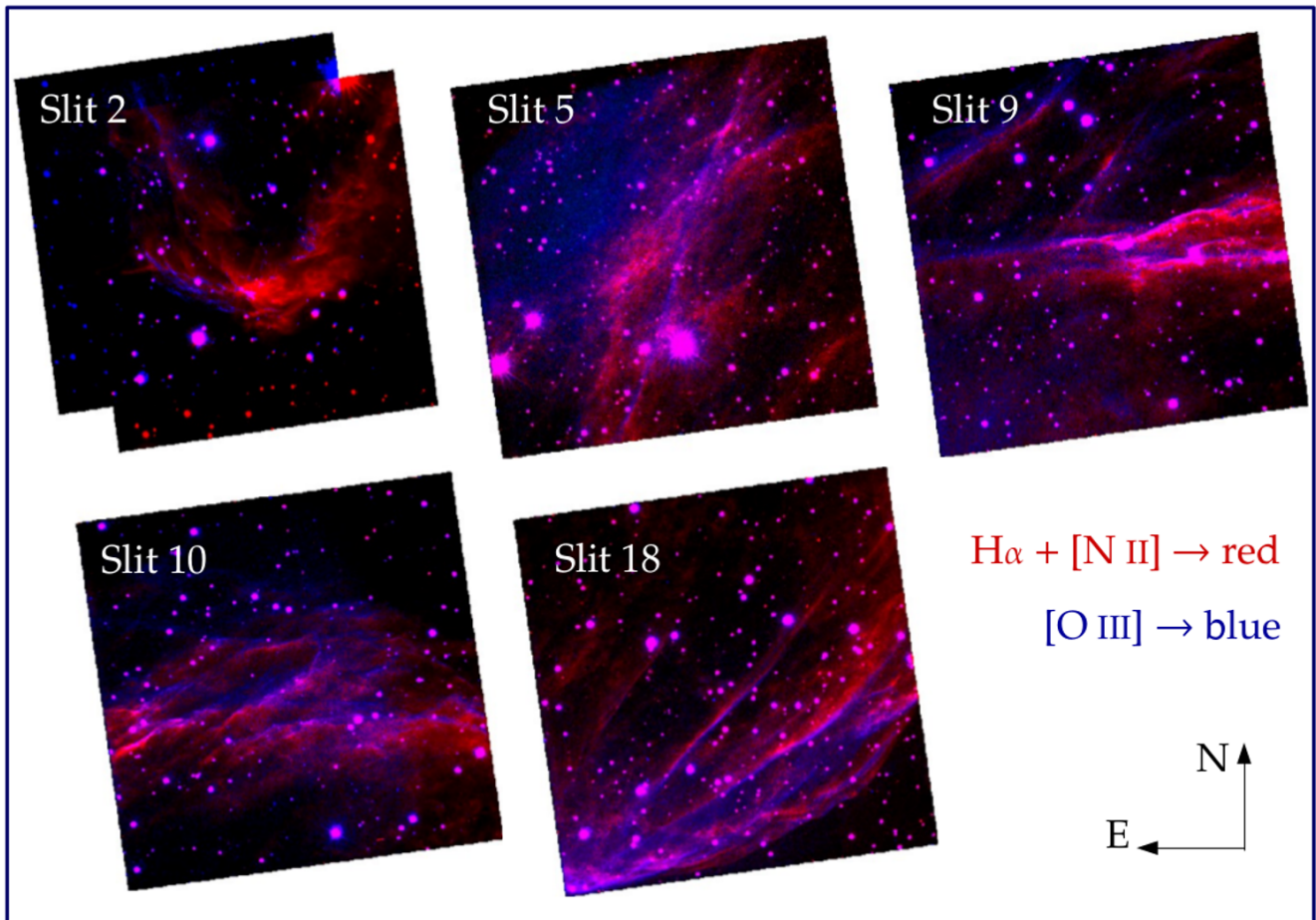
Figure 5.11: We illustrate high resolution images of five out of six regions of VRO, where we have obtained echelle spectra, too. These images which are a composite overlay of Hα 6563 Å images (in red) and [O III] images (in blue), present the co-existence of both emission lines at these specific regions of VRO.

its different kinematics ($V_{\text{exp.hat}}$ =90$\pm$20 km s^{-1}) and the protrusion it presents with respect to the "wing" component. Finally, we found that, although the "shell" seems to be morphologically unified, its upper part (green region in Fig. 5.6c) expands with a higher velocity of V_{exp} = 155$\pm$15 km s^{-1}.

Our 3D MK model showed that the remnant's morphology displays a roughly axial symmetry in the azimuthal and polar dimension, in agreement with the assumption we made for the modeling of VRO in the first place. This result advocates that VRO most likely was shaped under an axis or central symmetric mechanism linked to the nature and evolution of the progenitor system. From this perspective our results are aligned to the scenario proposed by Chiotellis et al. (2019), based on the 2D Hydrodynamical model performed for VRO. This is a time-dependent model whose sequential evolutionary stages are illustrated in Fig. 5.13.

According to this 2D HD model, the progenitor star of VRO was a rapidly-rotating, massive star, supersonically moving with respect to the local sound-speed. This star was characterized
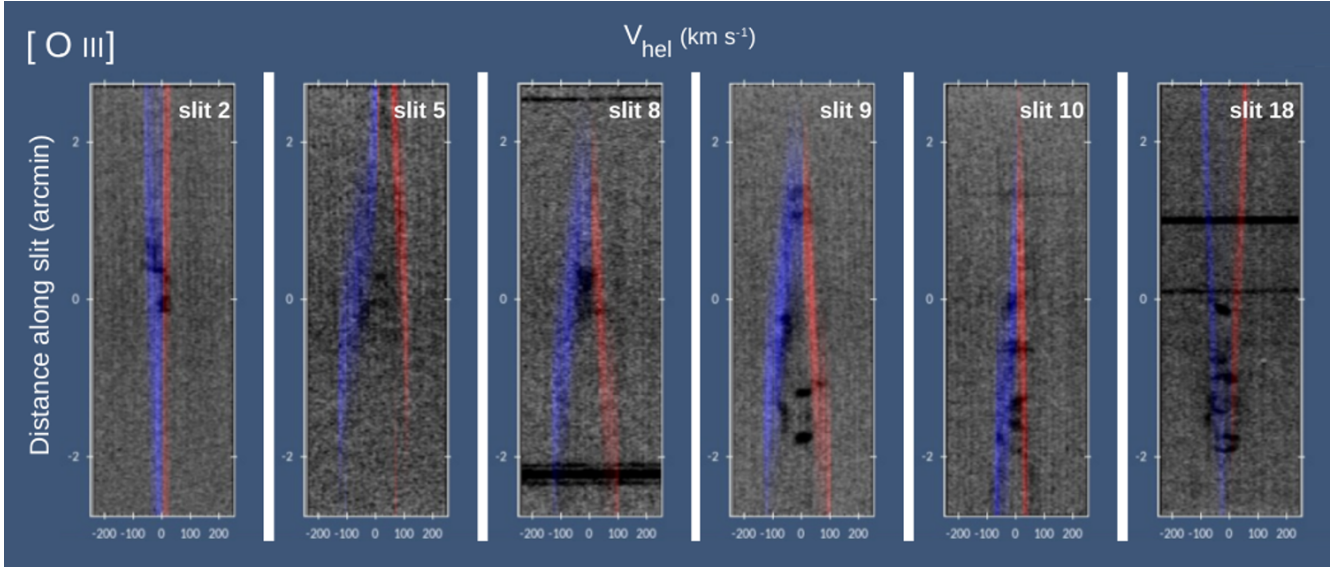
Figure 5.12: The PV diagrams of [O III] emission line deduced from the echelle spectra, as these were obtained from six selected regions of VRO (slits 2, 5, 8, 9, 10 and 18 in Fig. 5.6). In black are the observational spectra, while in blue-red the synthetic spectra produced with SHAPE code. The latter correspond to the blue-red shifted regions of the nebula respectively. For description see Section 5.5.
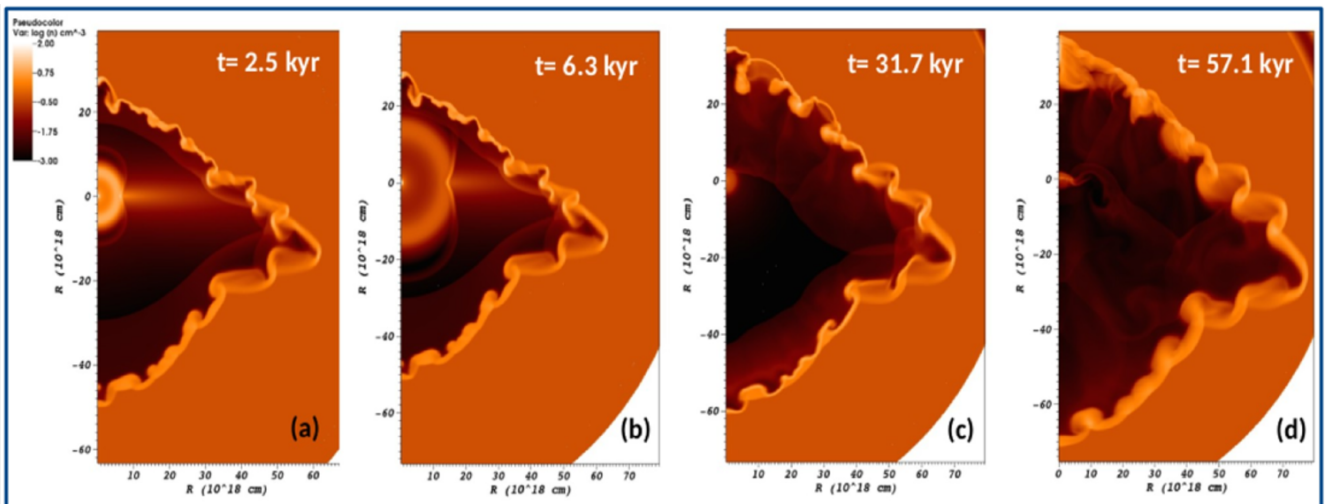
Figure 5.13: The 2D HD model of VRO. (a) and (b) The progenitor star is moving supersonically upwards, while due to its rotation and strong stellar winds, a wind-bubble cavity is created around it. (c) The star explodes inside this bubble, and its SN ejecta is propagating through this cavity. (d) The SN ejecta has filled out the cavity, resulting in the shape of VRO we currently observe. According to the orientation of this model, the "hat" component is upwards, while the "shell" is downwards.

by strong stellar winds, which resulted in the excavation of a wind-bubble around it (for "Wind Bubbles" see Section 1.9). When the star finally exploded as a Supernova, the explosion took place inside the pre-existed wind-cavity. Within the framework of this model, the similar velocities that the "shell" and the "wing" display –despite their different shapes and sizes- can be attributed to the deceleration of the remnant caused by the collision of the SN blast wave with the density walls of the wind-bubble. In the fast expanding upper part of the "shell" (green region) we may witness a shock breakout, where the blast wave penetrated the CSM density wall and is currently propagating in the lower density ambient medium. Finally, the "hat" component coincides with the region of the bow shaped CSM where the stagnation point is lying, the latter created due to the supersonical movement of the progenitor star towards this direction. The high circumstellar densities expected in the area of the stagnation point (e.g Chiotellis et al., 2012) is aligned with the low velocities we gain from the "hat" component of the remnant.

The scenario of having two shock breakouts at these two diametrical points of VRO is reinforced by the presence of strong [O III] at these areas, as it is shown in Fig. 5.10. This is because, in general, [O III] is encountered in the region behind the shock front, while its presence indicates shock velocities of $>100\,\mathrm{km\,sec^{-1}}$ (see theoretical shock models of Raymond 1979). Similar cases of evolved SNRs which show strong oxygen emission are reported in How et al. (2018), Boumis et al. (2004) and Williams et al. (1997).

The values of the V_{exp} for Hα 6563 Å and [O III] deduced from the SHAPE model are almost the same and are presented in Table 5.1.

At this point it should be clarified that from a Morphokinematic model of a SNR, we can extract the expansion velocity of this object, but we can not deduce its shock velocity. This is because, the latter refers to the velocity of the shock wave that drives the propagation of the ejecta. On the other hand, what we observe of an object in imaging and specta, is the ionized gas that is located behind the shock wave. This gas is observable in the optical, due to its cooling after the heating it underwent when the shock wave passed through it. What we use for the modeling of the object are these emission lines, not the shock wave. The value of the shock velocity can be calculated through the flux ratio of specific emission lines (e.g. [O III] 5007 Å/ Hβ) deduced from low resolution spectra (Kopsacheili et al. 2020, Allen et al. 2008).

An ISM density discontinuity suggested by Pineault et al. (1987) could also be possible to explain the VRO properties as extracted by our 3D MK modeling. Within this model the "wing" had evolved in the low density region of the ISM and thus, it gained its extended size compared to the "shell". Currently, one may say that the "shell" and the "wing" have swept

up about the same mass and as a result they display similar expansion velocities. However, an extra ISM density gradient toward the NE and SW direction is required in order to explain the high and low velocity of the upper "shell" and the "hat" respectively, that were deduced from the 3D MK model.

From the case of VRO, it is obvious that the outcomes of the 3D MK model can be used as inputs for a HD modelling. This is of crucial usefulness as the probing of an object through two different kinds of models, can result in a more thorough investigation of it.

5.7 Conclusion

We presented for the first time a 3D Morpho-Kinematic model of a SNR, VRO 42.05.01. The principal conclusions from this study are:

1. VRO can be represented by three basic distinct components, i.e. a "shell", a "wing", and a "hat", each one of which presents specific morphological and kinematical characteristics.

2. In Hα 6563 Å emission line, the "shell" and the "wing" reveal similar expansion velocities of V_{exp} = 115$\pm$5 km s^{-1} while the "hat" is expanding with V_{exp} = 90$\pm$20 km s^{-1}. Finally, the upper part of the "shell" displays the higher expansion velocity of the SNR equal to V_{exp} = 155$\pm$15 km s^{-1}.

3. Similar kinematic results were found for the components of VRO, using the [O III] emission line. In particular, the upper "shell" (slits 5, 8 and 9) expand at V_{exp}=190$\pm$10 km s^{-1}, the rest "shell" (slits 2 and 10) is expanded at a velocity of V_{exp} = 130$\pm$10 km s^{-1}, while the expansion velocity of the "hat" component (slit 18) is V_{exp} = 110$\pm$20 km s^{-1}.

4. The remnant has an inclination of $\sim$3 - 5 degrees with respect to the plane of the sky and a systemic velocity of V_{sys} = -17$\pm$3 km s^{-1}.

5. The northern part of the "wing" component is tilted with respect to its eastern counterpart, due to a possible interaction with a denser ambient medium in this region of the SNR.

6. Our results are in line with the wind-bubble interaction model suggested by Chiotellis et al. (2019). However, a local ISM discontinuity in the vicinity of VRO suggested by Pineault et al. (1987) cannot be excluded.

Chapter 6

6   Future work

-SNR G 132.7 + 1.3 (HB3):

In this work, new observational imaging data (wide-field and high resolution) in Hα+[N II] 6548, 6584 Å, [S II] 6716, 6731 Å and [O III] emission lines are presented, along with low-dispersion, long-slit spectra. Through this new study, we aim to contribute to the interpretation of the physical properties of this SNR. My task is related with the data analysis and imaging process (P. Boumis, A. Chiotellis, V. Fragkou, S. Akras, S. Derlopa, M. Kopsacheili, E. Harvey, J. Alikakos, D. Souropanis, I. Leonidaki, MNRAS, 2021, to be submitted).

-HD 185806:

This project deals with the classification of HD 185806, and also focuses on the probe of the bow-shock structure which accompanies this source. My task is to deduce the echelle spectra analysis and to reconstruct the 3D Morpho-kinematic model of this bow-shock structure, using SHAPE code (Z. Spetsieri, P. Boumis, A. Chiotellis, S. Akras, S. Derlopa, MNRAS, 2021, to be submitted).

-PNe NGC 5189 and NGC 2818:

This project I am working on, in collaboration with Dr. Panos Boumis and Dr. Stavros Akras at the National Observatory of Athens, concerns the 3D MK models of the PNe NGC 5189 and NGC 2818 (Fig. 6.1). For this, long-slit echelle spectra in the optical from the SMP catalogue (San Pedro Martir Kinematic catalogue of Galactic PNe) are used, in conjunction with the high-resolution 3D IFU data (velocity calibrated channel maps) of the nebulae obtained with

the SAM-FP instrument (SOAR Adaptive Module Fabry-Perot) at the 4.1m SOAR Telescope. The purpose is to use to already obtained knowledge in 3D modeling, and take it one step further, creating the most detailed 3D MK model ever created for a PN.

In the second part of the project, low-resolution ESO MUSE IFU (Multi Unit Spectroscopic Explorer) data cubes of the PNe available in the VLT (Very Large Telescope) archive will be used for a thorough study of the fundamental physical properties of the PNe, such as electron temperature and density, which parametrize the physics of their nebular gas and help us to determine its physical processes.
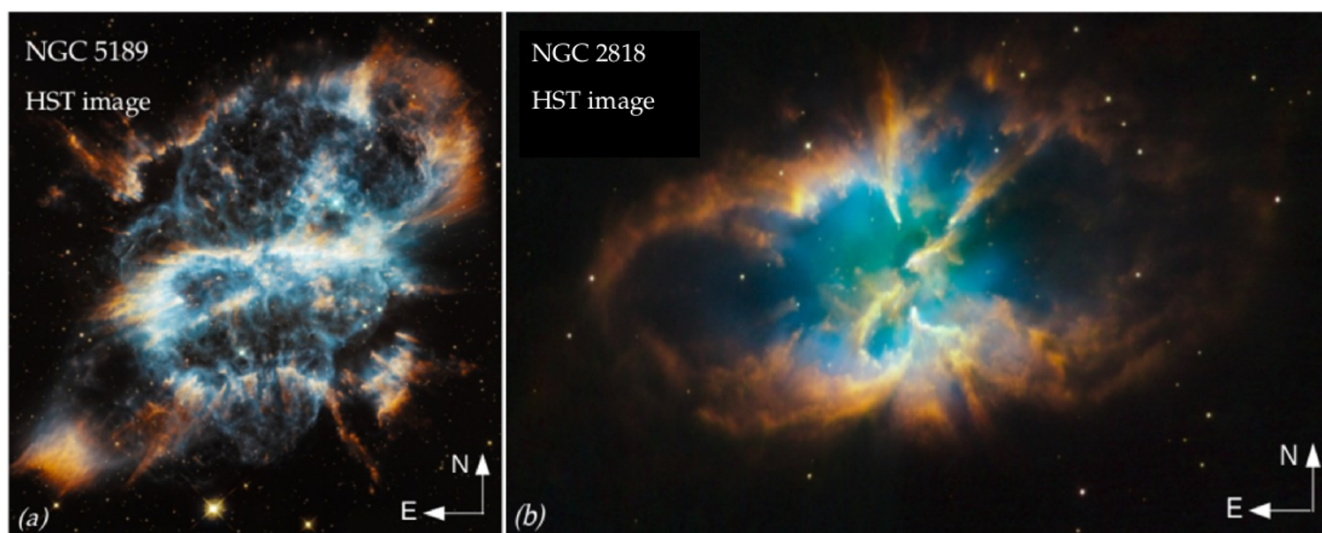
Figure 6.1: a) The PN NGC 5189. b) The PN NGC 2818.

Chapter 7

7   Appendix

7.1   Degenerate He core – He flash

As the He core contracts, it becomes very dense, consisting of He nuclei and free electrons. Electrons, which are fermions, obey the Pauli's Exclusion Principle which states that two identical fermions cannot be at the same time in the same quantum state, i.e. have the same spin, location and momentum[1]. A highly dense gas consisting of fermionic matter that satisfies the Pauli's Exclusion Principle, is called degenerate gas. In this kind of gas, since the electrons have to share the same space due to the high density, they have to differ in their momentum in order not to be under exactly the same conditions of space and velocity with each other. This kinetic energy of electrons provides the pressure in this dense gas, and is called *Electron Degeneracy pressure*. This pressure is so strong that can resist to the intense gravitational force of the shrinking He core, keeping the core in Hydrostatic Equilibrium for a period of time.

While an ideal gas's pressure depends on temperature ($PV = nRT$), a degenerate gas's pressure is independent of T. "Degenerate" electrons can provide pressure even if the temperature of the gas is low. Degeneracy pressure can rise if the volume of the core is reduced, forcing the electrons to move even faster in their attempt not to be at the same positions with each other in the gas. Therefore, even though the temperature in the He core rises up to its ignition point

---

[1]Composite particles such as nuclei, consisting of protons and neutrons which also belong to fermions, can be bosons or fermions, depending on the number of particles (fermions) they contain. Odd number of fermions in a nuclei means half-integer spin in the end, so this nuclei is also a fermion. The opposite applies for even number of fermions. In our case, the He nuclei in the He core contain two protons and two neutrons (even number of fermions) which means that these nuclei are not fermions, so they don't obey Pauli's explosion principle.
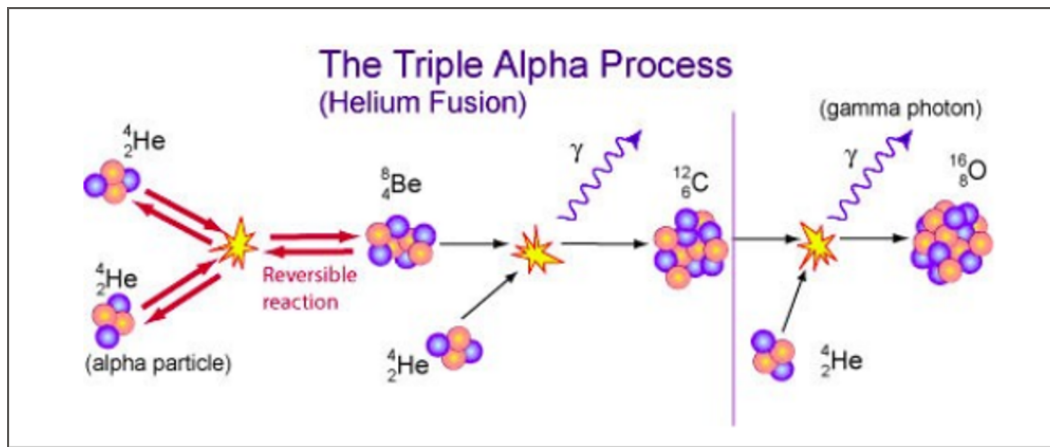
Figure 7.1: The triple alpha process for post-main sequence stars. Two helium nuclei ^{4}He (alpha-particles) fuse to form a ^{8}Be (beryllium) nucleus, releasing a γ photon too. ^{8}Be is unstable and normally decays back into two ^{4}He nuclei within a fraction of a second. However, given the high number of ^{4}He nuclei in the core, ^{8}Be may collide with one ^{8}He before it has had a chance to decay. This produces a ^{12}C nucleus and releases a γ photon. The ^{12}C nucleus in turn may fuse with another ^{4}He nucleus to produce ^{16}O and again a γ photon. ^{20}Ne may also be formed by oxygen nuclei fusing with helium, but only negligible amounts are produced.

($T = 10^8\ K$) due to its contraction, its pressure does not increases so the He degenerate core does not expand and, consequently, does not cool down. However, due to the high temperature, He ignition takes place through the triple-alpha process according to which three ^{4}He nuclei (alpha particles) are transformed into Carbon (^{12}C) (see Fig. 7.1 and description in the caption):

$$^4_2\text{He} + {}^4_2\text{He} \longrightarrow {}^8_4\text{Be} + \gamma \tag{7.1}$$

$$^8_4\text{Be} + {}^4_2\text{He} \longrightarrow {}^{12}_6\text{C} + \gamma \tag{7.2}$$

As the He core in low-mass stars is degenerate, which means it doesn't expand, the He fusion has no space for decompression resulting in an explosion known as **Helium Flash** (Shu p. 169, Mestel 1952, Schwarzschild and Harm 1962 -> reference for me). The flash lasts only for a few seconds but the released energy is proportional to $\sim T^{40}$. It is not observable since the photons produced in the explosion are trapped in the hydrogen layers. However, we know its existence from from astrophysical models. After the Helium flash, the star immediately rolls down to the **Horizontal branch** (Fig. 1.4) (Section 1.2.3).

7.2   Relationship between mass and radius in a White Dwarf

It was soon realized that the gas inside a white dwarf was too dense to behave as an ideal gas and, instead, it was degenerate. For normal stars, if you increase the mass, the star gets

larger and its radius increases. However, for white dwarfs the opposite is true: by increasing their mass, the star shrinks (Fig. 7.2) according to the equation $R{\sim}M^{-\frac{1}{3}}$, the plot of which is illustrated in Fig. 7.3. Notice that when the mass reaches the value 1.4 M$_\odot$ (*Chandrasekhar limit*), then the radius of the star goes to zero. Physically, that means that the star collapses and eventually it explodes.
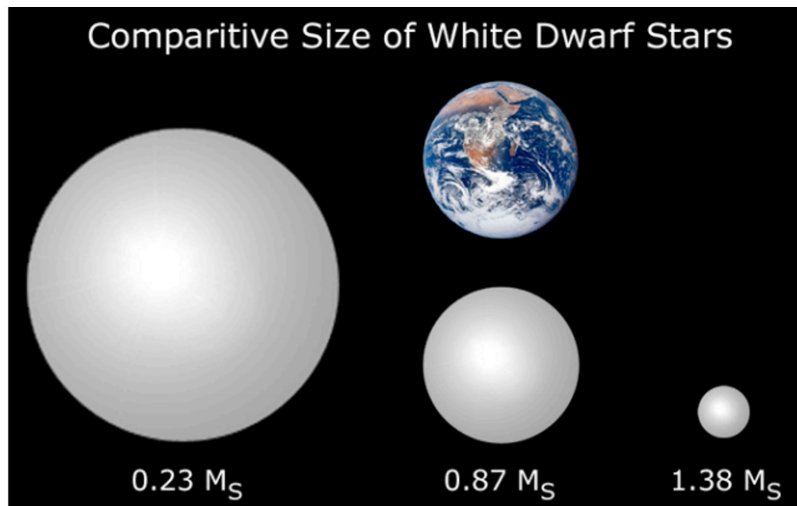
Figure 7.2: This image illustrates three White Dwarfs of increasing masses (Ms stands for solar mass). As we can see, the WDs become smaller as they become heavier, in agreement with the plot of Fig. 7.3. The middle WD has the size of Earth, but it's by far denser if we consider that the Earth's mass is $3{\times}10^{-6}$ M$_\odot$.

Explanation: The size of a star is a balance between pressure and gravity. Gravity pulls the outer layers of the star inward, while pressure pushes those layers upward. Therefore, as you add mass to a white dwarf, the increased gravity must be balanced by the degeneracy pressure, in order for the dwarf not to collapse.

Since degeneracy pressure depends on density, the only way for the former to get increased is by shrinking the size of the WD. Therefore a WD must shrink in order to increase the density and thereby the degeneracy pressure through the kinetic energy of the electrons of the gas, in order to sustain the gravitational forces from an increase in mass.

Notice, however, that the mass-radius relation for white dwarfs denotes that you cannot keep adding mass to a star forever, for eventually its radius goes to zero (Fig. 7.3). This happens because, in that case of over-limit mass addition, electrons would have to move faster than the speed of light in order to create enough degeneracy pressure to halt the gravitational collapse. But, they cannot move faster than light so the core in this case will collapse.

Following that we can say that stars with C-O core mass greater than 1.4 M$_\odot$ "must" shed
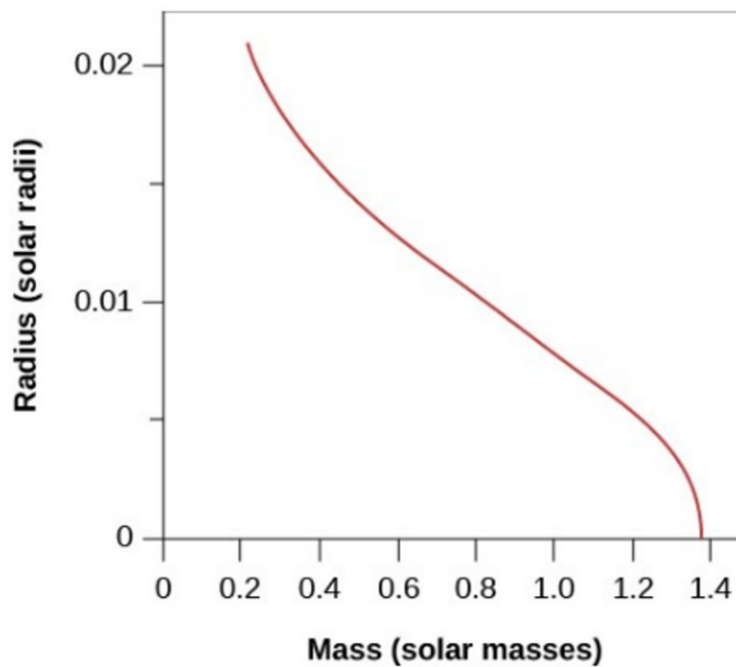
Figure 7.3: Radius vs mass (solar units) for a White Dwarf. As the mass of the star increases, its radius gets smaller and smaller. When mass equals (or exceeds) 1.4 $M_{\odot}$ (*Chandrasekhar limit*), the radius goes to zero, i.e. the star collapses and explodes.

most of their mass as planetary nebula, if they want their core to survive. If the mass can not be shed, the stars follow a different evolutionary path becoming either neutron stars or black holes, after they undergo a Supernova explosion (see Sections 1.3 and 1.5 respectively).

7.3   Supernova explosion – Fe burning

Iron: the end–point of nuclear reactions, the onset of the Supernova explosion:

When the star develops an Fe core, exothermic reactions (fusion or fission) must occur, in order the released energy in the core to stabilize the gravitational pull of the outer layers. As we can see in Fig. 7.4, elements lighter than Fe are "glued" together (fusion) to form heavier elements, as long as the reactants are lighter than Fe. For higher mass numbers, elements heavier than Fe are split into lighter elements (fission), as long as the reactants are heavier than Fe too.

However Fe, which is the most stable element, needs to consume energy (endothermic reaction) in order to change its stable nuclear structure. Since there is no way of this to happen right now, nuclear reactions stop in the Fe core which is now supported only by the degenerate pressure of electrons, just as a White Dwarf does.

Meanwhile fusion still occurs in the shells that surround the core and the ashes of their

Figure 7.4: Elements lighter than Fe release energy through fusion reaction, while elements heavier than Fe release energy through fission (both reactions are exothermic). Fe is the most stable element which needs to consume energy (endothermic reaction) in order to change its nuclear structure.

last reaction fall onto the Fe-dwarf core. Consequently, its mass increases, its radius decreases (for explanation see Fig. 7.3) while its density increases too. However, electron degeneracy pressure is independent of temperature. Therefore, the compression that the core undergoes does not lead to its further heating. At this point, the center of the star is already extremely hot from the previous burning stages. Silicon burning which produced Fe in the core, occurred at a temperature of 10^9 K. Photons of this high energy, now restricted in a small region due to contraction, bombard Fe and split it into He, protons and neutrons through the endothermic photo-disintegration reaction (Fig. 7.5). By this way, they take away thermal energy from the core which could be used to balance gravity. Furthermore, the core density becomes so high ($\sim$ 10^9 gr cm^{-3}), that protons (released by the photo-disintegration) and free electrons (responsible for the electron degeneracy pressure) combine together to form neutrons and neutrinos through the inverse beta decay reaction:

$$p^+ + e^- \longrightarrow n + \nu_e \tag{7.3}$$

The consumption of the electrons in this reaction, removes the supporting electron pressure that was helping in the stability of the core. A third factor of energy loss from the core, is the

Fe photo-disintegration in CC Supernova

$$\gamma + {}^{56}Fe \rightarrow 13\ {}^{4}He + 4n$$

$$\gamma + {}^{4}He \rightarrow 2p^{+} + 2n$$

Figure 7.5: The endothermic reaction of photo-disintegration: a high energy photon is absorbed by the Fe nucleus in the core of the star, forming α particles (^{4}He) and neutrons. These He nuclei in turn are split into protons and neutrons, also through photo-disintegration. These reactions absorb energy from the core, and signal the start of the core collapsing of the star.

extreme amount of energy that neutrinos carry away with them while escaping from the star (without interacting with matter), which is of the order of $\sim 10^{53}$ erg.

This triple energy loss makes the core to contract further, increasing these reactions which in turn remove even more energy from the core. In the end, when there is no adequate force against gravity any more, the inner part of the core collapses rapidly, while its outer part goes into free fall onto the inner core. At this stage, the core has a radius of a few km, while its outer part collapses at a speed of $\sim$70.000 km sec^{-1}, driven by the strong gravitational force of the super-dense inner core. For comparison, under such conditions the Earth would be compressed into a sphere of 50 km radius within just one second.

After the neutrinos escape from the core, the only particles left there now are the neutrons. The density in this neutron core rises during the collapse until the point of *neutron degeneracy* is reached, i.e. 10^{15} gr cm^{-3} (we don't have *electron degeneracy* any more, since the electrons of the core were merged with the protons to form neutrons and neutrinos). At this point, neutron degeneracy provides the outward pressure needed in order to prevent the further gravitational collapse of the inner core. The outer collapsing parts of the core run into the forming degenerate core, fall onto its hard surface causing a "bounce" or rebound. This collision creates a *shock wave* which propagates outwards, colliding with all the outer layers of the star that encounters, heating them at very high temperatures and finally expel them into space at velocities of $\sim$10.000 km sec^{-1}. This expanding, blast wave is in practise a massive explosion which is called **Supernova (SN)**.
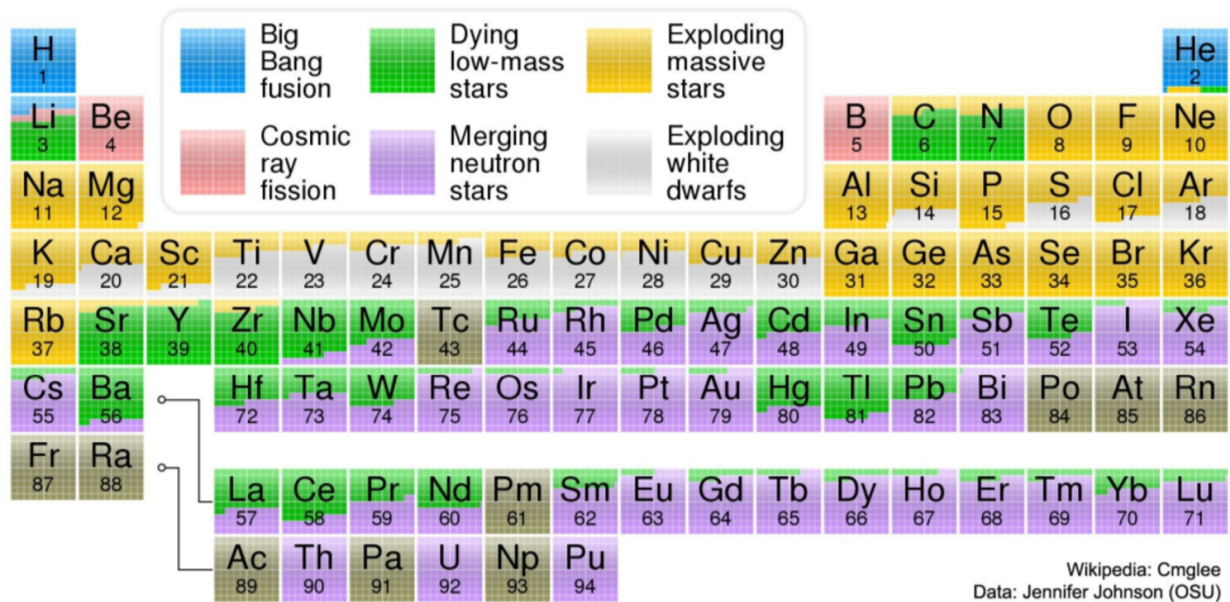
Figure 7.6: Periodic Table showing the currently believed origins of each chemical element. We see that in the beginning of the Universe, the only available elements were H and He, along with some trace elements of Li. The rest of them were created during the evolution of the Universe through the mechanisms of the Supernova explosions in the stars.

This huge amount of released energy during a SN explosion can provide the necessary fuel which allows the endothermic Fe fusion reaction to create very high mass elements such as Uranium (remember that Fe has been formed from Si fusion in the shell that surrounds the star's core). Thus, the SNe explosion mechanism is a rational explanation for all the elements with masses larger than Fe found in the universe. Remember that according to the best fit models about the beginning of the history of the universe, everything starts with two elements available: Hydrogen and Helium. This means that the rest elements were created over time. Fig. 7.6 illustrates the Periodic Table of elements, where the chemical elements are coloured according to their origin mechanism.

7.4 CCD camera

Charge coupled devices, or CCDs, are optical devices, which among other numerous applications, are also widely used in **optical telescope** cameras in order to collect the emitted light of the observed object and convert it into a digital image. They were invented in the late 1960s by Willard Boyle and George E. Smith who, in 2009, received the Nobel Prize in physics for their work. All the cameras used in the observations of the project, were of CCD type.

The general idea of their function is to collect the photoelectrons emitted from a semi-

conductor substrate due to photoelectric phenomenon, when this substrate is hit by the photons of the object.

The basic technical features of a CCD camera are:

–**Quantum Efficiency (QE) or spectral response:** it is the ratio of the finally detected photons, over the initial photons falling on the CCD. As an example we present the QE of the LN2 CCD camera of "Aristarchos" telescope in Fig. 7.7.
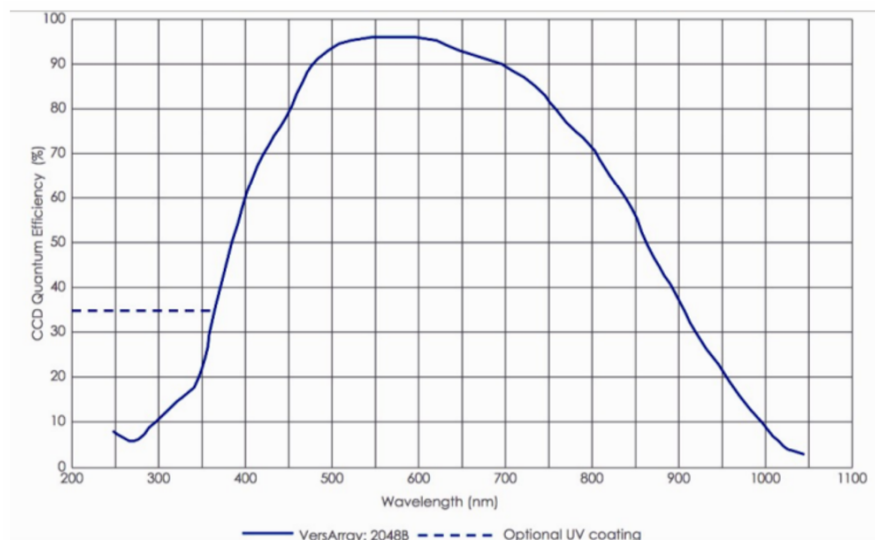
Figure 7.7: In this plot, the Quantum Efficiency of the LN2 CCD camera of "Aristarchos" telescope is presented.

–**Linearity:** it expresses the relationship between the final output digital signal, i.e. the produced photoelectrons, to the initial photons incident on the CCD. (Digital signal = Constant x amount of incident light).

–**Noise:** these are extra electrons registered from the detector which, however, are not related to the photoelectrons produced from the photons of the object incident on the CCD. These unwanted electrons must be removed from the final image. An example of this it is shown in Fig. 7.8.

Next, we present the operation of a CCD camera in more details, but yet in a simplified version.

In Fig. 7.9a, a piece of silicon (semi-conductive material) is divided with insulating channel stops (white horizontal lines in Fig. 7.9b). This Si slab is covered by a very thin layer of silicon dioxide (faint white area in Fig. 7.9b), while tiny strips of charged aluminium (electrodes) are laid perpendicular to the channel stops (grey lines in Fig. 7.9c). This Si surface is etched on by a two-dimensional grid of individual light sensing elements called pixels (red frame in Fig. 7.9d) (pixel stands for "picture elements"- basic light-sensitive unit of the sensor). As we can
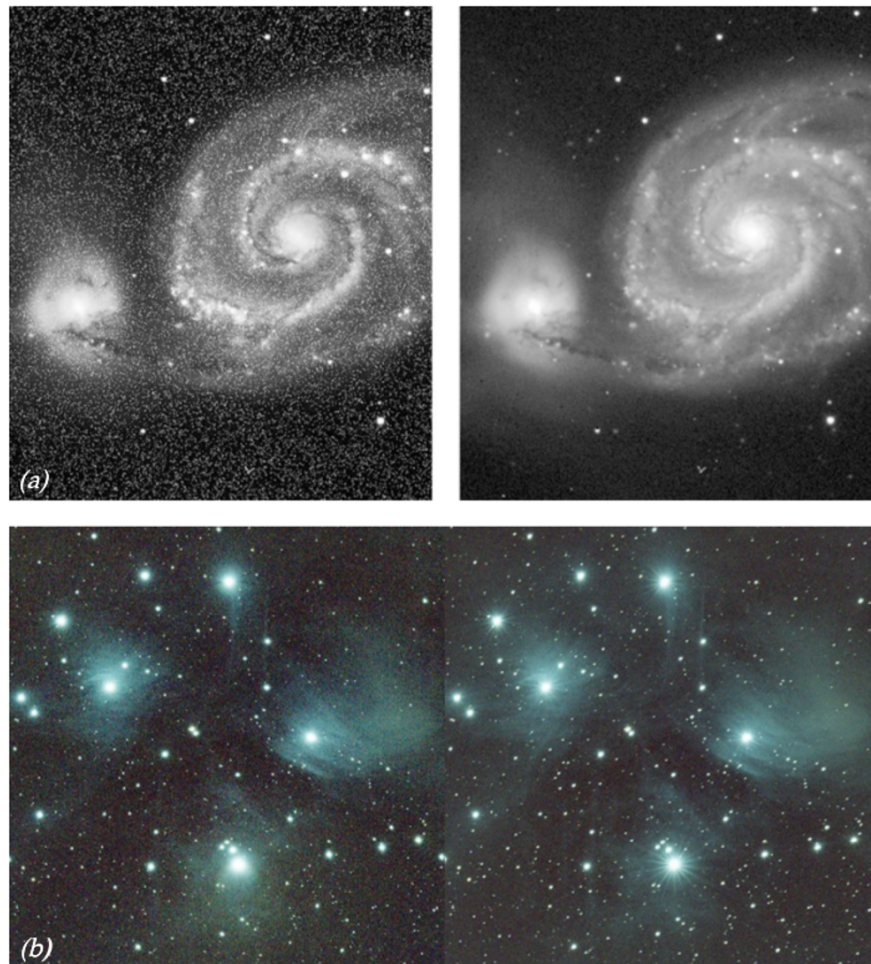
Figure 7.8: On the left of both images (a) and (b), we can see the initial image obtained with the telescope, while on the right, the same images are illustrated after the "noise" subtraction.

see in the image, each pixel on this sensor is bound on the sides by a channel stop with three aluminum stops on top, middle and bottom. A typical size of a pixel is $\sim\mu$m, while the thickness of the silicon substrate is $\sim$50μm, about the same as a tissue paper.

The CCD camera is placed at the focal plane of the telescope. When the exposure starts and the shutter of the camera opens, light (photons) of the observed object fall onto the sensor. Then due to the photoelectric effect, some of the electrons bounded in the Si atoms absorb the photon's energy, escape from their atoms and are moving free in the lattice of the silicon crystal (Fig. 7.9e). In the silicon semi-conductive surface, the energy that a bounded, outer-shell electron needs to absorb in order to "jump" from the valence band to the conduction band of its atom (Fig. 7.10a), is 1.26 eV[2]. Photons with that energy correspond to radiation of λ

---

[2]In practise, this is the energy a valence electron must gain in a material in order to reach the conduction band, and by this way the material to become a conductor of electricity. This band gap is different from the ionization energy, which is the energy required to remove an electron from the outermost shell/valence shell of an isolated, gaseous atom to a position at infinity with respect to the atom.
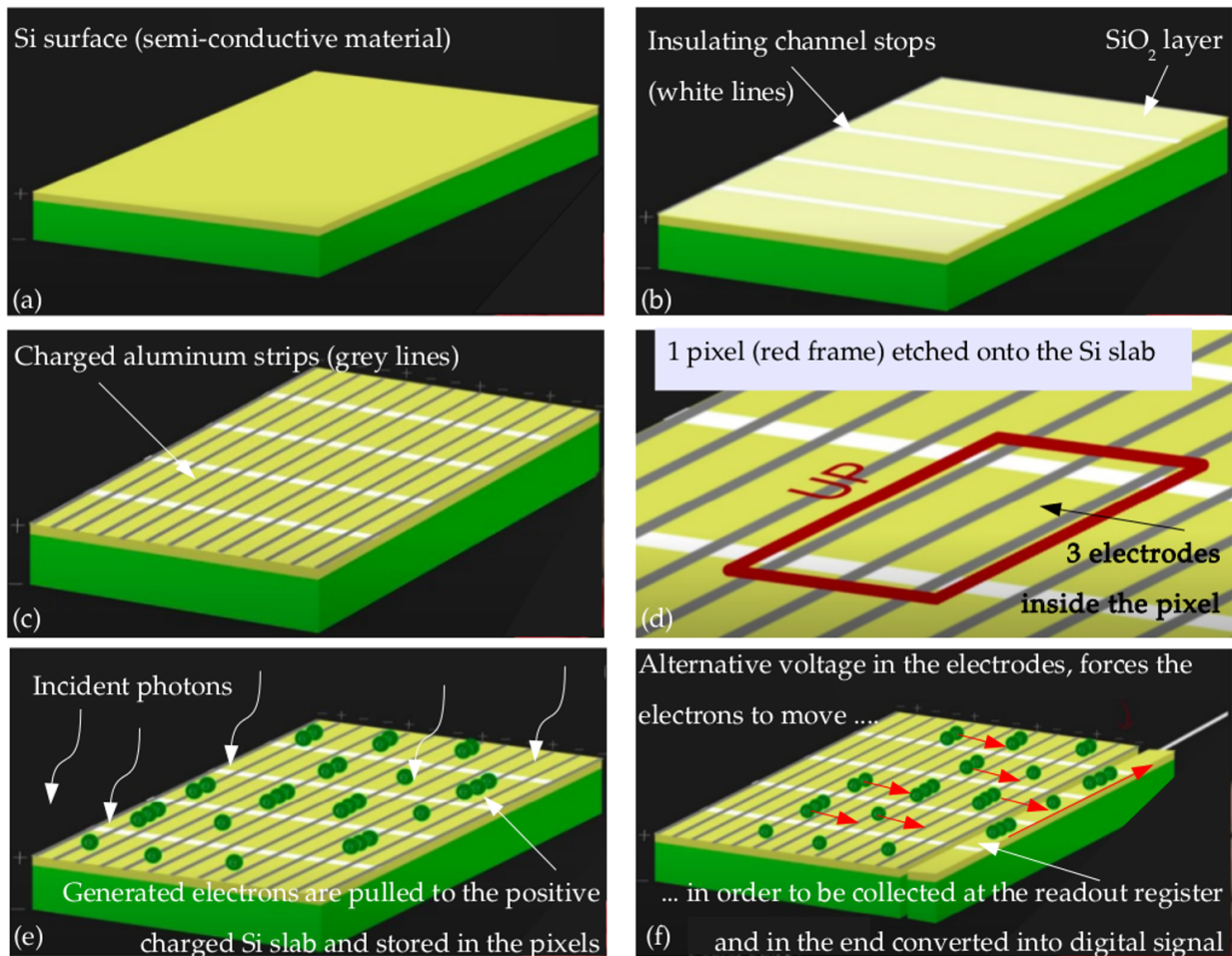
Figure 7.9: The CCD element function. For description see in the text.

~1000 nm, which contains the optical band $400 - 700$ nm detected from the objects. Beyond this wavelength silicon becomes transparent and CCDs constructed from silicon become insensitive.

Electron's "detachment" from the Si atoms leaves behind a "hole" (empty space) which acts like a positively charged carrier. In the absence of an external electric field the "hole" and electron would quickly re-combine and be lost. Therefore, in a CCD an electric field is introduced through the electrodes we mentioned above, in order to sweep these charge carriers apart and prevent recombination. Due to this electric field, electrons migrate to the top of the silicon slab where they are stored in the pixels (Fig. 7.9e).

The exposure time of the observation must be sufficient to cause the pixel to fill with electrons, but not to saturate (not to "burned off"). When the exposure ends and the shutter of the camera closes, the sensor holds the charge (produced photoelectrons) from the exposure in the pixels (also called potential wells). Next, the collected charges are horizontally transferred from one pixel to the other (from left to right in Fig. 7.9f), ending to the readout register, positioned at the edge of the grid. What moves the electrons along one row, is the synchronized voltage alternation of each electrode, caused by applying current of alternative polarity. Horizontal
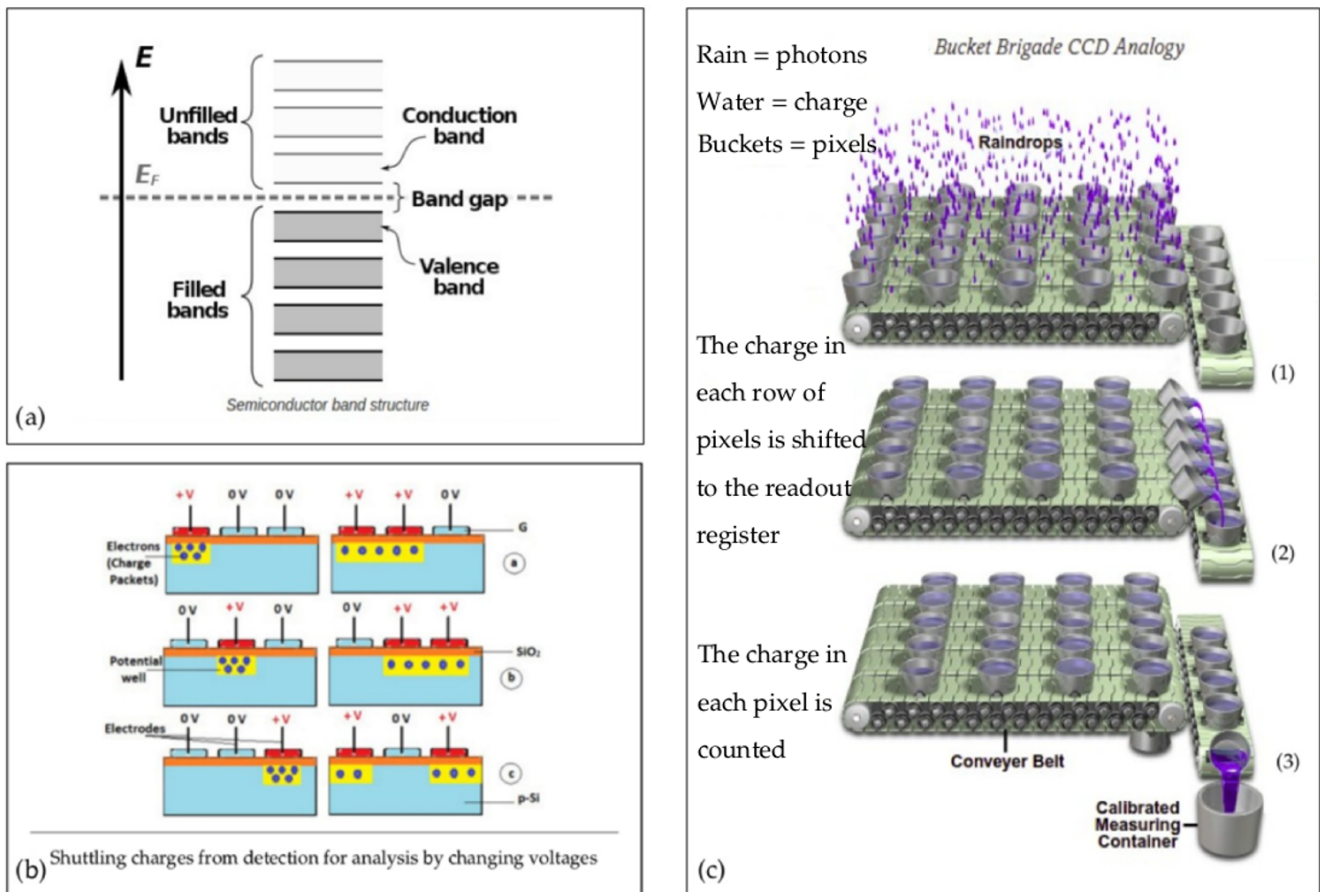
Figure 7.10: a) The energy gap (1.26 eV) that an electron must cover in a Si semi-conductor, in order to excited from the valence band to the conduction band. The Fermi level (E_F) is the highest energy occupied by electron orbital at absolute zero. b) Side view of a pixel's function in a CCD. For descriprion seee in the text. c) Four steps of image production in a CCD element: 1) generate photoelectrons-rain drops, 2) collect electrons-the buckets, 3) transfer the collected charges-the conveyer belts, 4) read the charges - waiting device at the edge of the element.

charge transfer is paused while charge packages at the output register are transferred vertically to an output electronic amplifier, and then read one by one. The cycle is repeated for each row until all the charges of all pixels are transferred and finally read out. The entire chip can be read in ~10 sec. The image that we see on screen in the end, is the pattern of electric charge transformed to a digital reconstruction.

Fig. 7.10b shows a pixel's structure from a side view. We can see the Si substrate, the produced photoelectrons stored at the pixel, the three electrodes of alternate voltage that force the electrons to move, and of course the final, horizontal movement of the electrons from pixel to pixel. Fig. 7.10c illustrates the classical example of "drop rain-buckets", which presents in a very representative way the function of a CCD pixel.

7.5   Echelle spectrometer

Echelle spectroscopy is used for separating polychromatic light collected from faint sources, like the SNRs, into its constituent monochromatic components, at the highest achieved resolution. In this section, we present the basic theoretical background necessary for the comprehension of the MES-SPM spectrograph, the echelle spectrometer used for obtaining the spectra for this project.

Reflecive diffraction grating: A reflective diffraction grating is the optical device of the spectrograph through which the incident beam is finally analysed in its components. It is a non-uniform surface on which a periodically repeated pattern of grooves (diffraction elements) has been cut (Fig. 7.11). If this pattern is "serrated", and the incident beam is reflected onto it, then it is named "echelle" reflective diffraction grating (echelle means ladder in French). If d is the length of each groove, then we define the parameter *groove frequency* or *groove density*, or more commonly used "grooves per mm", as: G = 1/d.
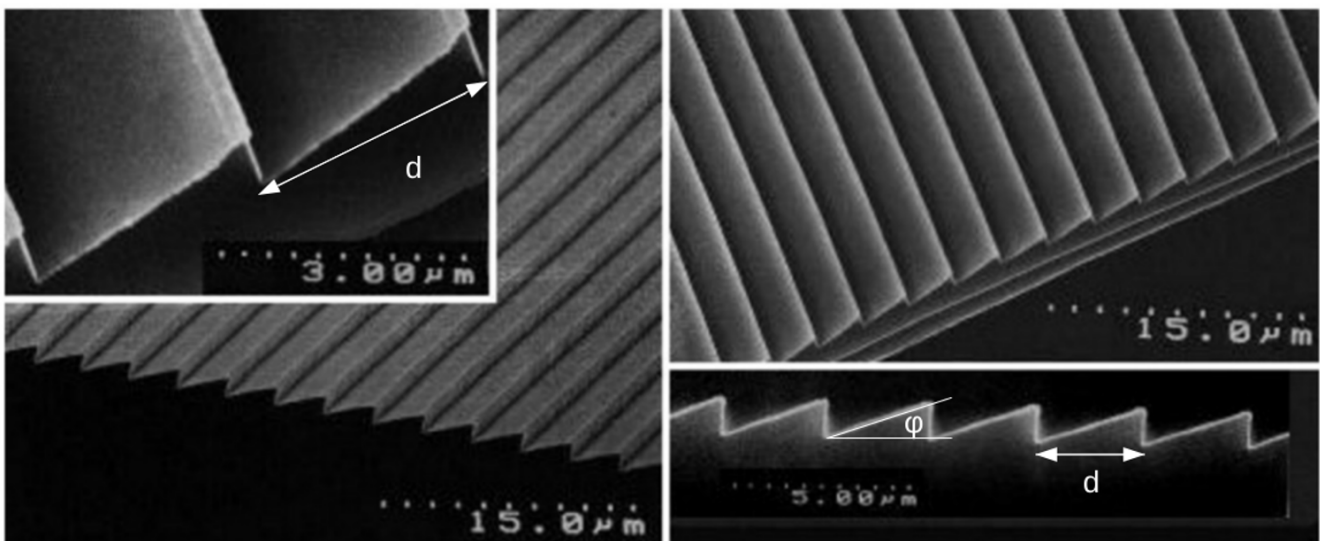
Figure 7.11: Scanning electron microscope of an echelle reflective diffraction grating. On the left, the length of the groove is d=3μm, while on the right d=2.5μm. Also labelled is the blazed angle ϕ of the grating. For description see in the text.

Grating equation: Exploiting the wave property of light (and not its particle property), we assume a planar wavefront (surface of constant phase) composed by two parallel rays, 1 and 2, falling on a groove, spacing d apart (Fig. 7.12a). α and β are the incident and the diffraction angles respectively, with respect to the grating normal. As we can see, different parts of the
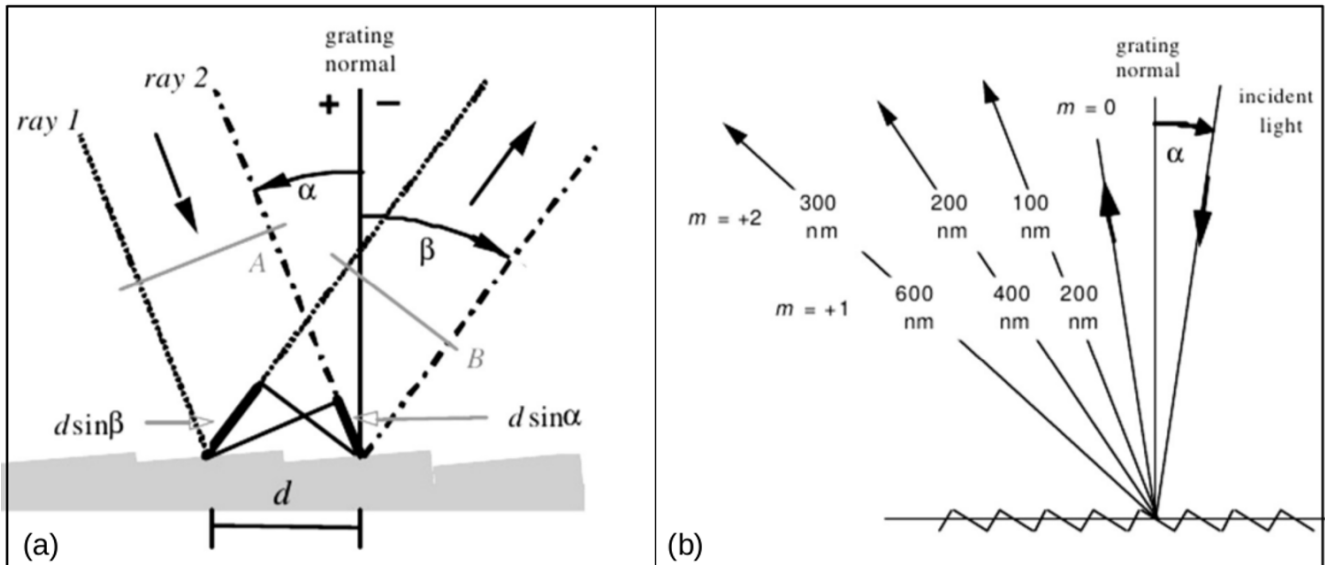
Figure 7.12: a) Geometry of diffraction for planar wavefronts, on an echelle reflective diffraction grating. For description see in the text. b) Overlapping of spectral orders: the light for wavelengths 100, 200 and 300 nm in the second order $m = 2$ is diffracted in the same direction as the light for wavelengths 200, 400 and 600 nm in the first order $m = 1$. Credits: "Diffraction grating handbook", Christopher Palmer, Erwin Loewen.

wavefront strike on the groove at different times. Hence, ray 1 arrives on the groove first, and ray 2 follows it after covering a distance dsinα. Subsequently, ray 1 is the first which is reflected from the groove and, after it has covered a distance dsinβ, ray 2 begins its reflection from the groove too.

In the case we study, the elementary law of reflection cannot be applied (i.e. the reflection angle is equal to the angle of incidence). This is only valid when the incident surface is totally smooth and the surface is much larger than the wavelength of the incident light, which is not the case here. In our case, Huygens principle can be applied, according to which, each part of the wavefront that encounters the groove acts as a source of secondary wavefronts (spherical sources of light) after its reflection. In order for these secondary wavefronts to present constructive interference (to show maxima of radiation), the path difference of the two rays must be an integer multiple of their wavelength λ:

$$m\lambda = d\left(sin\alpha + sin\beta\right) \tag{7.4}$$

This relationship is known as the "grating equation". In this, m is called *spectral order* or *diffraction order*, and quantifies how many λ of path difference are introduced between successive grooves on the grating. The groove spacing d is a feature of the grating, and the angle of the incident light α will be the same for all wavelengths. So, the only remaining variables

are the diffraction angle β and the wavelength λ. It is therefore clear that β must depend on λ, which is to say that the grating is a means of sending light of different wavelengths λ in different directions β, i.e. producing a spectrum – in our case, the spectrum of the SNR. Fig. 7.13 presents the diffraction of a polychromatic light from a grating and the produced spectrum on a panel at the laboratory. It is clear that in a diffraction grating the beam is not simply reflected, but analysed into its components like a fan, towards specific directions. This is the result of diffraction, i.e. the bending and diffusion of light when it encounters an obstacle. The obstacle here, is the sharp edge of each groove.

Spectral (diffraction) orders m: For particular values of d, λ and α, it is obvious that grating equation is satisfied by more than one diffraction angle β. On the other hand, as $|\sin\alpha + \sin\beta| \leq 2$, only these orders for which $|m\lambda/d| \leq 2$ exist. For $\beta = -\alpha$, $m = 0$ (*zero order* for specular reflection). By convection, when $m > 0$ the diffracted ray lies to the left of the zero order, while for $m < 0$ the diffracted ray lies to the right of the zero order (Fig. 7.12b).
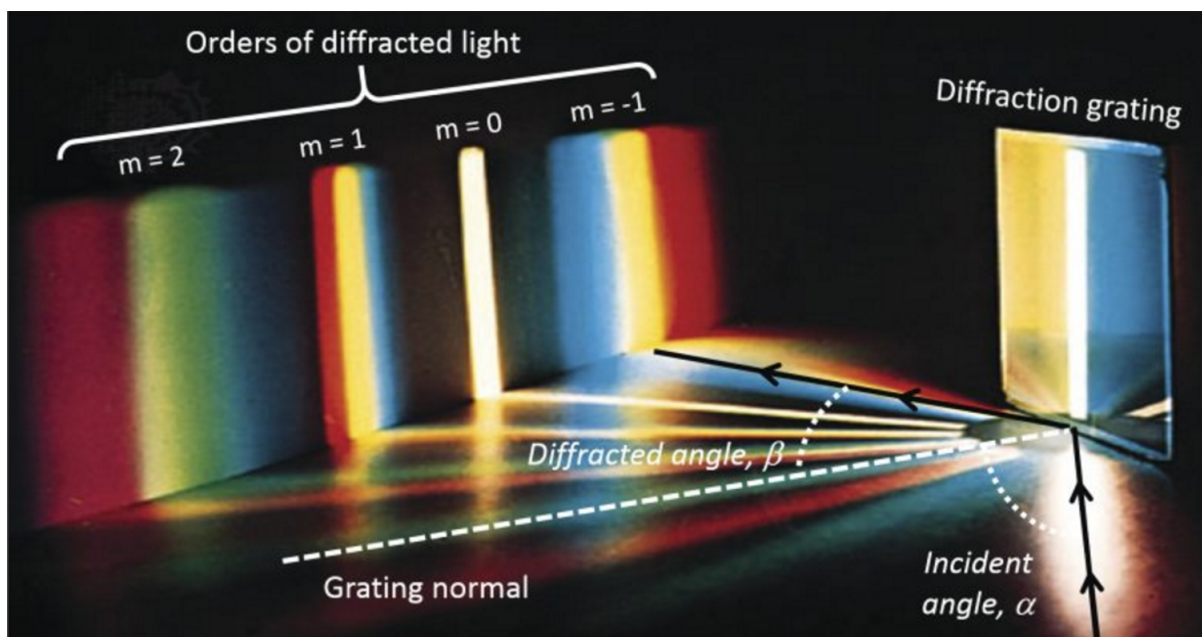
Figure 7.13: Experimental demonstration of polychromatic light diffracted from a grating. For the explanation of the spectral orders, see description in the text.

Blazed grating: The fact that the incoming light splits into many spectral orders m (positive and negative) shows that the spectrum of a single order will contain only a small fraction of the incoming radiation. As a solution, the diffraction elements of the grating are tilted by a *blazed angle* ϕ (Fig. 7.11), so that the direction of normal geometric reflection to coincide with the chosen order of diffraction. In other words, *blazed grating* enhances diffraction in one
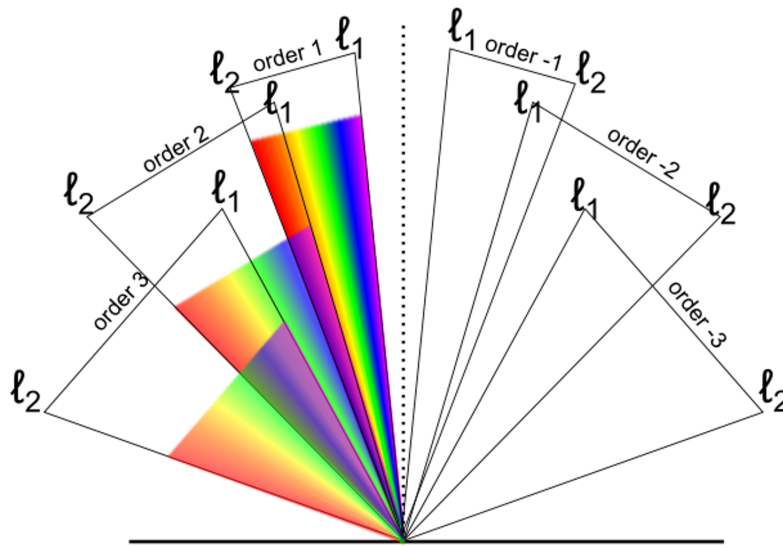
Figure 7.14: Overlapping spectra of adjacent spectral orders in a reflective diffraction grating.

direction in order to maximize the collected radiation in a specific order.

Overlapping of spectral orders: Superposition of wavelengths is inherent in the grating equation, and can be seen through an example in Fig. 7.12b: the light of wavelength $\lambda = 600$ nm (red) diffracted in the $m = 1$ order, will coincide with the light of wavelength $\lambda/2 = 300$nm (UV) diffracted in the $m = 2$ order. This would lead in doubtful results in the produced spectrum, but can be prevented by suitable filtering, called *order sorting*, which blocks out some wavelengths, or by the use of detectors sensitive at desired wavelengths.

Free spectral range:

It is defined as the largest range of wavelengths in a given spectral order m for which superposition of light from adjacent orders does not occur:

$$F_\lambda = \Delta\lambda = \frac{\lambda}{m} \tag{7.5}$$

In Fig. 7.14, overlapping of adjacent spectral orders is demonstrated as an example, and this is exactly what we want to avoid in an obtained spectrum.

Resolving power R:

It is a measure of the ability of the grating to distinguish two adjacent spectral lines $\lambda 1$ and $\lambda 2$, of average wavelength λ (see Fig. 7.15):

$$R = \frac{\lambda}{\Delta\lambda} = mN \tag{7.6}$$

177

Figure 7.15: Four 1-D echelle spectra of absorption lines from the same source are presented, obtained with increased resolution R each time. We see that, the higher the R the more detailed spectrum of a specific waveband range can be obtained. For the definition of resolution R, see in the text.
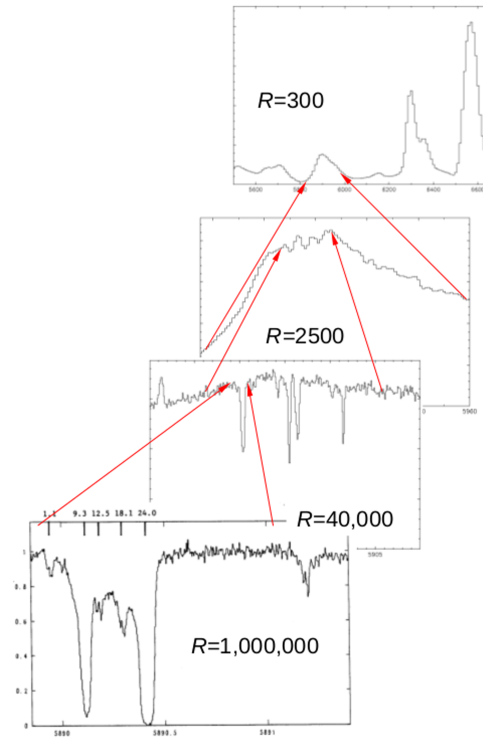
where $\Delta\lambda$ is the *limit of resolution* or simply *resolution*, i.e. the difference in wavelength between two lines of equal intensity that can be distinguished, m is the spectral order and N is the total number of grooves illuminated on the surface of the grating. In literature, the terms *resolving power* and *resolution* are sometimes interchanged.

In Fig. 7.16 the function of an echelle spectrometer is demonstrated. We can follow the line path of the beam from the point of its entrance to the slit, up to the point that is finally analysed into its components on the detector.
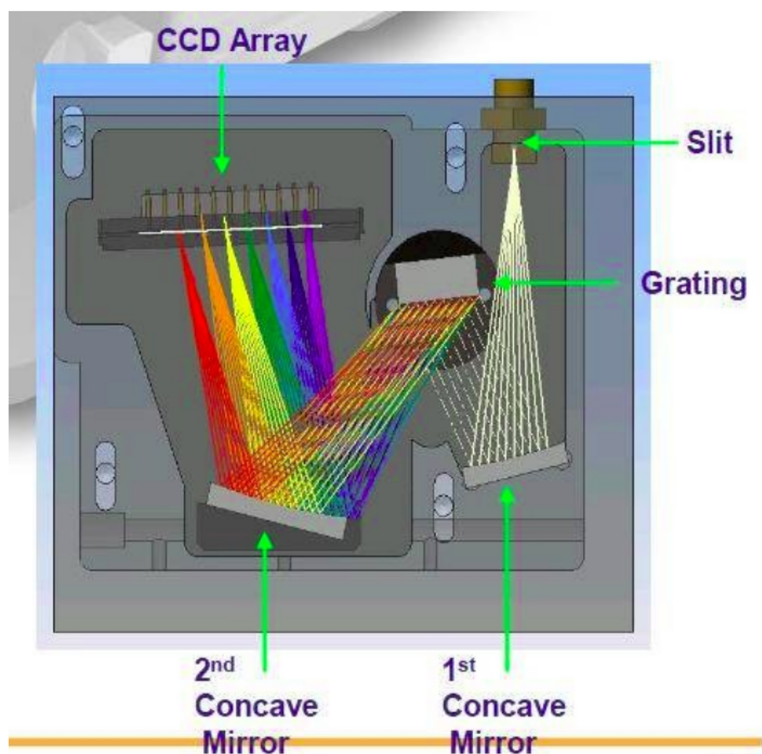
Figure 7.16: An example of the line path of a beam inside an echelle spectrometer: the beam enters through the slit, is reflected on the first mirror, is diffracted onto the echelle grating, is reflected for a second time and in the end every emission line is depicted onto the detector (CCD array.)

References

Abellán, F. J., Indebetouw, R., Marcaide, J. M., Gabler, M., Fransson, C., Spyromilio, J., Burrows, D. N., Chevalier, R., Cigan, P., Gaensler, B. M., Gomez, H. L., Janka, H. T., Kirshner, R., Larsson, J., Lundqvist, P., Matsuura, M., McCray, R., Ng, C. Y., Park, S., Roche, P., Staveley-Smith, L., van Loon, J. T., Wheeler, J. C., and Woosley, S. E. (2017). Very Deep inside the SN 1987A Core Ejecta: Molecular Structures Seen in 3D. apjl, 842(2):L24.

Acker, A. and Neiner, C. (2003). Quantitative classification of WR nuclei of planetary nebulae. A&A, 403:659–673.

Akashi, M., Sabach, E., Yogev, O., and Soker, N. (2015). Forming equatorial rings around dying stars. MNRAS, 453:2115–2125.

Akashi, M. and Soker, N. (2008). Shaping planetary nebulae by light jets. MNRAS, 391:1063–1074.

Akras, S., Boumis, P., Meaburn, J., Alikakos, J., López, J. A., and Gonçalves, D. R. (2015). Evidence for a [WR] or WEL-type binary nucleus in the bipolar planetary nebula Vy 1-2. MNRAS, 452:2911–2929.

Akras, S., Clyne, N., Boumis, P., Monteiro, H., Gonçalves, D. R., Redman, M. P., and Williams, S. (2016). Deciphering the bipolar planetary nebula Abell 14 with 3D ionization and morphological studies. MNRAS, 457:3409–3419.

Akras, S. and Gonçalves, D. R. (2016). Low-ionization structures in planetary nebulae - I. Physical, kinematic and excitation properties. MNRAS, 455:930–961.

Akras, S., Gonçalves, D. R., and Ramos-Larios, G. (2017). H_2 in low-ionization structures of planetary nebulae. MNRAS, 465:1289–1296.

Akras, S. and López, J. A. (2012). Three-dimensional modelling of the collimated bipolar outflows of compact planetary nebulae with Wolf-Rayet-type central stars. MNRAS, 425:2197–2202.

Akras, S. and Steffen, W. (2012). 'Distance mapping' and the 3D structure of BD +30° 3639. mnras, 423:925–933.

Alarie, A., Bilodeau, A., and Drissen, L. (2014). A hyperspectral view of Cassiopeia A. MNRAS, 441(4):2996–3008.

Alfvén, H. and Herlofson, N. (1950). Cosmic Radiation and Radio Stars. Physical Review, 78(5):616–616.

Allen, M. G., Groves, B. A., Dopita, M. A., Sutherland, R. S., and Kewley, L. J. (2008). The MAPPINGS III Library of Fast Radiative Shock Models. ApJS, 178(1):20-55.

Araya, M. (2013). Detection of gamma-ray emission in the region of the supernova remnants G296.5+10.0 and G166.0+4.3. MNRAS, 434(3):2202-2208.

Arias, M., Domek, V., Zhou, P., and Vink, J. (2019a). The environment of supernova remnant VRO 42.05.01 as probed with IRAM 30m molecular line observations. A&A, 627:A75.

Arias, M., Vink, J., Iacobelli, M., Domek, V., Haverkorn, M., Oonk, J. B. R., Polderman, I., Reich, W., White, G. J., and Zhou, P. (2019b). A low-frequency view of mixed-morphology supernova remnant VRO 42.05.01, and its neighbourhood. A&A, 622:A6.

Baade, W. (1944). The Resolution of Messier 32, NGC 205, and the Central Region of the Andromeda Nebula. ApJ, 100:137.

Bailer-Jones, C. A. L., Rybizki, J., Fouesneau, M., Mantelet, G., and Andrae, R. (2018). Estimating Distance from Parallaxes. IV. Distances to 1.33 Billion Stars in Gaia Data Release 2. AJ, 156:58.

Balick, B. (1987). The evolution of planetary nebulae. I - Structures, ionizations, and morphological sequences. AJ, 94:671-678.

Balick, B., Alexander, J., Hajian, A. R., Terzian, Y., Perinotto, M., and Patriarchi, P. (1998). FLIERs and Other Microstructures in Planetary Nebulae. IV. Images of Elliptical PNs from the Hubble Space Telescope. AJ, 116:360-371.

Balick, B., Rugers, M., Terzian, Y., and Chengalur, J. N. (1993). Fast, low-ionization emission regions and other microstructures in planetary nebulae. ApJ, 411:778-793.

Bell, A. R. (1978a). The acceleration of cosmic rays in shock fronts - I. MNRAS, 182:147-156.

Bell, A. R. (1978b). The acceleration of cosmic rays in shock fronts - II. MNRAS, 182:443-455.

Biggs, J. D. and Lyne, A. G. (1996). A Search for Radio Pulsars in Globular Clusters, Supernova Remnants and Transient X-Ray Sources. MNRAS, 282(2):691-698.

Blandford, R. D. and Ostriker, J. P. (1978). Particle acceleration by astrophysical shocks. apjl, 221:L29-L32.

Bocchino, F., Miceli, M., and Troja, E. (2009). On the metal abundances inside mixed-morphology supernova remnants: the case of IC 443 and G166.0+4.3. A&A, 498(1):139-145.

Boffin, H. M. J., Miszalski, B., Rauch, T., Jones, D., Corradi, R. L. M., Napiwotzki, R., Day-Jones, A. C., and Köppen, J. (2012). An Interacting Binary System Powers Precessing Outflows of an Evolved Star. Science, 338:773.

Bolte, J., Sasaki, M., and Breitschwerdt, D. (2015). 3D hydrodynamic simulations of the Galactic supernova remnant CTB 109. A&A, 582:A47.

Borkowski, K. (1996). A Search for Jets in Planetary Nebulae. HST Proposal.

Boumis, P. (2019). Optical study of the peculiar supernova remnant VRO 42.05.01 (G 166+4.3). In Supernova Remnants: An Odyssey in Space after Stellar Death II, page 13.

Boumis, P., Akras, S., Leonidaki, I., Chiotellis, A., Kopsacheili, M., Alikakos, J., Nanouris, N., and Mavromatakis, F. (2016). A deep optical study of the supernova remnant G 166+4.3 (VRO). In Supernova Remnants: An Odyssey in Space after Stellar Death, page 15.

Boumis, P., Akras, S., Xilouris, E. M., Mavromatakis, F., Kapakos, E., Papamastorakis, J., and Goudis, C. D. (2006). New planetary nebulae in the Galactic bulge region with l >0°- II. mnras, 367:1551–1561.

Boumis, P., Alikakos, I., and Mavromatakis, F. (2012). Deep optical observations and study of the VRO supernova remnant. In Papadakis, I. and Anastasiadis, A., editors, 10th Hellenic Astronomical Conference, pages 27–27.

Boumis, P., Meaburn, J., López, J. A., Mavromatakis, F., Redman, M. P., Harman, D. J., and Goudis, C. D. (2004). The kinematics of the bi-lobal supernova remnant G 65.3+5.7. II.. A&A, 424:583–588.

Boumis, P., Paleologou, E. V., Mavromatakis, F., and Papamastorakis, J. (2003). New planetary nebulae in the Galactic bulge region with l > 0°- I. Discovery method and first results. MNRAS, 339(3):735–747.

Braun, R. and Strom, R. G. (1986). Observations of post-shock neutral hydrogen in four evolved supernovaremnants. A&AS, 63:345.

Burrows, D. N. and Guo, Z. (1994). ROSAT Observations of VRO 42.05.01. apjl, 421:L19.

Castor, J., McCray, R., and Weaver, R. (1975). Interstellar bubbles. apjl, 200:L107–L110.

Chiotellis, A., Boumis, P., Derlopa, S., and Steffen, W. (2019). VRO 42.05.01: A supernova remnant resulted by a supersonic, mass losing progenitor star. arXiv e-prints, page arXiv:1909.08947.

Chiotellis, A., Schure, K. M., and Vink, J. (2012). The imprint of a symbiotic binary progenitor on the properties of Kepler's supernova remnant. A&A, 537:A139.

Chu, Y.-H., Guerrero, M. A., and Gruendl, R. A. (2000). X-rays from Planetary Nebulae. In Kastner, J. H., Soker, N., and Rappaport, S., editors, Asymmetrical Planetary Nebulae II: From Origins to Microstructures, volume 199 of Astronomical Society of the Pacific Conference Series, page 419.

Cioffi, D. F., McKee, C. F., and Bertschinger, E. (1988). Dynamics of Radiative Supernova Remnants. ApJ, 334:252.

Clyne, N., Akras, S., Steffen, W., Redman, M. P., Gonçalves, D. R., and Harvey, E. (2015a). A morpho-kinematic and spectroscopic study of the bipolar nebulae: M 2-9, Mz 3, and Hen 2-104. A&A, 582:A60.

Clyne, N., Akras, S., Steffen, W., Redman, M. P., Gonçalves, D. R., and Harvey, E. (2015b). A morpho-kinematic and spectroscopic study of the bipolar nebulae: M 2-9, Mz 3, and Hen 2-104. A&A, 582:A60.

Corradi, R. L. M., García-Rojas, J., Jones, D., and Rodríguez-Gil, P. (2015). Binarity and the Abundance Discrepancy Problem in Planetary Nebulae. ApJ, 803:99.

Corradi, R. L. M., Manso, R., Mampaso, A., and Schwarz, H. E. (1996). Unveiling low-ionization microstructures in planetary nebulae. A&A, 313:913–923.

Corradi, R. L. M., Perinotto, M., Villaver, E., Mampaso, A., and Gonçalves, D. R. (1999). Jets, Knots, and Tails in Planetary Nebulae: NGC 3918, K1-2, and Wray 17-1. ApJ, 523:721–733.

Corradi, R. L. M., Sabin, L., Miszalski, B., Rodríguez-Gil, P., Santander-García, M., Jones, D., Drew, J. E., Mampaso, A., Barlow, M. J., Rubio-Díez, M. M., Casares, J., Viironen, K., Frew, D. J., Giammanco, C., Greimel, R., and Sale, S. E. (2011). The Necklace: equatorial and polar outflows from the binary central star of the new planetary nebula IPHASX J194359.5+170901. MNRAS, 410:1349–1359.

Crowley, C. (2006). Red Giant Mass-Loss: Studying Evolved Stellar Winds with FUSE and HST/STIS. PhD thesis, School of Physics, Trinity College Dublin, Dublin 2, Ireland Ireland.

Danehkar, A. (2014). Evolution of Planetary Nebulae with WR-type Central Stars. PhD thesis, Macquarie University, Australia.

Decin, L., Montargès, M., Richards, A. M. S., Gottlieb, C. A., Homan, W., McDonald, I., El Mellah, I., Danilovich, T., Wallström, S. H. J., Zijlstra, A., Baudry, A., Bolte, J., Cannon, E., De Beck, E., De Ceuster, F., de Koter, A., De Ridder, J., Etoka, S., Gobrecht, D., Gray, M., Herpin, F., Jeste, M., Lagadec, E., Kervella, P., Khouri, T., Menten, K., Millar, T. J., Müller, H. S. P., Plane, J. M. C., Sahai, R., Sana, H., Van de Sande, M., Waters, L. B. F. M., Wong, K. T., and Yates, J. (2020). (Sub)stellar companions shape the winds of evolved stars. Science, 369(6510):1497–1500.

DeLaney, T., Rudnick, L., Stage, M. D., Smith, J. D., Isensee, K., Rho, J., Allen, G. E., Gomez, H., Kozasa, T., Reach, W. T., Davis, J. E., and Houck, J. C. (2010). The Three-dimensional Structure of Cassiopeia A. ApJ, 725(2):2038–2058.

Derlopa, S., Akras, S., Boumis, P., and Steffen, W. (2019). High-velocity string of knots in the outburst of the planetary nebula Hb4. MNRAS, 484(3):3746–3754.

Devine, D., Bally, J., Reipurth, B., and Heathcote, S. (1997). Kinematics and Evolution of the Giant HH34 Complex. AJ, 114:2095.

Dickel, J. R., McGuire, J. P., and Yang, K. S. (1965). Radio Emission from a Supernova Remnant in Auriga. ApJ, 142:798.

D'Odorico, S. and Sabbadin, F. (1977). A spectroscopic survey of supernova remnant candidates in the $\lambda\lambda$6000-6800 Å spectral region: The observations. A&AS, 28:439.

Dubner, G. and Giacani, E. (2015). Radio emission from supernova remnants. aapr, 23:3.

Dwarkadas, V. V. (2005). The Evolution of Supernovae in Circumstellar Wind-Blown Bubbles. I. Introduction and One-Dimensional Calculations. ApJ, 630(2):892–910.

Dwarkadas, V. V. and Rosenberg, D. (2015). X-ray Emission from Ionized Wind-Bubbles around Wolf-Rayet Stars. In Hamann, W.-R., Sander, A., and Todt, H., editors, Wolf-Rayet Stars, pages 329–332.

Esipov, V. F., Kaplan, S. A., Lozinskaya, T. A., and Podstrigach, T. S. (1972). Spectrophotometric Investigations of Filamentary Nebulae. sovast, 16:81.

Espey, B. R. and Crowley, C. (2008). Mass-loss from Red Giants. In Evans, A., Bode, M. F., O'Brien, T. J., and Darnley, M. J., editors, RS Ophiuchi (2006) and the Recurrent Nova Phenomenon, volume 401 of Astronomical Society of the Pacific Conference Series, page 166.

Fang, X., Zhang, Y., Kwok, S., Hsia, C.-H., Chau, W., Ramos-Larios, G., and Guerrero, M. A. (2018). Extended Structures of Planetary Nebulae Detected in H_2 Emission. ApJ, 859(2):92.

Fermi, E. (1949). On the Origin of the Cosmic Radiation. Physical Review, 75(8):1169–1174.

Fesen, R. A., Blair, W. P., and Kirshner, R. P. (1985). Optical emission-line properties of evolved galactic supernova remnants. ApJ, 292:29–48.

Fesen, R. A., Gull, T. R., and Ketelsen, D. A. (1983). Deep O III interference filter imagery of the supernova remnants G 65.3+5.7, G 126.2+1.6, CTA 1 and VRO 42.05.01. ApJS, 51:337–344.

Filippenko, A. V. (1997). Optical Spectra of Supernovae. araa, 35:309–355.

Franco, J., Tenorio-Tagle, G., Bodenheimer, P., and Rozyczka, M. (1991). Evolution of Supernova Remnant Inside Preexisting Wind-Driven Cavities. PASP, 103:803.

Frank, A., Chen, Z., Reichardt, T., De Marco, O., Blackman, E., and Nordhaus, J. (2018). Planetary Nebulae Shaped By Common Envelope Evolution. ArXiv e-prints.

Frew, D. J., Parker, Q. A., and Bojii, I. S. (2016). The $H\alpha$ surface brightness-radius relation: a robust statistical distance indicator for planetary nebulae. MNRAS, 455:1459–1488.

Gaia Collaboration (2018). VizieR Online Data Catalog: Gaia DR2 (Gaia Collaboration, 2018). VizieR Online Data Catalog, 1345.

García-Díaz, M. T., López, J. A., Steffen, W., and Richer, M. G. (2012). A Detailed Morpho-kinematic Model of the Eskimo, NGC 2392: A Unifying View with the Cat's Eye and Saturn Planetary Nebulae. ApJ, 761:172.

García-Rojas, J., Peña, M., Morisset, C., Delgado-Inglada, G., Mesa-Delgado, A., and Ruiz, M. T. (2013). Analysis of chemical abundances in planetary nebulae with [WC] central stars. II. Chemical abundances and the abundance discrepancy factor. A&A, 558:A122.

García-Segura, G., Langer, N., Róyczka, M., and Franco, J. (1999). Shaping Bipolar and Elliptical Planetary Nebulae: Effects of Stellar Rotation, Photoionization Heating, and Magnetic Fields. ApJ, 517:767–781.

García-Segura, G., López, J. A., Steffen, W., Meaburn, J., and Manchado, A. (2006). The Dynamical Evolution of Planetary Nebulae after the Fast Wind. apjl, 646:L61–L64.

García-Segura, G., Ricker, P. M., and Taam, R. E. (2018). Common Envelope Shaping of Planetary Nebulae. ApJ, 860:19.

García-Segura, G., Villaver, E., Langer, N., Yoon, S.-C., and Manchado, A. (2014). Single Rotating Stars and the Formation of Bipolar Planetary Nebula. ApJ, 783:74.

García-Segura, G., Villaver, E., Manchado, A., Langer, N., and Yoon, S.-C. (2016). Rotating Stars and the Formation of Bipolar Planetary Nebulae. II. Tidal Spin-up. ApJ, 823:142.

Gómez, J. F., Niccolini, G., Suárez, O., Miranda, L. F., Rizzo, J. R., Uscanga, L., Green, J. A., and de Gregorio-Monsalvo, I. (2018). ALMA imaging of the nascent planetary nebula IRAS 15103-5754. MNRAS, 480:4991-5009.

Gómez-Gordillo, S., Akras, S., Gonçalves, D. R., and Steffen, W. (2020). Distance mapping applied to four well-known planetary nebulae and a nova shell. MNRAS, 492(3):4097-4111.

Gonçalves, D. R., Corradi, R. L. M., and Mampaso, A. (2001). Low-Ionization Structures in Planetary Nebulae: Confronting Models with Observations. ApJ, 547:302-310.

Górny, S. K., Stasiska, G., Escudero, A. V., and Costa, R. D. D. (2004). The populations of planetary nebulae in the direction of the Galactic bulge. Chemical abundances and Wolf-Rayet central stars. A&A, 427:231-244.

Green, D. A. (2019). A revised catalogue of 294 Galactic supernova remnants. Journal of Astrophysics and Astronomy, 40(4):36.

Guerrero, M. A. and Miranda, L. F. (2012). NGC 6778: a disrupted planetary nebula around a binary central star. A&A, 539:A47.

Guo, Z. and Burrows, D. N. (1997). ASCA Observations of the Supernova Remnant VRO 42.05.01. apjl, 480(1):L51-L54.

Hajian, A. R., Balick, B., Terzian, Y., and Perinotto, M. (1997). FLIERs and Other Microstructures in Planetary Nebulae. III. ApJ, 487:304-313.

Harman, D. J., Bryce, M., López, J. A., Meaburn, J., and Holloway, A. J. (2004). J320 (PN G190.3-17.7) as a poly-polar planetary nebula surrounded by point-symmetric knots. MNRAS, 348:1047-1054.

Hartigan, P., Raymond, J., and Hartmann, L. (1987). Radiative Bow Shock Models of Herbig-Haro Objects. ApJ, 316:323.

Heger, A., Fryer, C. L., Woosley, S. E., Langer, N., and Hartmann, D. H. (2003). How Massive Single Stars End Their Life. ApJ, 591(1):288-300.

Hester, J. J. (2008). The Crab Nebula : an astrophysical chimera. araa, 46:127-155.

Höfner, S. and Olofsson, H. (2018). Mass loss of stars on the asymptotic giant branch. Mechanisms, models and measurements. aapr, 26(1):1.

How, T. G., Fesen, R. A., Neustadt, J. M. M., Black, C. S., and Outters, N. (2018). Optical emission associated with the Galactic supernova remnant G179.0+2.6. MNRAS, 478(2):1987–1993.

Huarte-Espinosa, M., Carroll-Nellenback, J., Nordhaus, J., Frank, A., and Blackman, E. G. (2013). The formation and evolution of wind-capture discs in binary systems. MNRAS, 433:295–306.

Icke, V. (1988). Blowing bubbles. A&A, 202:177–188.

Jones, D., Boffin, H. M. J., Miszalski, B., Wesson, R., Corradi, R. L. M., and Tyndall, A. A. (2014). The post-common-envelope, binary central star of the planetary nebula Hen 2-11. A&A, 562:A89.

Kiepenheuer, K. O. (1950). Cosmic Rays as the Source of General Galactic Radio Emission. Physical Review, 79(4):738–739.

Kopsacheili, M., Zezas, A., and Leonidaki, I. (2020). A diagnostic tool for the identification of supernova remnants. MNRAS, 491(1):889–902.

Kwok, S. (1975). Radiation pressure on grains as a mechanism for mass loss in red giants. ApJ, 198:583–591.

Kwok, S. (2010). Morphological Structures of Planetary Nebulae. pasa, 27(2):174–179.

Kwok, S., Purton, C. R., and Fitzgerald, P. M. (1978). On the origin of planetary nebulae. apjl, 219:L125–L127.

Landecker, T. L., Pineault, S., Routledge, D., and Vaneldik, J. F. (1982). VRO 42.05.01 - One supernova remnant or two. apjl, 261:L41–L45.

Landecker, T. L., Pineault, S., Routledge, D., and Vaneldik, J. F. (1989). The interaction of the supernova remnant VRO 42.05.01 with its HI environment. MNRAS, 237:277–297.

Livio, M. and Soker, N. (1988). The common envelope phase in the evolution of binary stars. ApJ, 329:764–779.

Lopez, J. A., Meaburn, J., and Palmer, J. W. (1993). Kinematical Evidence for a Rotating, Episodic Jet in the Planetary Nebula Fleming 1. apjl, 415:L135.

López, J. A., Steffen, W., and Meaburn, J. (1997). Bipolar, Collimated Outbursts in the Planetary Nebula Hb 4. ApJ, 485:697–702.

Lopez, J. A., Vazquez, R., and Rodriguez, L. F. (1995). The Discovery of a Bipolar, Rotating, Episodic Jet (BRET) in the Planetary Nebula KjPn 8. apjl, 455:L63.

Lorimer, D. R., Lyne, A. G., and Camilo, F. (1998). A search for pulsars in supernova remnants. A&A, 331:1002–1010.

Lozinskaia, T. A. (1979). The supernova remnants IC 443 and VRO 42.05.01: fast filaments and high-velocity gas. Australian Journal of Physics, 32:113–121.

Manchado, A., Stanghellini, L., Villaver, E., García-Segura, G., Shaw, R. A., and García-Hernández, D. A. (2015). High-resolution Imaging of NGC 2346 with GSAOI/GeMS: Disentangling the Planetary Nebula Molecular Structure to Understand Its Origin and Evolution. ApJ, 808:115.

Matheson, H. and Safi-Harb, S. (2010). The Plerionic Supernova Remnant G21.5-0.9 Powered by PSR J1833-1034: New Spectroscopic and Imaging Results Revealed with the Chandra X-ray Observatory. ApJ, 724(1):572–587.

Mathewson, D. S. and Clarke, J. N. (1973). Supernova remnants in the Large Magellanic Cloud. ApJ, 180:725–738.

Matsumura, H., Uchida, H., Tanaka, T., Tsuru, T. G., Nobukawa, M., Nobukawa, K. K., and Itou, M. (2017). Localized recombining plasma in G166.0+4.3: A supernova remnant with an unusual morphology. pasj, 69(2):30.

Mauron, N. and Josselin, E. (2011). The mass-loss rates of red supergiants and the de Jager prescription. A&A, 526:A156.

Mayer, C. H., McCullough, T. P., and Sloanaker, R. M. (1957). Evidence for Polarized Radio Radiation from the Crab Nebula. ApJ, 126:468.

McKee, C. F. (1974). X-Ray Emission from an Inward-Propagating Shock in Young Supernova Remnants. ApJ, 188:335–340.

McKee, C. F. (1988). Supernova Remnant Shocks in an Inhomogeneous Interstellar Medium. In Roger, R. S. and Landecker, T. L., editors, IAU Colloq. 101: Supernova Remnants and the Interstellar Medium, page 205.

McKee, C. F. and Ostriker, J. P. (1977). A theory of the interstellar medium: three components regulated by supernova explosions in an inhomogeneous substrate. ApJ, 218:148–169.

Meaburn, J., López, J. A., Gutiérrez, L., Quiróz, F., Murillo, J. M., Valdéz, J., and Pedrayez, M. (2003). The Manchester Echelle Spectrometer at the San Pedro Mártir Observatory (MES-SPM). rmxaa, 39:185-195.

Milisavljevic, D. and Fesen, R. A. (2013). A Detailed Kinematic Map of Cassiopeia A's Optical Main Shell and Outer High-velocity Ejecta. ApJ, 772(2):134.

Miszalski, B., Acker, A., Parker, Q. A., and Moffat, A. F. J. (2009). Binary planetary nebulae nuclei towards the Galactic bulge. II. A penchant for bipolarity and low-ionisation structures. A&A, 505:249-263.

Miszalski, B., Corradi, R. L. M., Boffin, H. M. J., Jones, D., Sabin, L., Santander-García, M., Rodríguez-Gil, P., and Rubio-Díez, M. M. (2011). ETHOS 1: a high-latitude planetary nebula with jets forged by a post-common-envelope binary central star. MNRAS, 413:1264-1274.

Oort, J. H. (1951). Interaction of Nova and Supernova Shells With the Interstellar Medium. In Problems of Cosmical Aerodynamics, page 118.

Orlando, S., Ono, M., Nagataki, S., Miceli, M., Umeda, H., Ferrand, G., Bocchino, F., Petruk, O., Peres, G., Takahashi, K., and Yoshida, T. (2019). Hydrodynamic simulations unravel the progenitor-supernova-remnant connection in SN 1987A. arXiv e-prints, page arXiv:1912.03070.

Orosz, G., Gomez, J. F., Imai, H., Tafoya, D., Torrelles, J. M., Burns, R. A., Frau, P., Guerrero, M. A., Miranda, L. F., Perez-Torres, M. A., Ramos-Larios, G., Rizzo, J. R., Suarez, O., and Uscanga, L. (2018). Rapidly-evolving episodic outflow in IRAS 18113-2503: clues to the ejection mechanism of the fastest water fountain. ArXiv e-prints.

Osterbrock, D. E. and Ferland, G. J. (2006). Astrophysics of gaseous nebulae and active galactic nuclei.

Paczyski, B. (1971). Evolution of Single Stars. VI. Model Nuclei of Planetary Nebulae. actaa, 21:417.

Palmer, J. W., Lopez, J. A., Meaburn, J., and Lloyd, H. M. (1996). The kinematics and morphology of the planetary nebula Fleming 1. Bullets, jets and an expanding ring. A&A, 307:225.

Parker, R. A. R., Gull, T. R., and Kirshner, R. P. (1979). An emission-line survey of the Milky Way, volume 434.

Peña, M., Ruiz-Escobedo, F., Rechy-García, J. S., and García-Rojas, J. (2017). The kinematic behaviour of optical recombination lines and collisionally excited lines in Galactic planetary nebulae*†. mnras, 472:1182-1194.

Perea-Calderón, J. V., García-Hernández, D. A., García-Lario, P., Szczerba, R., and Bobrowsky, M. (2009). The mixed chemistry phenomenon in Galactic Bulge PNe. A&A, 495:L5-L8.

Perinotto, M. (2000). Gas Dynamics in Planetary Nebulae: From Macro-structures to FLIERs. apss, 274:205-219.

Pineault, S., Landecker, T. L., and Routledge, D. (1987). VRO 42.05.01: A Supernova Remnant Reenergizing an Interstellar Cavity. ApJ, 315:580.

Pineault, S., Pritchet, C. J., Landecker, T. L., Routledge, D., and Vaneldik, J. F. (1985). Optical and radio imaging of the supernova remnant VRO 42.05.01 (G 166.0+4.3). A&A, 151:52-60.

Potter, T. M., Staveley-Smith, L., Reville, B., Ng, C. Y., Bicknell, G. V., Sutherland, R. S., and Wagner, A. Y. (2014). Multi-dimensional Simulations of the Expanding Supernova Remnant of SN 1987A. ApJ, 794(2):174.

Pradhan, P., Bozzo, E., Paul, B., Manousakis, A., and Ferrigno, C. (2019). Probing Clumpy Wind Accretion in IGR J18027-2016 with XMM-Newton. ApJ, 883(2):116.

Rabaça, C. R., Cuisinier, F., Lorenz-Martins, S., Epitácio Pereira, D. N., Gonçalves, D. R., and Lastennet, E. (2003). New Insight on Hubble 4. In Kwok, S., Dopita, M., and Sutherland, R., editors, Planetary Nebulae: Their Evolution and Role in the Universe, volume 209 of IAU Symposium, page 491.

Raga, A. C., Riera, A., Mellema, G., Esquivel, A., and Velázquez, P. F. (2008). Line ratios from shocked cloudlets in planetary nebulae. A&A, 489:1141-1150.

Raymond, J. C. (1979). Shock waves in the interstellar medium. ApJS, 39:1-27.

Reynolds, S. P. (2017). Dynamical Evolution and Radiative Processes of Supernova Remnants, page 1981.

Rho, J. and Petre, R. (1998). Mixed-Morphology Supernova Remnants. apjl, 503(2):L167-L170.

Riera, A., García-Lario, P., Manchado, A., Bobrowsky, M., and Estalella, R. (2002). New Observations of the High-Velocity Outflows of the Proto-Planetary Nebula Hen 3-1475. In Henney, W. J., Steffen, W., Binette, L., and Raga, A., editors, Revista Mexicana de Astronomia y Astrofisica Conference Series, volume 13 of Revista Mexicana de Astronomia y Astrofisica Conference Series, pages 127-132.

Robinson, G. J., Reay, N. K., and Atherton, P. D. (1982). Measurements of expansion velocities in planetary nebulae. MNRAS, 199:649-657.

Ruiz, N., Chu, Y. H., Gruendl, R. A., Guerrero, M. A., Jacob, R., Schönberner, D., and Steffen, M. (2013). Detection of Diffuse X-Ray Emission from Planetary Nebulae with Nebular O VI. ApJ, 767(1):35.

Safi-Harb, S. (2012). Plerionic supernova remnants. In Aharonian, F. A., Hofmann, W., and Rieger, F. M., editors, American Institute of Physics Conference Series, volume 1505 of American Institute of Physics Conference Series, pages 13–20.

Sahai, R., Morris, M. R., and Villar, G. G. (2011). Young Planetary Nebulae: Hubble Space Telescope Imaging and a New Morphological Classification System. AJ, 141:134.

Schwarz, H. E., Corradi, R. L. M., and Melnick, J. (1992). A catalogue of narrow band images of planetary nebulae. A&AS, 96:23–113.

Sedov, L. I. (1959). Similarity and Dimensional Methods in Mechanics.

Sharpless, S. (1959). A Catalogue of H II Regions. ApJS, 4:257.

Shklovsky, I. S. (1956). The nature of planetary nebulae and their nuclei. azh, 33:315–329.

Soker, N. and Livio, M. (1994). Disks and jets in planetary nebulae. ApJ, 421:219–224.

Soker, N. and Rappaport, S. (2000). The Formation of Very Narrow Waist Bipolar Planetary Nebulae. ApJ, 538:241–259.

Steffen, W. and Koning, N. (2017). Hybrid polygon and hydrodynamic nebula modeling with multi-waveband radiation transfer in astrophysics. Astronomy and Computing, 20:87–96.

Steffen, W., Koning, N., Wenger, S., Morisset, C., and Magnor, M. (2011). Shape: A 3D Modeling Tool for Astrophysics. IEEE Transactions on Visualization and Computer Graphics, Volume 17, Issue 4, p.454-465, 17:454–465.

Steffen, W. and López, J. A. (2006). Morpho-Kinematic Modeling of Gaseous Nebulae with SHAPE. rmxaa, 42:99–105.

Taylor, G. (1950). The Formation of a Blast Wave by a Very Intense Explosion. I. Theoretical Discussion. Proceedings of the Royal Society of London Series A, 201(1065):159–174.

Tocknell, J., De Marco, O., and Wardle, M. (2014). Constraints on common envelope magnetic fields from observations of jets in planetary nebulae. MNRAS, 439:2014–2024.

Toledo-Roy, J. C., Velázquez, P. F., Esquivel, A., and Giacani, E. (2014). A blowout numerical model for the supernova remnant G352.7-0.1. MNRAS, 437(1):898–905.

van den Bergh, S. (1960). An Optical Search for Possible Supernova Remnants. zap, 51:15.

van den Bergh, S., Marscher, A. P., and Terzian, Y. (1973). An Optical Atlas of Galactic Supernova Remnants. ApJS, 26:19.

van Loon, J. T., Cioni, M. R. L., Zijlstra, A. A., and Loup, C. (2005). An empirical formula for the mass-loss rates of dust-enshrouded red supergiants and oxygen-rich Asymptotic Giant Branch stars. A&A, 438(1):273-289.

Vaytet, N. M. H., Rushton, A. P., Lloyd, M., López, J. A., Meaburn, J., O'Brien, T. J., Mitchell, D. L., and Pollacco, D. (2009). High-speed knots in the hourglass-shaped planetary nebula Hubble 12. MNRAS, 398:385-393.

Vink, J. (2004). A Review of X-ray Observations of Supernova Remnants. Nuclear Physics B Proceedings Supplements, 132:21-30.

Vink, J. (2012). Supernova remnants: the X-ray perspective. aapr, 20:49.

Vink, J. (2017). X-Ray Emission Properties of Supernova Remnants, page 2063.

Weaver, R., McCray, R., Castor, J., Shapiro, P., and Moore, R. (1977). Interstellar bubbles. II. Structure and evolution. ApJ, 218:377-395.

Weidmann, W. A., Schmidt, E. O., Vena Valdarenas, R. R., Ahumada, J. A., Volpe, M. G., and Mudrik, A. (2016). Atlas of monochromatic images of planetary nebulae. A&A, 592:A103.

Williams, B. J., Coyle, N. M., Yamaguchi, H., Depasquale, J., Seitenzahl, I. R., Hewitt, J. W., Blondin, J. M., Borkowski, K. J., Ghavamian, P., Petre, R., and Reynolds, S. P. (2017). The Three-dimensional Expansion of the Ejecta from Tycho's Supernova Remnant. ApJ, 842(1):28.

Williams, B. J. and Temim, T. (2017). Infrared Emission from Supernova Remnants: Formation and Destruct page 2105.

Williams, R. M., Chu, Y.-H., Dickel, J. R., Beyer, R., Petre, R., Smith, R. C., and Milne, D. K. (1997). Supernova Remnants in the Magellanic Clouds. I. The Colliding Remnants DEM L316. ApJ, 480(2):618-632.

Woltjer, L. (1972). Supernova Remnants. araa, 10:129.

Woosley, S. E., Pinto, P. A., Martin, P. G., and Weaver, T. A. (1987). Supernova 1987A in the Large Magellanic Cloud: The Explosion of a approximately 20 M_{sun} Star Which Has Experienced Mass Loss? ApJ, 318:664.